Experimental Studies of Flapping Foils for Energy Extraction

by

Bradley James Simpson

B.S., Mechanical Engineering
University of California, San Diego (2006)

Submitted to the Department of Mechanical Engineering
in partial fulfillment of the requirements for the degree of

Master of Science in Mechanical Engineering

at the

MASSACHUSETTS INSTITUTE OF TECHNOLOGY

September 2009

Author .....
Department of Mechanical Engineering
August 10, 2009

Certified by. .....
Michael S. Triantafyllou
Professor of Mechanical and Ocean Engineering
Thesis Supervisor

Accepted by .....
David E. Hardt
Professor of Mechanical Engineering
Chairman, Departmental Committee on Graduate Students

Experimental Studies of Flapping Foils for Energy Extraction

by

Bradley James Simpson

Submitted to the Department of Mechanical Engineering
on August 10, 2009, in partial fulfillment of the
requirements for the degree of
Master of Science in Mechanical Engineering

Abstract

For centuries scientists have looked to nature for inspiration for novel and efficient solutions to engineering problems. Recently, research on fish and other marine mammals has shown their ability to efficiently extract energy from both steady and unsteady flows. Our research uses this previous work as motivation for experimentally examining the hydrodynamic performance of flapping foils to extract energy in a two-dimensional flow. We focused on identifying the effects that foil motion parameters had on the hydrodynamic energy extraction efficiency and resolving the wake structure downstream of the foil. The primary foil motion parameters investigated were the non-dimensional flapping frequency of the foil, the non-dimensional excursion amplitude of the foil, and the profile of the foil path during a typical energy extraction cycle. The heave and pitch of the fin was approximated by a NACA 0012 foil heaving and pitching sinusoidially 90° out of phase at a Reynolds number of 13,800. Energy extraction efficiencies of up to $\eta = 0.45$ were found within a very small parametric region for small oscillation amplitudes while broad regions of appreciable efficiency were found at large oscillation amplitudes. The highest efficiency regions were all found to exhibit the same 2P vortex shedding mode. Further, the similitude between experiments for varying oscillation amplitude was not consistent when parameterized by the Strouhal number. This study shows parameterizing the flapping frequency by the reduced frequency results in vortex modes and efficiency contours aligning between varying oscillation amplitudes.

Thesis Supervisor: Michael S. Triantafyllou
Title: Professor of Mechanical and Ocean Engineering

Acknowledgments

First and foremost, my advisors, Professor Michael Triantafyllou and Professor Franz Hover, have been incredibly helpful in this entire process and I cannot thank them enough for their time and guidance over the last two years. They have been incredible advisors and have always given their time for random and last minute questions and advice along with encouragement, which is infinitely appreciated.

The people who I worked with in the MIT Towing Tank lab were also amazingly helpful in this entire process and I owe much to them. Jason Dahl was always around for sanity checks and invaluable experimental advice as well as last minute questions. He also proved to be a formidable bocce ball opponent during lunch lab breaks which were great. Stephen Licht also helped out a great deal with advice on experiments and data techniques, as well as building a pretty great robotic turtle which was fun to play with while it was swimming. Ricky Galvao as well helped throughout the two years and proved a semi-good bocce ball opponent.

Contents

List of Figures

List of Tables

Chapter 1

Introduction

Designs inspired by nature have appeared in science and engineering for centuries. Under the assumption that evolution has produced near-optimal solutions, natural designs lend themselves to be used in applications utilizing their evolutionary design advantages. Research done on fish has shown that both their streamlined shape and structural properties enable efficient energy extraction from fluid flows. It has been shown that the fluid-structure interaction between fish and periodically shed vortices can result in passive upstream propulsion. This fluid-structure interaction lends itself to further study as a novel way of efficiently harnessing energy from both steady and unsteady flows.

1.1 Research Motivation

Global energy demand is expected to increase almost 50% by the year 2030. This astronomical growth in global demand for both energy and improved methods of harnessing energy, has led to an increase in research into alternative and efficient energy harnessing methods. While wind and solar have both received significant attention, hydropower, and more specifically ocean energy, has also emerged as an important player in the energy space. The comparatively large power density offered by ocean energy has made it worthwhile to investigate new ways of harnessing this energy. A recent study found that an average power density of 2-3 kW/m^2 measured

below the ocean surface and perpendicular to the wave front is the largest of all renewable energy sources and is sufficient to meet the worlds current energy demands [7].

There have been many methods designed for ocean energy extraction including ocean thermal energy [21, 29], wave energy [7, 18, 20], and current energy [5, 28]. Our research focuses on wave and current systems due to the fact that ocean thermal systems have been studied more extensively. Wave energy devices rely on surface waves and near-surface waves for energy. Devices recently designed including oscillating water columns, surging, pitching, and heaving devices. Energy extraction methods utilizing currents rely on the periodic rise and fall of the ocean surface as a means of generating energy. Most devices which extract energy from marine and tidal currents resemble windmills and use horizontal axis turbines. However, some variations exist including vertical axis turbines, oscillating vanes, and venturi constrictions [5].

Seemingly unrelated is the field of biomimetics which is concerned with the application of natural biological systems, methods, and processes to traditional engineering systems. Based on the premise that evolution has created some of the most optimized systems, biomimetics uses these designs, which have been refined over millions of years, as inspiration for efficient designs. Biomimetics can clearly be seen demonstrated throughout a gamut of engineering designs, from DaVincian aircraft to modern hull design to modern morphing aircraft wings. Further, observations of fish and other marine mammals have consistently yielded novel designs such as the first military submarine aptly named the Turtle.

Recent studies of biomimetic foils have found them to be extremely efficient at generating thrust and rapid maneuvering [22, 13, 23, 6, 16, 30, 24, 27, 3, 1, 10, 26]. See [25] for a review. Complimentary work has focused on how fish and biomimetic foils exploit existing vortex structures to produce thrust upstream[11, 4, 17, 27, 2, 8]. In the extreme case, passive upstream swimming is observed [2]. Our research uses these aforementioned benefits as inspiration for the study of a biomimetic flapping foil as an energy extraction device from underwater flows.

1.2 Previous Work

While our research deals with energy extraction from flows via a flapping foil, biomimetic propulsion research is a closely related area of work which has been studied extensively. Notably, operating parameters for high efficiency propulsion could lead to insight into areas of high efficiency for energy extraction. As such, the work is briefly reviewed.

Work by Anderson, Streitlien, Barrett, and Triantafyllou experimentally and numerically investigated oscillating foils for propulsion [1]. The parametric study included the phase angle between the heave and pitch motion of the foil, ϕ, the non-dimensional heave amplitude, h_0/c, the maximum angle of attack, α_{max}, and the Strouhal number, St, which is used as a non-dimensional oscillation frequency parameter. The phase angles tested were $\phi = 75°$, $90°$, and $105°$. The non-dimensional heave amplitudes tested were $h_0/c = 0.25$, 0.5, and 0.75. The maximum angle of attack was varied from $5°$ to $30°$ in $5°$ increments. Finally, the Strouhal number was varied from 0.05 to 0.6 in small increments. The experimental setup included a NACA 0012 foil that heaved and pitched in the MIT Towing Tank.

It was found that numerical predictions, both linear and non-linear, of efficiency underestimated the thrust efficiency, which was attributed to inability to take into account flow separation including leading-edge vortices (LEV) forming at high angles of attack. Experimental results found a maximum efficiency of 87% for the largest h_0/c of 0.75, $\phi = 75°$, $St = 0.30$, and $\alpha_{max} = 20.2°$. The largest coefficient of thrust was observed at $h_o/c = 0.75$, $\phi = 90°$, $St = 0.48$ and $\alpha_{max} = 30°$. The efficiency was found to be 70% in this case. The vortex formation pattern was also indicative of the thrust performance, most notably the formation of a strong leading-edge vortex (LEV) which is convected downstream and interacts with the trailing-edge vortex (TEV).

Flapping foil energy extraction research began in 1981 when McKinney and DeLaurier analyzed the "wingmill", an oscillating-wing windmill that could heave and pitch in a wind tunnel [19]. A quasi-steady numerical analysis was carried out in

addition to experimental tests in order to generate time-varying coefficient of lift profiles for comparison with experimental results. McKinney and DeLaurier constructed the apparatus using harmonic motions for the heave and pitch including a variable phase offset between these motions. A friction brake was used in order to the measure power output of the oscillating NACA 0012 foil. The speeds tested were 6.2 and 8.0 m/s, the non-dimensional heave amplitude was held constant at $h_0/c = 0.3$, the pitch amplitude values, θ_0, were set to 25° and 30°.

It was found that theoretical predictions generally underestimated the power output by approximately 20% due to dynamic stall effects and LEV suction. Maximum power output of 9 watts occurred at $\phi \approx 110°$ while a maximum efficiency of 28.3% occurred at $\phi \approx 90°$ and $f \approx 4.5$ Hz.

Isshiki and Grue later experimented with submerged foils as a means of self-propulsion [11, 9] and analytically and experimentally verified that a simple hydrofoil attached to the underside of the boat can propel a boat forward in both head and following wave seas by translating the heaving of the ship to the foil which in turn generates vortices resembling a jet. See Grue for a detailed analysis of the vortex generation.

Further work in flapping foil energy extraction was also experimentally performed by Liao, Beal, Lauder and Triantafyllou in physical fish specimen [17]. They used a euthanized trout and placed it to a flow comprised of periodically shed vortices behind a D-cylinder. Using a combination of visualization techniques and measuring muscle activity using electromyography, they found that when exposed to the vortex street, the trout would use comparatively less muscle activity to swim as it slalomed through vortices. This suggests that fish could exploit the vortices present in natural flows to reduce the locomotive effort when compared to conventional undulatory swimming.

Numerical parametric studies of flapping foil energy extraction have also been carried out since the original experimental work of McKiney and DeLaurier. Jones and Platzer have performed several numerical analysis of flapping-wing power extraction in order to corroborate McKinney and DeLaurier's experimental work as well as attempt to find operating regimes for local efficiency and power extraction maxima[13,

14, 12]. Jones and Platzer found an optimal efficiency of 26% for a reduced frequency $k = 0.25$. They found that greater efficiencies exist in regions that were not possible to attain with the experimental apparatus in [19]. However, their numerical results were still limited to a maximum angle of attack of 15° because they were unable to account for flow separation.

Kinsey and Dumas furthered numerical analysis research on flapping foil energy extraction with a two-dimensional laminar-flow simulation using the computational fluid dynamic program FLUENT [15]. They analyzed a non-dimensional frequency and pitching-amplitude domain: $0 < f^* < 0.25$ and $0° < \theta_0 < 90°$. For these numerical experiments the heave to chord ratio was fixed at $h_0/c = 1$, the Reynolds number was fixed at $Re = 1100$, and the pitching point was fixed at 1/3 the chord length. For their analysis, Kinsey and Dumas's NACA 0015 foil underwent harmonic pitching and heave as well, resulting in a non-harmonic angle of attack profile. They found efficiencies as high as 34% for $f^* \approx 0.12$-0.18. The highest efficiency point was noted to have $\alpha_{max} \approx 35°$ and the max heave velocity nearly equal to the freestream flow speed. Dynamic stall was also noted which was favorably phased with the pitching of the foil near the maximum excursion point, helping to reduce input energy for rotating the foil through transition point.

Zhu and Peng also performed a numerical analysis on energy harvesting by a flapping foil specifically concentrating on low Reynolds number flows and vorticity control mechanisms in order to increase energy capture potential of the system [31]. Phasing of LEVs were shown to play an important role in energy input to the system. At high angles of attack, LEV can form and travel down the length of the foil until they are shed at the trailing edge. If timed correctly, the LEV can actually help the pitching of the foil and transfer energy back into the system. If timed incorrectly, increased energy was required to supply the righting moment from the unfavorably-phased low-pressure field.

1.3 Chapter Preview

Chapter two will introduce background concepts and nomenclature relevant to flapping foils used throughout the rest of the thesis. Descriptions of relevant parameters and kinematics of flapping foil energy extraction are also given.

Chapter three describes the various experiments that are performed along with descriptions of the experimental apparatus used. Descriptions of the experimental methods will also be given including calibration and filtering methods, and digital particle image velocimetry (DPIV) techniques.

Chapters four presents the experimental results of our parametric study focusing on the non-dimensional Strouhal number, the angle-of-attack profile, and the non-dimensional excursion amplitude. In this chapter we will examine the effects that each parameter has on periodic hydrodynamic forcing, the hydrodynamic energy extraction efficiency, and the downstream wake.

Chapter five discusses the results, correlating the hydrodynamic energy extraction efficiencies with general trends in force phasing, leading edge vortex (LEV) shedding, and the downstream wake from the parametric study.

Chapter six draws conclusions on the research. Future work on the project is proposed and recommendations are also made based on the current research.

Chapter 2

Background

2.1 Relevant Parameters

One of the principle defining parameters of a flow is the Reynolds number, Re, which is the ratio of inertial to viscous forces. It is defined below where U is the free stream velocity, L is the characteristic length and ν is the kinematic viscosity of the fluid.

$$Re = \frac{UD}{\nu} \tag{2.1}$$

As the Reynolds number changes so does the flow around the object immersed in the flow, in our case a hydrofoil. At low Reynolds numbers, flows are similar to those predicted by potential flow theory, with the flow remaining attached to the foil and a steady wake. As Reynolds numbers increase, the flow can separate from the foil, causing localized rotating regions of flow which can shed from the foil producing a vortex.

A common dimensionless parameter used to characterize such vortex shedding, particularly a periodic vortex street such as one encountered in the wake of a flapping foil or a bluff body, is the Strouhal number, St, defined below. The Strouhal number characterizes the oscillating flow and is described by the frequency of vortex shedding, f, the characteristic length, L, and the free stream velocity, U. For flapping foils, the characteristic length is commonly the total heave excursion, or the amplitude, A,

which is equal to twice the heave distance, h_o. It should be noted that the frequency of vortex shedding is typically unknown initially and it is common to substitute the flapping frequency for f.

$$St = \frac{fA}{U} \tag{2.2}$$

While the Strouhal number emphasizes the importance of the foil kinematics, the reduced frequency, f_r, is a dimensionless parameter which describes an oscillating wake in terms of the foil geometry instead of the foil kinematics. The reduced frequency is described by the frequency of vortex shedding or the flapping, f, the chord length, c, and the free stream velocity, U.

$$f_r = \frac{fc}{U} \tag{2.3}$$

It is also necessary to define some several important fluid dynamic properties seen in these flows. Circulation describes the flow around a closed contour, or a "macro-vorticity". In many cases it is used in many cases in order to predict lift forces through the Kutta-Joukowski theorem. Circulation is defined as the line integral of fluid velocity tangent to the integration path around a close loop of fluid flow and is given by:

$$\Gamma = \oint_C \mathbf{V} \cdot \mathbf{dl} \tag{2.4}$$

The Kutta-Joukowski theorem relates the lift on an object given its circulation (with the closed loop integral around the object), the density of the fluid, and the velocity of the object through the flow. It is defined as:

$$L = \rho V \Gamma \tag{2.5}$$

Finally, vorticity, which is a measurement of the local angular rate of rotation of a fluid is defined as the curl of the velocity field:

$$\omega = \nabla \times \mathbf{V} \tag{2.6}$$

The relation between the vorticity, circulation, and lift is important as it is possible to determine the lift distribution over a wing using vorticity alone. Using Stokes' theorem to transform a closed-loop line integral to a surface integral over an area, it is possible to rewrite Equation 2.4 in terms of vorticity, in order to relate vorticity to lift distribution along an object's surface.

$$\Gamma = \oint_C \mathbf{V} \cdot \mathbf{dl} \tag{2.7}$$

$$= \iint_S (\nabla \times \mathbf{V}) \cdot \mathbf{dS} \tag{2.8}$$

$$= \iint_S \omega \cdot \mathbf{dS} \tag{2.9}$$

2.2 Equations of Motion

The kinematics of an oscillating foil is a combination of the heave motion, $h(t)$, which is defined as the translation of the foil transverse to the free stream velocity, and the pitching motion, which is defined as rotation of the foil about a pitching point viewed from the chord-wise planform. Other motions are possible such as inline motion and span wise pitching, however we limit our study to heave and pitch. For the ideally two-dimensional system we are considering we limit motion to this two degree of freedom system. Combining motions in these two degrees of freedom results in an angle of attack, $\alpha(t)$. As seen in Figure 2-1, these variables determine the angle of attack profile.

Since there are more variables than degrees of freedom, we must choose which variables are independent and which are dependent. Based on previous work with fish, we use the commonly cited assumption that flapping motions can be modeled as sinusoids [16, 17, 24, 27]. The three main time-based parameters we can control are angle of attack, pitch, and heave. In order to determine the dependency of one

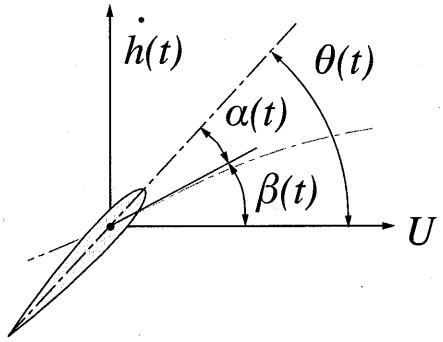

Figure 2-1: Angle of attack, $\alpha(t)$, Pitch Angle, $\theta(t)$, Combined Velocity Angle, $\beta(t)$, Free Stream Velocity, U, Heave Velocity, $\dot{h}(t)$

parameter on the other we examine the parameters.

The combined velocity angle, $\beta(t)$ is defined as $\dot{h}(t)/U$. Therefore, as seen in Figure 2-1, the pitch angle, $\theta(t)$ is defined as

$$\theta(t) = \alpha(t) + \beta(t) \tag{2.10}$$

$$= \alpha(t) + \arctan\left(\frac{\dot{h(t)}}{U}\right) \tag{2.11}$$

From Equation 2.11 we see that we can only command two of the three kinematic parameters without having an overdetermined system. There are three combinations possible in this case: 1) harmonic angle of attack profile and pitch profile with a driven heave profile 2) harmonic angle of attack profile and heave profile with a driven pitch profile and 3) harmonic pitch profile and heave profile with a driven angle of attack profile. To see the advantages of forcing a harmonic angle of attack we will quickly look at the effect of not forcing it. We assume a harmonic heave motion,

$$h(t) = h_0 \sin(\omega t) \tag{2.12}$$

where h_0 is the heave amplitude in meters, ω is the frequency of oscillation in

rad/sec, and t is time in seconds. We also force the pitch motion to be harmonic,

$$\theta(t) = \theta_0 \sin(\omega t + \psi) \tag{2.13}$$

where θ_0 is the pitch amplitude in radians and ψ is the phase angle between the pitch and heave in radians.

If we refer to Figure 2-1 again, we can see that the angle of attack due to forced harmonic heave and oscillation motions is

$$\alpha(t) = \theta(t) - \arctan\left(\frac{\dot{h(t)}}{U}\right) \tag{2.14}$$

$$\alpha(t) = \theta_0 \sin(\omega t + \psi) - \arctan\left(\frac{h_0 \omega \cos(\omega t)}{U}\right) \tag{2.15}$$

Instead of producing a resultant harmonic motion, it is seen from Equation 2.15 that the angle of attack profile will vary greatly within the parametric space. An example of this degradation can be seen in Figure 2-2 which shows the resultant angle of attack profiles for varying Strouhal numbers. For this example, an iterative solving method was used to find the pitch amplitude, θ_0, corresponding to $\alpha_{max} = 15°$ for the given ω and h_0. As the frequency increases we note an introduction of higher harmonics into the angle of attack profile which would result in spurious vortex formation as LEV formation is largely a function of angle attack.

We therefore use a harmonic pitch motion (Equation 2.13) and a harmonic angle of attack profile,

$$\alpha(t) = \alpha_0 \sin(\omega t) \tag{2.16}$$

where α_0 is the maximum angle of attack during one cycle. From Equation 2.16 we see that α_{max} occurs at $\pi/2$ and $3\pi/2$ when the heave excursion is zero and the heave velocity is a maximum. Our final equation used for generating motions is then,

$$\theta(t) = \alpha(t) + \arctan\left(\frac{\dot{h(t)}}{U}\right) \tag{2.17}$$

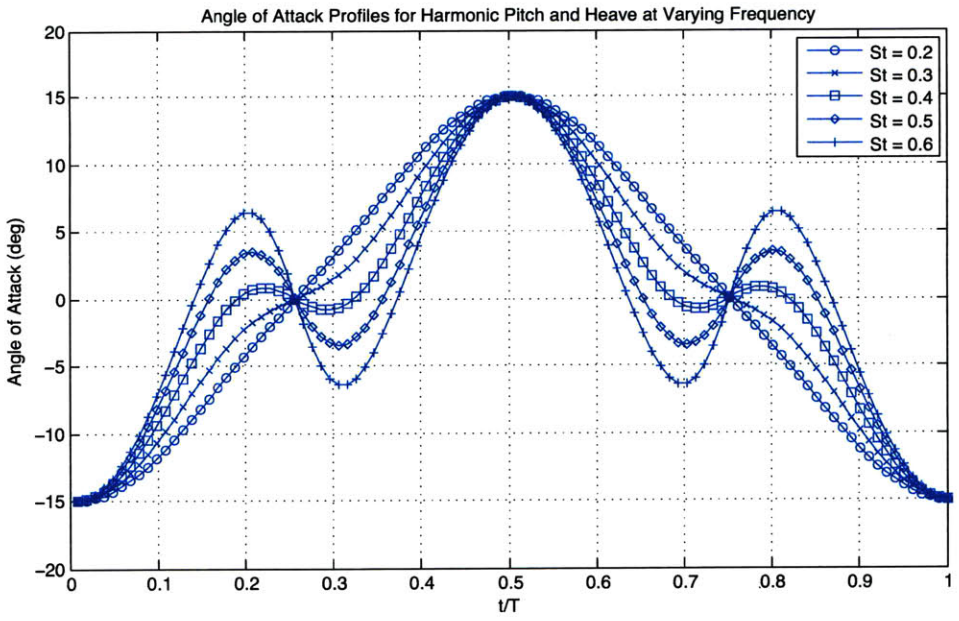

Figure 2-2: Effect of Harmonic Heave and Pitch Motions on Angle of Attack Profiles for $\alpha_{max} = 15°$ for Varying Frequencies

In order to solve for $h(t)$ we simply rearrange 2.17 and integrate $\dot{h(t)}$ to get

$$h(t) = U \int_0^t \tan(\theta(t) - \alpha(t))\, dt \tag{2.18}$$

In practice, an iterative solver was used to find the θ_0 value for a given α_{max} which would produce the desired forced heave motion of amplitude h_0.

2.3 Power Extraction

A flapping foil oscillating in both pitch and heave can exist in two domains of operation: a thrust producing mode and a power extraction mode. This is dictated by the downstream wake structure which results from the foil kinematics. The two different modes are illustrated for one cycle in Figure 2-3. It should be noted the difference between the two is simply the sign of the angle of attack. For power extraction, $\alpha_{max} < 0°$ and for thrust producing, $\alpha_{max} > 0°$.

Figure 2-4 shows the instantaneous velocity field at a given time and illustrates

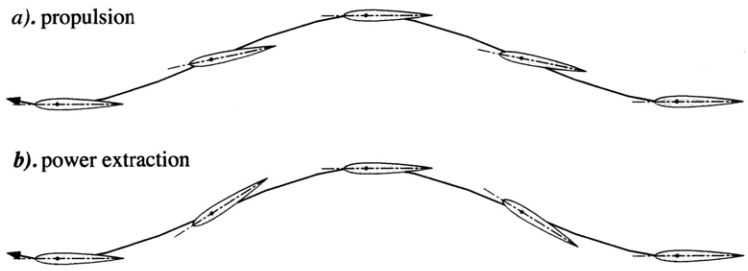

Figure 2-3: Domains of Operation: a) Thrust producing mode and b) Power extraction mode

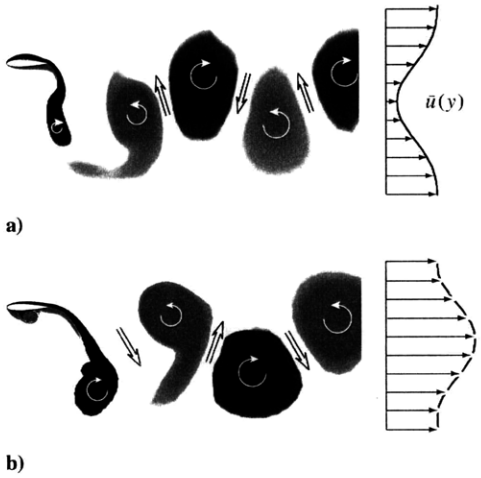

Figure 2-4: Instantaneous Vortices and Downstream Wake for a) Power Extraction and b) Thrust production modes (Adapted from [15])

how the vortices combine to produce a downstream jet or wake deficit. In the power extraction mode, we see a vortex pattern similar to that originally identified by von Karman and commonly called a von Karman street. This pattern is also seen in most other bluff-body drag instances. The inline velocity induced by wake vortices is seen to have a deficit indicating a transfer of energy to the system. In the thrust producing mode we see a reverse von Karman street which induces an increased downstream inline velocity, producing a jet, indicating a transfer of energy from the system to the fluid in order to generate thrust.

In order to quantify the power extracted from the flow using forces measured on the foil, we provide some basic equations for power. Since we only have two degrees of

freedom on the system, pitch and heave, the power will have to be extracted through these degrees of freedom. This corresponds to a horizontal component of force on the foil and a torque applied about the pitching center by the foil. The basic equation which takes into account these two contributions is as follows

$$P(t) = P_L(t) + P_\theta(t) = F_T\dot{h}(t) + M(t)\dot{\theta}(t) \tag{2.19}$$

where $P(t)$ is the time-varying power, $P_L(t)$ is the power due to the heave component, $P_\theta(t)$ is the power due to the torque about the pitching center, F_T is the transverse hydrodynamic force on the foil, $\dot{h}(t)$ is the heave velocity, $M(t)$ is the torque about the pitching center, and $\dot{\theta}(t)$ is the angular velocity of the foil.

In the power extraction mode, as previously stated, $\alpha_{max} < 0°$. If we look at the force components on the foil it is clear why this is the case: with the given angle of attack sign, the transverse component of the hydrodynamic force is typically in phase with the heave velocity. As seen in Figure 2-5, the transverse force, F_Y, acts in the same direction as the heave velocity. From Equation 2.19 we see that in order for $P_L(t)$ to be positive (power into the system), the heave velocity and transverse force must be the same sign, i.e. they both must be pointing in the same direction. Additionally, if the torque applied to the pitching center is in the same rotational direction as the angular velocity, the system can absorb rotational energy in this degree of freedom as well.

The efficiency of the system can be defined in several ways. For these experiments we choose to define the efficiency as the ratio of the mean total power extracted to the total potential power of the oncoming flow that the pitching point of the foil sweeps through.

$$\eta = \frac{\overline{P}}{P_{total}} \tag{2.20}$$

$$= \frac{\overline{P}_L(t) + \overline{P}_\theta(t)}{\frac{1}{2}\rho U^3 2h_0 s} \tag{2.21}$$

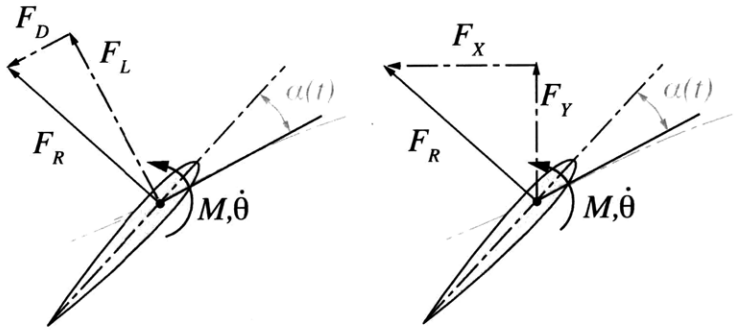

a) hydrodyanmic forces *b)* component-resolved forces

Figure 2-5: Instantaneous forces acting on foil: M is the torque, $\dot{\theta}$ is the rotational velocity, F_L is the hydrodynamic lift, F_D is the hydrodynamic drag, F_Y is the transverse component of the hydrodynamic forces, F_X is the in-line component of the hydrodynamic forces, and F_R is the resultant force. Forces depicted as a) Hydrodynamic forces and b) Resolved cartesian components

Equation 2.20 gives a formula for the efficiency where ρ is the density of water, U is the free stream velocity, A is the cross-sectional area swept out by the foil during one cycle, h_0 is the heave amplitude, and s is the span of the foil.

Chapter 3

Experimental Setup

Experiments were carried out in the MIT Towing Tank testing facility. All tests were carried out in the small tank which is enabled with DPIV for flow visualization. Force data was used in addition to flow visualization data in order to get a more complete explanation of optimal parameters for power extraction and the flow mechanisms behind these points of high efficiency. This section will detail the experimental apparatus, sensors, motion control, and techniques used for collecting and analyzing data.

3.1 Small Tank and Carriage

The tank used to perform experiments is located in the MIT Towing Tank testing facility. It measure 2.4m x 0.75m x 0.7m and is made of glass with an external rigid frame made of 80/20 aluminum. The glass is joined at the seams by caulk and length-wise and width-wise bowing is kept to a minimum with the external frame. The external frame also provides the surface for the carriage to be towed on. A computer-generated model of the small tank can be seen in Figure 3-1.

The lip of the 80/20 frame provides contact points for the wheels of the small carriage which is towed length-wise using a belt-drive with variable towing speed. The carriage is made of aluminum and provides the base for the experimental equipment. The basic components of the experimental equipment involve the motion control

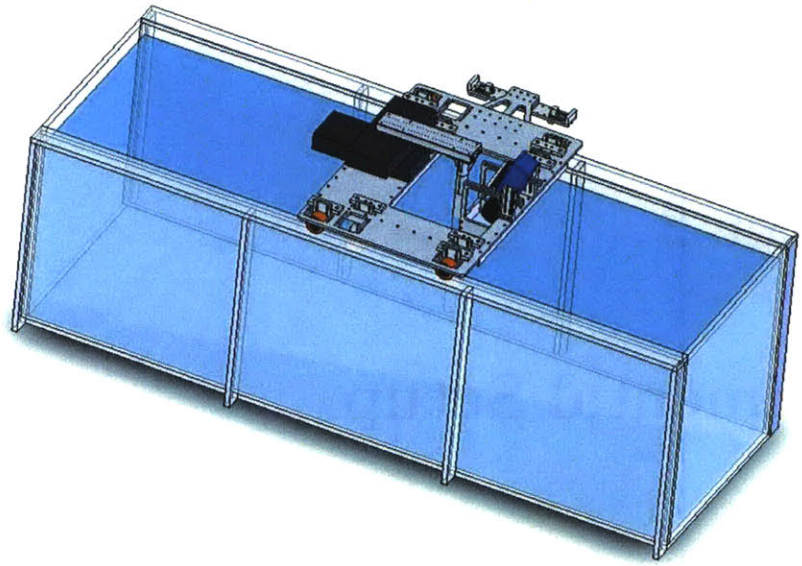

Figure 3-1: Computer-generated Model of the Small Tank and Towing Carriage

components, the force sensor components, and the imaging components. A close up of these components can be seen in Figure 3-2.

3.2 Motion Control

The small carriage has three-axis of motion available for experiments; inline, transverse, and pitch motion. For our experiments we only employ transverse and pitch motions.

Inline and transverse motions are generated by a set of Parker Trilogy T2SB14 open-ended linear motors. One motor controls movement in the inline direction while the other motor is mounted on top and controls movement in the transverse direction. Their motion is programmed and loaded into the PMAC software located on a lab computer which then writes the commands to the PMAC controller card. When the motion is run, this controller card outputs a signal to an amplifier supplied by Parker Trilogy which amplifies the output to the levels required by the motors. The six-axis load cell, pitch motor, and foil are mounted onto a cantilevered arm which is attached to the two-axis linear motor in order to generate required motion.

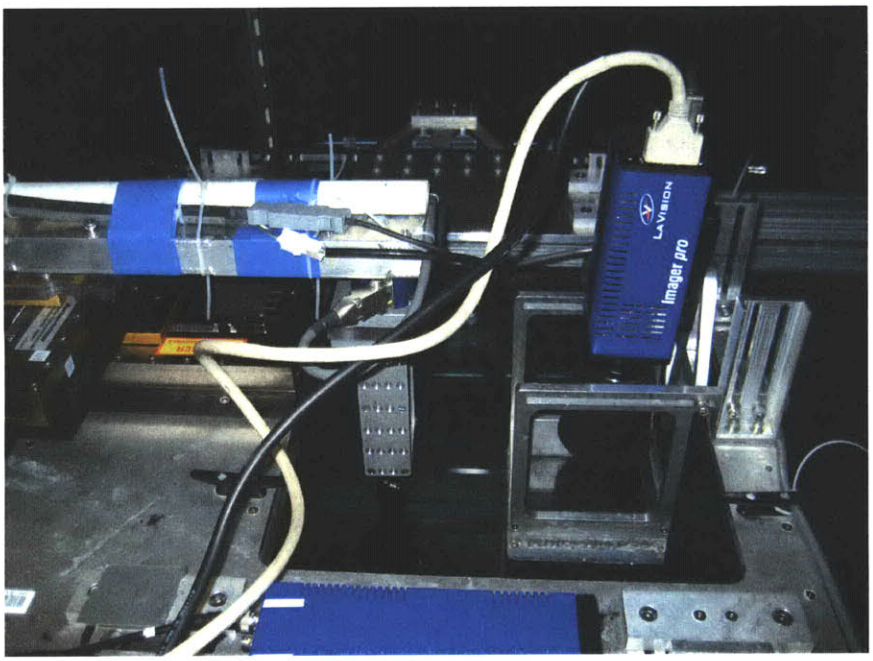

Figure 3-2: Small Carriage Setup: Cantilevered arm is shown mounted on Parker-Trilogy two-axis linear motors. JR3 Load cell is attached to cantilevered arm and pitch motor housing is attached to laod cell. Foil is seen protruding into water. LaVision Imager Pro HS is seen mounted on camera housing angled towards the foil.

The pitch motion is controlled by Yaskawa SGMM-A2S312 AC servo motor. The motion is programmed and executed similarly to that of the linear motors previously explained. The pitch motor's shaft is coupled to a machined shaft with mounting holes for the foil to attach at the rotation point. An image of the experimental setup showing the cantilevered arm and its components including the pitch motor and force sensor are shown in Figure 3-3.

3.3 Force Sensor

The force sensor used in the experiments is a JR3 model 20E12A-125 six-axis load transducer which is mounted at the end of the cantilevered arm, positioned between the arm and the pitch motor. The moments and forces are measured via strain-gauges internal to the force sensor. It has a 110 N maximum load rating in each of the three force axis and a 5 N-m maximum load rating in the moment axis. The forces are

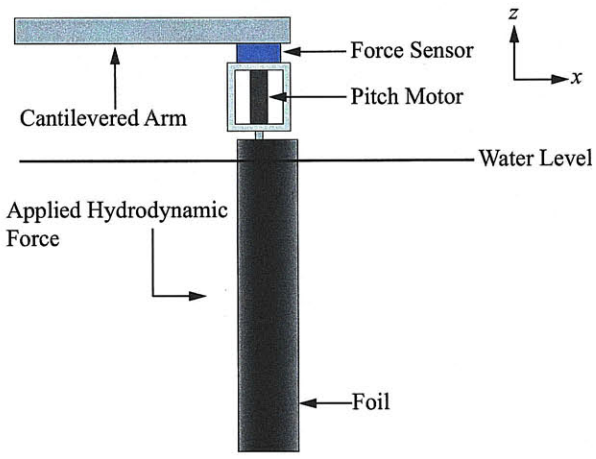

Figure 3-3: Graphical illustration of cantilevered arm and attached force sensor, pitch motor, and NACA 0012 foil.

transmitted to an amplifier which also has basic filtering abilities to eliminate system noise from the force measurements.

A factory calibration was supplied with the force sensor, however, because the experimental setup and the applied loads varied so much from the factory calibration setup, applied and measured forces had large discrepancies when using the factory supplied calibration. It was therefore necessary to calibrate the six-axis force sensor with applied loads and moments more similar to the ones consistent with that of the experiment.

3.3.1 Calibration

Due to the nature of mutli-axis load cells, cross-coupling of forces is typically encountered. The load cell outputs a voltage which is related to the measured moments and forces ($F_x, F_y, F_z, M_x, M_y, M_z$) by some proportional constants. For our experiments, the dominant forces and moments that were of importance was the lift force, F_y, the drag force, F_x, and the applied torque to the foil, M_z. Because these forces are coupled with moments, M_x and M_y respectively, these are also important in our calibration setup. The only remaining force, F_z, is the buoyant force of the submerged foil which does not change throughout the experiments and will therefore have no effect on the

calibration matrix. Leaving out F_z, the calibration matrix will be 5 x 5, or 6 x 6 with a row of zeros.

The sensor outputs six voltage channels which are multiplied by coefficients in order to get the output force, described by the relation shown in Equations 3.1, where F is the force, C is the calibration coefficient in force/volt, and V is the output voltage. For the calibration, we applied known forces and recorded the output voltage for all of the channels. We performed 182 different measurements of known forces, producing an F and V both of size 6 x 182 which were used to calculate C.

$$F = C * V \tag{3.1}$$

The calibration apparatus was as similar to the experimental apparatus as possible in order to retain similarity in calibration forces and experimental forces. However, in order to apply a static moment about the z-axis, the pitch motor was removed. Additionally, a test cylinder of approximately the same length as the test foil was attached to the force sensor instead of the foil in order to have a constant diameter for applying moments about the z-axis and for ease of hanging calibration weights.

There were two primary arrangements of the calibration setup: one orientation for measuring F_x, M_y, and M_z, which is called the drag orientation, and one orientation for measuring F_y, M_x, and M_z, which is called lift orientation. The different orientations can be seen in Figure 3-4.

In the various orientations it was necessary to first level all the axes to make sure that the applied forces were in fact applied only in the axes desired and so that forces were not inadvertently applied to other axes. For every measurement, an initial reading was taking to make sure the individual offsets were all taken into account, although there was no noticeable sensor drift over time. Taking measurements for F_x, F_y, M_x, and M_y were relatively simple. This consisted of suspending weights varying in mass from 50 grams to 500 grams at locations along the cylinder's length and automatically recording voltage measurements for each channel. In order to get data for M_z we had to attach a clamp to the cylinder from which weights could be

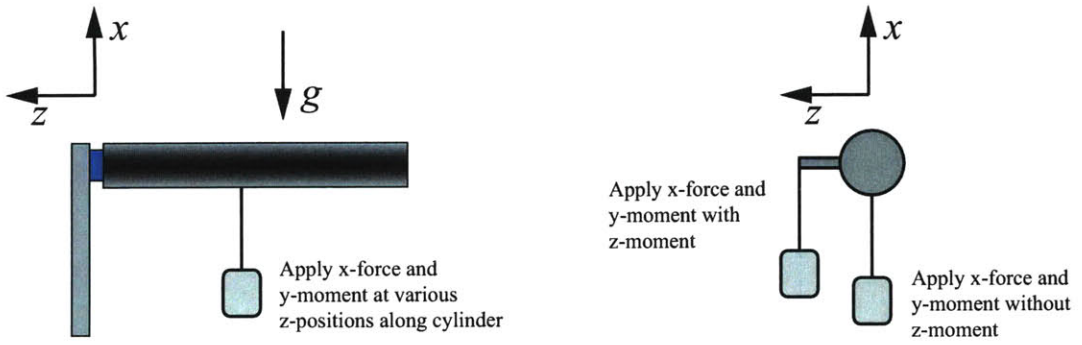

a) Drag Calibration

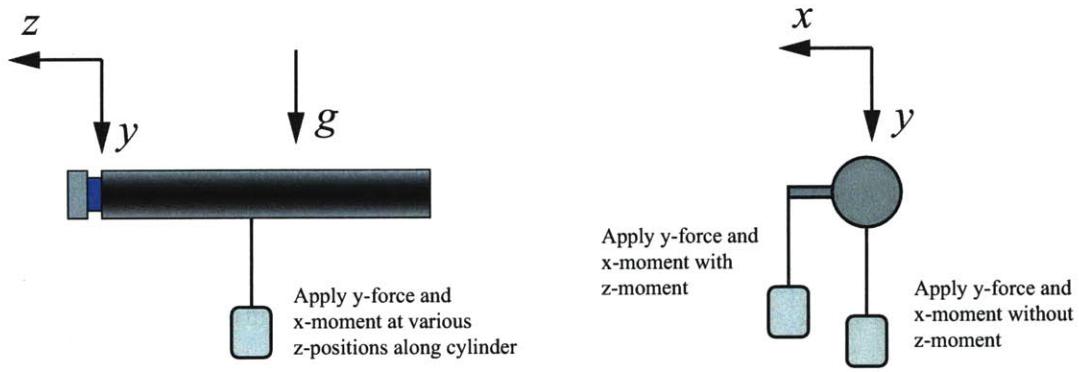

b) Lift Calibration

Figure 3-4: Calibration setup for six axis force sensor: a) Drag calibration involves loading cylinder at various z-positions and measure force in the x-axis with corresponding moment in y-axis. Moments in the z-axis are also measured when applicable. b) Lift calibration involves the cantilevered arm rotated 90° and loadings similar to those described for the drag calibration.

	F_x	F_y	F_z	M_x	M_y	M_z
F_x	13.0371	-0.4955	1.4331	-0.8586	-0.2703	0.8107
F_y	0.3314	13.1023	1.4076	0.1821	-1.5790	0.7400
F_z	0	0	0	0	0	0
M_x	-0.0678	0.1755	-4.6343	0.4863	0.0874	0.2208
M_y	-0.2065	0.0131	-1.1782	-0.0173	0.7100	0.0310
M_z	0.0580	0.0189	1.5305	0.0514	-0.0336	0.5354

Table 3.1: Calibration Matrix

radially suspended in order to produce an axial moment.

The results of the calibrations can be seen in Figure 3-5 and the 6 x 6 calibration matrix is shown in Table 3.1. The majority of the dotted points, which represent the experimentally calibrated forces, lie on the solid lines, which represent the applied forces, indicating a good calibration. It should be noted that the moment axes had the largest deviations between ideal and calibrated forces. These are noted to occur in Figures 3-5c, 3-5d, and 3-5e. These lines exhibit poor calibration performance due to these measurements being taken with the largest weights loaded at the furthest point on the cylinder (32 in) resulting in saturated readings in moment channels and non-linear performance. Particularly in the M_z channel which is largely due to only calibrating with a small moment arm (0.75 in) and the sensitivity of the load cell at such small levels. However, the average percentage error for each channel is acceptable and are as follows: F_x 0.57% error, F_y 0.54% error, M_x 1.16% error, M_y 1.33% error, M_z 5.14% error.

Data acquisition for force data was done using a National Instruments USB NI-6218 and LabView. Data from the six-axis force sensor and the motor encoders (inline, transverse, and pitch) were both recorded. The sampling frequency of the DAQ card was 1000 Hz and the encoder sampling frequency was approximately 500 Hz.

3.3.2 Foils

Two separate foils were used in these experiments. Both foils had NACA 0012 profiles machined out of 7075 aluminum. One foil had a chord which measured 1" in length

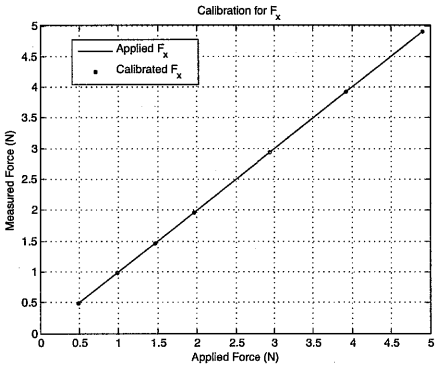

(a) F_x Calibration

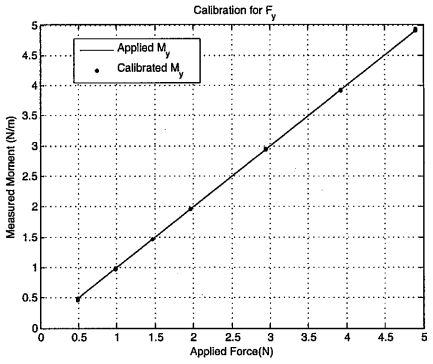

(b) F_y Calibration

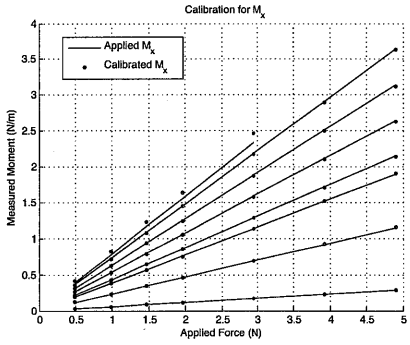

(c) M_x Calibration

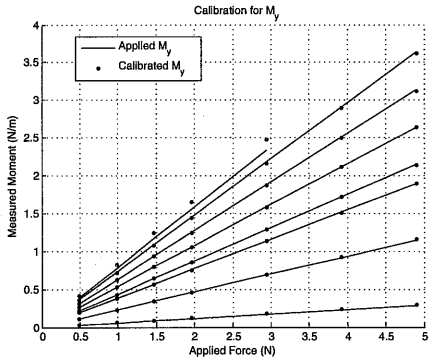

(d) M_y Calibration

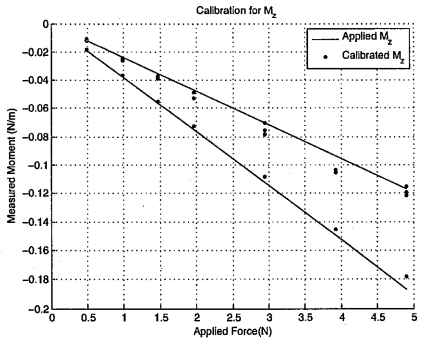

(e) M_z Calibration

Figure 3-5: Calibration Results

and had a submerged span of 15" (aspect ratio of 15) while the second foil had a chord which measured 2.73" in length and had a submerged span of approximately 21.5" (aspect ratio of 7.9). As explained below in Section 3.3.4, the larger chord foil was used for force measurements and imaging while the shorter chord foil was used strictly for imaging due to the relatively large contribution of inertial forcing to the overall force signal.

3.3.3 Foil Centering

Before each set of experiments it was necessary to locate the zero degree pitching point of the foil, in order to prevent a biased angle of attack profile. Ten individual runs were performed at fixed angles of attack and the mean drag coefficients were recorded. The static angles of attack used in the calibration runs were kept below the angle of attack at which separation would occur in order to have a linear coefficient of lift line. The point at which the coefficient of lift line crossed the coefficient of drag curve was the point of minimum drag and minimum lift which corresponds to the zero degree angle of attack.

3.3.4 Inertial Measurements

The data which the force signal records before processing includes inertial forcing of anything attached below the force sensor. In this case, that includes the pitch motor and housing as well as the foil. Since the hydrodynamic forcing is our primary interest in this research, it is necessary to subtract inertial forcing from the force sensor signal, otherwise, force data would include the inertial forcing due to the heave and pitch movements. Rotational moments of inertia were calculated for the various foils using Solidworks and computer-generated models of the foils. We calculated the inertial forcing based off of fundamental inertial equations and the foil's kinematics for each particular run. To verify we were only subtracting inertial forcing, the tank was drained and force measurements were taken. Assuming that aerodynamic forces are negligible for these measurements, we then expect the calculated inertial forces to

match almost exactly with the measured force. Results of these measurements for the smallest foil and the largest foil are shown in Figure 3-6. The forces shown in the graphs are the forces in the heave direction, used in the energy extraction calculations. For the smaller 1" chord foil, harmonic pitch and heave motions were used (which produced a non-harmonic heave motion and inertial forcing) while the larger 2.75" chord foil was actuated with a harmonic heave and pitch motion, resulting in harmonic inertial forcing. At a Strouhal number of 0.6 the percent error was low around 3%, but for smaller Strouhal numbers of 0.2 the percent error was larger around 10%. When running experiments with the 1" chord foil it was found that the inertial forcing was significantly larger than the hydrodynamic forces. For comparison, the mass of the foil was 0.15 grams while the mass of the pitch motor housing, motor, and noise-reduction plate combined was 1.1 kg. When subtracting the inertial forcing with an error of 10% it was found that the hydrodynamic force signal was noisy and not significantly resolved to use for measurements. We therefore used the 2.73" chord foil for measurements and imaging and used the 1" chord foil for additional imaging to see further wake developments downstream and for larger heave to chord movements. See Figures A-1 and A-2 for a more complete set of inertial measurements done.

3.4 DPIV

Digital Particle Image Velocimetry (DPIV) is a technique commonly used in order to visualize a real-world flow field. It relies on particles suspended in a fluid being illuminated by a sheet of high intensity laser beam and having a camera record successive images of the 2-D illuminated plane. Post-processing is done on the images using correlation techniques in order to generate a vector field of the flow which can be used for visualization and analysis.

3.4.1 DPIV Components

The imaging system used in our experiments is comprised primarily of the illuminating laser and the high speed recording camera.

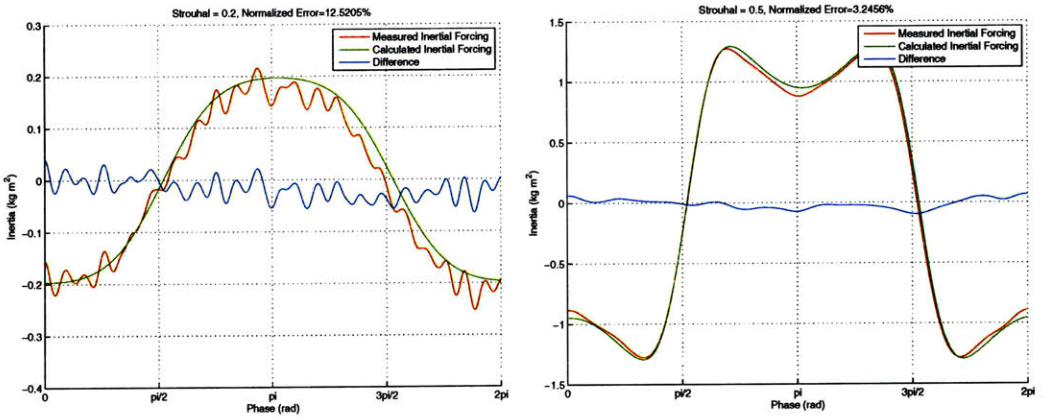

(a) 1" Foil, Strouhal 0.2

(b) 1" Foil, Strouhal 0.5

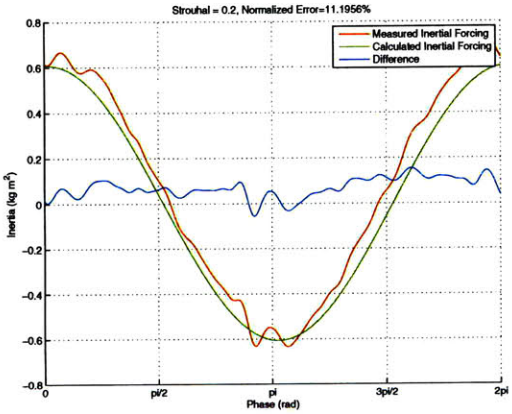

(c) 2.75" Foil, Strouhal 0.2

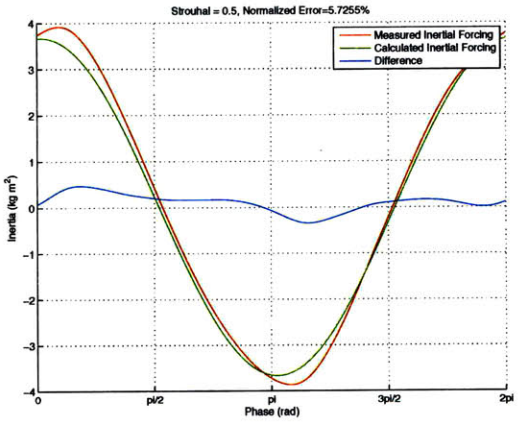

(d) 2.75" Foil, Strouhal 0.5

Figure 3-6: Inertia Measurement Verification – Red lines indicate the measured inertial forcing, Green lines indicated the calculated inertial forcing, Blue lines indicate the error between the measured and calculated

The laser used was a Quantronix Darwin 527 Series Nd:YLF laser. It is a high-speed pulsed laser outputting a coherent wavelength of 532 nm. The firing pulse is triggered via the computer and is synchronized with the camera firing as well. The range of frequencies over which it can output is large with the highest intensity output occurring around 1000 Hz. The coherent beam produced from the laser is routed through an optical arm which then passes through a light sheet which is spread parallel to the water's surface (for chord-wise flow), illuminated a 2-D plane of the flow.

In order to illuminate the flow field it is necessary to seed the fluid with reflecting particles. We used polyamid seeding particles (PSP) which are primarily used for water flow applications and are produced by a polymerization process to be round, but typically aspherical to increase reflectivity. The specific particles we used had a mean particle diameter of 50 μm.

The camera system used is a LaVision Imager Pro HS. Various lenses were used in order to get different fields of view, even including post-processed stitched vector fields, but ultimately a Sigma 20mm 1:1.8 EX DG lens was used which mounted to the Imager Pro. The Imager Pro HS has a CMOS array with a maximum resolution of 1280 x 1024 pixels. This full resolution is exposed every time the laser is fired unlike low speed cameras which usually gate half of the image and alternate this. The maximum frame rate that the camera can capture at is 638 Hz. In order for the camera to view the flow field without distortion we employ a viewing box which is an extended from the moving carriage into the water and provides an unobstructed view into the water through glass. Otherwise, ripples and movement on the free surface would create a severely distorted and unusable view of the flow field.

3.4.2 DPIV Techniques

Considerations must be taken into account when using DPIV in order to produce the most accurate results possible. The first is alignment of the laser parallel to the free surface in order to ensure 2D flow field. This was done with horizontal slides running the length and width of the tank which were used in order to align the laser

beam sheet. The sheet was also focused to be as thin as possible in order to prevent capturing a 3D image.

Post-processing of the image data was done using DaVis software provided with the camera hardware. This software does the bulk of the image processing and vector field computation in addition to image calibration. We use it to do basic vortex structure identification and flow visualization and rely on the precision of the six-axis force sensor for forces and correlate the two to provide a comprehensive view of the fluid-structure interaction.

Image calibration is necessary in order to correct for the angle at which the camera is viewing the flow field. Ideally the camera is perfectly perpendicular to the field with zero image distortion, however this is not the case in our setup. A calibration plate is suspended in the plane of interest which has hatch marks at measured intervals. Images are taken with the camera and the dimensions of the plate are supplied. DaVis then calculates the rotation of the camera in all three axis, and the lens distortion, and attempts to apply a correction factor to the image. This is later used on the images recorded in order to prevent distortion.

Vector field computation is what we use in order to turn the images of the silver particles into vector fields. DaVis uses a technique which divides the large 1280 x 1024 pixel image into smaller interrogation windows and then uses correlation techniques between frames and interrogation windows to calculate corresponding vectors. For our experiments we did 2- and 3-pass cross-correlations using an interrogation window of initial size 64 x 64 pixels in order to define the large structures and ended with a window size of 32 x 32 pixels in order to identify smaller structures.

Finally, lead-precipitation tests were performed in the span-wise direction to ensure three-dimensional effects were minimal, particularly in the DPIV plane.

Chapter 4

Results

4.1 Parameter Space

The parameter space tested in the experiments included the non-dimensional oscillatory heave amplitude (heave to chord ratio, h_0/c), the non-dimensional oscillation frequency (Strouhal number, St), and the maximum angle of attack, α_{max}. A matrix of St and corresponding α_{max} was used for the varying h_0/c ratios. The parameter space tested is shown in Table 4.1. Overall, 165 unique experiments were performed.

Using harmonic angle of attack and pitch profiles, it was found that the highest efficiency of $\eta = 0.45 \pm 0.04$ occured at $h_0/c = 0.75$. For $h_0/c = 1.0$, an efficiency of $\eta = 0.39 \pm 0.04$ was achieved, and for $h_0/c = 1.23$, an efficiency of $\eta = 0.35 \pm 0.02$ was achieved. Contour plots of the average efficiencies over one cycle are shown in Figures 4-1, 4-9, and 4-17. The corresponding tables of efficiencies with errors can be found in the Appendinx in Tables B.1, B.2, and B.3.

Parameter	Value
h_0/c	0.75, 1.0, 1.23
St	0.2, 0.3, 0.4, 0.5, 0.6
α_{max} (rad)	0.2, 0.28, 0.36, 0.44, 0.52, 0.6, 0.68, 0.76, 0.84, 0.92, 1.0

Table 4.1: Experimental Parameter Space

4.2 $h_0/c = 0.75$

Over the h_0/c ratios tested, this particular ratio resulted in the largest efficiency of $\eta = 0.45 \pm 0.04$ at $St = 0.2$ and $\alpha_{max} = 38.9°$. The majority of the parametric space tested for this specific h_0/c ratio resulted in negative efficiencies, indicating unfavorable phasing of forces on the foil. The largest efficiencies were found to be at large angles of attack. However, the frequency range over which energy could be extracted at high angles of attack was notably smaller than at low angles of attack. For example, at a $\alpha_{max} = 55°$, energy is extracted over the Strouhal range from 0.2 to 0.3. At $\alpha_{max} = 20°$, energy can be extracted over the Strouhal range 0.2 to 0.4. This indicates that motions with a lower α_{max} are more robust at having favorable force phasing over a broad range of flapping frequencies. A table of the overall efficiencies can be found in the Appendix in Table B.1. Because energy extraction from the flow is governed by Equation 2.19, the phasing of the lift force and heave velocity, as well as the rotational moment and pitch velocity, are the components which dictate whether the individual motion will extract energy or require energy during the cycle.

We use two sample force plots to illustrate this example. Figure 4-2 shows force coefficients plotted over one cycle for the highest efficiency experiment tested for $h_0/c = 0.75$. The magenta line is the coefficient of power (C_P), the blue line is the coefficient of lift (C_L), the dotted blue line is the heave velocity normalized by the free stream flow (V_y/U), the red line is the normalized pitch moment ($C_{M,n}$), and the dotted red line is the normalized rotational velocity ($V_{\theta,n}$). The heave force is entirely in phase with the lift force for the entire cycle, both having similar signs and crossing the x-axis at $\phi = \pi$. Over the entire cycle, energy can be extracted from this degree of freedom.

However, the pitch moment is not entirely in phase with the rotational velocity. It should be noted that from approximately $\phi = 3\pi/4$ to $\phi = \pi$ and from $\phi = 7\pi/4$ to $\phi = 2\pi$ the pitch moment is in phase with the rotational velocity meaning that the foil rotates in the direction of the pitching moment. This indicates a net energy extraction from the flow due to rotation of the foil. The question arises as to how the

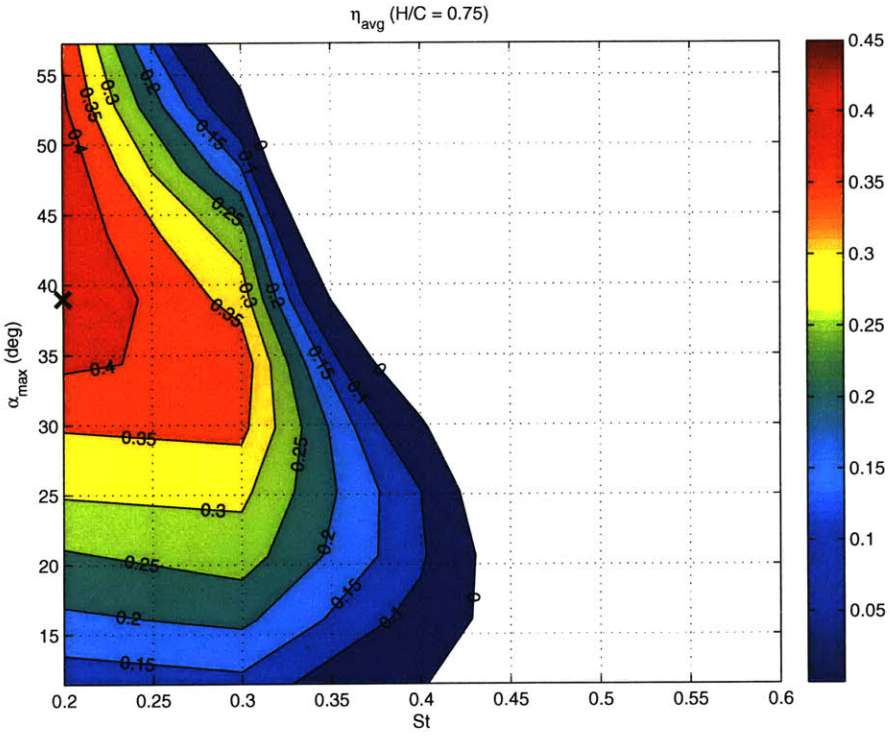

Figure 4-1: Average Efficiency Contours for $h_0/c = 0.75$. Regions of net energy extraction are shown in color while white regions indicate areas where net energy was input into the system.

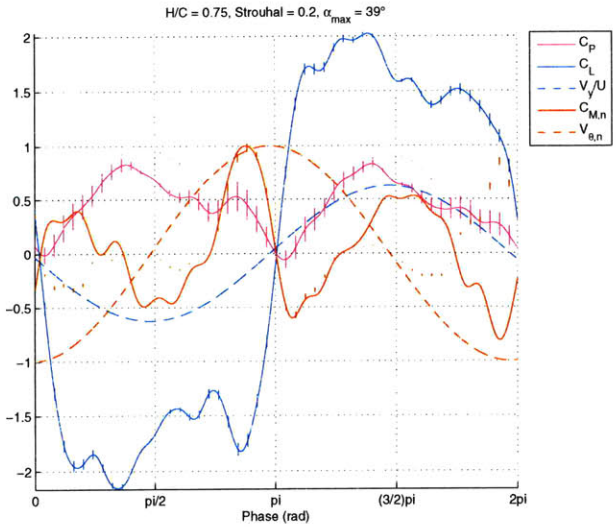

Figure 4-2: Force Phasing for $h_0/c = 0.75$, $St = 0.2$, $\alpha_{max} = 38.9°$. Error bars are shown with vertical lines.

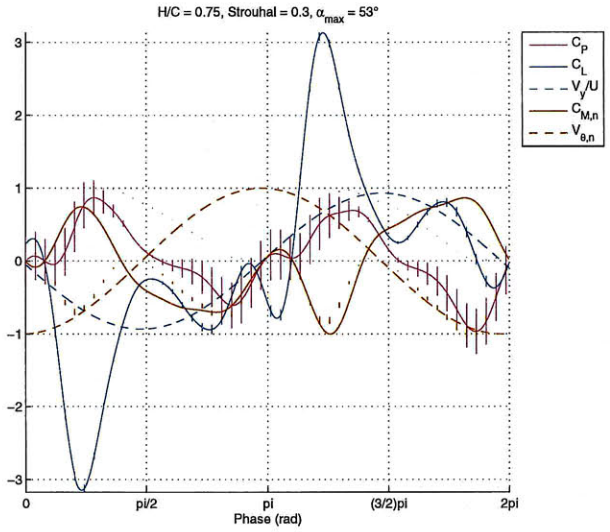

Figure 4-3: Force Phasing for $h_0/c = 0.75$, $St = 0.3$, $\alpha_{max} = 53°$

fluid is transferring energy back into rotational motion.

DPIV is employed in order to see how the fluid structures evolve. Figure 4-4 shows six DPIV images which compares a low-efficiency experiment ($\eta = 0.04$), shown in the left hand column, with a high-efficiency run ($\eta = 0.45$), shown in the right hand column. The force data for $\eta = 0.04$ is shown in Figure 4-3 while the force data for $\eta = 0.45$ is shown in Figure 4-2. In all DPIV images the flow is moving from the top of the frame towards the bottom, negative vorticity (clockwise rotation) is shaded blue and positive vorticity (counter-clockwise rotation) is shaded yellow.

For the maximum efficiency run shown in Figures 4-4b, 4-4d, and 4-4f, it can be that the LEV is an important mechanism in the transfer of fluid energy to the rotational motion of the foil during the rotational energy recovery period from $\phi = 3\pi/4$ to $\phi = \pi$. The LEV forms as the foil moves from A_x/C = -0.75 to $A_x/C = 0$. As the foil rotates from $\alpha = 39°$ at $\phi = \pi/2$ to $\alpha = 0°$ at $\phi = \pi$, the LEV is shed from the leading-edge (LE) of the foil towards the trailing-edge (TE). This is clearly visible in Figures 4-4b, 4-4d, and 4-4f. In Figure 4-4f it is possible to see another vortex which rotates in the opposite direction of the newly shed LEV. This counter-rotating fluid is entrained from the opposing side of foil by the large clockwise LEV. In the case of this motion, two vortices of opposing signs are generated every half cycle (2P mode),

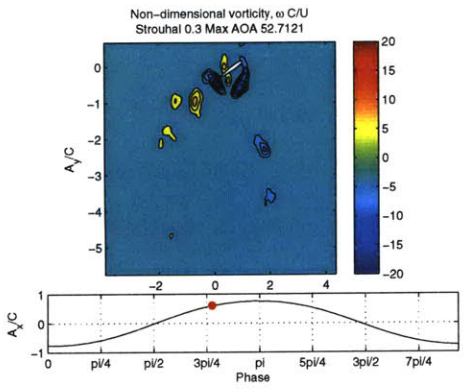

(a) $\eta = 0.04, \phi = 3\pi/4$

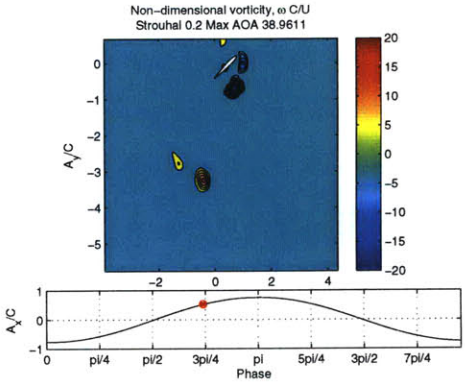

(b) $\eta = 0.45, \phi = 3\pi/4$

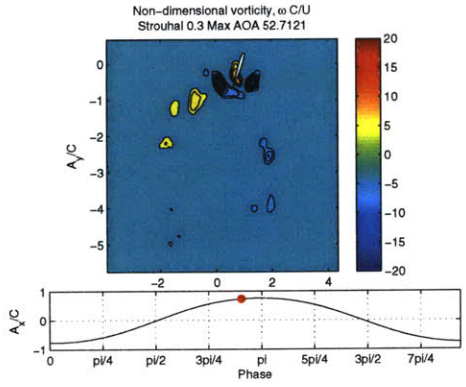

(c) $\eta = 0.04, \phi = 7\pi/8$

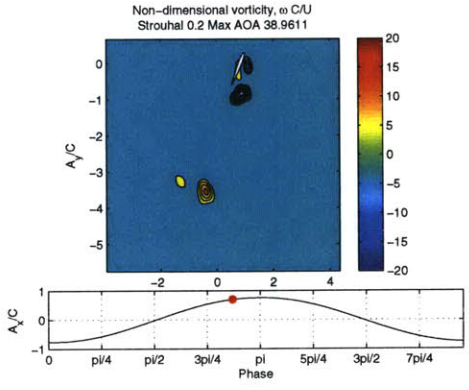

(d) $\eta = 0.45, \phi = 7\pi/8$

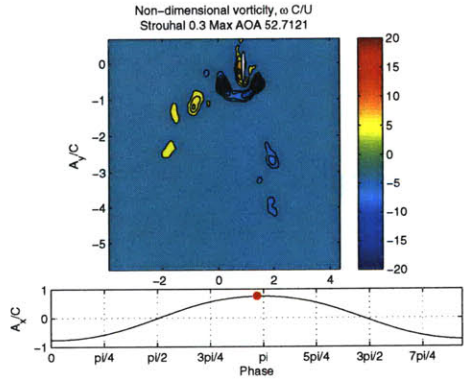

(e) $\eta = 0.04, \phi = \pi$

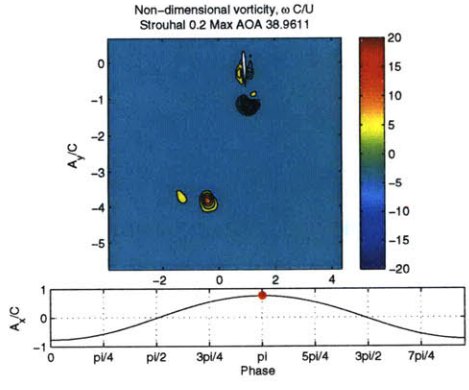

(f) $\eta = 0.45, \phi = \pi$

Figure 4-4: DPIV Results for $St = 0.3$, $\alpha_{max} = 52°$ ($\eta = 0.04$) and $St = 0.2$, $\alpha_{max} = 39°$ ($\eta = 0.45$). Flow moves from top-to-bottom in all images. Blue vortex cores indicate negative vorticity (clockwise rotation) and yellow vortex cores indicate positive vorticity (counter-clockwise rotation).

with the vortices being shed at the extremes of the heave oscillation.

The fast-spinning core of the LEV produces a low-pressure region which, because fluid moves from high-pressure regions to low-pressure regions, imparts a force acting towards the low-pressure region on the foil. The largest vortex seen near the TE in Figure 4-4b is rotating clockwise (negative vorticity) and is positioned behind the pitching point of the foil which is located at $c/3$. It imparts a coupled force and moment in the same direction as the rotation of the foil as the foil rotates towards $\alpha = 0$, transferring energy back to the foil. In Figure 4-4f a vortex of opposite sign begins forming on the opposing side of the foil. However, it is significantly smaller in size and in magnitude and the negative vorticity dominates the force on the foil.

The low efficiency run ($\eta = 0.04$) force data in Figure 4-3 shows extremely different force phasing. The lift force is in phase with the heave velocity for approximately half of the entire cycle (from $\phi = 0$ to $\phi = \pi/2$ and from $\phi = \pi$ to $\phi = 3\pi/2$), whereas the pitch moment is essentially never in phase with the rotational velocity of the foil, indicating that the hydrodynamic moment applied on the foil are always opposing the foil motion, requiring external energy input to actuate the foil.

Looking at DPIV data for the low-efficiency run shows why this is the case. The rotational velocity of the foil for the low-efficiency run is approximately twice the magnitude of that for the high-efficiency run, due to both the increased Strouhal number and increased angle-of-attack. This produces an entirely different vortex street, namely two same-sign vortices per half cycle (2P* mode), causing different moments on the foil. An extremely large LEV is generated during first part of the cycle which stays in front of the pitching point on the foil. The foil is rotating counter-clockwise while the LEV generates a clockwise moment (due to its position in front of the pitching point), requiring energy to pitch the foil. The rapid pitching of the foil generates a trailing-edge vortex (TEV) as seen in Figure 4-4c which forms on the left side of the foil while the LEV remains on the right side of the foil, essentially canceling the benefits that arise from a single LEV positioned behind the pitching point. The opposing clockwise vortex, which forms on the left side of the foil, paired with the TEV generate a large moment which opposes the foil rotation at $\phi = \pi$,

	0.2	0.3	0.4	0.5	0.6
57.3	-	-	-	-	-
52.7	2P	2P*	2P*+S	2P*+S	-
48.1	-	-	-	-	-
43.5	-	-	-	-	-
38.9	2P	2P*	2P*+S	2P*+S	-
34.4	-	-	-	-	-
29.8	-	-	-	-	-
25.2	2S	2P*	2P*+S	2P*+S	-
20.6	-	-	-	-	-
16.0	-	-	-	-	-
11.5	2S	2S	2P*	2P*	-

Table 4.2: Wake Patterns for $h_0/c = 0.75$ (2S - Single Vortex per Half Cycle, 2P - Two Opposing-Sign Vortices per Half Cycle, 2P* - Two Same-Sign Vortices per Half Cycle, 2P*+S - Two Same-Sign Vortices and One Opposing-Sign Vortex per Half Cycle)

where rotational velocity is maximum.

Force data was recorded over the entire parametric range while DPIV data was taken for select points over the range in order to gain a qualitative understanding of the downstream wake patterns. The data was further filtered and processed in order to emphasize the major vortex structures present in the flow. There were four main types of wakes observed for $h_0/c = 0.75$; a single vortex per half cycle (2S), two opposing-sign vortices per half cycle (2P), two same-sign vortices per half cycle (2P*), and two same-sign vortices and one opposing-sign vortex per half cycle (2P*+S). A table presenting the wake patterns for the tested parameters are shown in Table 4.2. Several trends are noted from Table 4.2 and corresponding DPIV images.

4.2.1 2S Mode

At small flapping frequencies and angles of attack for $h_0/c = 0.75$, a 2S wake pattern was found. In these instances, LEVs were small and remained attached during the motion from $-h_0$ to h_0. Depending on the foil kinematics, the LEV was shed at different points in the cycle, typically shedding at the extreme of the heave oscillation or shortly thereafter. Time series DPIV data for $St = 0.3$ and $\alpha_{max} = 11°$ is shown

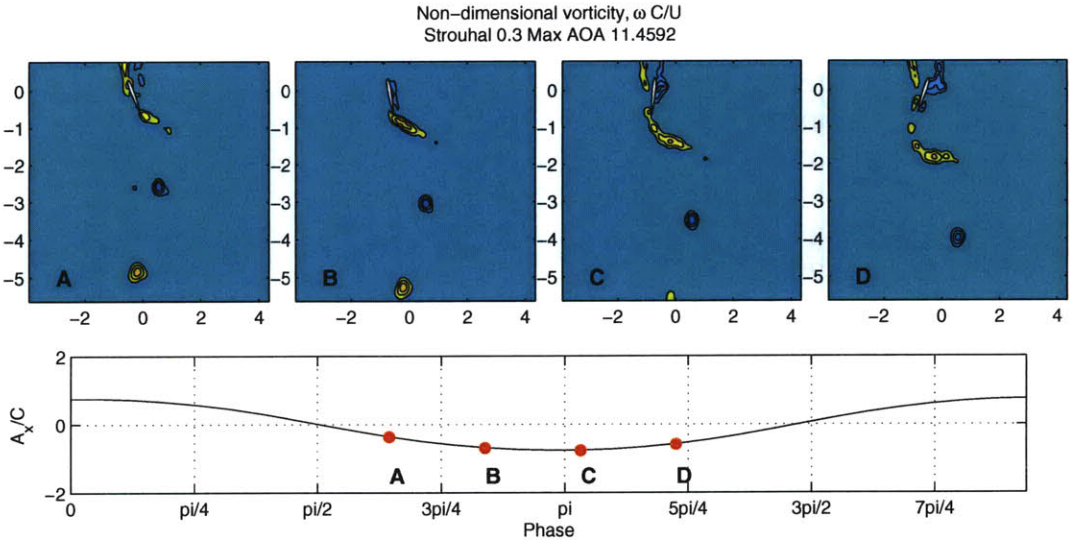

Figure 4-5: 2S Wake Pattern for $h_0/c = 0.75$

in Figure 4-5. In Panel A, a counter-clockwise LEV as well as a TEV, which is generated from the rotational motion of the foil, are seen. Two previously shed vortices are clearly visible downstream from previous heave excursions. In Panel C the LEV is visible upstream of the well-developed TEV which is beginning to roll-up into a single vortex. Panel D shows the LEV shedding off the TE of the foil directly before it combines with the TEV. The new clockwise LEV which is forming during the return motion is also visible in Panel D. Another small counter-clockwise vortex should be noted near the TE of the foil as it plays an important roll in other vortex shedding modes.

4.2.2 2P Mode

As the angle of attack is increased, the LEVs grow in magnitude due to the increased pressure recovery experienced between the two sides of the foil. This is visible in Figure 4-6, Panel A. Figure 4-6 shows a typical wake pattern for the 2P mode. In Panel A the large clockwise vortex near the TE of the foil is the LEV generated during the heave motion. When the foil approaches near parallel to the flow (zero angle-of-attack), the large LEV sheds and entrains counter-rotating fluid from the other side of the foil, forming an opposing-sign vortex which sheds in tandem with

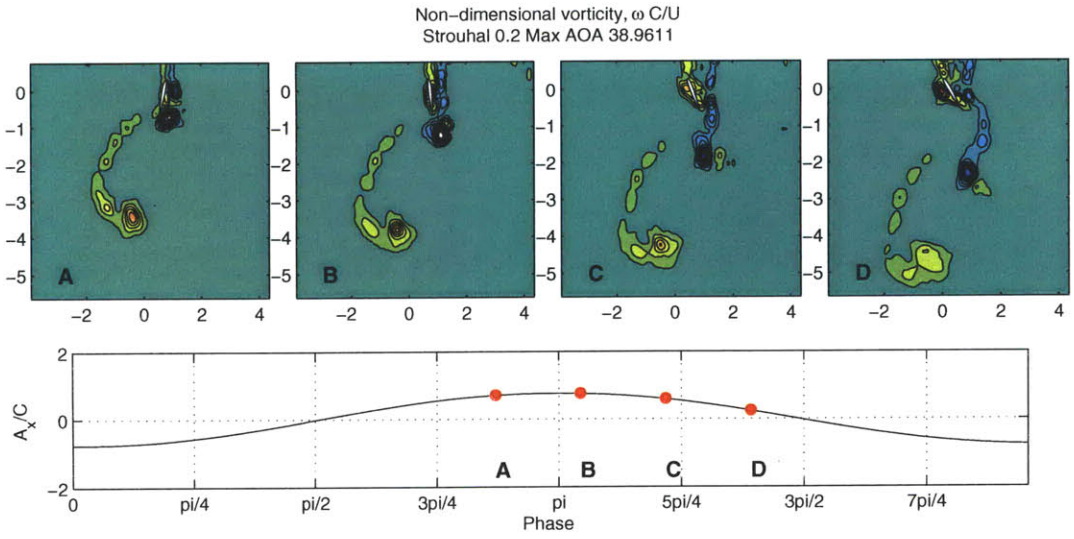

Figure 4-6: 2P Wake Pattern for $h_0/c = 0.75$

the clockwise LEV. This is visible in Panels B, C, and D, where the two opposite-sign vortices induce rotation around one another. The counter-clockwise vortex that is shed is of significantly smaller magnitude which can be seen in the induced rotation as the clockwise LEV rotates the smaller vortex around its core.

4.2.3 2P* Mode

Once the flapping frequency reached $St = 0.3$, a new vortex shedding mode was observed. This mode consists of two similar sign vortices being shed every half cycle, which we call the 2P* mode. Time series DPIV data for $St = 0.3$, $\alpha_{max} = 25°$ is shown in Figure 4-7. Increased flapping frequency necessarily increases the rotational velocity of the foil as it completes more cycles per second. In turn, increased rotational velocity leads to larger TE velocities and pressure differences, resulting in larger TEV. Such is the case in the 2P* mode. In Figure 4-7 Panel A the TEV is seen behind the TE while the LEV can clearly be seen on the left hand side of the foil directly in front of the TEV. Panels B and C shows the foil continuing its clockwise rotation and the TE tip of the foil encountering the LEV as it moves backwards along the length of the foil. These panels also show a new counter-clockwise LEV starting to form. The vortices are completely shed from the foil by Panel D and show clearly differentiated

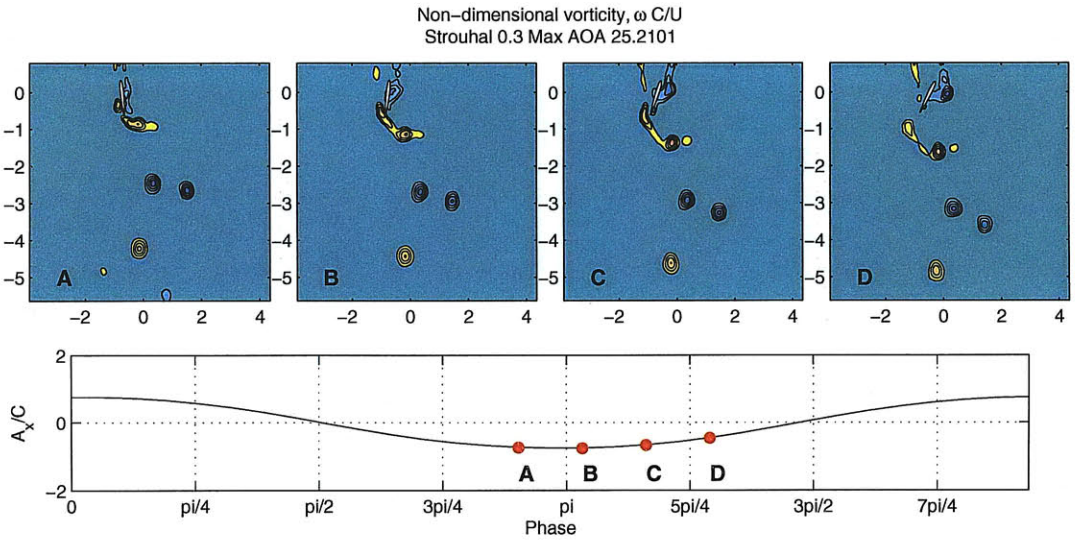

Figure 4-7: 2P* Wake Pattern for $h_0/c = 0.75$

cores.

Further downstream two pairs of vortices (four vortices total) are seen from the previous cycle. In Panel A one can see the counter-clockwise pair of vortices furthest downstream. However, by Panel B, the LEV vortex from the pair has dissipated, leaving only the TEV traveling downstream. This trend is also seen in the clockwise pair where the TEV, which is traveling down the $A_x/C = 0$ line, is seen to be larger magnitude than the LEV further to the right.

4.2.4 2P*+S Mode

The final vortex mode observed for $h_0/c = 0.75$ is shown in Figure 4-8. This 2P*+S mode consists of a pair of LEV and TEV both of the same sign vorticity in addition to another vortex rotating in the opposite direction. Figure 4-8 Panel A begins with the foil moving left. A large TEV is positioned at the TE of the foil and another large LEV near the pitching point of the foil on the right hand side. On the left side of the foil a large counter-clockwise LEV is seen forming in Panels A and B. Part of this counter-clockwise LEV from the left hand side of the foil is pulled off by the clockwise LEV on the right hand side of the foil as the right hand side LEV reaches the TE of the foil. Panels C and D clearly show the clockwise LEV pulling off the

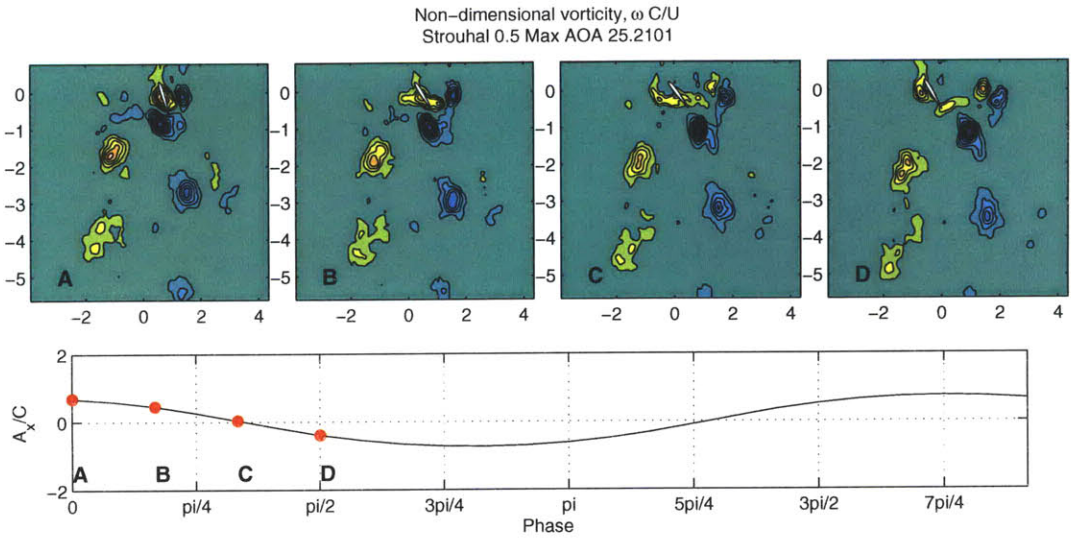

Figure 4-8: 2P*+S Wake Pattern for $h_0/c = 0.75$

counter-clockwise LEV from the left hand side. Panel D shows the two LEV paired as they begin to induce rotation around one another.

4.3 $h_0/c = 1.0$

Next we examine the results of the same Strouhal and angle of attack parametric range for a h_0/c ratio of 1.0. As seen in Figure 4-9, the range over which net energy extraction occurs is larger than that for a h_0/c ratio of 0.75. The maximum efficiency was found to be $\eta = .39 \pm .04$ at $St = 0.3$ and $\alpha_{max} = 38.9°$. Motions with large α_{max} resulted in energy extraction over a small range of Strouhal numbers while motions with small α_{max} resulted in an increased Strouhal range over which energy extraction was possible. A table of the overall efficiencies can be found in the Appendix in Table B.2.

The force phasing for the highest efficiency experiment, shown in FIgure 4-10 shows characteristics similar to that found in Figure 4-2. The lift force and heave velocity are in phase for the entire cycle of motion, indicating power extraction from that degree-of-freedom. However, the pitch moment is opposite direction as the rotational velocity for most of the cycle. However, briefly before the foil reaches a zero

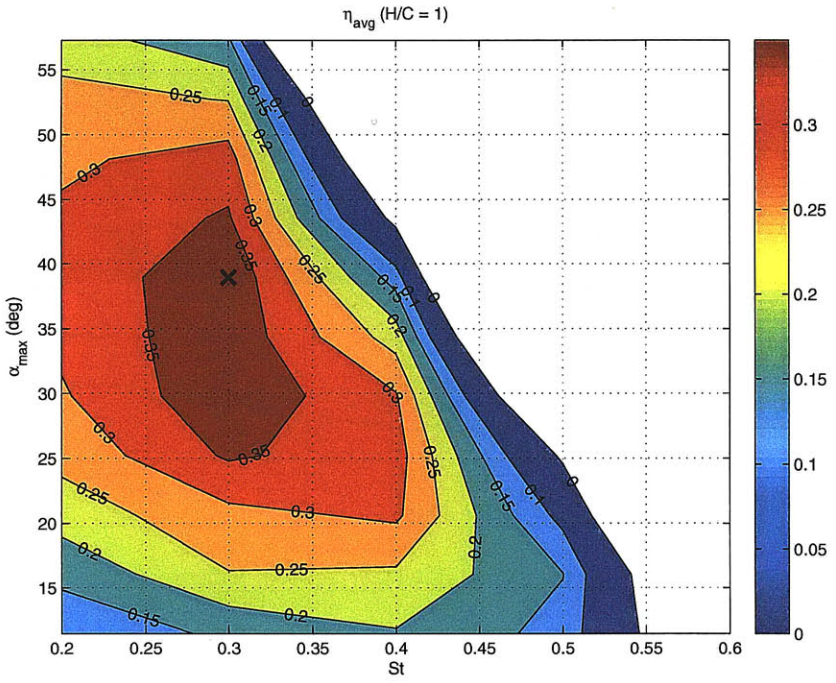

Figure 4-9: Average Efficiency Contours for $h_0/c = 1.0$. Regions of net energy extraction are shown in color while white regions indicate areas where net energy was input into the system.

degree angle of attack at $\phi = \pi$ and $\phi = 2\pi$, the rotational moment and velocity align in order to transfer energy back into the foil.

For comparison we look at the force phasing for a low efficiency run of η = -0.02 which was found for $St = 0.4$ and $\alpha_{max} = 44°$, shown in Figure 4-11.

In Figure 4-11, the lift force is in the same direction as the heave velocity for $\phi =$ 0 to $\phi = \pi/2$ and for $\phi = \pi$ to $\phi = 3\pi/2$. The heave velocity and lift force are out of phase for the remaining parts of the cycle. The pitch moment and pitch velocity, on the other hand, remain out of phase for the entire cycle, requiring energy input to actuate it the entire time. DPIV results for the high efficiency and low efficiency cases are presented below in Figure 4-12.

As previously mentioned in Section 4.2, the LEV plays an important role in energy recovery. The high efficiency experiment which is shown in Figures 4-12b, 4-12d, and 4-12f, shows a large leading edge vortex which is shed as the foil moves through the point of maximum rotational velocity. In the final DPIV image (Figure 4-12f),

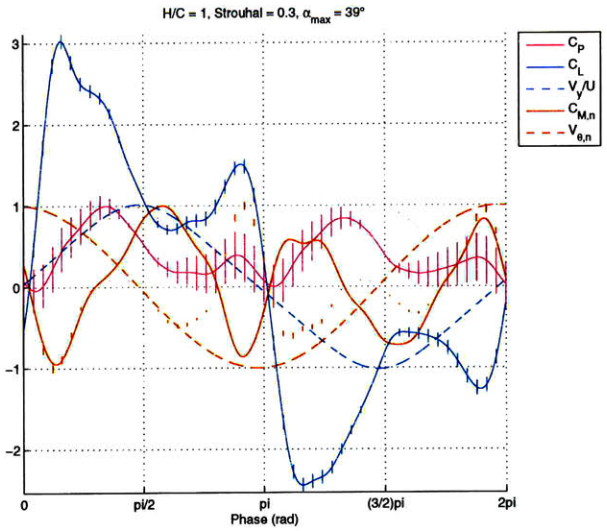

Figure 4-10: Force Phasing for $h_0/c = 1.0$, $St = 0.3$, $\alpha_{max} = 38.9°$

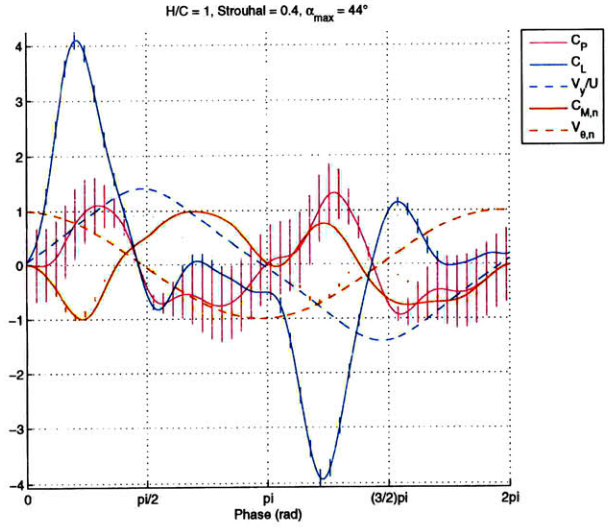

Figure 4-11: Force Phasing for $h_0/c = 1.0$, $St = 0.4$, $\alpha_{max} = 44°$

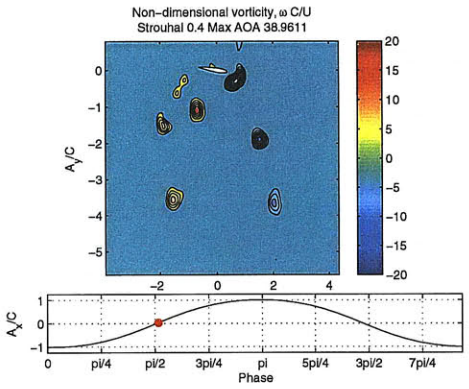

(a) $\eta = -0.02, \phi = \pi/2$

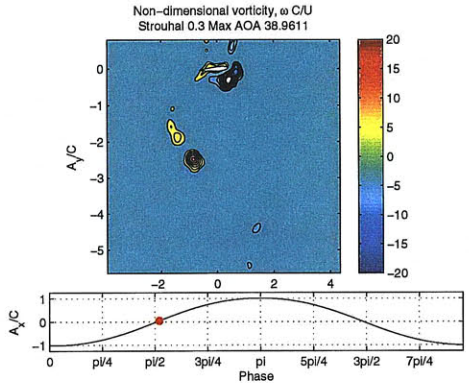

(b) $\eta = 0.39, \phi = \pi/2$

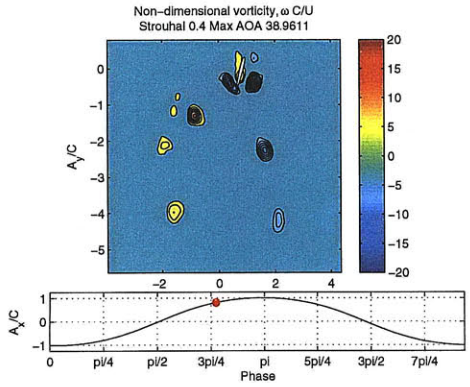

(c) $\eta = -0.02, \phi = 3\pi/4$

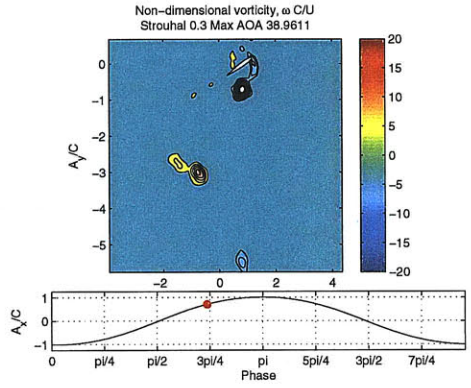

(d) $\eta = 0.39, \phi = 3\pi/4$

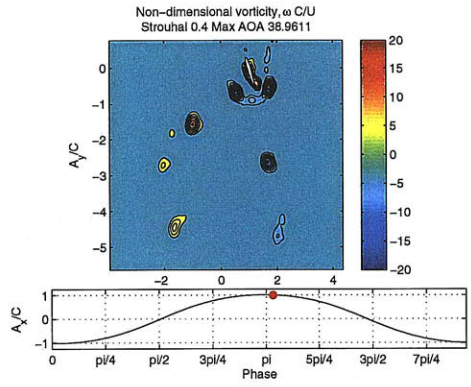

(e) $\eta = -0.02, \phi = \pi$

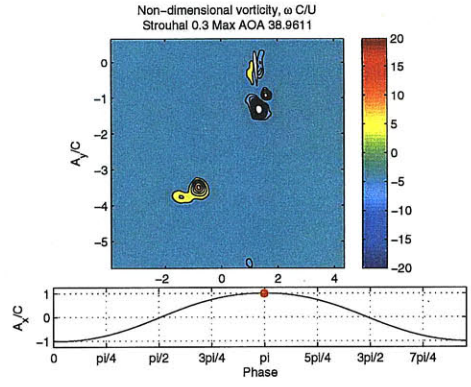

(f) $\eta = 0.39, \phi = \pi$

Figure 4-12: DPIV Results for $St = 0.3$, $\alpha_{max} = 39°$ ($\eta = 0.04$) and $St = 0.4$, $\alpha_{max} = 44°$ ($\eta = 0.45$). Flow moves from top-to-bottom in all images. Blue vortex cores indicate negative vorticity (clockwise rotation) and yellow vortex cores indicate positive vorticity (counter-clockwise rotation).

	0.2	0.3	0.4	0.5	0.6
57.3	-	-	-	-	-
52.7	2P	2P	2P*	2P*+S	-
48.1	-	-	-	-	-
43.5	-	-	-	-	-
38.9	2P	2P	2P*	2P*+S	-
34.4	-	-	-	-	-
29.8	-	-	-	-	-
25.2	2S	2P*	2P*	2P*+S	-
20.6	-	-	-	-	-
16.0	-	-	-	-	-
11.5	2S	2S	2P*	2P*	-

Table 4.3: Wake Patterns for $h_0/c = 1.0$ (2S - Single Vortex per Half Cycle, 2P - Two Opposing-Sign Vortices per Half Cycle, 2P* - Two Same-Sign Vortices per Half Cycle, 2P*+S - Two Same-Sign Vortices and One Opposing-Sign Vortex per Half Cycle, 2P*C - Two Same-Sign Vortices that Combine Downstream per Half Cycle)

the LEV is seen traveling off the TE of the foil, entraining an opposite sign vortex with it from the left hand side of the foil. As seen in the force data, this LEV which is shedding from $\phi = 3\pi/4$ to $\phi = \pi$ is the reason the pitch moment and rotational velocity align for that short period.

In Figures 4-12a, 4-12c, and 4-12e a vortex pattern similar to that produced for the low efficiency case for $h_0/c = 0.75$ is noted. The quick rotation of the foil generates a sizable TEV in addition to a LEV. The rapid displacement of fluid, seen particularly clearly in Figure 4-12e, is filled by fluid rotating in the opposite direction which can be seen on the left hand side of the foil in these images.

Sixteen DPIV experiments were carried out for $h_0/c = 1.0$ and were classified based on their vortex shedding patterns. Table 4.3 summarizes these results. Similar trends in wake transitions over the parameter space are observed between $h_0/c = 0.75$ and $h_0/c = 1.0$. Low frequency and low angle of attack motions resulted in fewer vortices being shed, while higher angles of attack produced larger LEV which could entrain fluid from the opposing side of the foil.

The four vortex shedding modes observed for this h_0/c ratio were 2S, 2P, 2P*, and 2P*+S. Sample images of these modes for $h_0/c = 1.0$ are shown below. Explanations for these modes can be found in the prior Section 4.2.

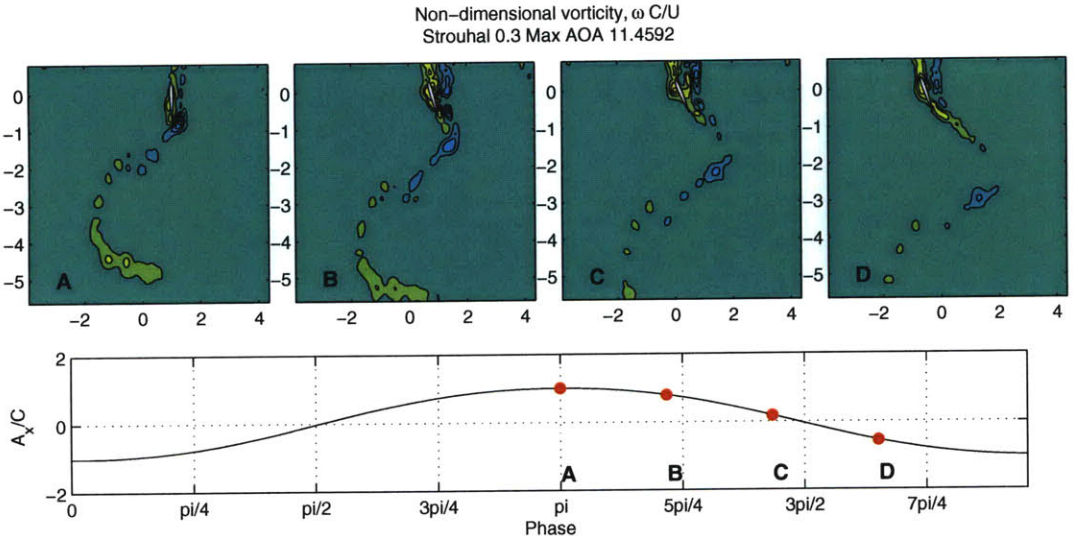

Figure 4-13: 2S Wake Pattern for $h_0/c = 1.0$

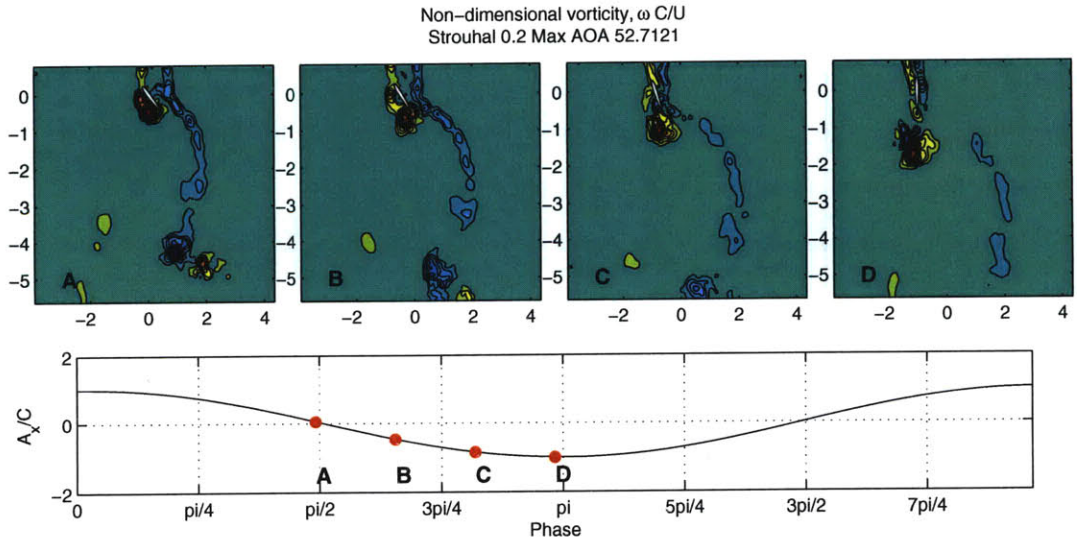

Figure 4-14: 2P Wake Pattern for $h_0/c = 1.0$

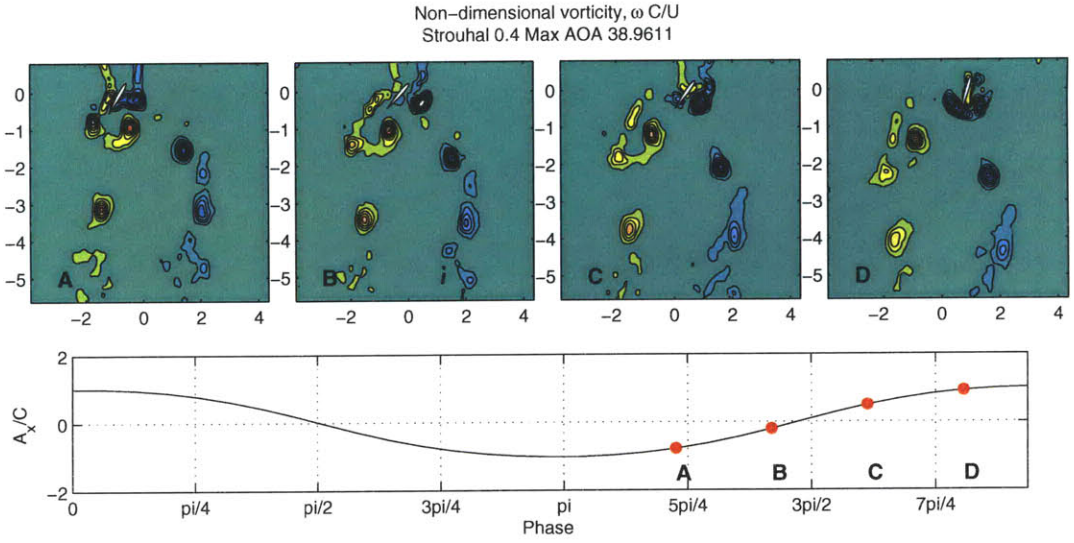

Figure 4-15: 2P* Wake Pattern for $h_0/c = 1.0$

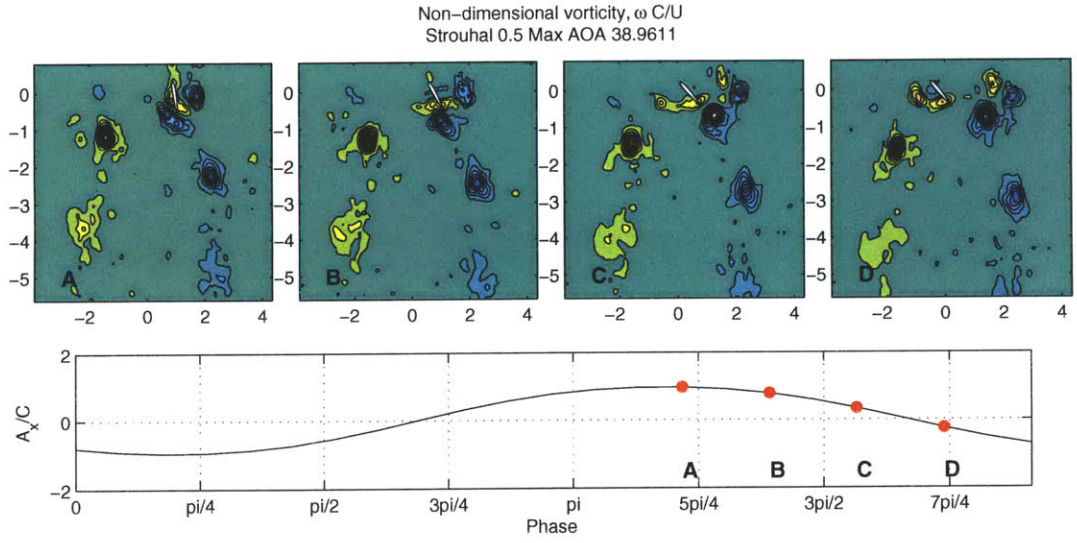

Figure 4-16: 2P*+ S Wake Pattern for $h_0/c = 1.0$

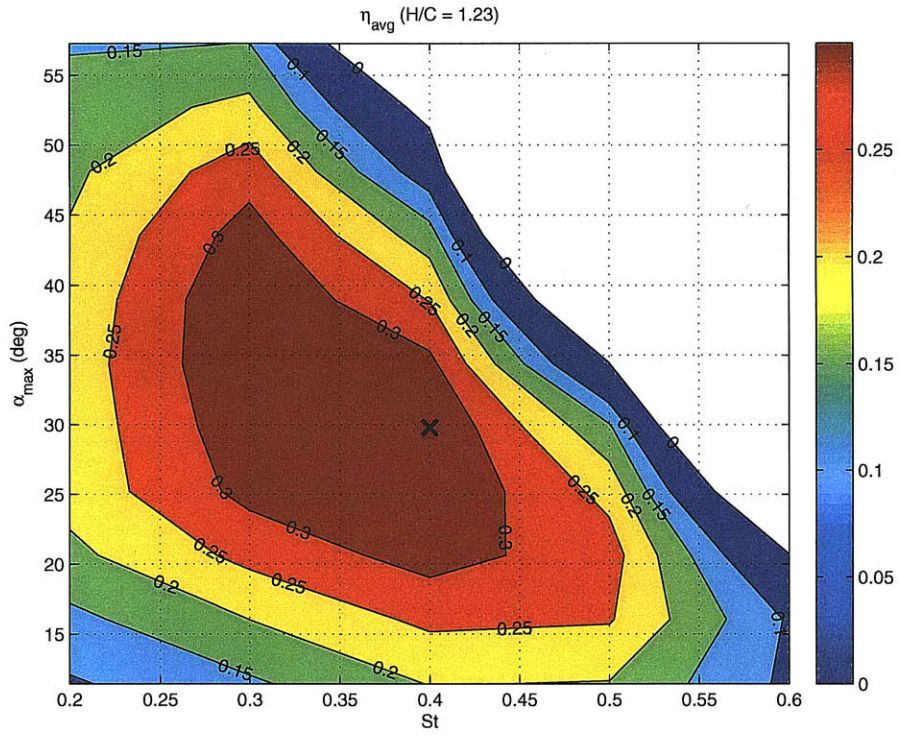

Figure 4-17: Average Efficiency Contours for $h_0/c = 1.23$. Regions of net energy extraction are shown in color while white regions indicate areas where net energy was input into the system.

4.4 $h_0/c = 1.23$

The final heave to chord ratio investigated was $h_0/c = 1.23$. For this heave to chord ratio, the largest parametric region of net average energy extraction was recorded, as visible in Figure 4-17. The maximum efficiency of $\eta = 0.35 \pm 0.02$ is recorded at $St = 0.4$ and $\alpha_{max} = 29°$. It should be noted that several motion parameters were found to have efficiencies close to η 0.35; $St = 0.3$ and $\alpha_{max} = 39°$, $St = 0.3$ and $\alpha_{max} = 34°$, and $St = 0.4$ and $\alpha_{max} = 25°$. A table of the overall efficiencies can be found in the Appendix in Table B.3.

DPIV images reveal four distinct wake patterns, a 2S mode, 2P mode, 2P* mode, and 2P*C mode. Table 4.4 show the resulting vortex patterns seen in the foil wake.

	0.2	0.3	0.4	0.5	0.6
57.3	-	-	-	-	-
52.7	2P	2P	2P*C	2P*	-
48.1	-	-	-	-	-
43.5	-	-	-	-	-
38.9	2P	2P	2P*C	2P*	-
34.4	-	-	-	-	-
29.8	-	-	-	-	-
25.2	2P	2P	2P*	2P*	-
20.6	-	-	-	-	-
16.0	-	-	-	-	-
11.5	2S	2S	2S	2S	-

Table 4.4: Wake Patterns for $h_0/c = 1.23$ (2S - Single Vortex per Half Cycle, 2P - Two Opposing-Sign Vortices per Half Cycle, 2P* - Two Same-Sign Vortices per Half Cycle, 2P*C - Two Same-Sign Vortices that Combine Downstream per Half Cycle)

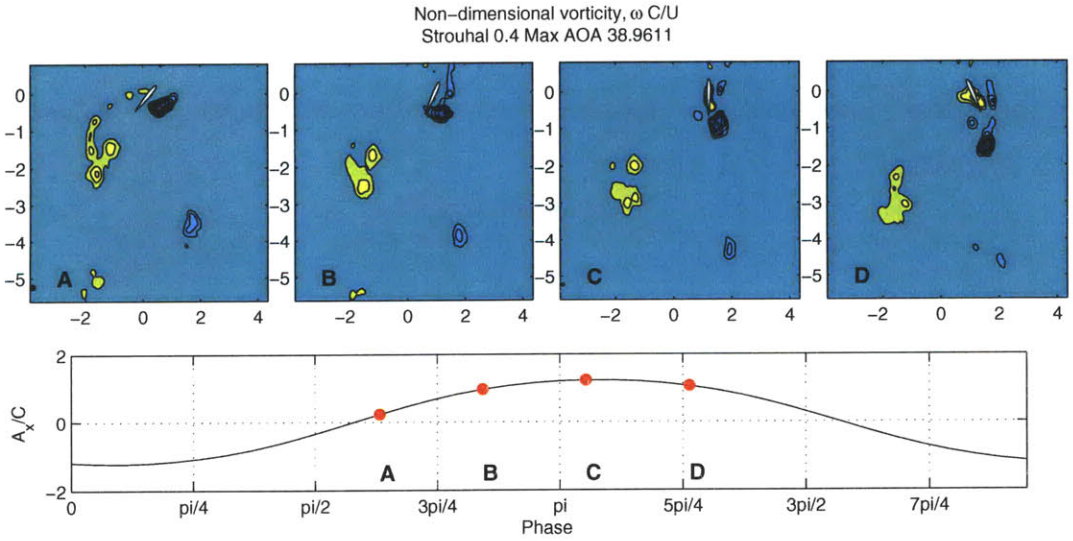

Figure 4-18: 2P*C Wake Pattern for $h_0/c = 1.23$

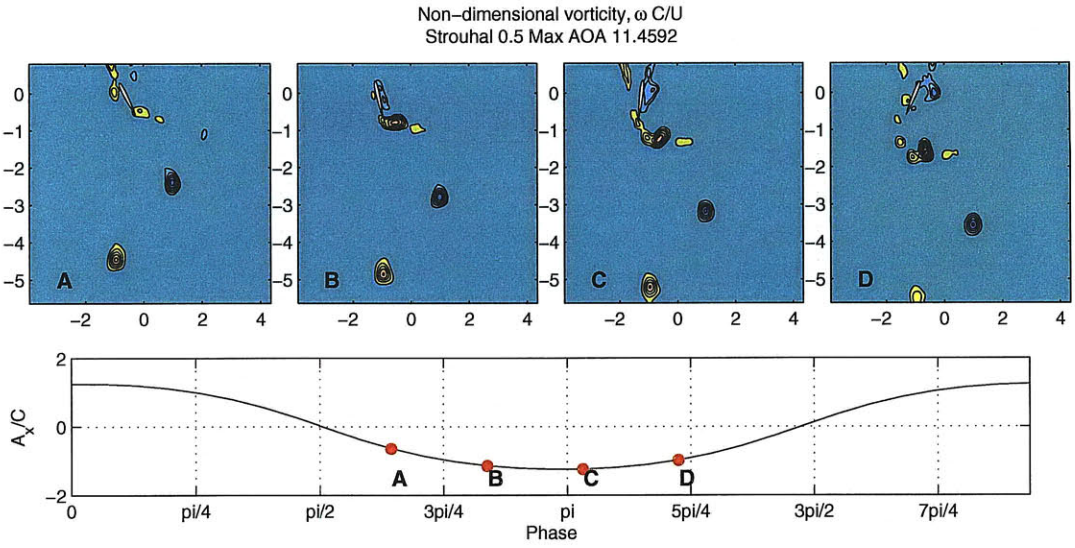

Figure 4-19: 2S Wake Pattern for $h_0/c = 1.23$

4.4.1 2P*C

This mode is characterized by two similar signed vortices which are shed every half-cycle, colliding downstream forming a larger region of smaller magnitude vorticity. An example of this mode is shown in Figure 4-18. In Panel A two clockwise vortices (LEV and TEV) can be seen on the left hand side, having just ben shed. Because they are both rotating in the same direction, when the edges of the spinning vortices meet they "tear" into each other, reducing their velocities while creating a dispersed region of rotation as seen in Panel D.

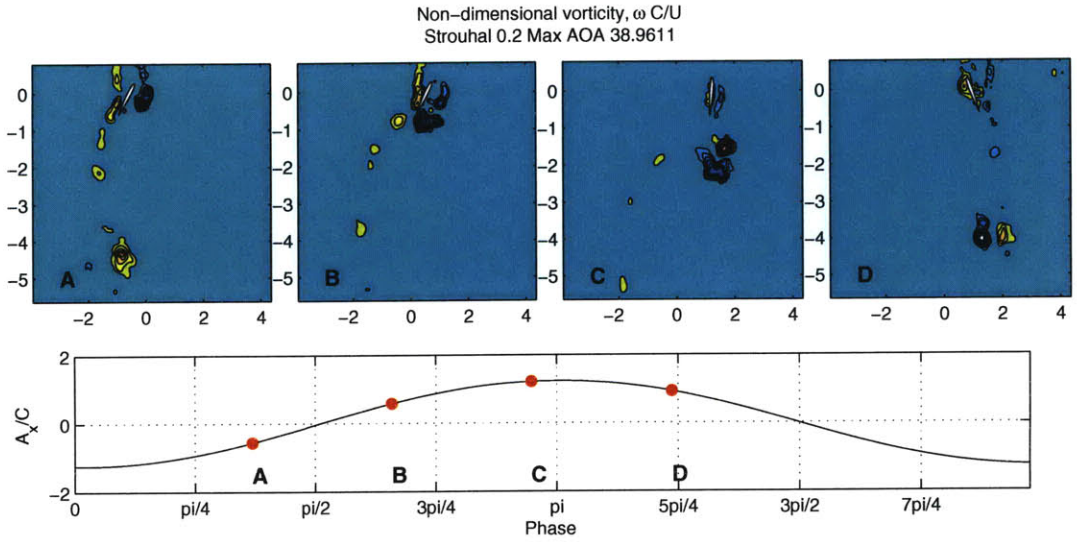

Figure 4-20: 2P Wake Pattern for $h_0/c = 1.23$

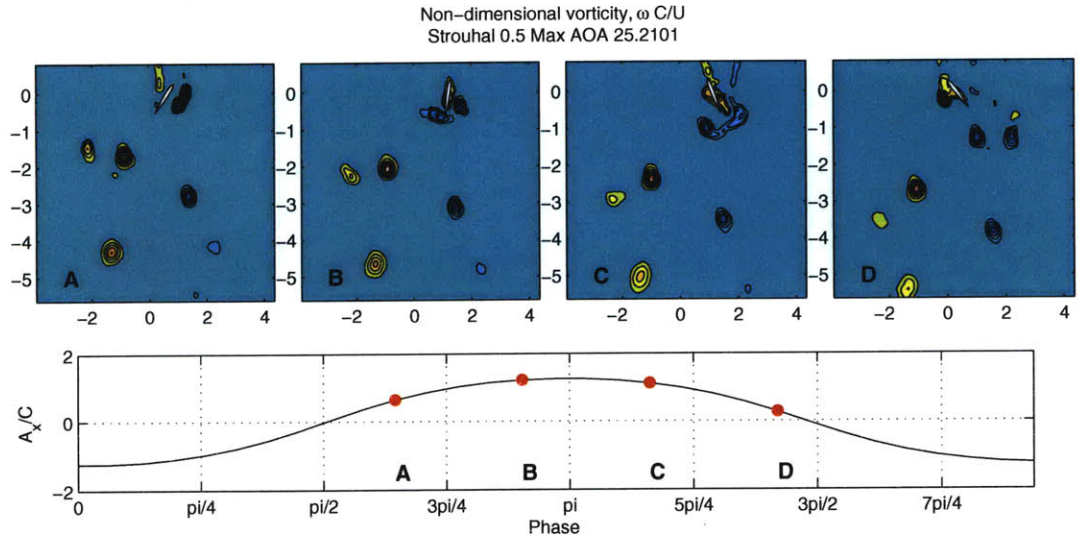

Figure 4-21: 2P* Wake Pattern for $h_0/c = 1.23$

Chapter 5

Discussion

The efficiency contour plots shown in Figures 4-1, 4-9, and 4-17 show an increasing operable range of positive energy extraction with increasing heave to chord ratio. At the lowest heave amplitude the Strouhal range over which energy can be extracted is relatively small compared with the other heave to chord ratios. Referring to Figure 4-1, the largest Strouhal number for which energy extraction occurs for this ratio is $St \simeq 0.4$. At $h_0/c = 1.0$, the largest Strouhal for energy extraction increases to $St \simeq 0.5$. Finally at $h_0/c = 1.23$, the largest recorded flapping frequency which energy is at is $St \simeq 0.6$, however it looks to extend beyond that range from the contour plot shown in Figure 4-17. The question arises as to why the operable range of energy extraction shifts drastically between these cases and the mechanisms in action.

5.1 Force Composition

We consider fluid forcing first in order to shed light on the efficiency shifts between the heave to chord ratios. The energy which could be extracted from the flow was derived by measuring the transverse lift force and the pitch moment of the foil in conjunction with the respective velocities. Since these motions were forced, several items must be taken into consideration when looking at the resulting force phasing plots.

The composition of the force signal should be noted. Because the force sensor is

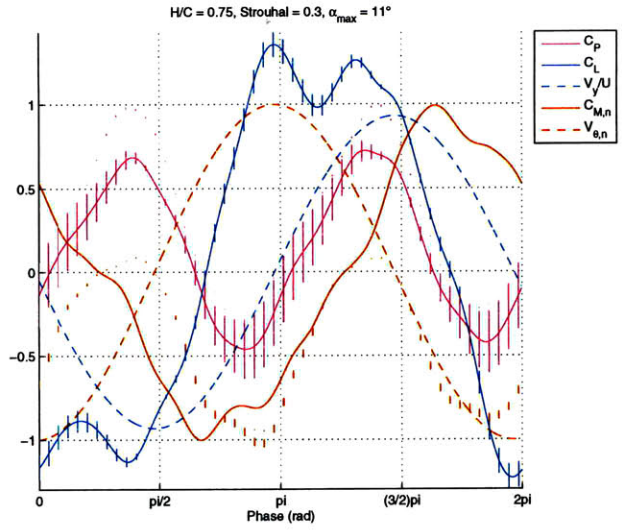

Figure 5-1: Force Data for $h_0/c = 0.75$, St $= 0.3$, $\alpha_{max} = 11°$. Note the phasing of maximum transverse force; the largest forces are seen at $\phi \simeq 0$ and $\phi \simeq \pi$.

mounted above the pitch motor and foil, the force sensor reads the mass inertia in addition to hydrodynamic forces. These inertial forces are calculated and subtracted out of the raw force signal, leaving only hydrodynamic forces. The hydrodynamic forces are comprised of circulation-based forces as well as added-mass forces. In these experiments we were strictly concerned with the transverse forces on the foil.

In cases where minimal vorticity is present, the added mass accounts for a significant portion of the transverse lift signal. Since it is proportional to the acceleration, this is largely seen at the extremes of the heave amplitude where the foil is undergoing maximum acceleration. Figure 5-1 shows force data for a low angle of attack and low Strouhal experiment. The largest transverse forces are seen at $\phi \simeq 0$ and $\phi \simeq \pi$ which corresponds to the point at which the foil is at the maximum heave amplitude at zero angle of attack, aligned parallel to the flow. In this case, the large transverse force is due almost exclusively to the added mass, where trasnverse and rotational accelerations are largest.

The drop in maximum efficiency between heave to chord ratios can be explained in several ways. First, we consider kinetic energy conservation. Earlier it was stated that for $\eta = 1.0$, the foil would extract all of the energy from the fluid leaving the fluid behind it motionless. Although this is impossible, it shows the downstream effect of

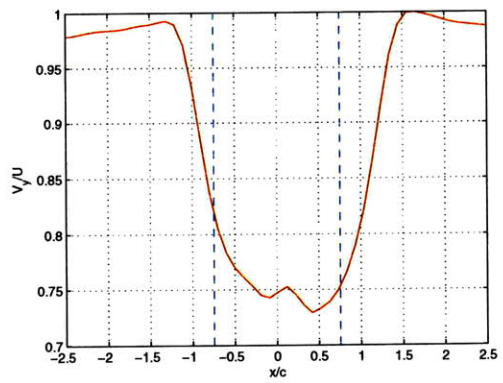

Figure 5-2: Average normalized vertical fluid velocity at $y/c = 1.0$ for $h_0/c = 0.75$, $St = 0.2$, $\alpha_{max} = 25°$.

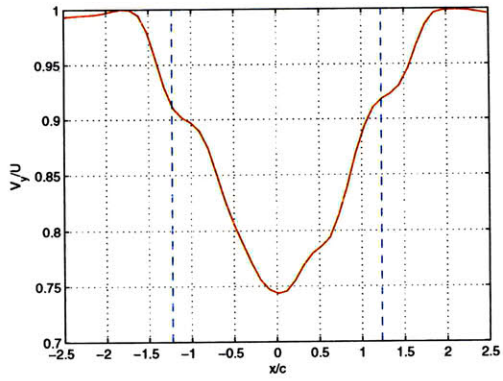

Figure 5-3: Average normalized vertical fluid velocity at $y/c = 1.0$ for $h_0/c = 1.23$, $St = 0.2$, $\alpha_{max} = 25°$.

absorbing kinetic energy from the flow. If we imagine an extremely large heave to chord ratio experiment, the foil will cover a small percentage of the flow window while traversing the flow. As such, the mean downstream fluid velocity averaged over time, will show little effect of the upstream foil. In comparison, during a small heave to chord ratio experiment, the foil can easily cover a large percentage of the flow window during the cycle. The downstream fluid velocity averaged over time will show a larger effect of the upstream foil.

Figures 5-2 and 5-3 illustrate this effect. These figures compare the time-averaged normalized vertical fluid velocity profiles for two different h_0/c ratios, measured at the same downstream distance of $y/c = 1.0$ using the same St and α_{max} parameters in order to show the wake deficit. Figure 5-2 shows the average vertical fluid velocity profile, $\overline{V_y}$, normalized by the free stream flow, U, for $h_0/c = 0.75$. The vertical blue dashed lines are the extent of the heave motion for the pitching point of the foil. In Figure 5-2 we see that $\overline{V_y} \sim 0.75$ within the majority of the heave region. Figure 5-3, on the other hand, only briefly crosses $\overline{V_y} = 0.75$ within the heave region. Energy is extracted from the entire flow window, not just the heave excursion window. This is seen in the wake deficit present in both cases outside of the heave excursion windows. While Figure 5-3 does show a broader region of wake deficit due to the larger heave to chord ratio, spatially averaging the velocity profiles over the x-axis yields nearly

equal values for both oscillation amplitudes. A smaller heave to chord ratio is able to extract more energy with respect to the flow window than the larger heave to chord ratio, as partially illustrated via the average wake deficit.

Second, the way we define the efficiency should be noted. In Chapter 2 the efficiency was defined as average power output divided by the power available in the area that the pitching point of the fluid sweeps out. At the maximum heave amplitudes, the foil pitches as it begins traversing across the flow. In some cases, namely large angles of attack and large flapping frequencies, the trailing edge of the foil will extend beyond the maximum heave amplitude of the pitching point. In smaller heave to chord ratio experiments, the trailing edge distance from the centerline of motion can be as much as 1.5 times the pitching point distance from the centerline of motion. The power available in the swept cross-sectional area is proportional to the swept distance. If we were to re-define the efficiency in terms of the trailing edge swept distance, large discrepancies between the three maximum efficiencies are reduced.

5.2 Force Phasing

At high efficiency points there is a well synchronized phasing of transverse force and transverse velocity. In some cases, rotational velocity and the pitch moment are synchronized as well. Figure 5-4 shows the highest efficiency point for $h_0/c = 1.0$.

Figure 5-4 shows the transverse force (added mass and circulation-based) completely synchronized with the sign of the transverse velocity, and the pitch moment in phase for roughly one quarter of the entire cycle. The lift curve shows four distinct peaks, two per each half cycle. As the foil moves from a $\alpha = 0°$ at $\phi = 0$, a large transverse force develops which then drops off near $\phi = \pi/2$ and has a local peak near $\phi = 7\pi/8$ before returning to zero at $\phi = \pi$.

In regions of high efficiency, the transverse force is similarly shaped to that shown in Figure 5-4. In most cases there are two peaks every half cycle and a well-timed transition of the transverse force. During the first part of the cycle ($\phi \sim 0 - \pi/4$),

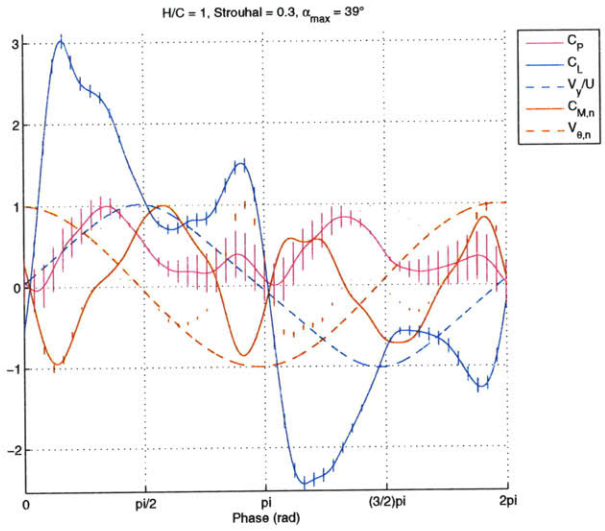

Figure 5-4: Force Data for $h_0/c = 1.0$, St $= 0.3$, $\alpha_{max} = 39°$. Note the phasing of lift and moment forces with their respective velocities.

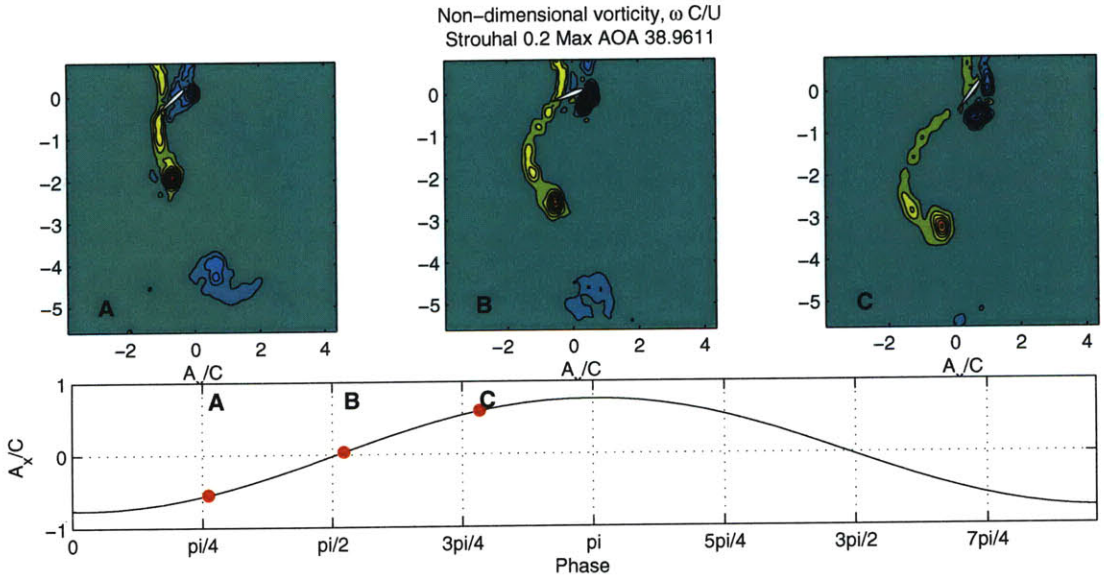

Figure 5-5: DPIV data for $h_0/c = 0.75$, $St = 0.2$, $\alpha_{max} = 39°$. This figure shows dynamic stall, formation of a large LEV and subsequent shedding, in addition to the formation of a second LEV

the foil rotates rapidly causing dynamic stall. The DPIV images show this clearly in Panel A of 5-5. This in turn imparts a rapid increase in the transverse force at $\phi \sim \pi/4$. Dynamic stall happens via rapid angle of attack changes and as the foil reaches the maximum angle of attack and zero rotation velocity at $\phi \sim \pi/2$, the LEV begins to shed. Panel B of Figure 5-5 shows the LEV as it begins traveling backwards along the length of the foil. As it detaches, a local decrease in lift can be seen in force data as a slight drop in the transverse force at $\phi = \pi/2$. The second spike in the transverse force data at $\phi \sim 3\pi/4$ is due to the generation of a second very small LEV begins recovering from α_{max} towards a zero degree angle of attack. The formation of the small LEV vortex can be seen in Panel C of the DPIV images. See the Appendices for entire force data and DPIV image sequences for high efficiency experiments for comparison.

At the smallest heave to chord ratio, we see a small operable region of energy extraction. The frequency of oscillation was the largest for the smallest heave to chord ratio, as given by $f = (StU)/(2h_0)$. As such, the transverse acceleration, as well as rotational acceleration, of the foil were the largest. Added mass, both steady and unsteady due to vorticity, accounts for a large amount of the force in these cases, as the foil must accelerate and then quickly decelerate a large amount of fluid.

As frequencies become larger, the transverse forcing required to move the foil also becomes larger. At combinations of high frequencies and high angles of attack, the force required to accelerate the fluid and foil is larger and opposite direction of the transverse lift force generated by the foil, resulting in transverse forces out of phase with the heave velocity. In some cases, the combination of large non-dimensional heave velocity and large angles of attack orient the foil so that the fluid force acting on the foil points in the opposing direction of the transverse motion. This is true for any point where the angle of attack is equal or greater than the angle of the foil motion. An illustration of this is shown in Figure 5-6. Whenever the angle of attack, $\alpha(t)$ is greater than or equal to the angle of the foil motion, $\theta_p(t)$, the resultant transverse force vector will point in the opposite direction of the heave velocity.

The transition point occurs for the following condition

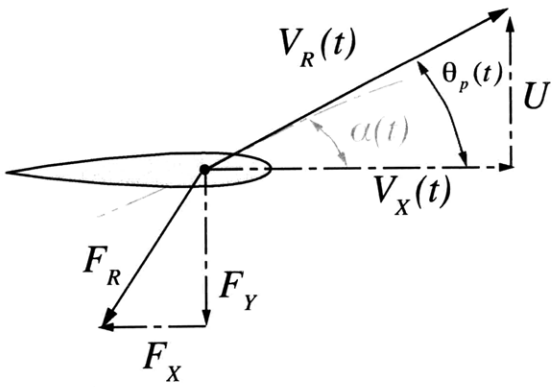

Figure 5-6: Resultant force vectors relation to angle of attack, $\alpha(t)$, and angle of foil motion, $\theta_p(t)$. V_x is the heave velocity, U is the free stream flow.

$$\alpha_{max} \geq \theta_p(t) \tag{5.1}$$

$$\geq \arctan\left(U/V_{x,max}\right) \tag{5.2}$$

From Equation 5.2 we see that larger $V_{x,max}$ values and larger α_{max} values combine to orient the foil in such a way as to generate opposing transverse forces to the motion. Figure 5-7 is presented to illustrate this case. The force data shown is for $h_0/c = 0.75$, St $= 0.5$, and $\alpha_{max} = 48°$. This corresponds to a flapping frequency of almost 1 Hz. Transverse forces are clearly seen at $\phi = \pi/2$ and $\phi = 3\pi/2$ which are opposite sign of the heave velocity and the rotational moment opposes the rotational velocity for the entirety of the cycle.

However, it should be noted that the angle of attack profile is sinusoidal and the foil will only cross this transition point briefly in most cases. In many instances the foil will cross this point but because the majority of the cycle encounters angles of attack lower than α_{max}, it is still possible to extract energy. We use $h_0/c = 1.23$ as an example to illustrate this. Figure 5-8 shows the efficiency contours with experiments where the foil crossed the transition point given in Equation 5.2 marked with black X's. The regions where energy is not extracted is entirely populated by these transition point markers. However, regions of relatively large efficiency also

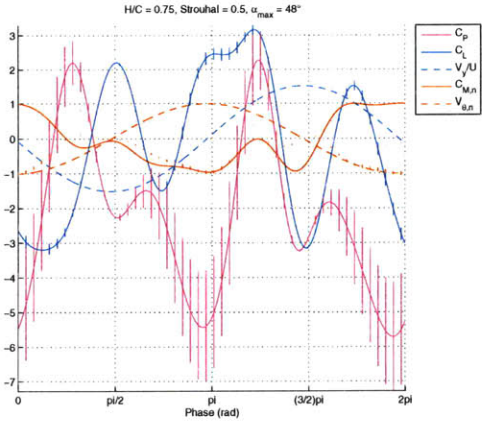

Figure 5-7: Force Data for $h_0/c = 0.75$, St $= 0.5$, $\alpha_{max} = 48°$.

are marked as well, as the foil only approaches this transition point briefly within the cycle. Force data from a representative experiment is shown in Figure 5-9 to illustrate the transverse force reversal.

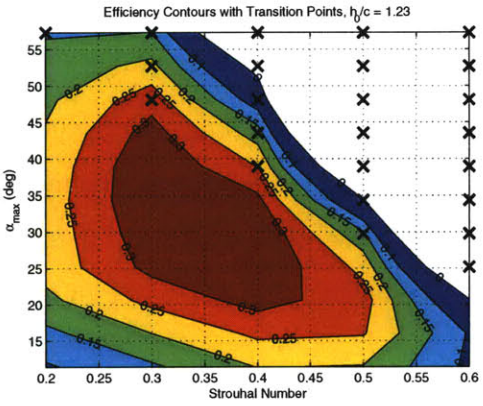

Figure 5-8: Efficiency contours with transition points marked with X's.

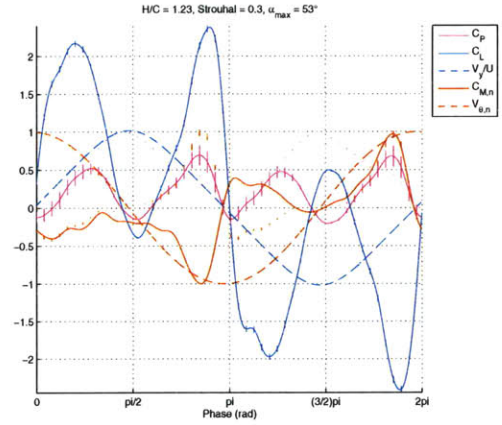

Figure 5-9: Force Data for $h_0/c = 1.23$, St $= 0.3$, $\alpha_{max} = 53°$.

When the foil approaches α_{max}, the transverse force, shown in solid blue, begins to drop. When the foil reaches α_{max} at $\phi = \pi/2$ and $3\pi/2$ the transverse force changes signs, opposing the heave velocity. However, the transverse lift for the majority of the cycle still aligns with the heave velocity, resulting in a net energy extraction from the fluid. Equation 5.2 also explains why the smaller heave to chord ratios exhibit a smaller operable region. Transition points were more frequent within the parameter

space for smaller heave to chord ratios due to the largest heave velocities.

5.3 Wake Patterns

Wake visualizations reveal the flow mechanisms behind the forces presented earlier. Vortex shedding, particularly LEVs, was seen to be critical in the transfer of energy between the fluid and the foil. In the results section it was noted that there were five distinct wake patterns recorded. These patterns are shown below in Figures 5-10, 5-11, 5-12, 5-13, and 5-14.

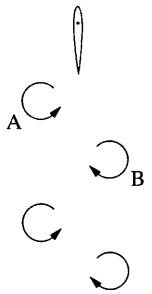

Figure 5-10: 2S Wake Pattern

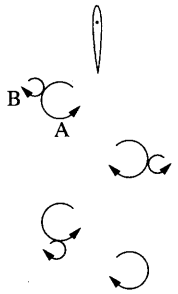

Figure 5-11: 2P Wake Pattern

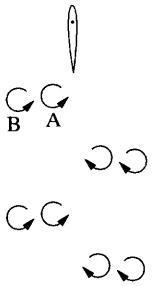

Figure 5-12: 2P* Wake Pattern

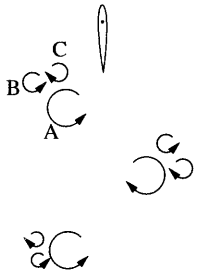

Figure 5-13: 2P*+S Wake Pattern

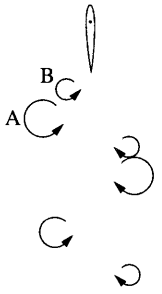

Figure 5-14: 2P*C Wake Pattern

Tables summarizing the wake patterns for the various visualization experiments are given in Tables 4.2, 4.3,and 4.4. Comparing these tables with their respective efficiency tables several trends are seen.

The 2S shedding mode shown in Figure 5-10 is typically seen in small transverse heave velocity and small angle of attack motions. These are stable and well behaved

wakes. Every half cycle as the foil reaches the maximum heave excursion, the LEV which has been forming throughout the transverse motion sheds and travels almost directly downstream, with negligible transverse velocity imparted to the vortex. All experiments that were characterized by this shedding mode had a positive net energy extraction.

The 2P shedding mode shown in Figure 5-11 was seen for experiments with larger angles of attack than the 2S modes. In the illustration, Vortex A is the LEV which is shed at the maximum heave amplitude. Due to the larger angle of attack, the LEV is significantly stronger than in the 2S mode, and when it sheds it is strong enough to entrain rotating fluid from the other side of the foil, generating Vortex B. The two vortices interact and Vortex A induces rotation of Vortex B around Vortex A's core. As the two vortices travel downstream, Vortex B is seen to rotate around Vortex A. All experiments with 2P shedding mode were able to extract energy from the flow. This mode also saw the most consistent transfer of energy from the LEV back to the foil. In most cases, the LEV was phased correctly with the pitching motion and reached the TE as the foil passed through $\alpha = 0°$, causing a large moment on the foil in the same direction as the rotation of the foil.

The 2P* mode is shown in Figure 5-12 and consists of two same-sign vortices shed per half cycle. These wake patterns occurred at frequencies larger than the 2P mode. Increased frequencies resulted in increased rotational velocities and the generation of significant TEV. In the illustration, Vortex A is the TEV which rolls up behind the foil as it pitches and Vortex B is the LEV generated during the traverse. These two vortices travel almost directly downstream as well.

The 2P*C mode was observed in only two of the visualizations for the largest heave to chord ratio. This mode resembles the 2P* mode except the two vortices shed every half cycle collide with each other and form a single vortex with a poorly defined core. This is illustrated in Figure 5-14. Vortex A and Vortex B in this illustration are shed near the maximum heave amplitude, and similar to the 2P* mode, Vortex A corresponds to the LEV while Vortex B is the TEV cause by the rapid rotation of the foil. The foil rotation also imparts a horizontal velocity to the

spinning fluid, translating the cores outwards from the center line. This mode appears to be a transition point between the 2P and 2P* mode.

The final mode observed was the 2P*+S mode, shown in Figure 5-13. It was only seen for $h_0/c = 0.75$ and 1.0. For a given angle of attack, this mode was observed at higher frequencies. Similar to the 2P* and 2P*C modes, the foil generates a LEV and TEV during the traverse and rotation, however these are strong enough vortices to entrain fluid from the other side of the foil which is rotating in the opposite direction. Vortex A is the LEV, Vortex B is the TEV, and Vortex C is the entrained fluid. All but one of the experiments where this mode was observed required energy input and were not able to extract net energy from the flow. These vortices undergo the largest outward horizontal translation as they travel downstream due to the fast heave and rotation motions.

Regions of maximum efficiency were all seen to produce the same wake pattern. In every instance, the maximum efficiency region was characterized by the 2P mode. The most energy intensive points were also characterized by the same wake pattern, the 2P*+S mode. However, between the different heave to chord ratios, the wake trends do not align when parameterized by the Strouhal number.

5.4 Parameterization

The Strouhal number, which is dependent on the foil kinematics, i.e. the heave amplitude, is originally used to characterize the oscillating mechanisms of the flow. In turn, the efficiency contours generated are parameterized in terms of the Strouhal number. However, several other non-dimensional parameters introduced in Section 2.1 exist which can be used to characterize the oscillating mechanisms of the flow. While the Strouhal number depends on foil kinematics, reduced frequency depends on the foil geometry. The reduced frequency is given by Equation 2.3, which states $f_r = fc/U$. Using this parameter to characterize the motions results in the contours collapsing nearly on top of each other.

To illustrate this we use the isolines of $\eta = 0.20$ and $\eta = 0.0$, for ease of viewing,

shown in Figure 5-15. Red lines depict contours for $\eta = 0.20$ and blue lines are used for $\eta = 0.0$. The corresponding h_0/c ratio is tagged on each of the isolines. In this Figure the efficiency isolines appear to "stretch" with increasing h_0/c towards higher Strouhal numbers.

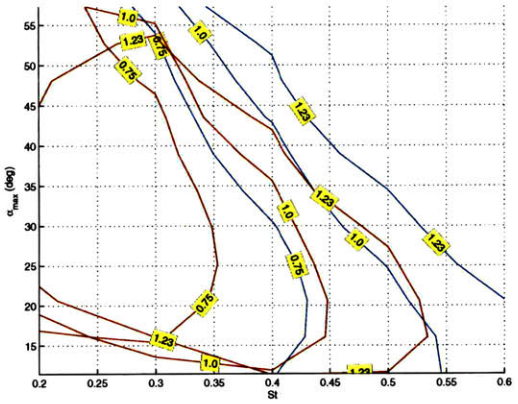

Figure 5-15: Isolines for $\eta = 0.20$ (red) and $\eta = 0.0$ (blue) for $h_0/c = 0.75$, 1.0, 1.23 plotted against St number with corresponding h_0/c ratio marking the isolines.

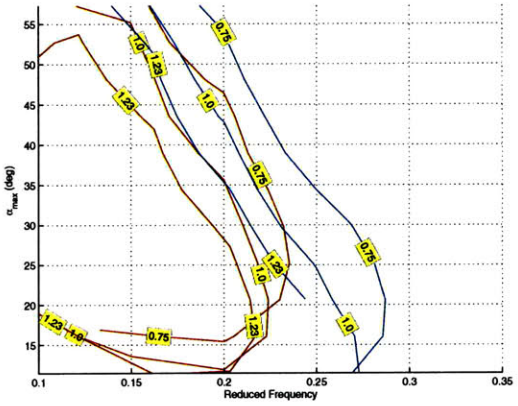

Figure 5-16: Isolines for $\eta = 0.20$ (red) and $\eta = 0.0$ (blue) for $h_0/c = 0.75$, 1.0, 1.23 plotted against the f_r with corresponding h_0/c ratio marking the isolines.

By using the reduced frequency, which is dependent on foil geometry only, we observe these isolines tending to collapse on top of each other. Figure 5-16 shows the effect of parameterizing by the reduced frequency. The isolines for both efficiencies show considerably better grouping in this case. Figures 5-17 and 5-18 show the isosurfaces for $\eta = 0.2$, 0.1, and 0 graphed in 3d space against the heave to chord ratio. Figure 5-17 which is graphed against St shows the efficiency contours "stretching" towards high St with increasing h_0/c. Figure 5-18 which is graphed against f_r, shows the same three efficiency levels remaining nearly constant with increasing h_0/c ratios, experiencing comparatively little divergence amongst the three oscillation amplitudes.

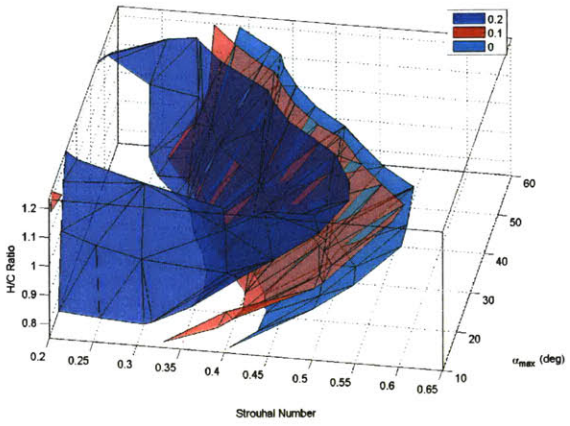

Figure 5-17: St parameterized isosurfaces for $\eta = 0.2$ (blue), 0.1 (red), and 0.0 (aqua). Note the divergence of the contour lines between the heave to chord ratios.

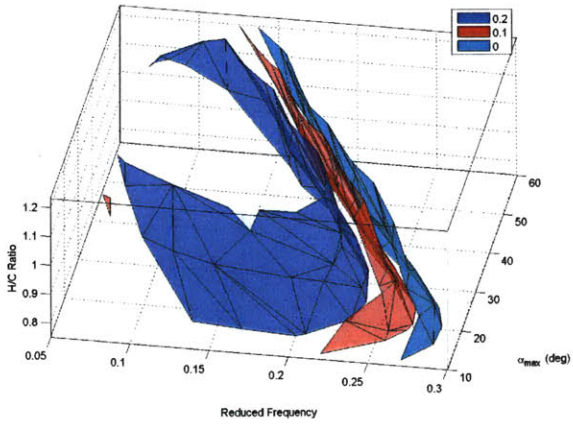

Figure 5-18: f_r parameterized isosurfaces for $\eta = 0.2$ (blue), 0.1 (red), and 0.0 (aqua). Note the grouping of contours between heave to chord ratios.

Further, if all of the efficiencies are parameterized in terms of the reduced frequency, a well defined region of maximum efficiency is seen to exist between the varying heave to chord ratios around $f_r \sim 0.12$ - 0.15. A table highlighting this region is shown in Table 5.1. The columns of the table originate from different heave to chord ratios, but when put in terms of their reduced frequencies, fit well together and show no observable discontinuities in efficiency trends around the region of interest. A table which includes all the experiments parameterized in terms of reduced frequency can be found in Table B.4.

Similarly, the wake patterns, when parameterized by the reduced frequency, collapse well and show well defined trends. A graphical illustration of the wake patterns based on the reduced frequency is shown in Figure 5-19. Table B.5 in the Appendix shows vortex shedding modes for all DPIV experiments collapsed and parameterized in terms of the reduced frequency as well. This trend suggests that using the reduced frequency, f_r, could be a better way to parameterize the results for comparison between unique oscillation amplitudes.

	0.08	**0.1**	**0.12**	**0.13**	**0.15**	**0.16**
57.3	0.15	0.23	0.15	0.39	0.16	-0.19
52.7	0.17	0.26	0.22	0.41	0.25	-0.03
48.1	0.19	0.29	0.28	0.44	0.33	0.07
43.5	0.20	0.31	0.32	0.44	0.36	0.17
38.9	0.22	0.31	0.35	0.45	0.39	0.25
34.4	0.22	0.31	0.35	0.41	0.39	0.31
29.8	0.22	0.29	0.33	0.35	0.39	0.35
25.2	0.22	0.27	0.32	0.31	0.36	0.35
20.6	0.19	0.22	0.26	0.24	0.29	0.32
16.0	0.14	0.16	0.20	0.19	0.25	0.26
11.5	0.09	0.12	0.14	0.12	0.16	0.20

Table 5.1: Efficiency values for $h_0/c = 0.75$, $h_0/c = 1.0$, and $h_0/c = 1.23$ parameterized by f_r, shown in the top row, and α_{max}, shown in the left column.

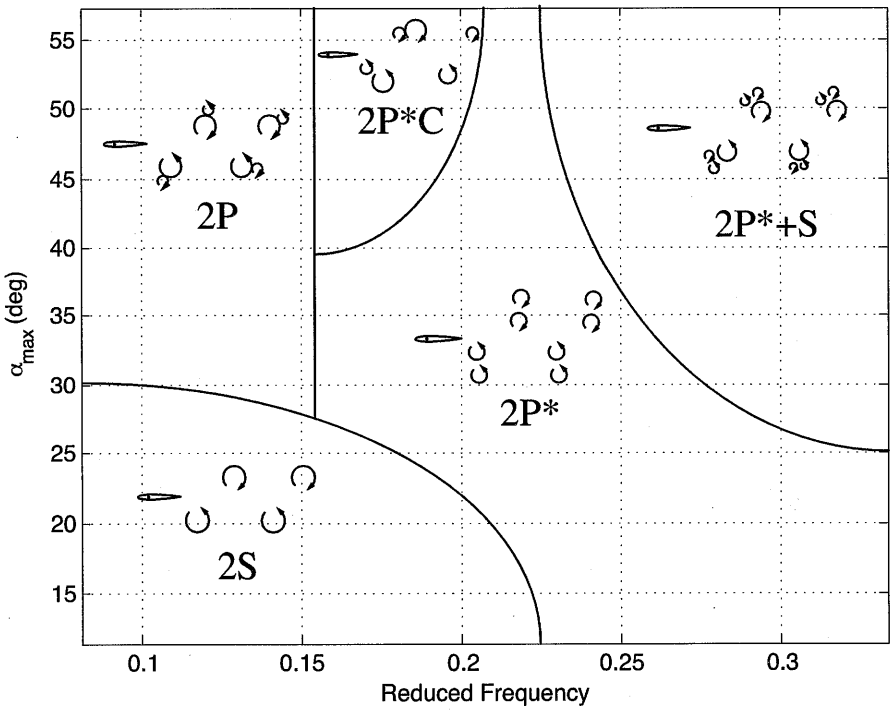

Figure 5-19: Wake Patterns based on Reduced Frequency and Maximum Angle of Attack

Comparisons with recent numerical studies find a good correlation between simulation results and the experimental results found in this thesis. Although the numerical studies mentioned have slightly different flow conditions, motions, and parameters, the range of reduced frequencies where large efficiencies occur are useful for comparison.

Kinsey and Dumas performed a numerical study of oscillating foil power-extraction using a sinusoidal pitch and heave motion as mentioned in Section 1.2 [15]. They found efficiencies as large as $\eta = 0.34$ for $f_r \sim 0.12$-0.18. LEV formation and subsequent transfer of energy into rotational motion of the foil was also found to be important for the highest efficiency cases. Similar force peaks and phasing were also found.

Another numerical model presented by Zhu and Peng, based on the Navier-Stokes equation at low Reynolds number ($\sim O(10^3)$), shows maximum efficiencies occurring around an equivalent $f_r \sim 0.15$-0.25 [31]. Adopting their efficiency definition, the adjusted regions of maximum efficiency found in this thesis occur within a similar region of $f_r \sim 0.10$-0.26.

Chapter 6

Conclusions

Bio-locomtion was used as inspiration for a novel fluid energy extraction device. Using sinusoidal motions similar to a fish, experiments were performed using a foil, undergoing forced harmonic actuation in heave and pitch, submerged in an oncoming flow. The foil motions were defined by the flapping frequency, oscillation amplitude, maximum angle of attack, and harmonically driven pitch and angle of attack profiles.

Overall, appreciable hydrodynamic energy extraction efficiencies were found within the parametric space. Broad regions of efficiencies around $\eta = 0.20$ were found for the largest oscillation amplitude, while narrow regions of high efficiency up to $\eta = 0.45$ were recorded for the smallest oscillation amplitude. It was found that lower flapping frequencies were more likely to produce well phased force and lift curves while larger frequencies tended to introduce higher harmonic forcing and poorly phased force and lift curves.

DPIV visualizations revealed clear connections between high efficiency regions and vortex shedding modes. Namely, the 2P shedding mode was exhibited in high efficiency regions while 2P*+S was indicative of poor performance. The 2P mode was also seen to exhibit the most consistent transfer of energy to the foil from the fluid via the LEV and the rotational motion of the foil. Leading-edge vortices and the phase of their shedding with respect to the foils rotation were seen to play an integral role in harnessing energy from the rotation degree-of-freedom. The DPIV results show transitions from well-behaved and clearly defined vortices at low flapping frequencies

to chaotic vortices with strong interactions at higher flapping frequencies.

Although the experiments were originally designed and parameterized in terms of the Strouhal number, reduced frequency was found to be a more appropriate way to characterize the motions. Using the Strouhal number to parameterize flapping frequency resulted in efficiency and wake pattern discontinuities when trying to compare between heave to chord ratios. When the reduced frequency was used to parameterize the motions, it was seen that the efficiency contours and vortex modes shared common trends between the heave to chord ratios. The efficiencies from the three different heave amplitudes collapsed well when combined by reduced frequency to create an overall table of efficiencies. Additionally, comparisons with recent numerical studies show several different sources independently finding regions of high efficiency at reduced frequencies near those found in this study.

While these experiments were successful in identifying regions of energy extraction, several considerations should be taken into account. Foremost, the efficiencies recorded in these experiments were the hydrodynamic efficiencies. The energy required to drive and control the foil was not accounted for. In a similar vein, these results are for a foil which is being controlled and driven by several motors. A system which is not actuated or is only actuated in one degree of freedom will likely perform differently. Ideally, a passively actuated system could obtain efficiencies near those recorded in the forced motions performed in this thesis.

Several suggestions are made for future work in the area. Experimentally, a finer parametric grid would improve the DPIV data and possibly reveal transition regions more clearly, similar to the 2P*C region found. While maximum efficiency regions were found, finer resolution would also clarify more specifically where these maxima occur. New experiments comparing the forced data to flow-driven motions in a passively actuated system would also be extremely valuable. This lends itself to numerical optimization of both the power take off systems, foil geometry, and kinematics. Finally, continuing with bio-inspired designs, investigation of compliant foils, as seen in aquatic mammals, would be worthwhile to see if the compliance can decrease the sensitivity to operating parameters, enabling broader parametric ranges of

energy extraction.

Appendix A

Transverse Inertial Measurement Figures

The following figures show the measured mass inertia in the transverse direction with predicted mass inertias which is used to correct the raw force signals.

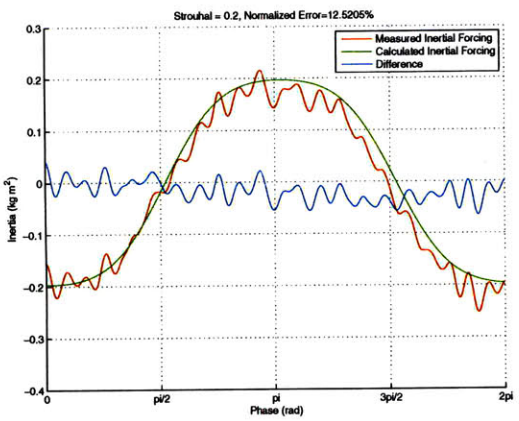

(a) Strouhal 0.2

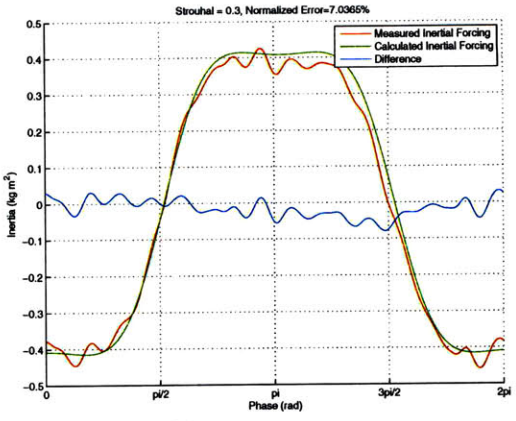

(b) Strouhal 0.3

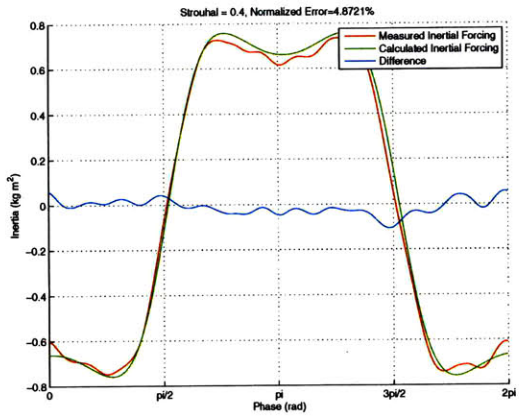

(c) Strouhal 0.4

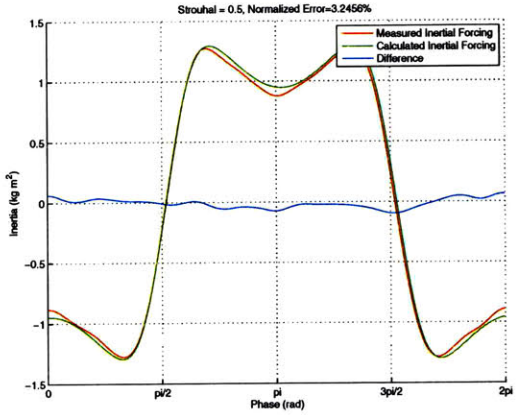

(d) Strouhal 0.5

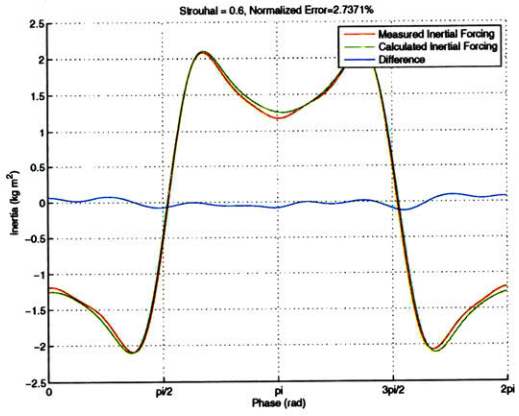

(e) Strouhal 0.6

Figure A-1: 1" Chord Foil – Inertia Measurement Verification – Red lines indicate the measured inertial forcing, Green lines indicated the calculated inertial forcing, Blue lines indicate the error between the measured and calculated

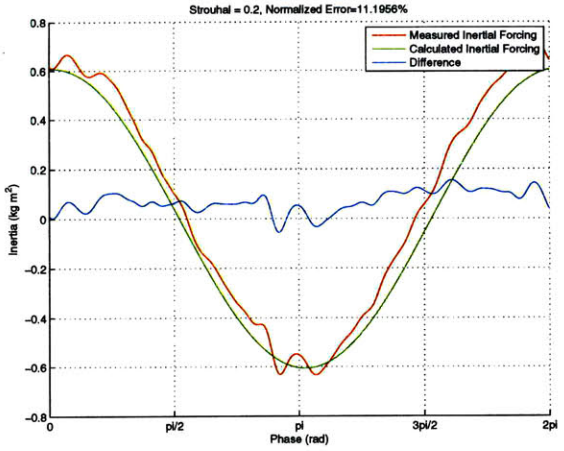

(a) Strouhal 0.2

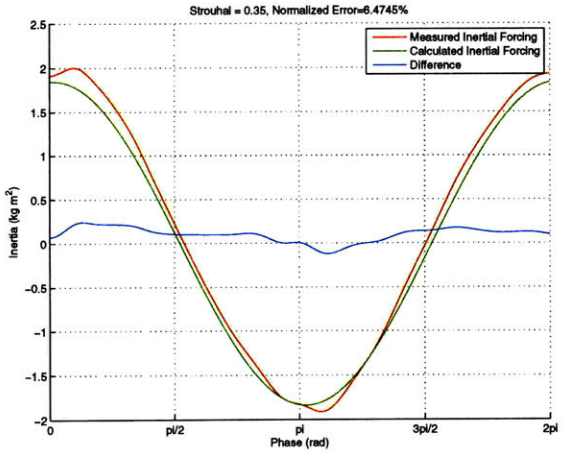

(b) Strouhal 0.35

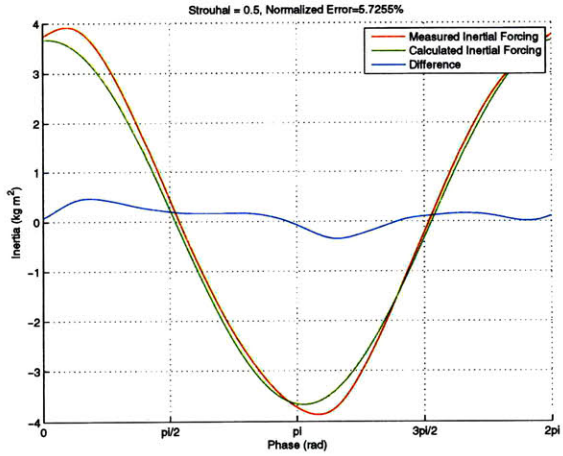

(c) Strouhal 0.5

Figure A-2: 2.75" Chord Foil – Inertia Measurement Verification – Red lines indicate the measured inertial forcing, Green lines indicated the calculated inertial forcing, Blue lines indicate the error between the measured and calculated

Appendix B

Energy Extraction Efficiency Tables

These tables represent the mean net energy extracted over one cycle of the foil motion. Negative efficiencies indicate more energy was required to actuate the foil than energy that could be extracted. NaN indicates that one or more force channels were saturated and data was therefore unsuitable for use.

	0.2	**0.3**	**0.4**	**0.5**	**0.6**
57.3	0.39 ± 0.04	-0.10 ± 0.02	-1.40 ± 0.70	NaN	NaN
52.7	0.41 ± 0.04	0.04 ± 0.01	-1.08 ± 0.52	NaN	NaN
48.1	0.44 ± 0.04	0.16 ± 0.03	-0.79 ± 0.37	NaN	NaN
43.5	0.44 ± 0.04	0.27 ± 0.05	-0.56 ± 0.25	-1.78 ± 0.16	NaN
38.9	0.45 ± 0.04	0.33 ± 0.06	-0.33 ± 0.15	-1.31 ± 0.15	NaN
34.4	0.41 ± 0.03	0.38 ± 0.07	-0.13 ± 0.05	-0.93 ± 0.14	NaN
29.8	0.35 ± 0.02	0.36 ± 0.06	0.03 ± 0.01	-0.59 ± 0.14	NaN
25.2	0.31 ± 0.02	0.31 ± 0.05	0.10 ± 0.04	-0.36 ± 0.13	-1.58 ± 1.95
20.6	0.24 ± 0.01	0.27 ± 0.04	0.11 ± 0.04	-0.25 ± 0.13	-1.19 ± 1.39
16.0	0.19 ± 0.01	0.21 ± 0.03	0.08 ± 0.03	-0.19 ± 0.12	-0.93 ± 1.03
11.5	0.12 ± 0.01	0.14 ± 0.02	0.01 ± 0.01	-0.23 ± 0.12	-0.76 ± 0.72

Table B.1: Efficiencies for $h_0/c = 0.75$

	0.2	**0.3**	**0.4**	**0.5**	**0.6**
57.3	0.23 ± 0.01	-17 ± 0.03	-0.60 ± 0.15	-2.18 ± 1.08	NaN
52.7	0.26 ± 0.01	0.25 ± 0.03	-0.28 ± 0.06	-1.83 ± 0.89	NaN
48.1	0.29 ± 0.01	0.32 ± 0.04	-0.15 ± 0.04	-1.47 ± 0.67	NaN
43.5	0.30 ± 0.01	0.36 ± 0.04	-0.02 ± 0.01	-1.07 ± 0.46	NaN
38.9	0.31 ± 0.01	0.39 ± 0.04	0.13 ± 0.03	-0.66 ± 0.27	NaN
34.4	0.31 ± 0.01	0.39 ± 0.04	0.23 ± 0.05	-0.40 ± 0.16	NaN
29.8	0.29 ± 0.01	0.38 ± 0.03	0.31 ± 0.06	-0.18 ± 0.07	-1.07 ± 0.73
25.2	0.27 ± 0.01	0.35 ± 0.03	0.32 ± 0.06	-0.01 ± 0.01	-0.68 ± 0.45
20.6	0.22 ± 0.01	0.29 ± 0.02	0.31 ± 0.05	0.01 ± 0.03	-0.39 ± 0.25
16.0	0.16 ± 0.01	0.25 ± 0.02	0.24 ± 0.04	0.15 ± 0.05	-0.21 ± 0.14
11.5	0.12 ± 0.01	0.16 ± 0.01	0.19 ± 0.03	0.13 ± 0.04	-0.16 ± 0.09

Table B.2: Efficiencies for $h_0/c = 1.0$

	0.2	**0.3**	**0.4**	**0.5**	**0.6**
57.3	0.15 ± 0.01	0.15 ± 0.01	-0.17 ± 0.03	-1.27 ± 0.38	NaN
52.7	0.17 ± 0.01	0.22 ± 0.01	-0.03 ± 0.01	-0.99 ± 0.28	NaN
48.1	0.19 ± 0.01	0.28 ± 0.02	0.07 ± 0.01	-0.68 ± 0.18	NaN
43.5	0.20 ± 0.01	0.32 ± 0.02	0.18 ± 0.02	-0.41 ± 0.10	NaN
38.9	0.22 ± 0.01	0.35 ± 0.02	0.25 ± 0.03	-0.17 ± 0.04	NaN
34.4	0.22 ± 0.01	0.35 ± 0.02	0.31 ± 0.04	0.01 ± 0.01	-0.72 ± 0.29
29.8	0.22 ± 0.01	0.34 ± 0.02	0.35 ± 0.04	0.16 ± 0.03	-0.40 ± 0.15
25.2	0.22 ± 0.01	0.32 ± 0.01	0.35 ± 0.04	0.24 ± 0.05	-0.17 ± 0.06
20.6	0.19 ± 0.01	0.27 ± 0.01	0.32 ± 0.03	0.27 ± 0.05	0.00 ± 0.01
16.0	0.14 ± 0.01	0.20 ± 0.01	0.26 ± 0.02	0.25 ± 0.05	0.09 ± 0.03
11.5	0.09 ± 0.01	0.14 ± 0.01	0.20 ± 0.02	0.19 ± 0.04	0.08 ± 0.03

Table B.3: Efficiencies for $h_0/c = 1.23$

	0.08	**0.10**	**0.12**	**0.13**	**0.15**	**0.16**	**0.20**	**0.20**	**0.20**	**0.25**	**0.27**	**0.33**
57.3	0.15	0.23	0.15	0.39	0.16	-0.19	-0.10	-0.61	-1.27	-2.23	-1.40	-3.25
52.7	0.17	0.26	0.22	0.41	0.25	-0.03	0.04	-0.28	-0.99	-1.86	-1.08	-2.75
48.1	0.19	0.29	0.28	0.44	0.33	0.07	0.16	-0.15	-0.68	-1.47	-0.79	-2.20
43.5	0.20	0.31	0.32	0.44	0.36	0.17	0.27	-0.02	-0.40	-1.08	-0.56	-1.78
38.9	0.22	0.31	0.35	0.45	0.39	0.25	0.33	0.13	-0.17	-0.66	-0.33	-1.31
34.4	0.22	0.31	0.35	0.41	0.39	0.31	0.38	0.23	0.00	-0.41	-0.13	-0.93
29.8	0.22	0.29	0.33	0.35	0.39	0.35	0.36	0.31	0.16	-0.19	0.03	-0.59
25.2	0.22	0.27	0.32	0.31	0.36	0.35	0.31	0.32	0.24	-0.01	0.10	-0.36
20.6	0.19	0.22	0.26	0.24	0.29	0.32	0.27	0.31	0.27	0.08	0.11	-0.25
16.0	0.14	0.16	0.20	0.19	0.25	0.26	0.21	0.24	0.25	0.15	0.08	-0.19
11.5	0.09	0.12	0.14	0.12	0.16	0.20	0.14	0.20	0.20	0.13	0.01	-0.23

Table B.4: Efficiencies for all experiments parameterized in terms of reduced frequency (shown in top row) and α_{max} (shown in left column).

	0.08	**0.10**	**0.12**	**0.13**	**0.15**	**0.16**	**0.20**	**0.20**	**0.20**	**0.25**	**0.27**	**0.33**
57.3	-	-	-	-	-	-	-	-	-	-	-	-
52.7	2P	2P	2P	2P	2P	2P*C	2P*	2P*	2P*	2P*+S	2P*+S	2P*+S
48.1	-	-	-	-	-	-	-	-	-	-	-	-
43.5	-	-	-	-	-	-	-	-	-	-	-	-
38.9	2P	2P	2P	2P	2P	2P*C	2P*	2P*	2P*	2P*+S	2P*+S	2P*+S
34.4	-	-	-	-	-	-	-	-	-	-	-	-
29.8	-	-	-	-	-	-	-	-	-	-	-	-
25.2	2P	2S	2S	2S	2S	2P*	2P*	2P*	2P*	2P*+S	2P*+S	2P*+S
20.6	-	-	-	-	-	-	-	-	-	-	-	-
16.0	-	-	-	-	-	-	-	-	-	-	-	-
11.5	2S	2S	2S	2S	2S	2S	2S	2S	2S	2P*	2P*	2P*

Table B.5: Vortex shedding modes for all experiments parameterized in terms of reduced frequency (shown in top row) and α_{max} (shown in left column).

Appendix C

Force Data: $h_0/c = 0.75$

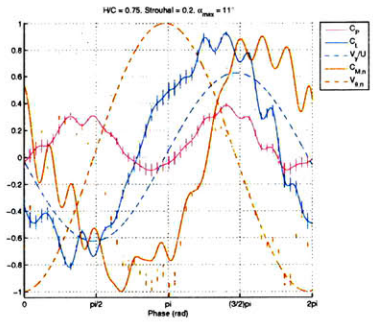

Figure C-1: Force Data for $h_0/c = 0.75$, St = 0.2 and $\alpha_{max} = 11°$

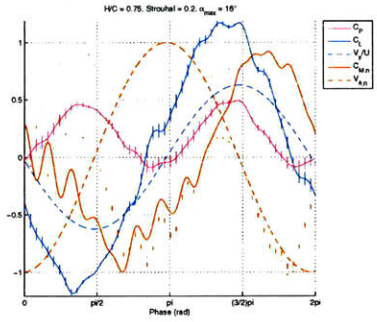

Figure C-2: Force Data for $h_0/c = 0.75$, St = 0.2 and $\alpha_{max} = 16°$

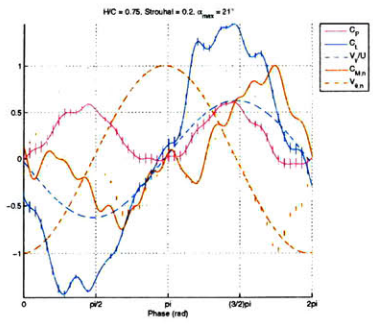

Figure C-3: Force Data for $h_0/c = 0.75$, St = 0.2 and $\alpha_{max} = 21°$

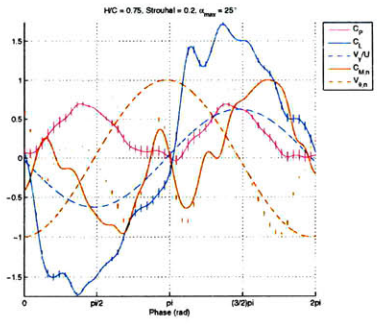

Figure C-4: Force Data for $h_0/c = 0.75$, St = 0.2 and $\alpha_{max} = 25°$

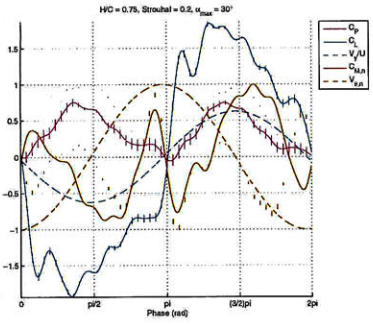

Figure C-5: Force Data for $h_0/c = 0.75$, $St = 0.2$ and $\alpha_{max} = 30°$

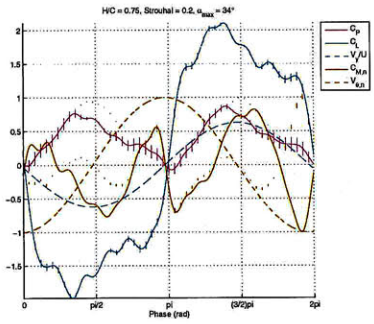

Figure C-6: Force Data for $h_0/c = 0.75$, $St = 0.2$ and $\alpha_{max} = 34°$

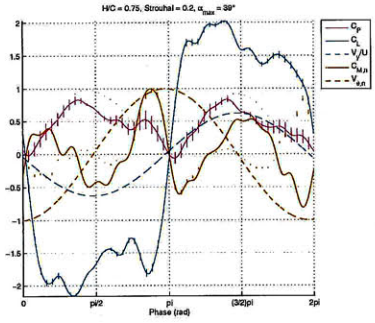

Figure C-7: Force Data for $h_0/c = 0.75$, $St = 0.2$ and $\alpha_{max} = 39°$

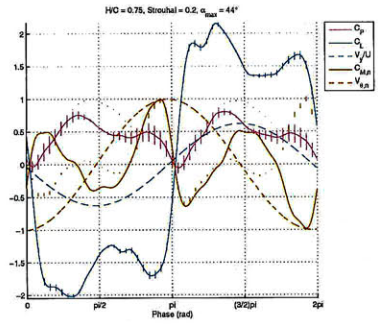

Figure C-8: Force Data for $h_0/c = 0.75$, $St = 0.2$ and $\alpha_{max} = 44°$

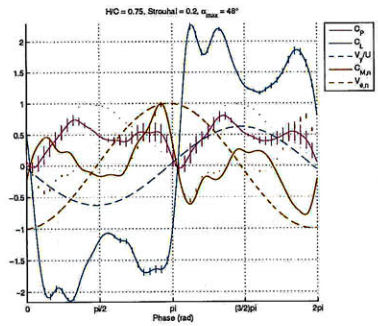

Figure C-9: Force Data for $h_0/c = 0.75$, $St = 0.2$ and $\alpha_{max} = 48°$

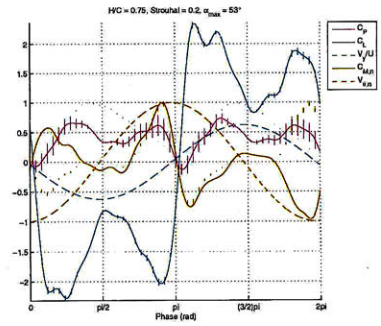

Figure C-10: Force Data for $h_0/c = 0.75$, $St = 0.2$ and $\alpha_{max} = 53°$

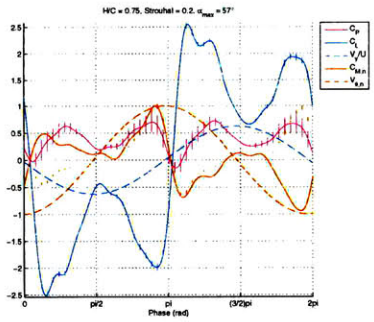

Figure C-11: Force Data for $h_0/c = 0.75$, $St = 0.2$ and $\alpha_{max} = 57°$

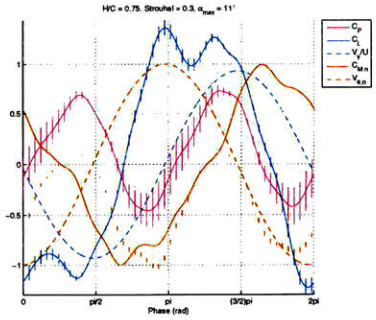

Figure C-12: Force Data for $h_0/c = 0.75$, $St = 0.3$ and $\alpha_{max} = 11°$

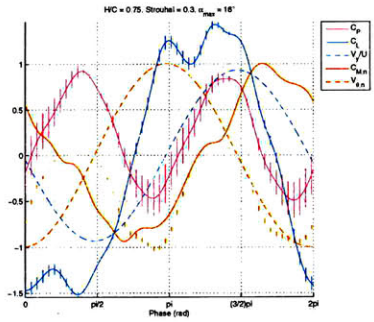

Figure C-13: Force Data for $h_0/c = 0.75$, $St = 0.3$ and $\alpha_{max} = 16°$

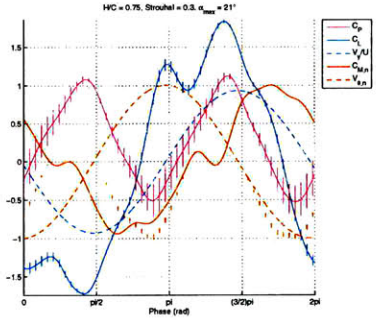

Figure C-14: Force Data for $h_0/c = 0.75$, $St = 0.3$ and $\alpha_{max} = 21°$

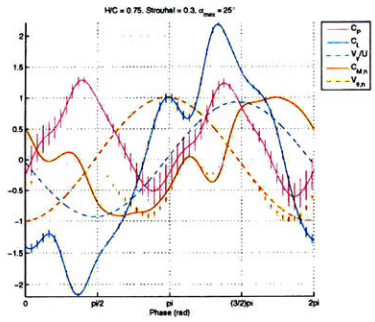

Figure C-15: Force Data for $h_0/c = 0.75$, $St = 0.3$ and $\alpha_{max} = 25°$

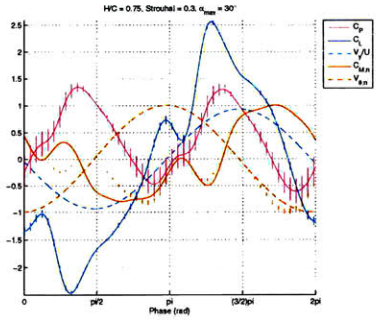

Figure C-16: Force Data for $h_0/c = 0.75$, $St = 0.3$ and $\alpha_{max} = 30°$

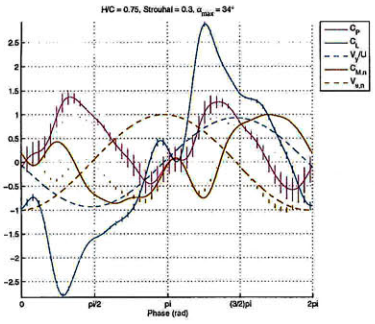

Figure C-17: Force Data for $h_0/c = 0.75$, $St = 0.3$ and $\alpha_{max} = 34°$

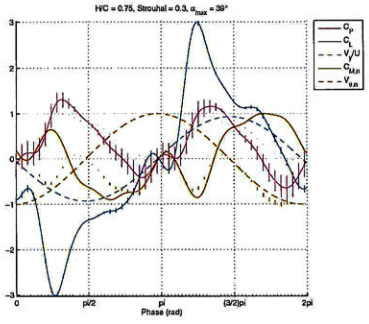

Figure C-18: Force Data for $h_0/c = 0.75$, $St = 0.3$ and $\alpha_{max} = 39°$

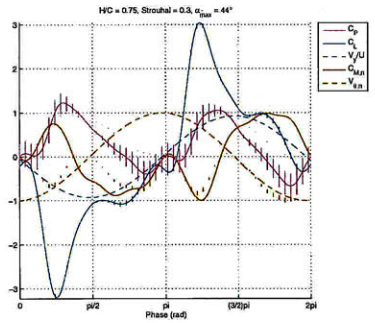

Figure C-19: Force Data for $h_0/c = 0.75$, $St = 0.3$ and $\alpha_{max} = 44°$

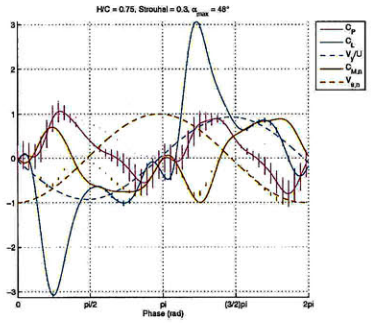

Figure C-20: Force Data for $h_0/c = 0.75$, $St = 0.3$ and $\alpha_{max} = 48°$

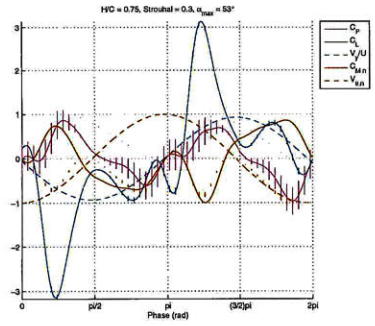

Figure C-21: Force Data for $h_0/c = 0.75$, $St = 0.3$ and $\alpha_{max} = 53°$

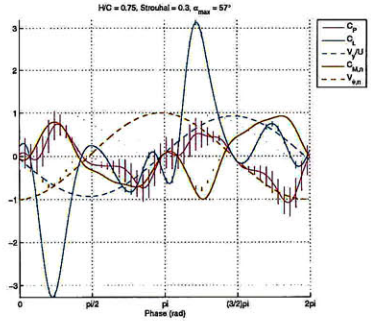

Figure C-22: Force Data for $h_0/c = 0.75$, $St = 0.3$ and $\alpha_{max} = 57°$

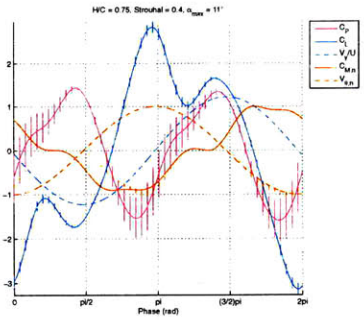

Figure C-23: Force Data for $h_0/c = 0.75$, $St = 0.4$ and $\alpha_{max} = 11°$

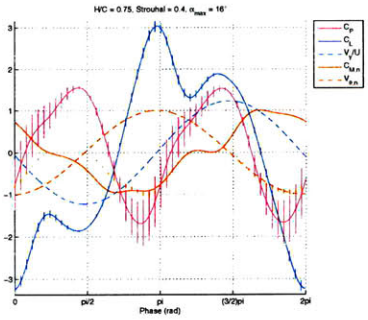

Figure C-24: Force Data for $h_0/c = 0.75$, $St = 0.4$ and $\alpha_{max} = 16°$

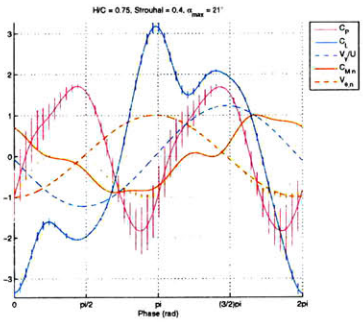

Figure C-25: Force Data for $h_0/c = 0.75$, $St = 0.4$ and $\alpha_{max} = 21°$

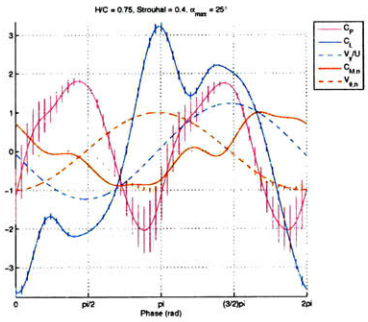

Figure C-26: Force Data for $h_0/c = 0.75$, $St = 0.4$ and $\alpha_{max} = 25°$

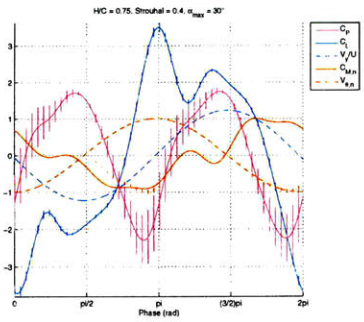

Figure C-27: Force Data for $h_0/c = 0.75$, $St = 0.4$ and $\alpha_{max} = 30°$

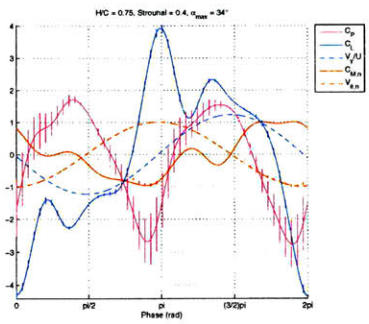

Figure C-28: Force Data for $h_0/c = 0.75$, $St = 0.4$ and $\alpha_{max} = 34°$

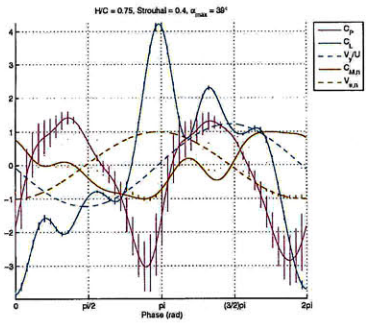

Figure C-29: Force Data for $h_0/c = 0.75$, $St = 0.4$ and $\alpha_{max} = 39°$

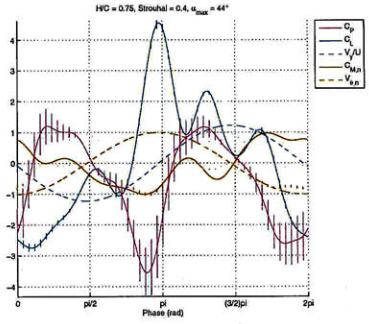

Figure C-30: Force Data for $h_0/c = 0.75$, $St = 0.4$ and $\alpha_{max} = 44°$

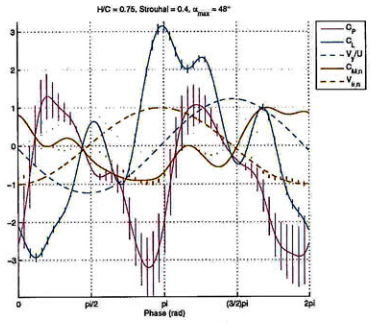

Figure C-31: Force Data for $h_0/c = 0.75$, $St = 0.4$ and $\alpha_{max} = 48°$

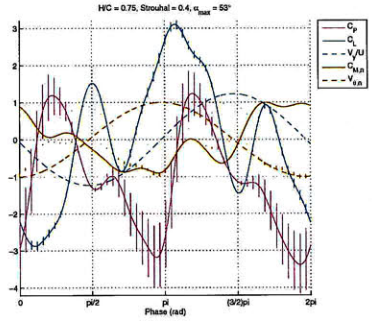

Figure C-32: Force Data for $h_0/c = 0.75$, $St = 0.4$ and $\alpha_{max} = 53°$

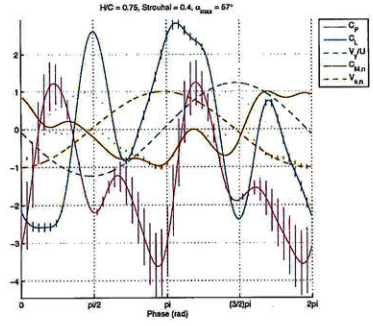

Figure C-33: Force Data for $h_0/c = 0.75$, $St = 0.4$ and $\alpha_{max} = 57°$

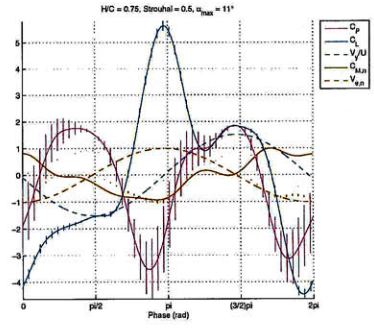

Figure C-34: Force Data for $h_0/c = 0.75$, $St = 0.5$ and $\alpha_{max} = 11°$

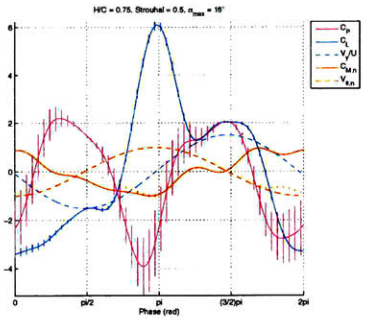

Figure C-35: Force Data for $h_0/c = 0.75$, $St = 0.5$ and $\alpha_{max} = 16°$

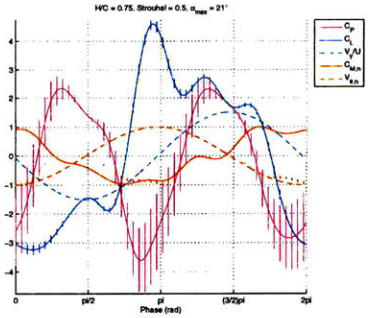

Figure C-36: Force Data for $h_0/c = 0.75$, $St = 0.5$ and $\alpha_{max} = 21°$

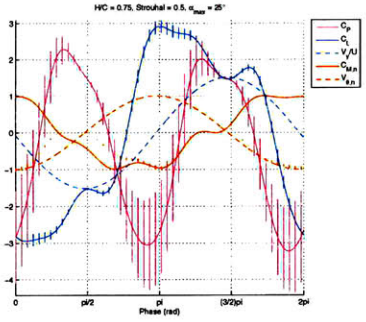

Figure C-37: Force Data for $h_0/c = 0.75$, $St = 0.5$ and $\alpha_{max} = 25°$

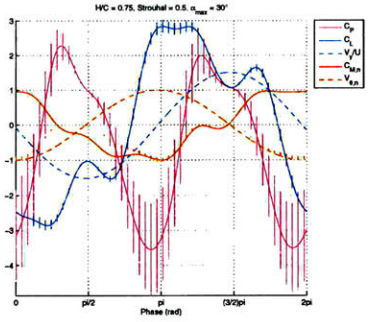

Figure C-38: Force Data for $h_0/c = 0.75$, $St = 0.5$ and $\alpha_{max} = 30°$

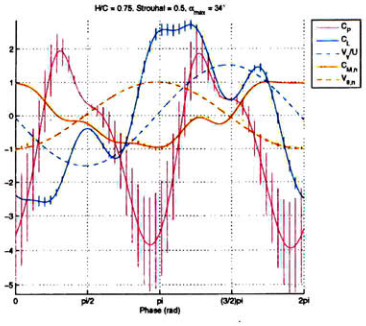

Figure C-39: Force Data for $h_0/c = 0.75$, $St = 0.5$ and $\alpha_{max} = 34°$

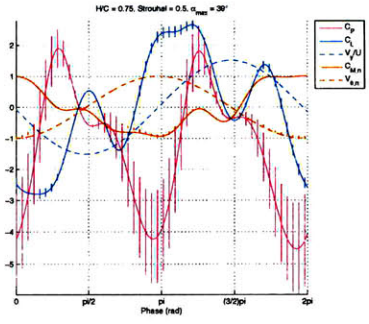

Figure C-40: Force Data for $h_0/c = 0.75$, $St = 0.5$ and $\alpha_{max} = 39°$

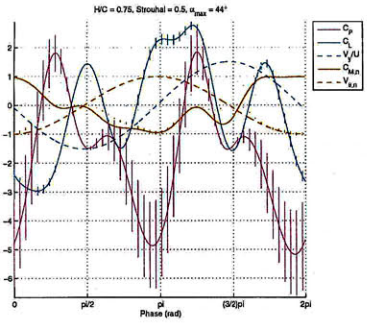

Figure C-41: Force Data for $h_0/c = 0.75$, $St = 0.5$ and $\alpha_{max} = 44°$

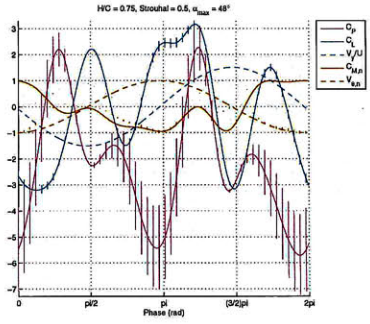

Figure C-42: Force Data for $h_0/c = 0.75$, $St = 0.5$ and $\alpha_{max} = 48°$

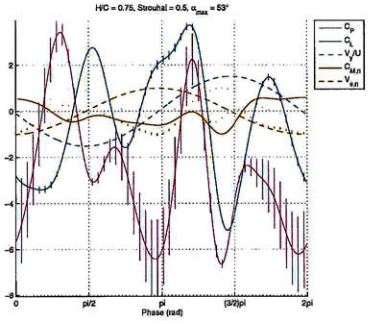

Figure C-43: Force Data for $h_0/c = 0.75$, $St = 0.5$ and $\alpha_{max} = 53°$

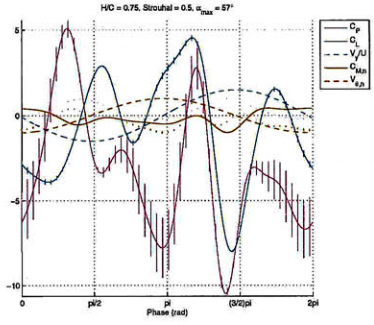

Figure C-44: Force Data for $h_0/c = 0.75$, $St = 0.5$ and $\alpha_{max} = 57°$

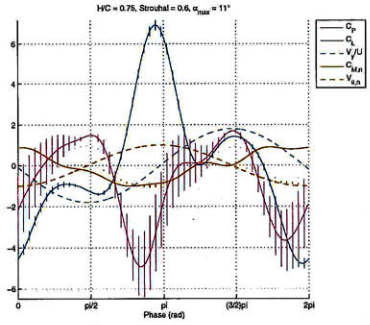

Figure C-45: Force Data for $h_0/c = 0.75$, $St = 0.6$ and $\alpha_{max} = 11°$

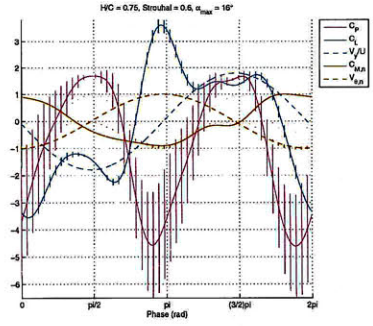

Figure C-46: Force Data for $h_0/c = 0.75$, $St = 0.6$ and $\alpha_{max} = 16°$

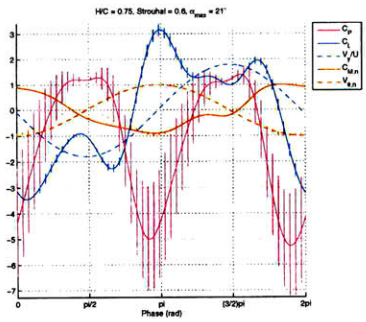

Figure C-47: Force Data for $h_0/c = 0.75$, $St = 0.6$ and $\alpha_{max} = 21°$

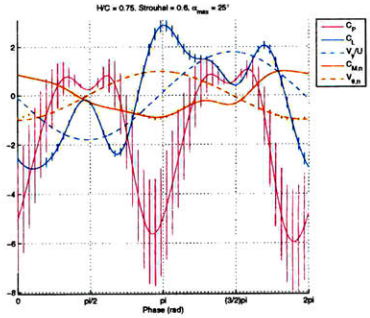

Figure C-48: Force Data for $h_0/c = 0.75$, $St = 0.6$ and $\alpha_{max} = 25°$

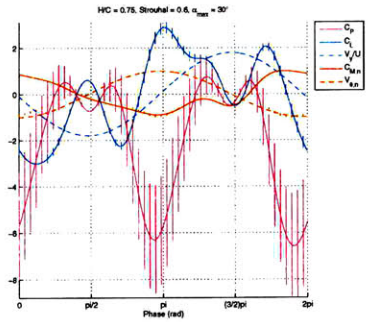

Figure C-49: Force Data for $h_0/c = 0.75$, $St = 0.6$ and $\alpha_{max} = 30°$

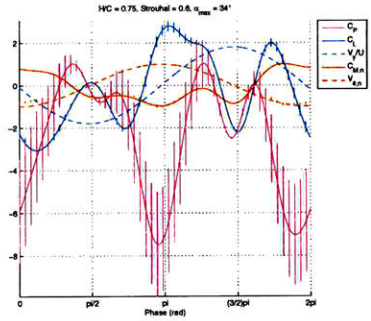

Figure C-50: Force Data for $h_0/c = 0.75$, $St = 0.6$ and $\alpha_{max} = 34°$

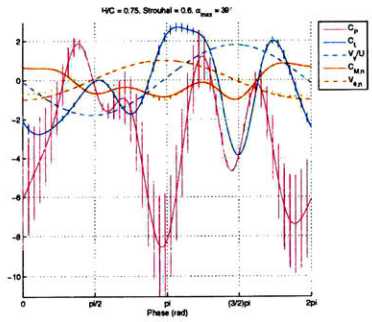

Figure C-51: Force Data for $h_0/c = 0.75$, $St = 0.6$ and $\alpha_{max} = 39°$

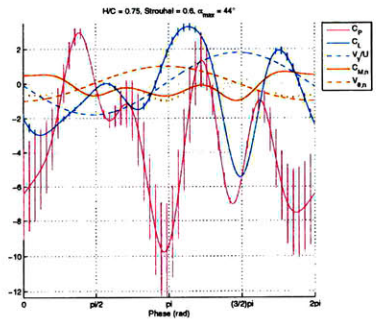

Figure C-52: Force Data for $h_0/c = 0.75$, $St = 0.6$ and $\alpha_{max} = 44°$

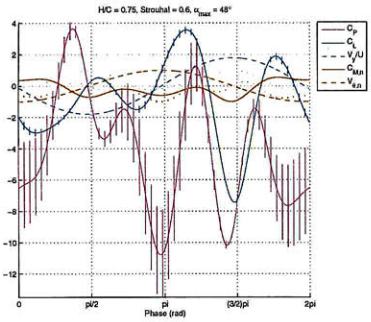

Figure C-53: Force Data for $h_0/c = 0.75$, $St = 0.6$ and $\alpha_{max} = 48°$

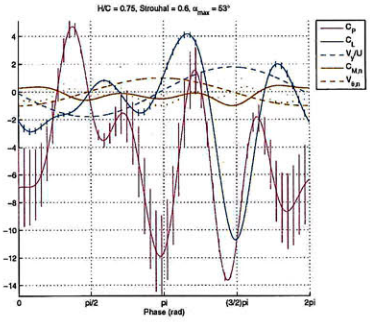

Figure C-54: Force Data for $h_0/c = 0.75$, $St = 0.6$ and $\alpha_{max} = 53°$

Appendix D

Force Data: $h_0/c = 1.0$

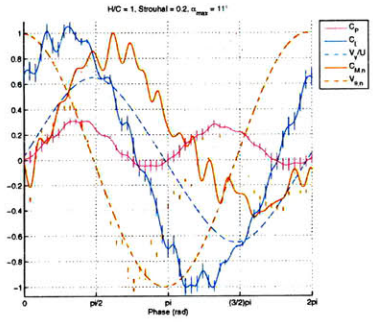

Figure D-1: Force Data for $h_0/c = 1.0$, St $= 0.2$ and $\alpha_{max} = 11°$

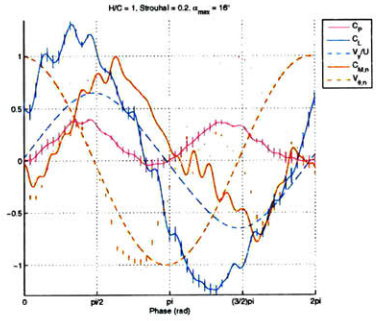

Figure D-2: Force Data for $h_0/c = 1.0$, St $= 0.2$ and $\alpha_{max} = 16°$

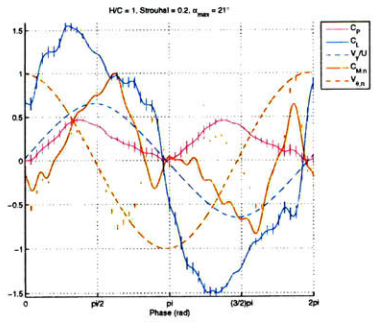

Figure D-3: Force Data for $h_0/c = 1.0$, St $= 0.2$ and $\alpha_{max} = 21°$

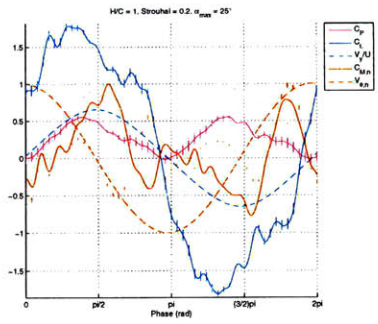

Figure D-4: Force Data for $h_0/c = 1.0$, St $= 0.2$ and $\alpha_{max} = 25°$

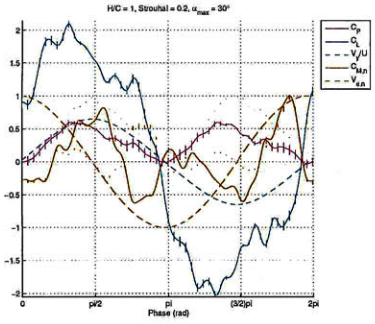

Figure D-5: Force Data for $h_0/c = 1.0$, $St = 0.2$ and $\alpha_{max} = 30°$

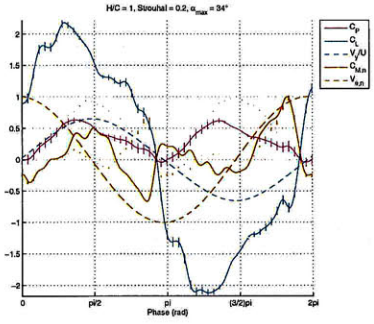

Figure D-6: Force Data for $h_0/c = 1.0$, $St = 0.2$ and $\alpha_{max} = 34°$

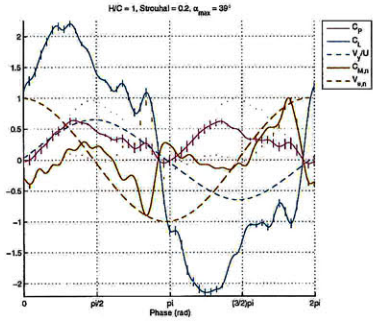

Figure D-7: Force Data for $h_0/c = 1.0$, $St = 0.2$ and $\alpha_{max} = 39°$

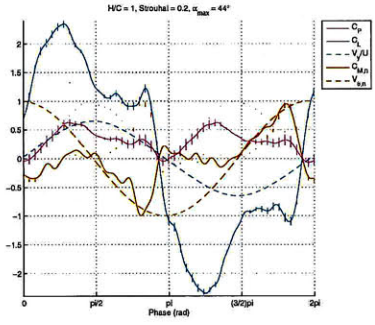

Figure D-8: Force Data for $h_0/c = 1.0$, $St = 0.2$ and $\alpha_{max} = 44°$

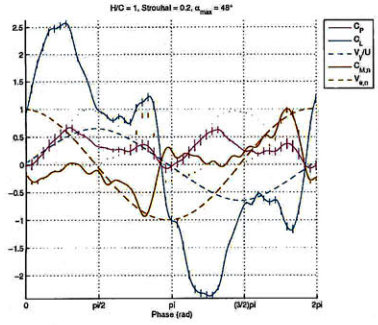

Figure D-9: Force Data for $h_0/c = 1.0$, $St = 0.2$ and $\alpha_{max} = 48°$

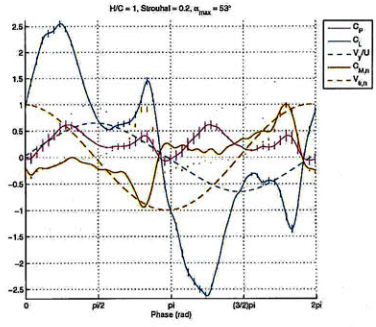

Figure D-10: Force Data for $h_0/c = 1.0$, $St = 0.2$ and $\alpha_{max} = 53°$

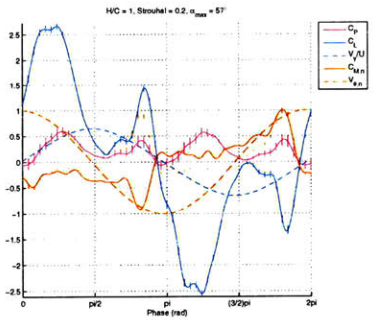

Figure D-11: Force Data for $h_0/c = 1.0$, $St = 0.2$ and $\alpha_{max} = 57°$

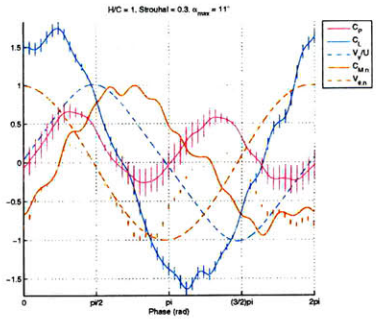

Figure D-12: Force Data for $h_0/c = 1.0$, $St = 0.3$ and $\alpha_{max} = 11°$

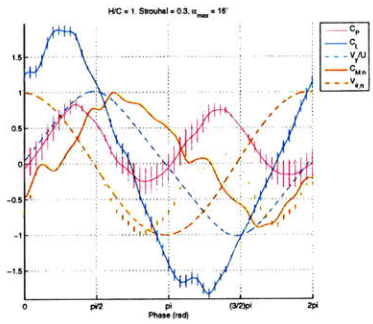

Figure D-13: Force Data for $h_0/c = 1.0$, $St = 0.3$ and $\alpha_{max} = 16°$

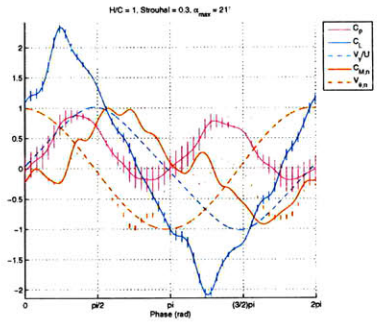

Figure D-14: Force Data for $h_0/c = 1.0$, $St = 0.3$ and $\alpha_{max} = 21°$

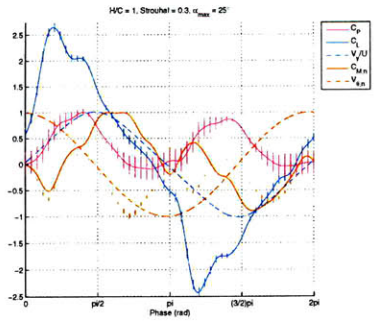

Figure D-15: Force Data for $h_0/c = 1.0$, $St = 0.3$ and $\alpha_{max} = 25°$

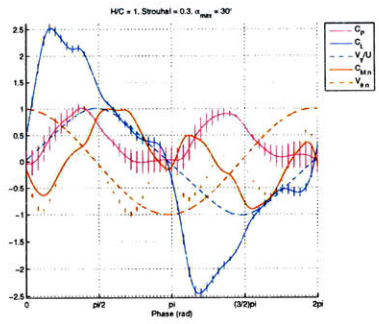

Figure D-16: Force Data for $h_0/c = 1.0$, $St = 0.3$ and $\alpha_{max} = 30°$

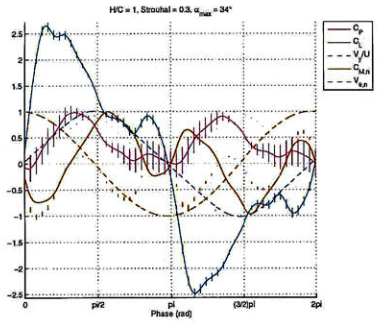

Figure D-17: Force Data for $h_0/c = 1.0$, $St = 0.3$ and $\alpha_{max} = 34°$

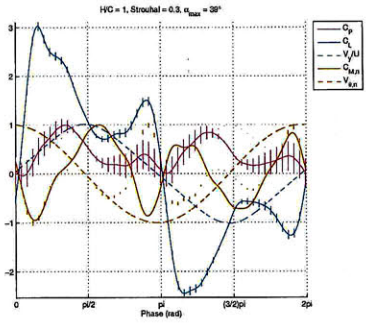

Figure D-18: Force Data for $h_0/c = 1.0$, $St = 0.3$ and $\alpha_{max} = 39°$

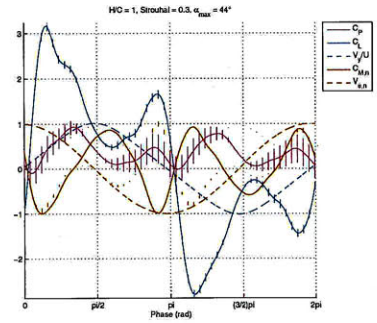

Figure D-19: Force Data for $h_0/c = 1.0$, $St = 0.3$ and $\alpha_{max} = 44°$

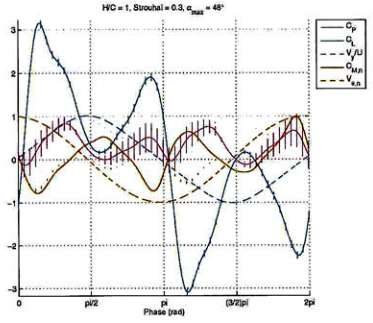

Figure D-20: Force Data for $h_0/c = 1.0$, $St = 0.3$ and $\alpha_{max} = 48°$

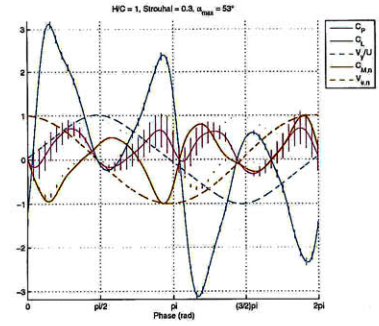

Figure D-21: Force Data for $h_0/c = 1.0$, $St = 0.3$ and $\alpha_{max} = 53°$

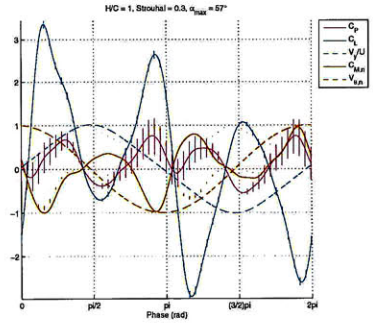

Figure D-22: Force Data for $h_0/c = 1.0$, $St = 0.3$ and $\alpha_{max} = 57°$

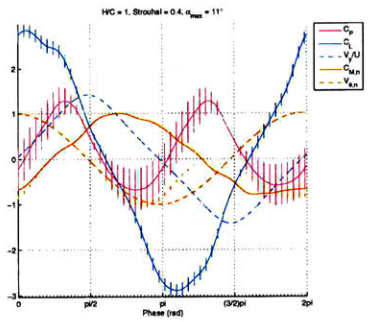

Figure D-23: Force Data for $h_0/c = 1.0$, $St = 0.4$ and $\alpha_{max} = 11°$

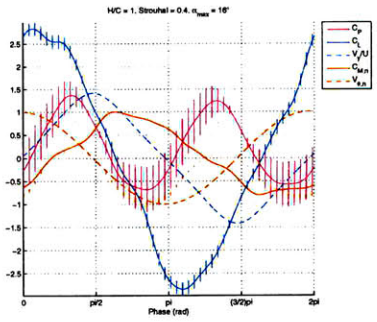

Figure D-24: Force Data for $h_0/c = 1.0$, $St = 0.4$ and $\alpha_{max} = 16°$

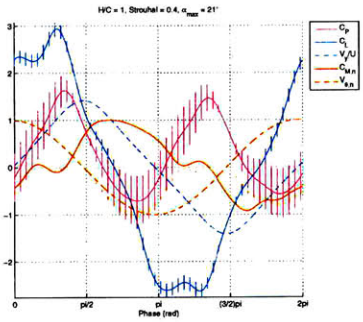

Figure D-25: Force Data for $h_0/c = 1.0$, $St = 0.4$ and $\alpha_{max} = 21°$

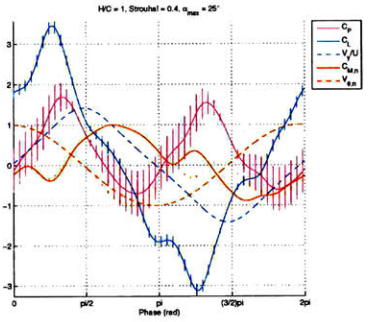

Figure D-26: Force Data for $h_0/c = 1.0$, $St = 0.4$ and $\alpha_{max} = 25°$

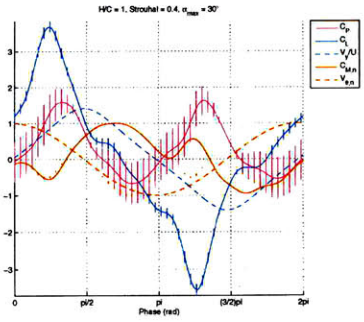

Figure D-27: Force Data for $h_0/c = 1.0$, $St = 0.4$ and $\alpha_{max} = 30°$

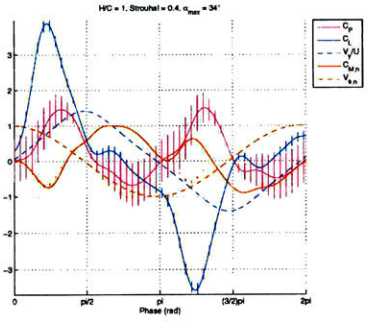

Figure D-28: Force Data for $h_0/c = 1.0$, $St = 0.4$ and $\alpha_{max} = 34°$

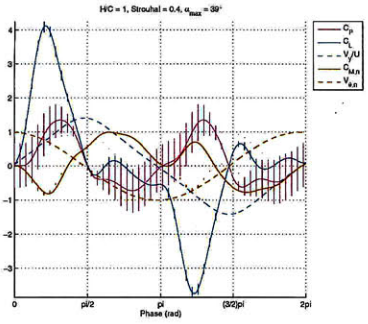

Figure D-29: Force Data for $h_0/c = 1.0$, $St = 0.4$ and $\alpha_{max} = 39°$

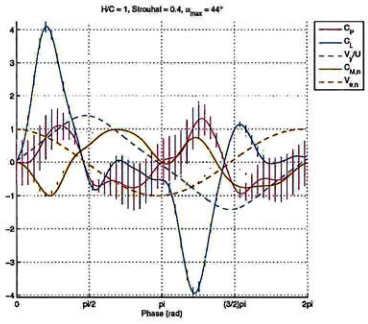

Figure D-30: Force Data for $h_0/c = 1.0$, $St = 0.4$ and $\alpha_{max} = 44°$

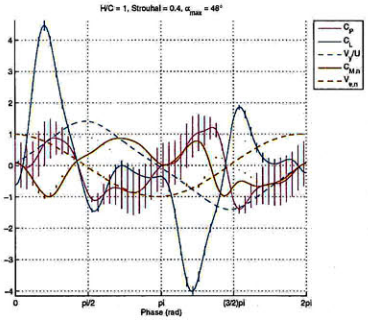

Figure D-31: Force Data for $h_0/c = 1.0$, $St = 0.4$ and $\alpha_{max} = 48°$

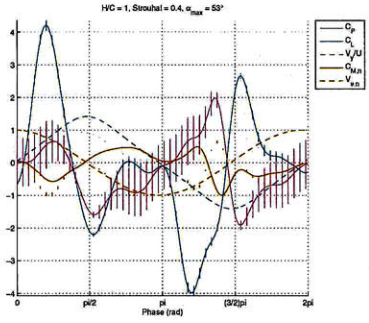

Figure D-32: Force Data for $h_0/c = 1.0$, $St = 0.4$ and $\alpha_{max} = 53°$

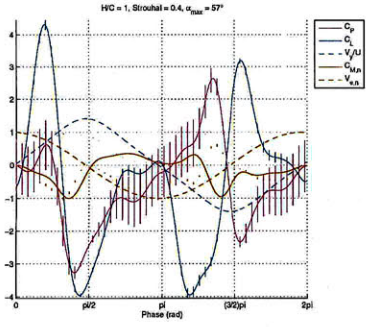

Figure D-33: Force Data for $h_0/c = 1.0$, $St = 0.4$ and $\alpha_{max} = 57°$

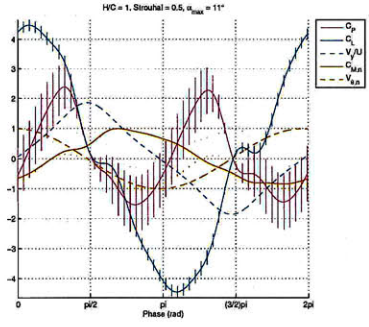

Figure D-34: Force Data for $h_0/c = 1.0$, $St = 0.5$ and $\alpha_{max} = 11°$

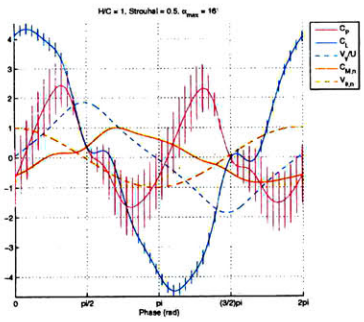

Figure D-35: Force Data for $h_0/c = 1.0$, $St = 0.5$ and $\alpha_{max} = 16°$

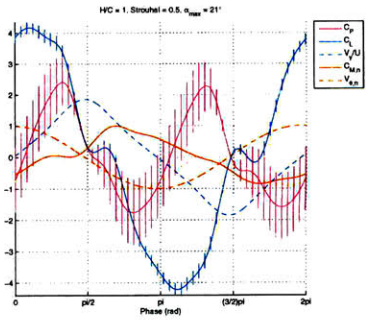

Figure D-36: Force Data for $h_0/c = 1.0$, $St = 0.5$ and $\alpha_{max} = 21°$

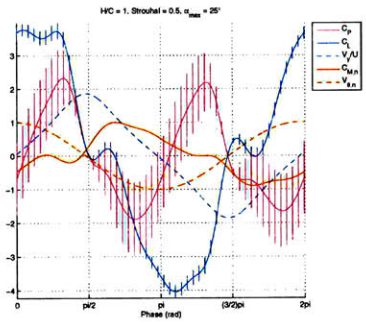

Figure D-37: Force Data for $h_0/c = 1.0$, $St = 0.5$ and $\alpha_{max} = 25°$

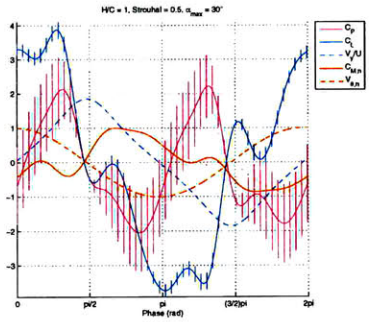

Figure D-38: Force Data for $h_0/c = 1.0$, $St = 0.5$ and $\alpha_{max} = 30°$

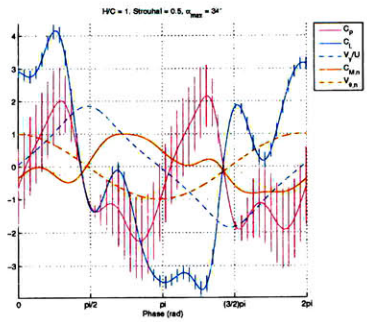

Figure D-39: Force Data for $h_0/c = 1.0$, $St = 0.5$ and $\alpha_{max} = 34°$

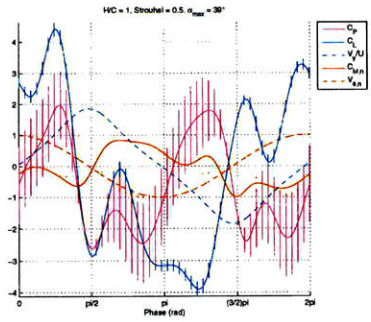

Figure D-40: Force Data for $h_0/c = 1.0$, $St = 0.5$ and $\alpha_{max} = 39°$

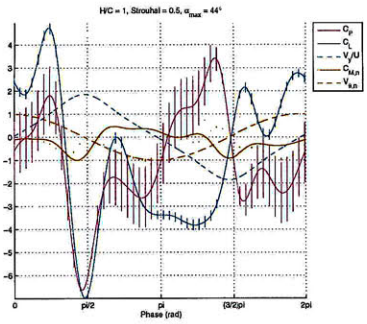

Figure D-41: Force Data for $h_0/c = 1.0$, $St = 0.5$ and $\alpha_{max} = 44°$

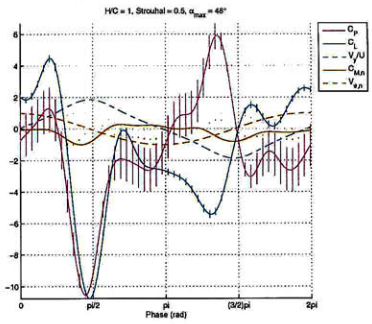

Figure D-42: Force Data for $h_0/c = 1.0$, $St = 0.5$ and $\alpha_{max} = 48°$

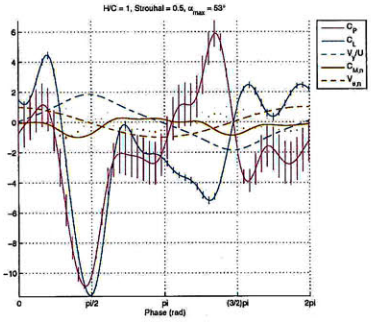

Figure D-43: Force Data for $h_0/c = 1.0$, $St = 0.5$ and $\alpha_{max} = 53°$

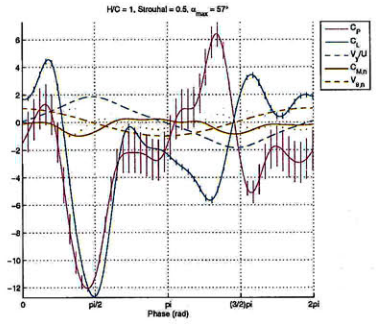

Figure D-44: Force Data for $h_0/c = 1.0$, $St = 0.5$ and $\alpha_{max} = 57°$

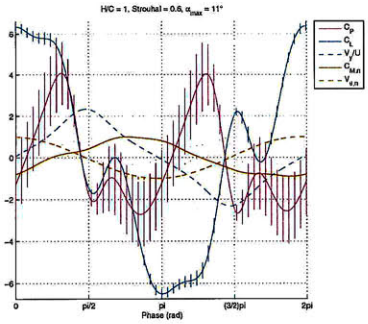

Figure D-45: Force Data for $h_0/c = 1.0$, $St = 0.6$ and $\alpha_{max} = 11°$

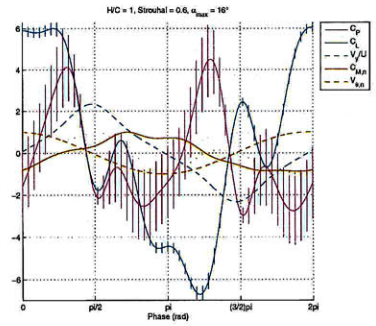

Figure D-46: Force Data for $h_0/c = 1.0$, $St = 0.6$ and $\alpha_{max} = 16°$

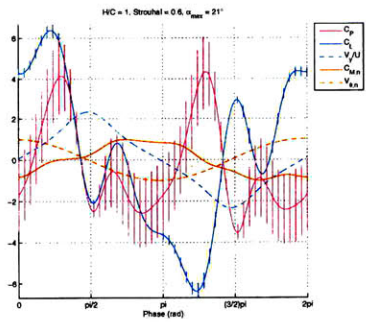

Figure D-47: Force Data for $h_0/c = 1.0$, St $= 0.6$ and $\alpha_{max} = 21°$

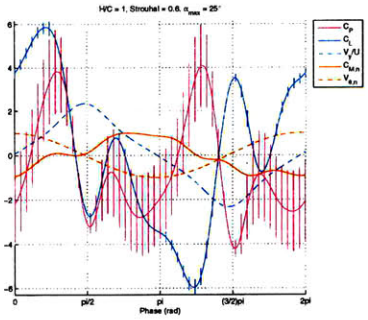

Figure D-48: Force Data for $h_0/c = 1.0$, St $= 0.6$ and $\alpha_{max} = 25°$

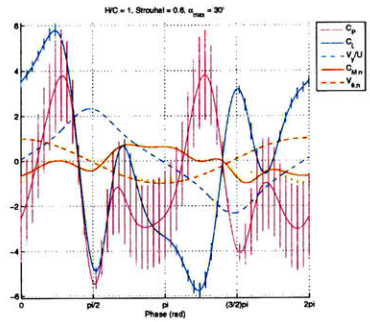

Figure D-49: Force Data for $h_0/c = 1.0$, St $= 0.6$ and $\alpha_{max} = 30°$

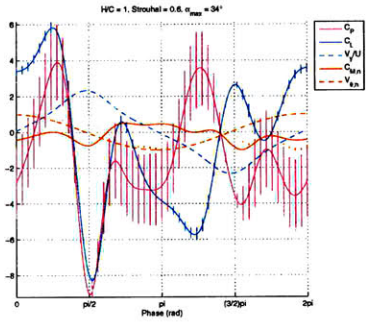

Figure D-50: Force Data for $h_0/c = 1.0$, St $= 0.6$ and $\alpha_{max} = 34°$

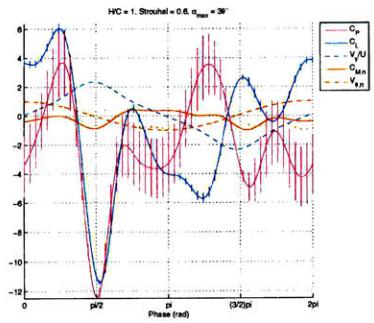

Figure D-51: Force Data for $h_0/c = 1.0$, St $= 0.6$ and $\alpha_{max} = 39°$

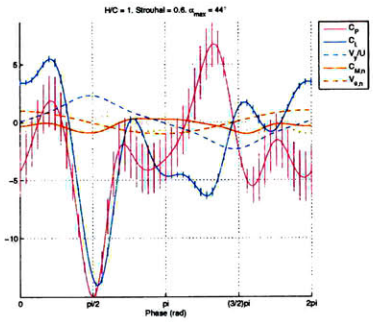

Figure D-52: Force Data for $h_0/c = 1.0$, St $= 0.6$ and $\alpha_{max} = 44°$

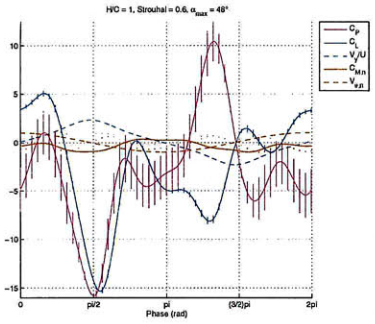

Figure D-53: Force Data for $h_0/c = 1.0$, $St = 0.6$ and $\alpha_{max} = 48°$

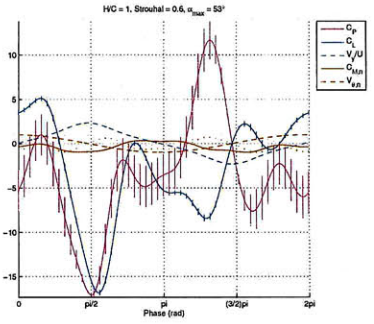

Figure D-54: Force Data for $h_0/c = 1.0$, $St = 0.6$ and $\alpha_{max} = 53°$

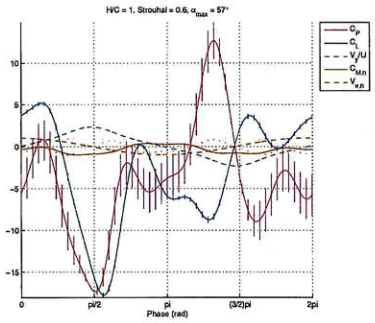

Figure D-55: Force Data for $h_0/c = 1.0$, $St = 0.6$ and $\alpha_{max} = 57°$

Appendix E

Force Data: $h_0/c = 1.23$

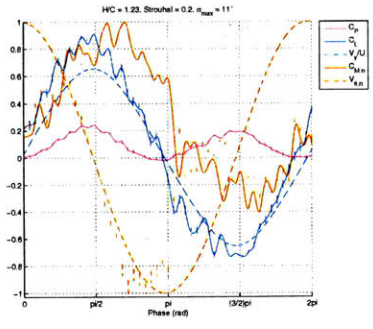

Figure E-1: Force Data for $h_0/c = 1.23$, $St = 0.2$ and $\alpha_{max} = 11°$

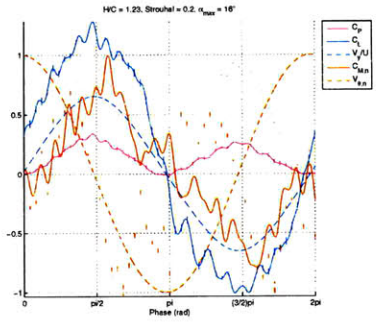

Figure E-2: Force Data for $h_0/c = 1.23$, $St = 0.2$ and $\alpha_{max} = 16°$

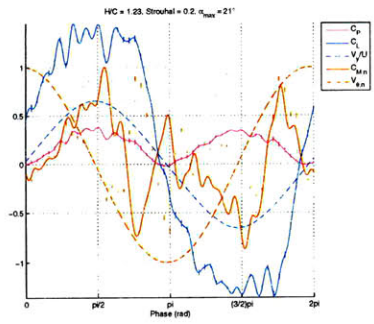

Figure E-3: Force Data for $h_0/c = 1.23$, $St = 0.2$ and $\alpha_{max} = 21°$

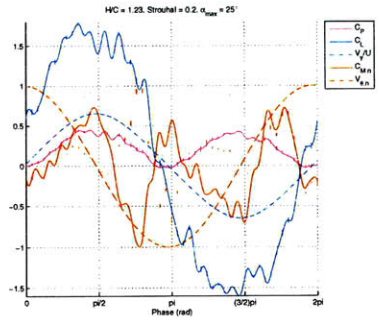

Figure E-4: Force Data for $h_0/c = 1.23$, $St = 0.2$ and $\alpha_{max} = 25°$

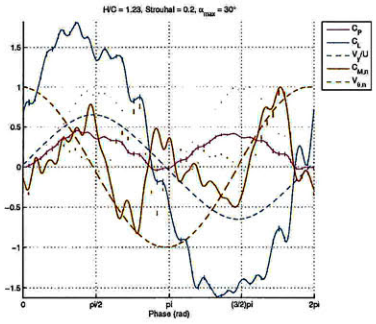

Figure E-5: Force Data for $h_0/c = 1.23$, $St = 0.2$ and $\alpha_{max} = 30°$

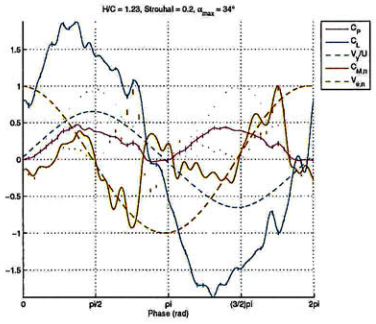

Figure E-6: Force Data for $h_0/c = 1.23$, $St = 0.2$ and $\alpha_{max} = 34°$

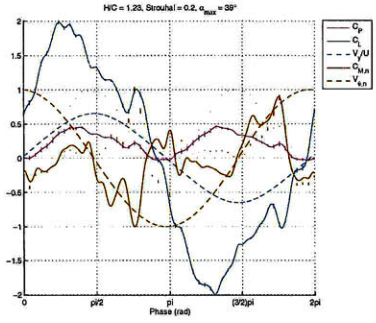

Figure E-7: Force Data for $h_0/c = 1.23$, $St = 0.2$ and $\alpha_{max} = 39°$

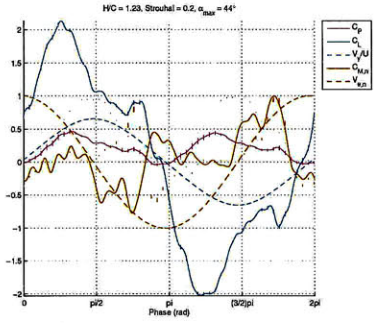

Figure E-8: Force Data for $h_0/c = 1.23$, $St = 0.2$ and $\alpha_{max} = 44°$

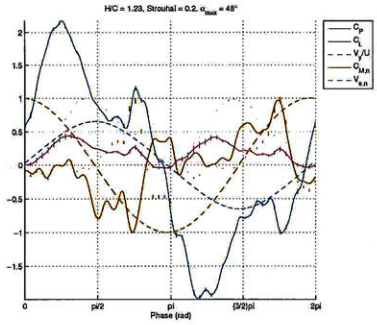

Figure E-9: Force Data for $h_0/c = 1.23$, $St = 0.2$ and $\alpha_{max} = 48°$

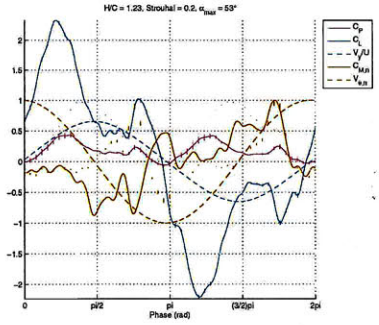

Figure E-10: Force Data for $h_0/c = 1.23$, $St = 0.2$ and $\alpha_{max} = 53°$

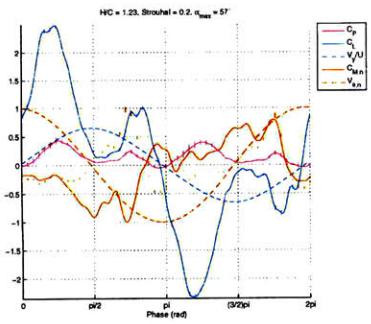

Figure E-11: Force Data for $h_0/c = 1.23$, $St = 0.2$ and $\alpha_{max} = 57°$

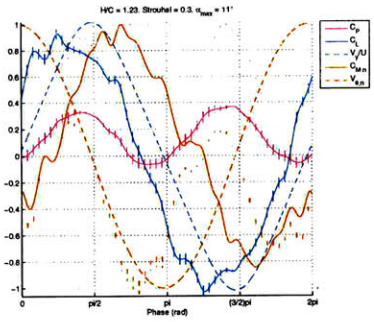

Figure E-12: Force Data for $h_0/c = 1.23$, $St = 0.3$ and $\alpha_{max} = 11°$

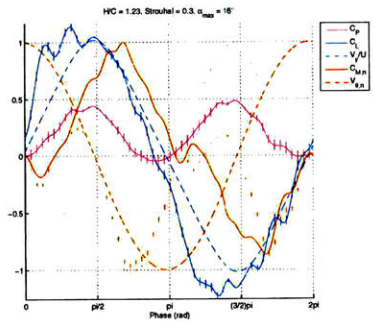

Figure E-13: Force Data for $h_0/c = 1.23$, $St = 0.3$ and $\alpha_{max} = 16°$

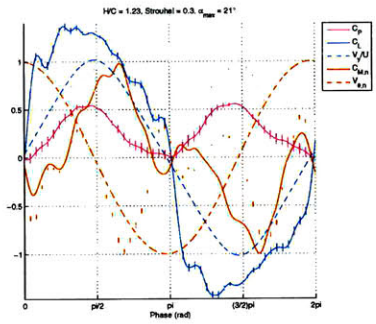

Figure E-14: Force Data for $h_0/c = 1.23$, $St = 0.3$ and $\alpha_{max} = 21°$

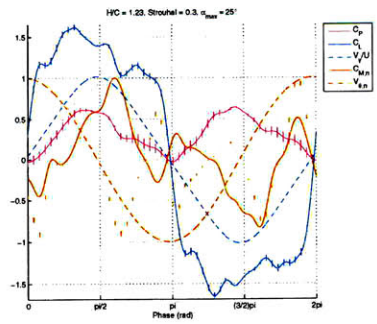

Figure E-15: Force Data for $h_0/c = 1.23$, $St = 0.3$ and $\alpha_{max} = 25°$

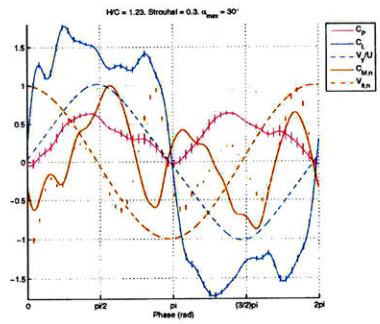

Figure E-16: Force Data for $h_0/c = 1.23$, $St = 0.3$ and $\alpha_{max} = 30°$

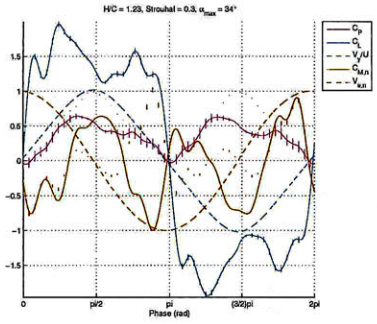

Figure E-17: Force Data for $h_0/c = 1.23$, $St = 0.3$ and $\alpha_{max} = 34°$

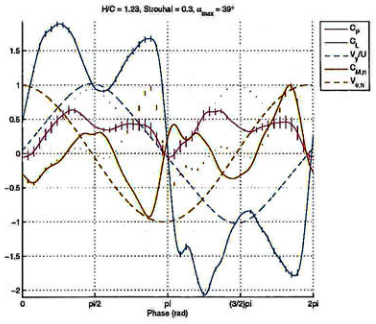

Figure E-18: Force Data for $h_0/c = 1.23$, $St = 0.3$ and $\alpha_{max} = 39°$

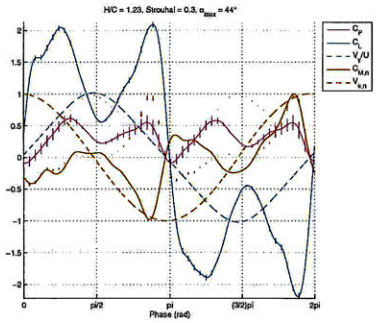

Figure E-19: Force Data for $h_0/c = 1.23$, $St = 0.3$ and $\alpha_{max} = 44°$

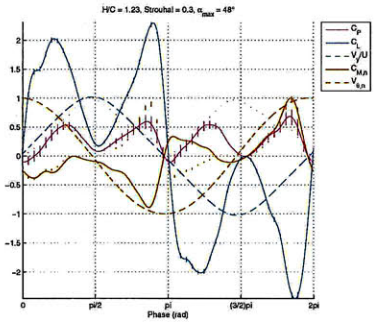

Figure E-20: Force Data for $h_0/c = 1.23$, $St = 0.3$ and $\alpha_{max} = 48°$

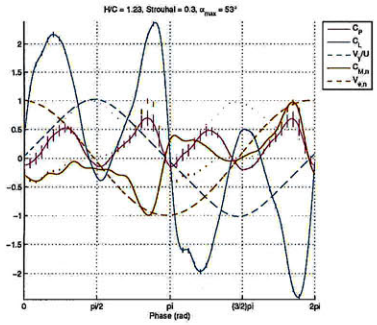

Figure E-21: Force Data for $h_0/c = 1.23$, $St = 0.3$ and $\alpha_{max} = 53°$

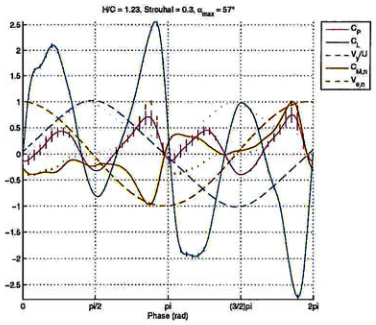

Figure E-22: Force Data for $h_0/c = 1.23$, $St = 0.3$ and $\alpha_{max} = 57°$

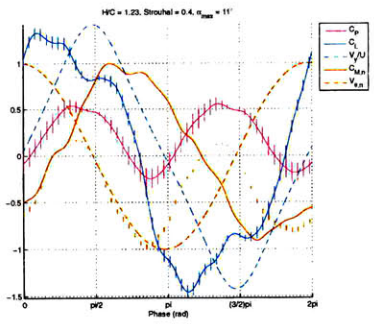

Figure E-23: Force Data for $h_0/c = 1.23$, $St = 0.4$ and $\alpha_{max} = 11°$

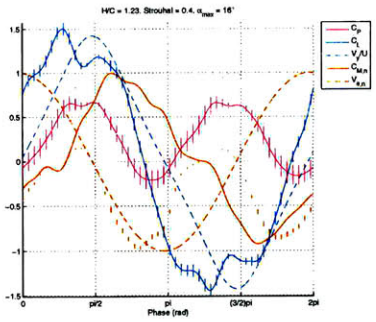

Figure E-24: Force Data for $h_0/c = 1.23$, $St = 0.4$ and $\alpha_{max} = 16°$

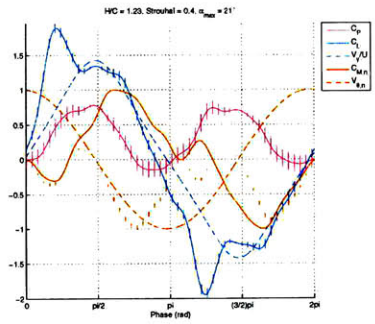

Figure E-25: Force Data for $h_0/c = 1.23$, $St = 0.4$ and $\alpha_{max} = 21°$

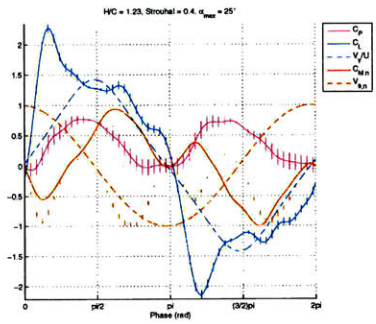

Figure E-26: Force Data for $h_0/c = 1.23$, $St = 0.4$ and $\alpha_{max} = 25°$

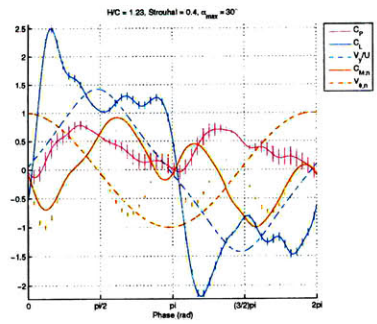

Figure E-27: Force Data for $h_0/c = 1.23$, $St = 0.4$ and $\alpha_{max} = 30°$

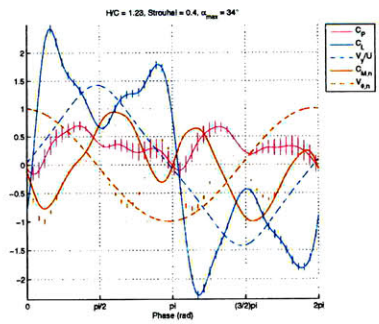

Figure E-28: Force Data for $h_0/c = 1.23$, $St = 0.4$ and $\alpha_{max} = 34°$

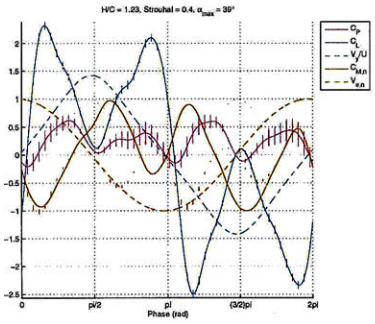

Figure E-29: Force Data for $h_0/c = 1.23$, $St = 0.4$ and $\alpha_{max} = 39°$

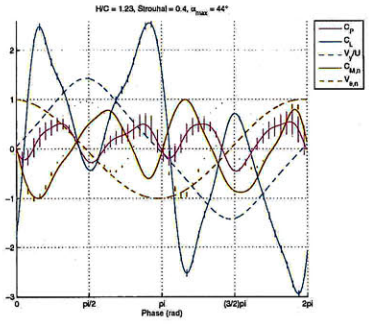

Figure E-30: Force Data for $h_0/c = 1.23$, $St = 0.4$ and $\alpha_{max} = 44°$

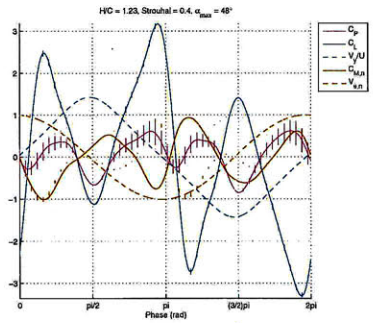

Figure E-31: Force Data for $h_0/c = 1.23$, $St = 0.4$ and $\alpha_{max} = 48°$

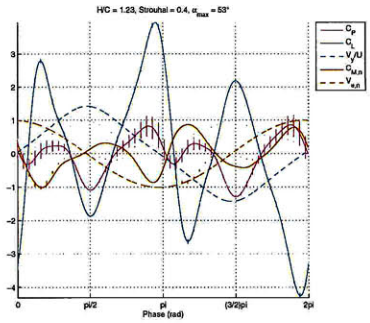

Figure E-32: Force Data for $h_0/c = 1.23$, $St = 0.4$ and $\alpha_{max} = 53°$

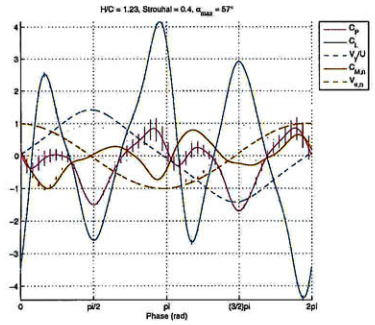

Figure E-33: Force Data for $h_0/c = 1.23$, $St = 0.4$ and $\alpha_{max} = 57°$

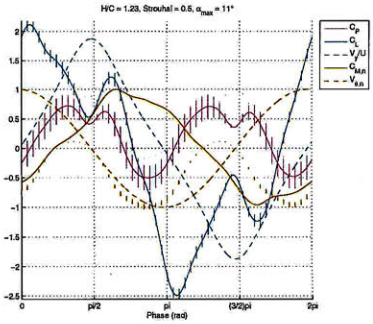

Figure E-34: Force Data for $h_0/c = 1.23$, $St = 0.5$ and $\alpha_{max} = 11°$

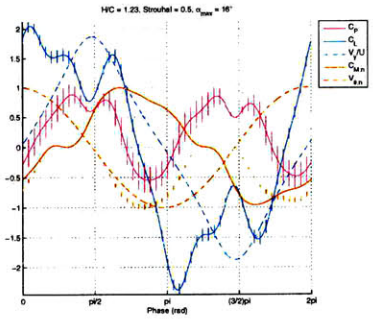

Figure E-35: Force Data for $h_0/c = 1.23$, $St = 0.5$ and $\alpha_{max} = 16°$

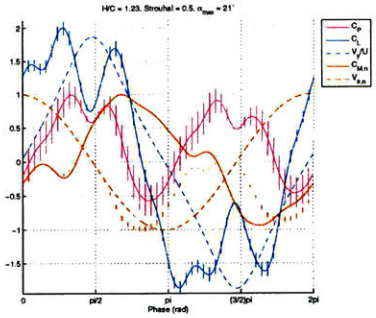

Figure E-36: Force Data for $h_0/c = 1.23$, $St = 0.5$ and $\alpha_{max} = 21°$

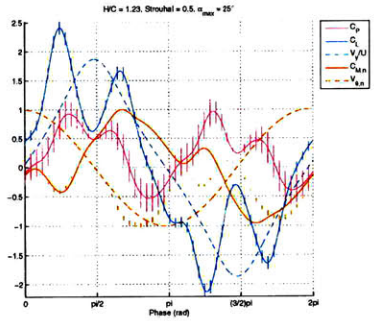

Figure E-37: Force Data for $h_0/c = 1.23$, $St = 0.5$ and $\alpha_{max} = 25°$

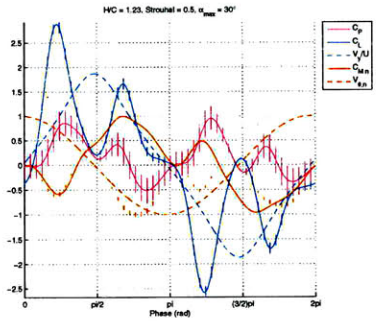

Figure E-38: Force Data for $h_0/c = 1.23$, $St = 0.5$ and $\alpha_{max} = 30°$

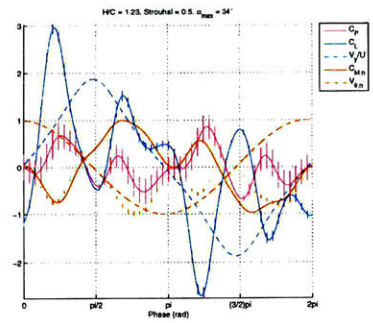

Figure E-39: Force Data for $h_0/c = 1.23$, $St = 0.5$ and $\alpha_{max} = 34°$

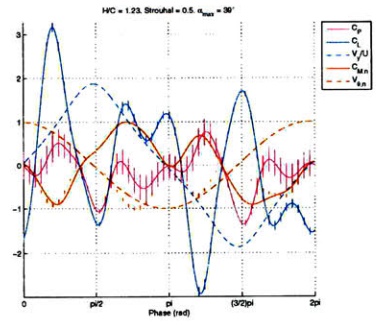

Figure E-40: Force Data for $h_0/c = 1.23$, $St = 0.5$ and $\alpha_{max} = 39°$

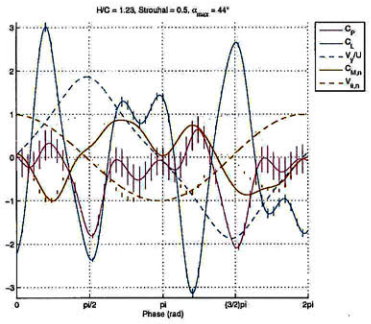

Figure E-41: Force Data for $h_0/c = 1.23$, $St = 0.5$ and $\alpha_{max} = 44°$

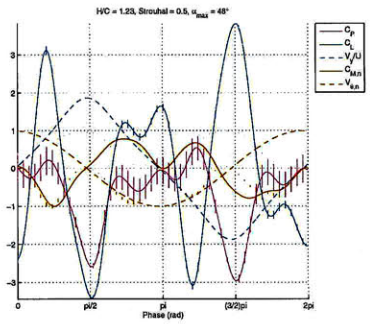

Figure E-42: Force Data for $h_0/c = 1.23$, $St = 0.5$ and $\alpha_{max} = 48°$

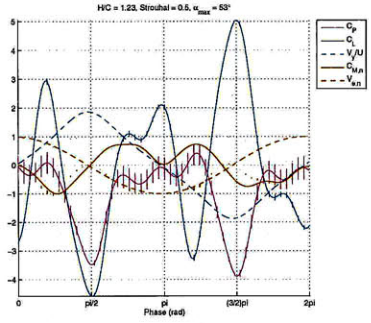

Figure E-43: Force Data for $h_0/c = 1.23$, $St = 0.5$ and $\alpha_{max} = 53°$

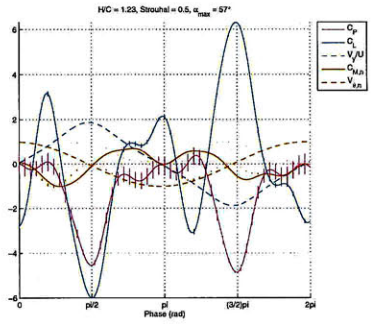

Figure E-44: Force Data for $h_0/c = 1.23$, $St = 0.5$ and $\alpha_{max} = 57°$

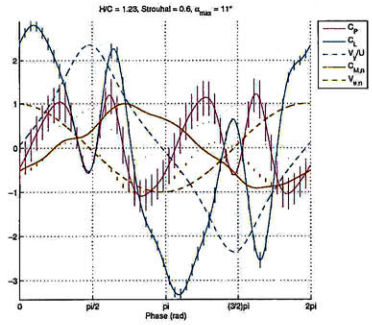

Figure E-45: Force Data for $h_0/c = 1.23$, $St = 0.6$ and $\alpha_{max} = 11°$

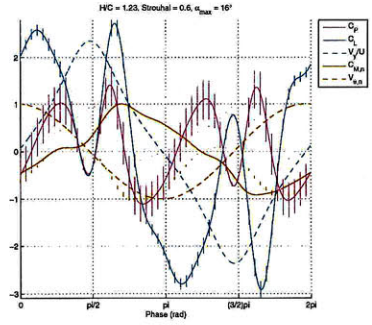

Figure E-46: Force Data for $h_0/c = 1.23$, $St = 0.6$ and $\alpha_{max} = 16°$

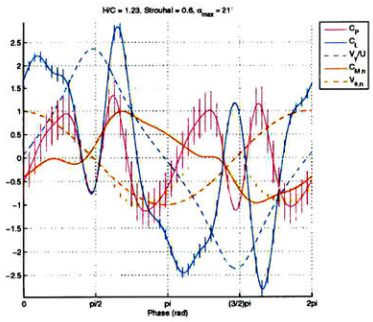

Figure E-47: Force Data for $h_0/c = 1.23$, $St = 0.6$ and $\alpha_{max} = 21°$

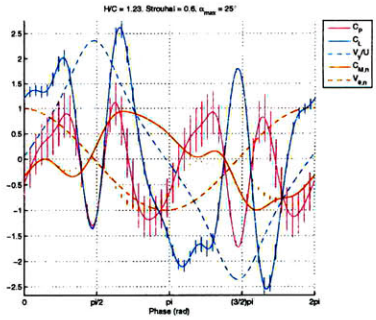

Figure E-48: Force Data for $h_0/c = 1.23$, $St = 0.6$ and $\alpha_{max} = 25°$

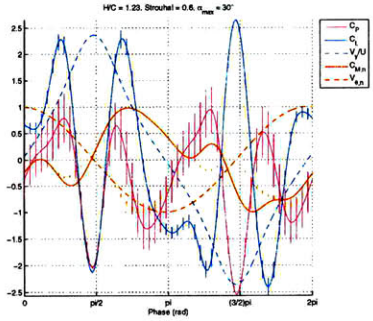

Figure E-49: Force Data for $h_0/c = 1.23$, $St = 0.6$ and $\alpha_{max} = 30°$

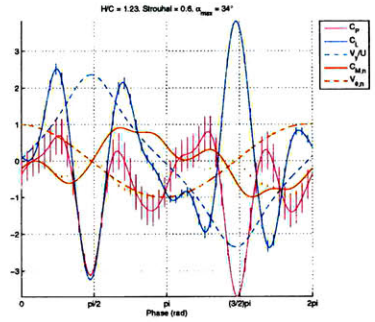

Figure E-50: Force Data for $h_0/c = 1.23$, $St = 0.6$ and $\alpha_{max} = 34°$

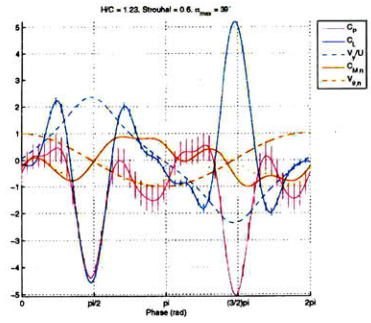

Figure E-51: Force Data for $h_0/c = 1.23$, $St = 0.6$ and $\alpha_{max} = 39°$

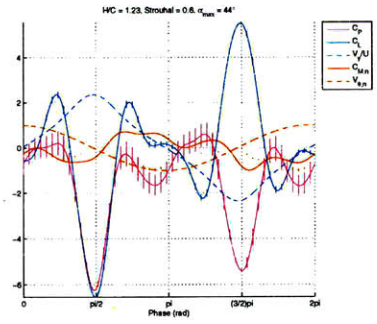

Figure E-52: Force Data for $h_0/c = 1.23$, $St = 0.6$ and $\alpha_{max} = 44°$

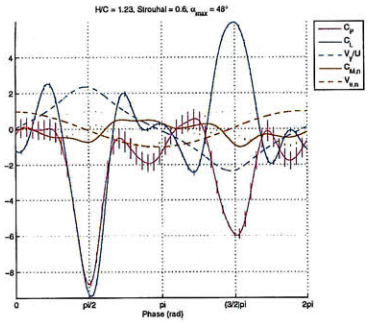

Figure E-53: Force Data for $h_0/c = 1.23$, $St = 0.6$ and $\alpha_{max} = 48°$

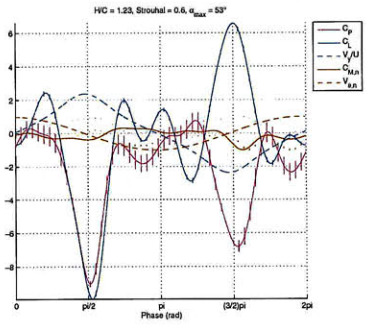

Figure E-54: Force Data for $h_0/c = 1.23$, $St = 0.6$ and $\alpha_{max} = 53°$

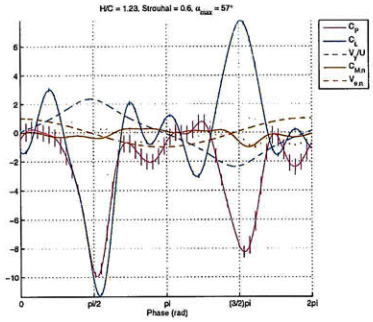

Figure E-55: Force Data for $h_0/c = 1.23$, $St = 0.6$ and $\alpha_{max} = 57°$

Appendix F

DPIV Data: $h_0/c = 0.75$

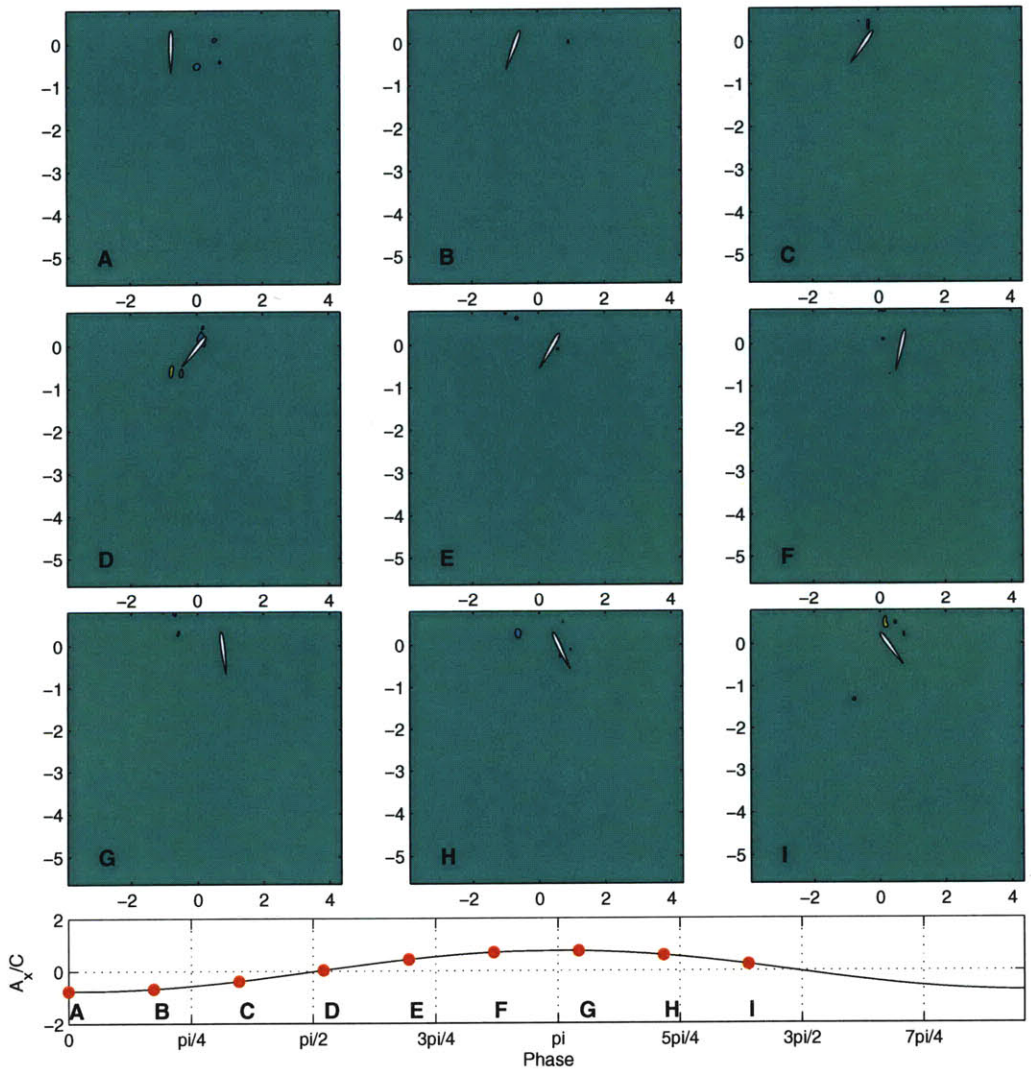

Figure F-1: Selected DPIV Images for $h_0/c = 0.75$, $St = 0.2$ and $\alpha_{max} = 11°$

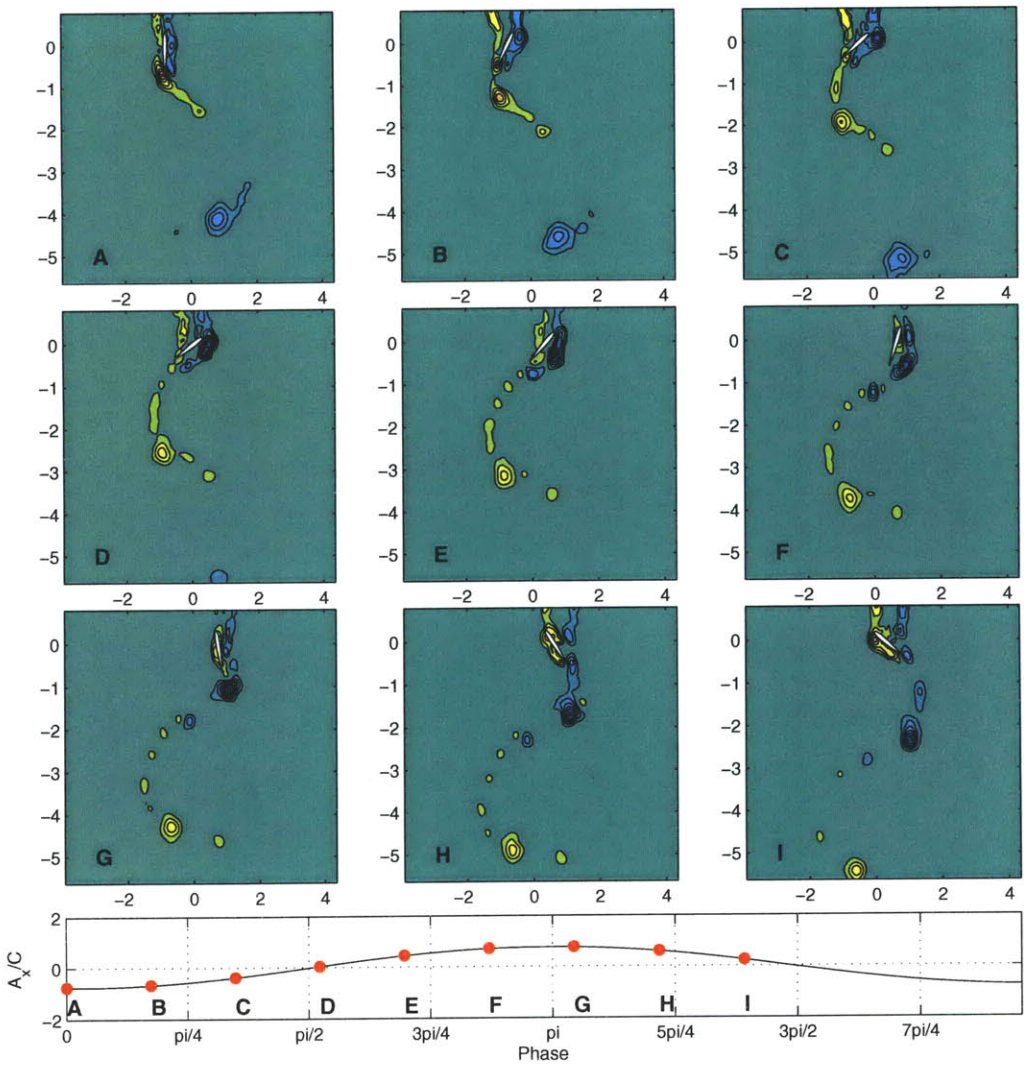

Figure F-2: Selected DPIV Images for $h_0/c = 0.75$, $St = 0.2$ and $\alpha_{max} = 25°$

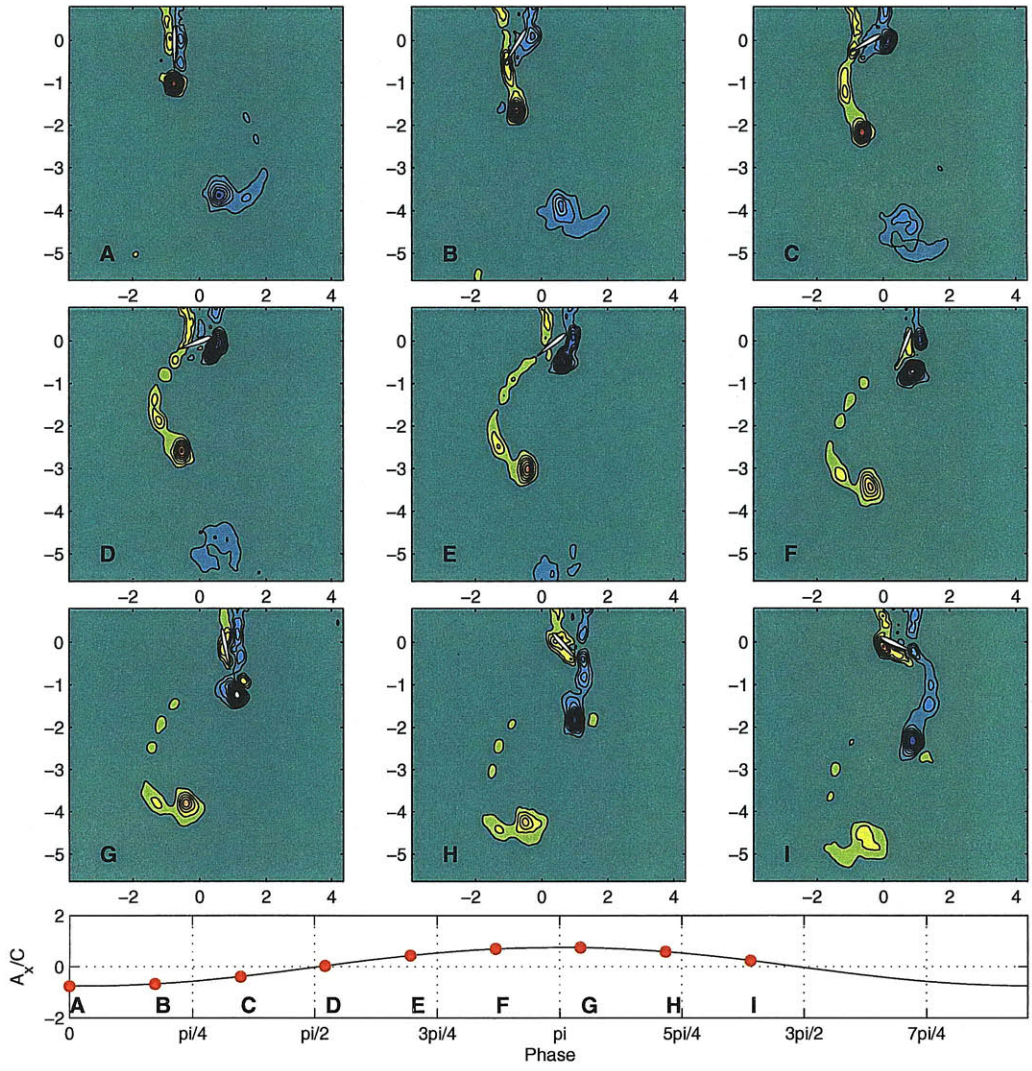

Figure F-3: Selected DPIV Images for $h_0/c = 0.75$, $St = 0.2$ and $\alpha_{max} = 39°$

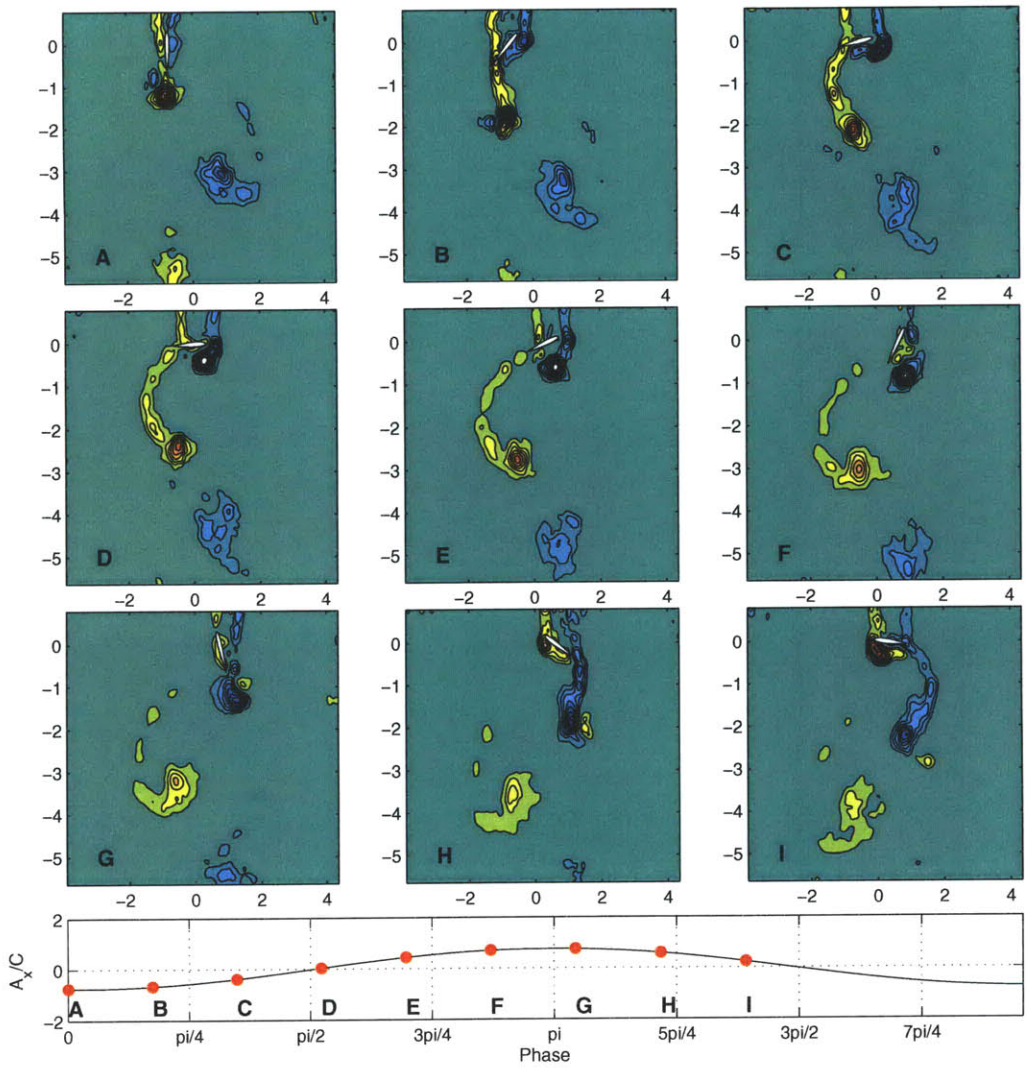

Figure F-4: Selected DPIV Images for $h_0/c = 0.75$, $St = 0.2$ and $\alpha_{max} = 53°$

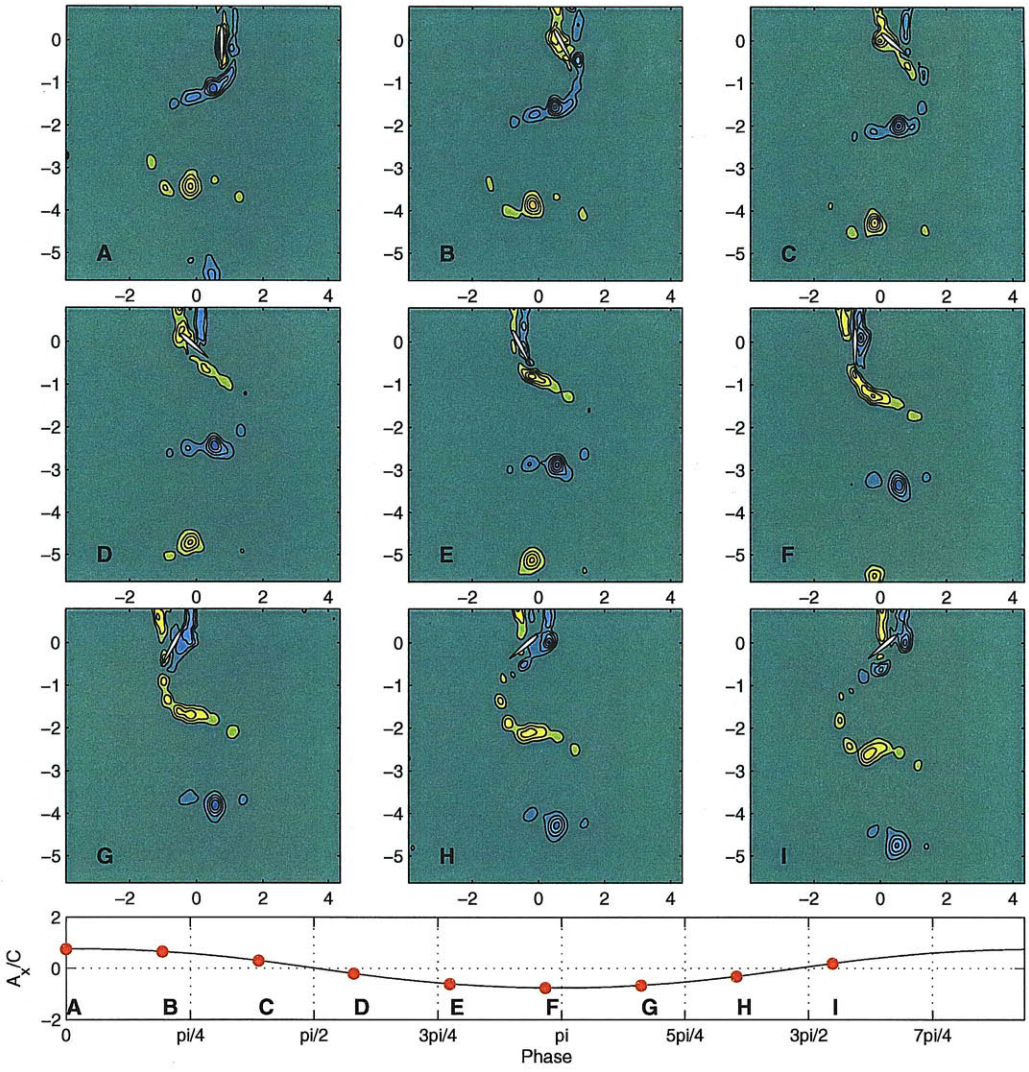

Figure F-5: Selected DPIV Images for $h_0/c = 0.75$, $St = 0.3$ and $\alpha_{max} = 11°$

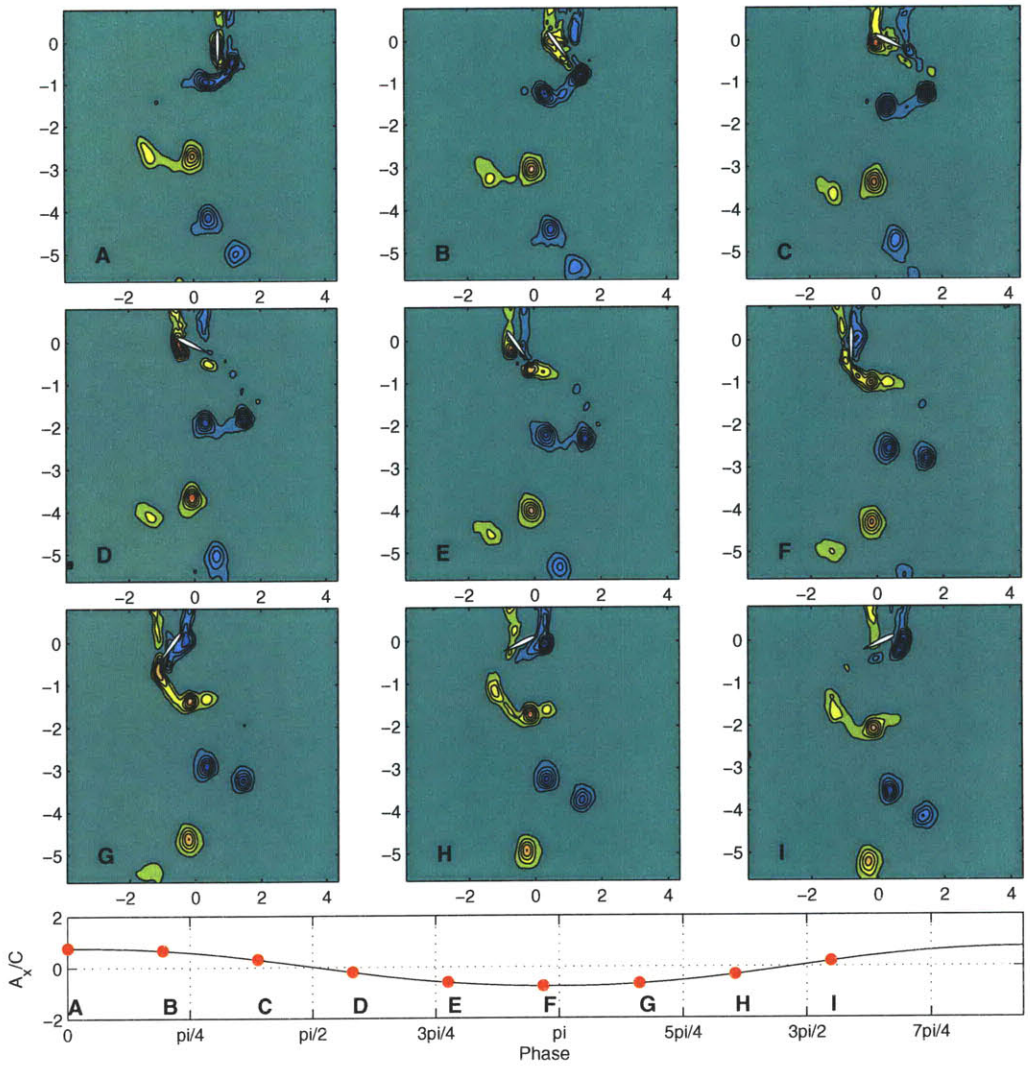

Figure F-6: Selected DPIV Images for $h_0/c = 0.75$, $St = 0.3$ and $\alpha_{max} = 25°$

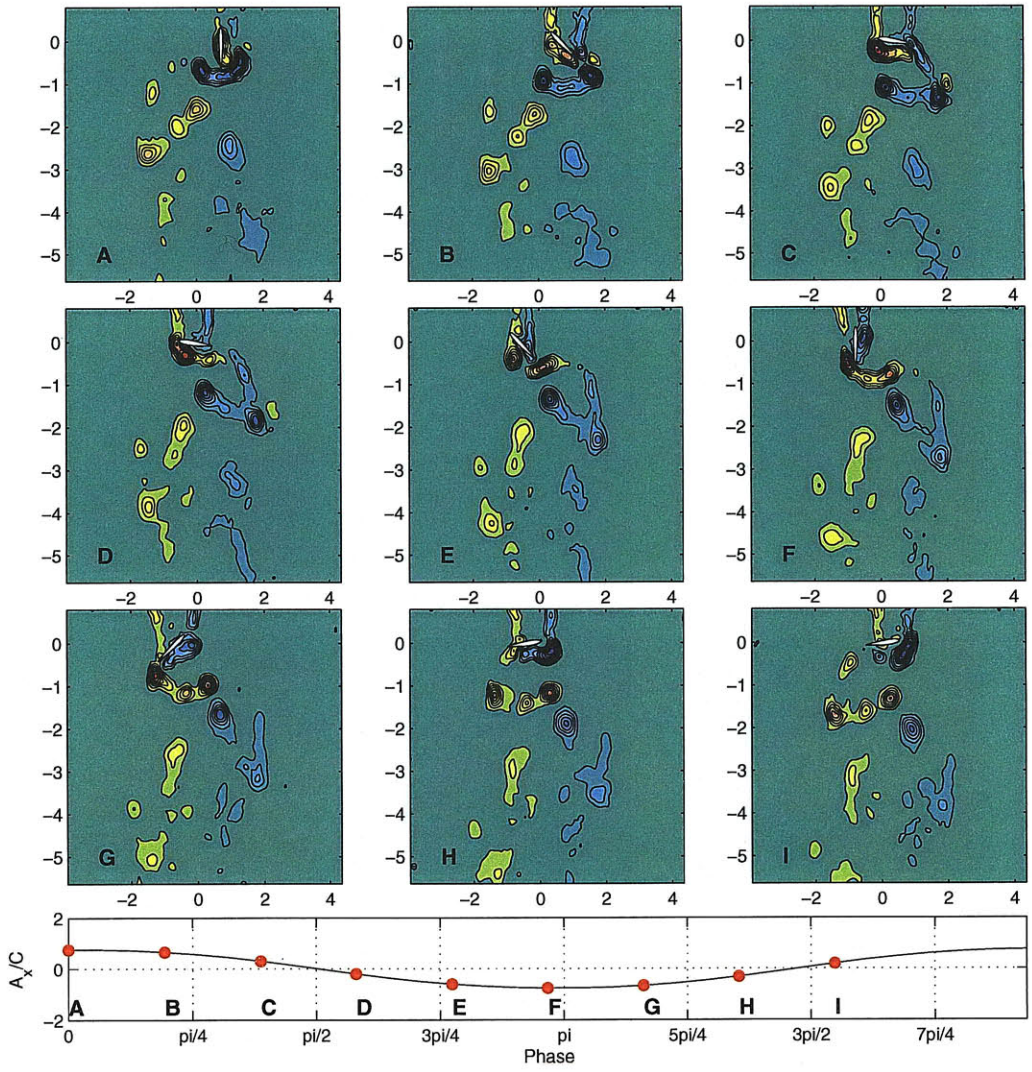

Figure F-7: Selected DPIV Images for $h_0/c = 0.75$, $St = 0.3$ and $\alpha_{max} = 39°$

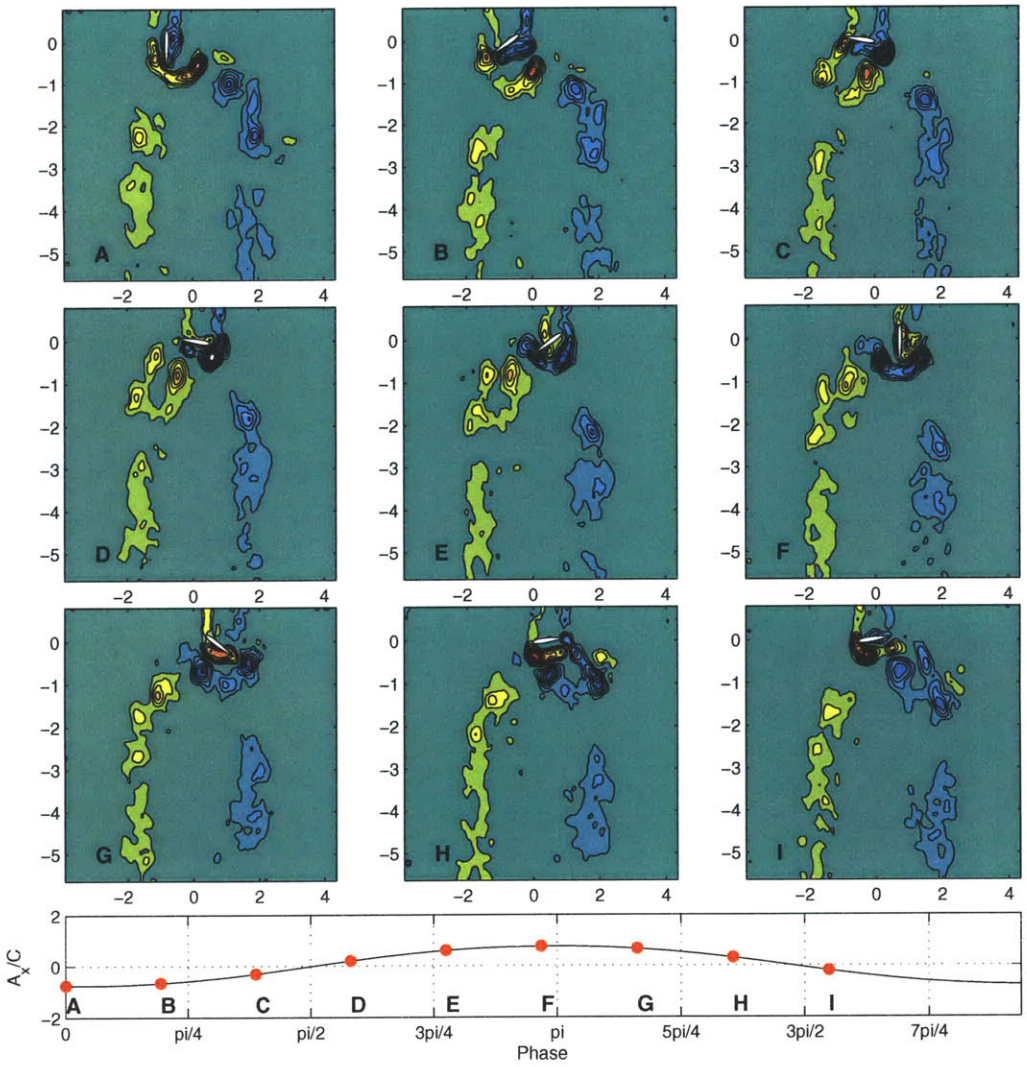

Figure F-8: Selected DPIV Images for $h_0/c = 0.75$, $St = 0.3$ and $\alpha_{max} = 53°$

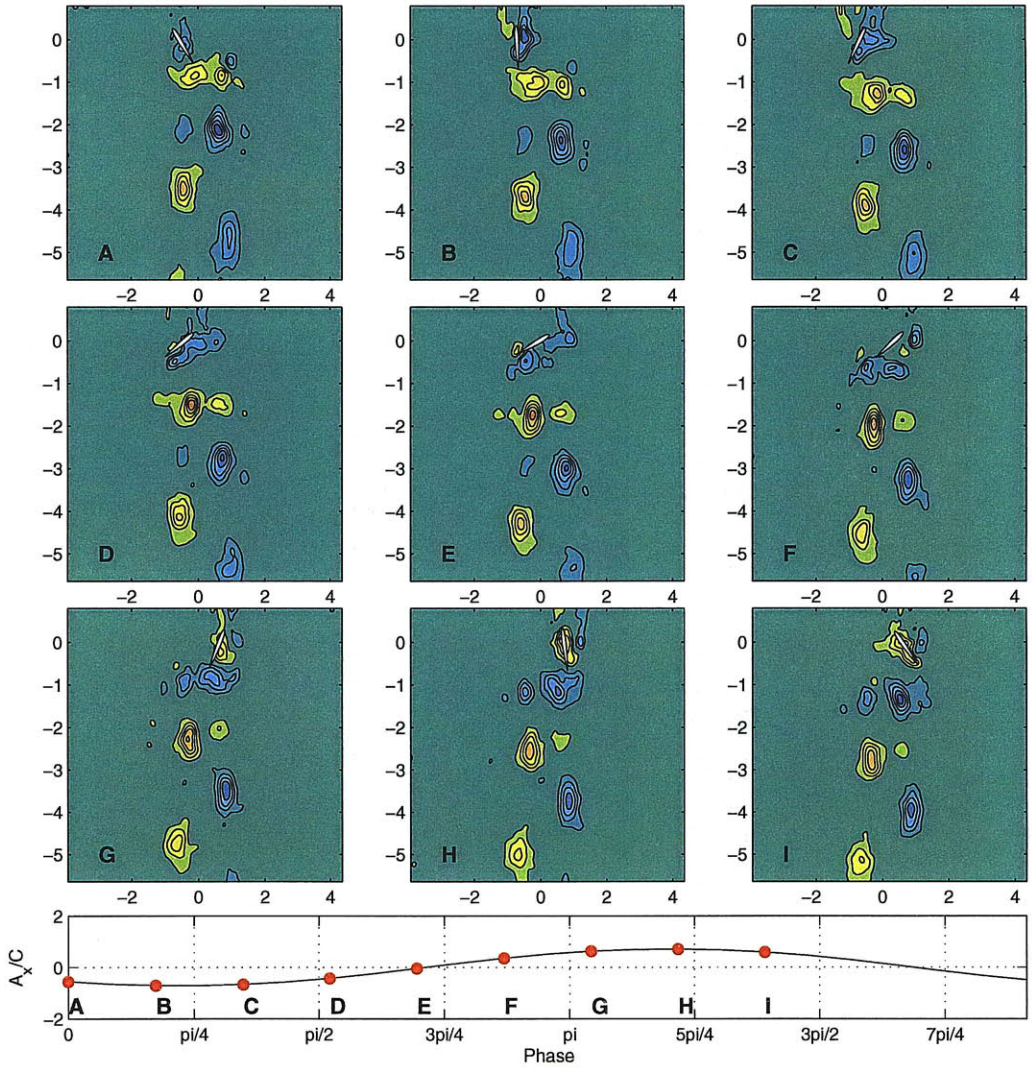

Figure F-9: Selected DPIV Images for $h_0/c = 0.75$, $St = 0.4$ and $\alpha_{max} = 11°$

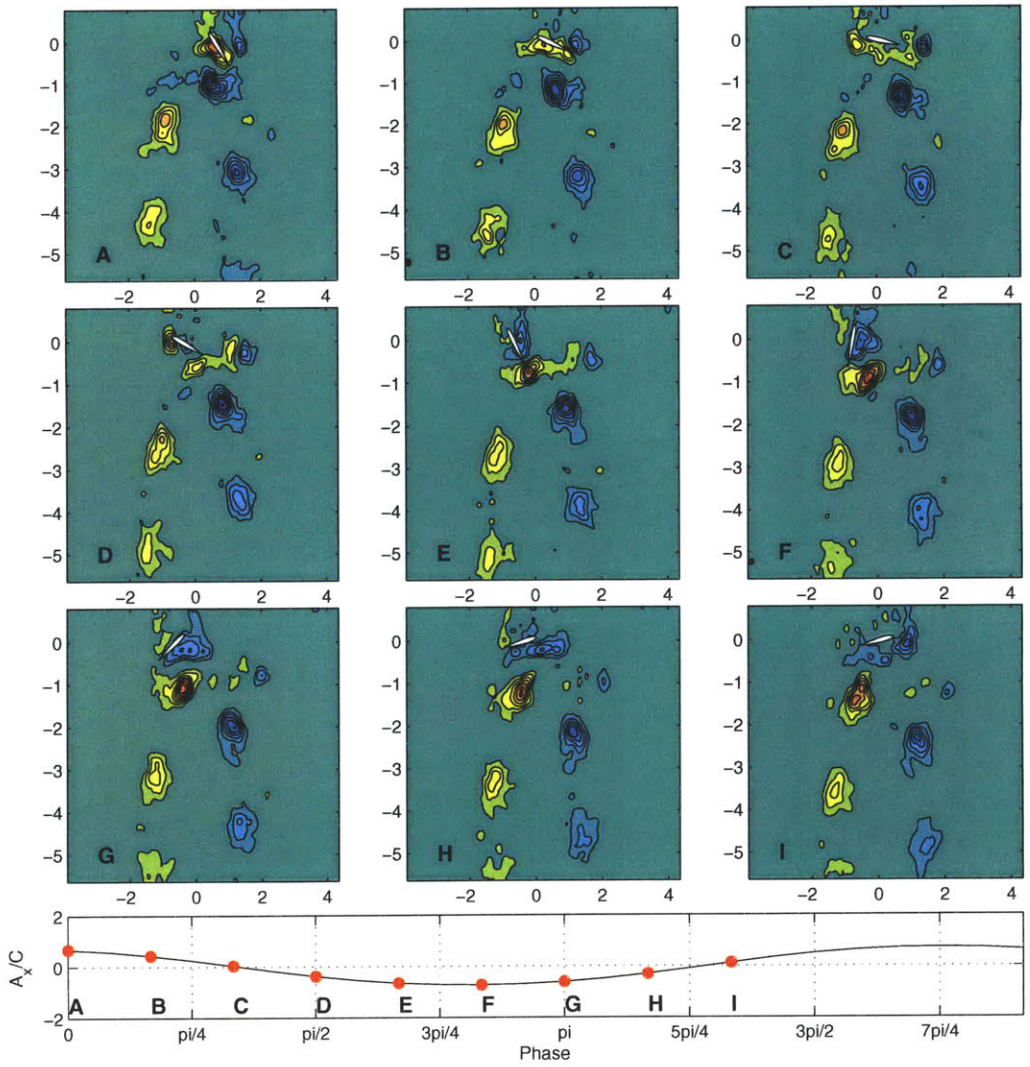

Figure F-10: Selected DPIV Images for $h_0/c = 0.75$, $St = 0.4$ and $\alpha_{max} = 25°$

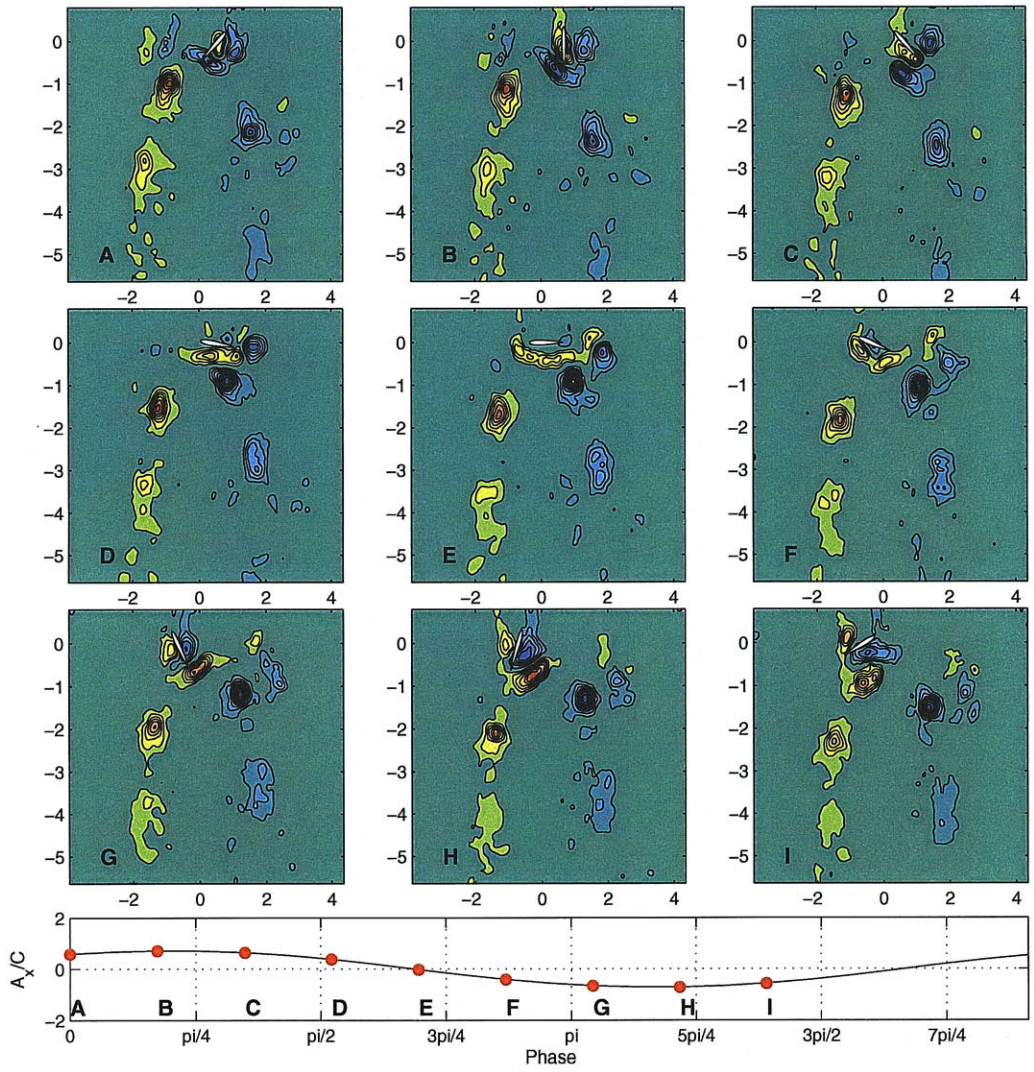

Figure F-11: Selected DPIV Images for $h_0/c = 0.75$, $St = 0.4$ and $\alpha_{max} = 39°$

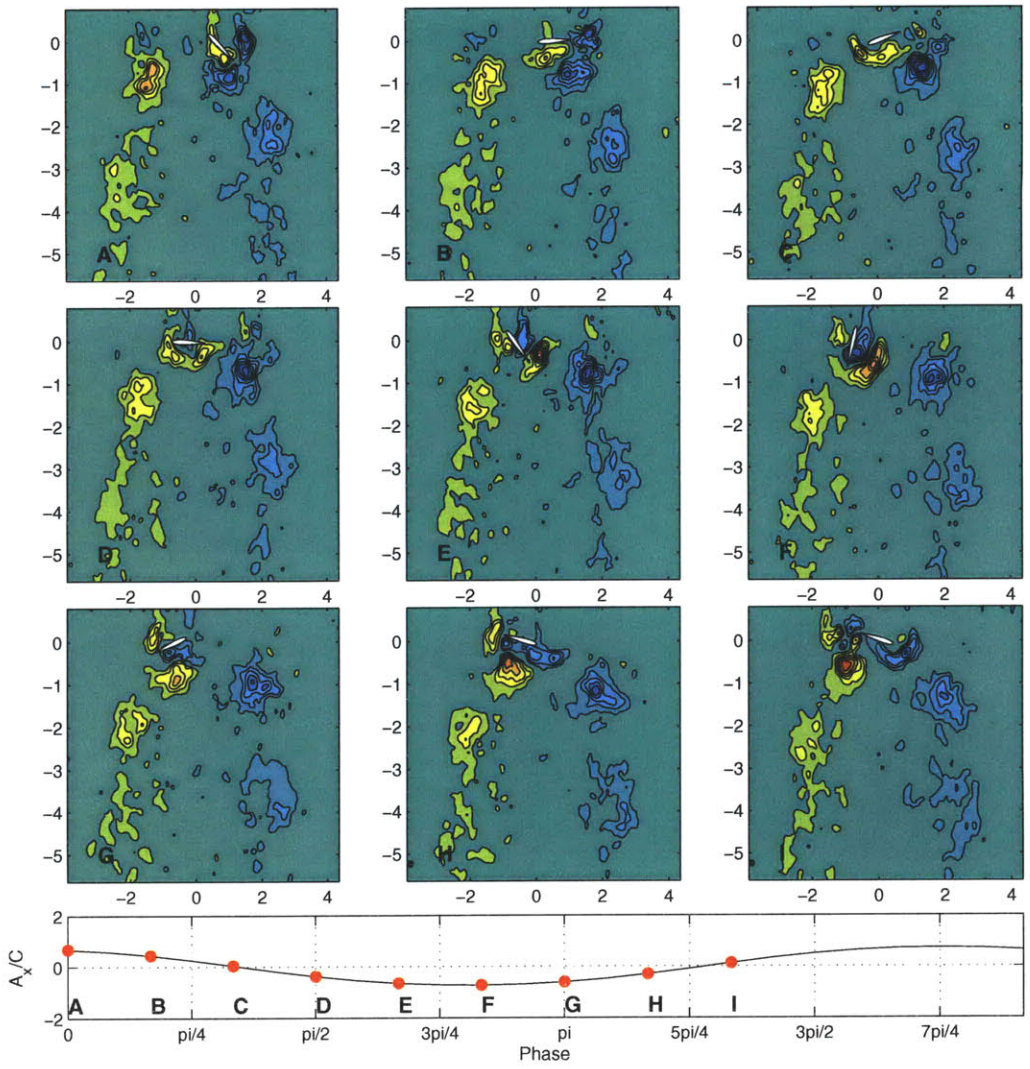

Figure F-12: Selected DPIV Images for $h_0/c = 0.75$, $St = 0.4$ and $\alpha_{max} = 53°$

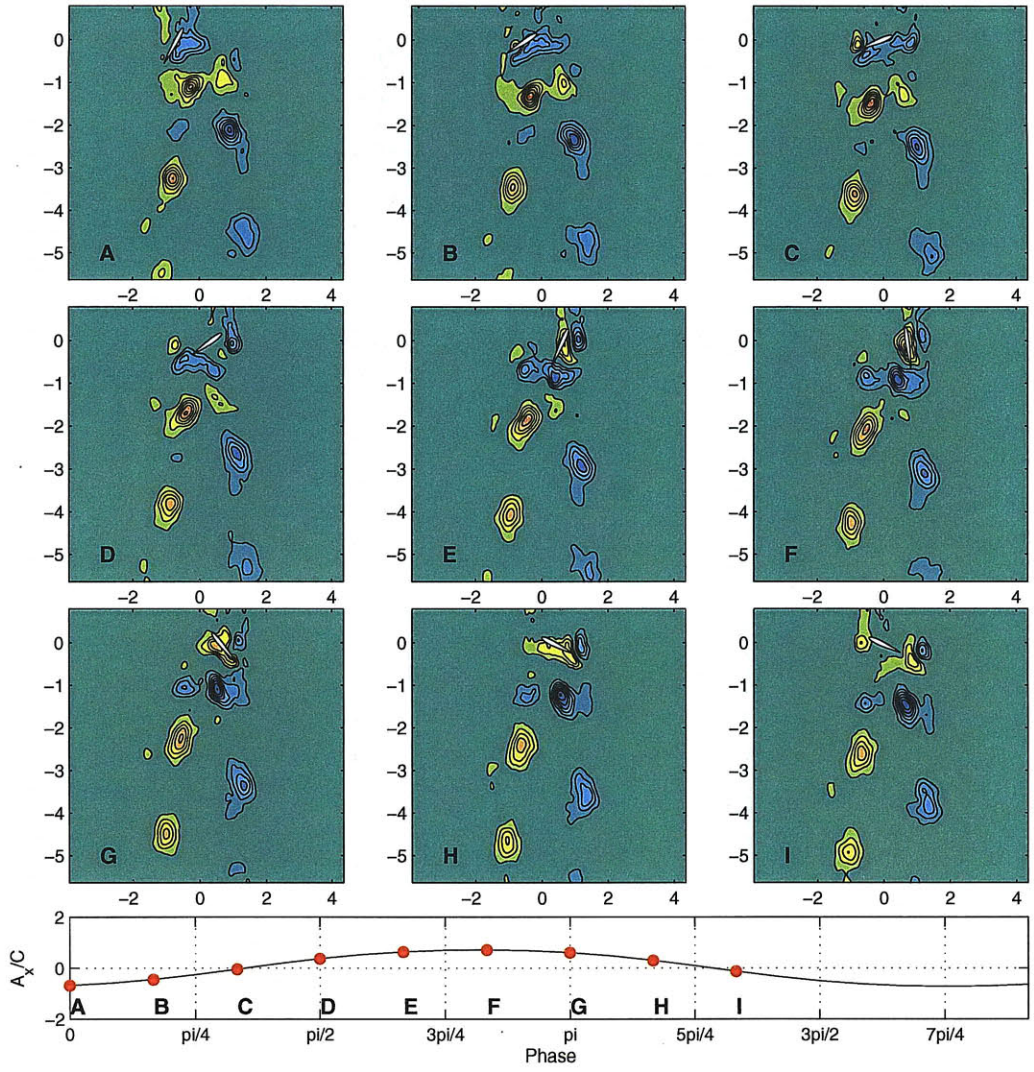

Figure F-13: Selected DPIV Images for $h_0/c = 0.75$, $St = 0.5$ and $\alpha_{max} = 11°$

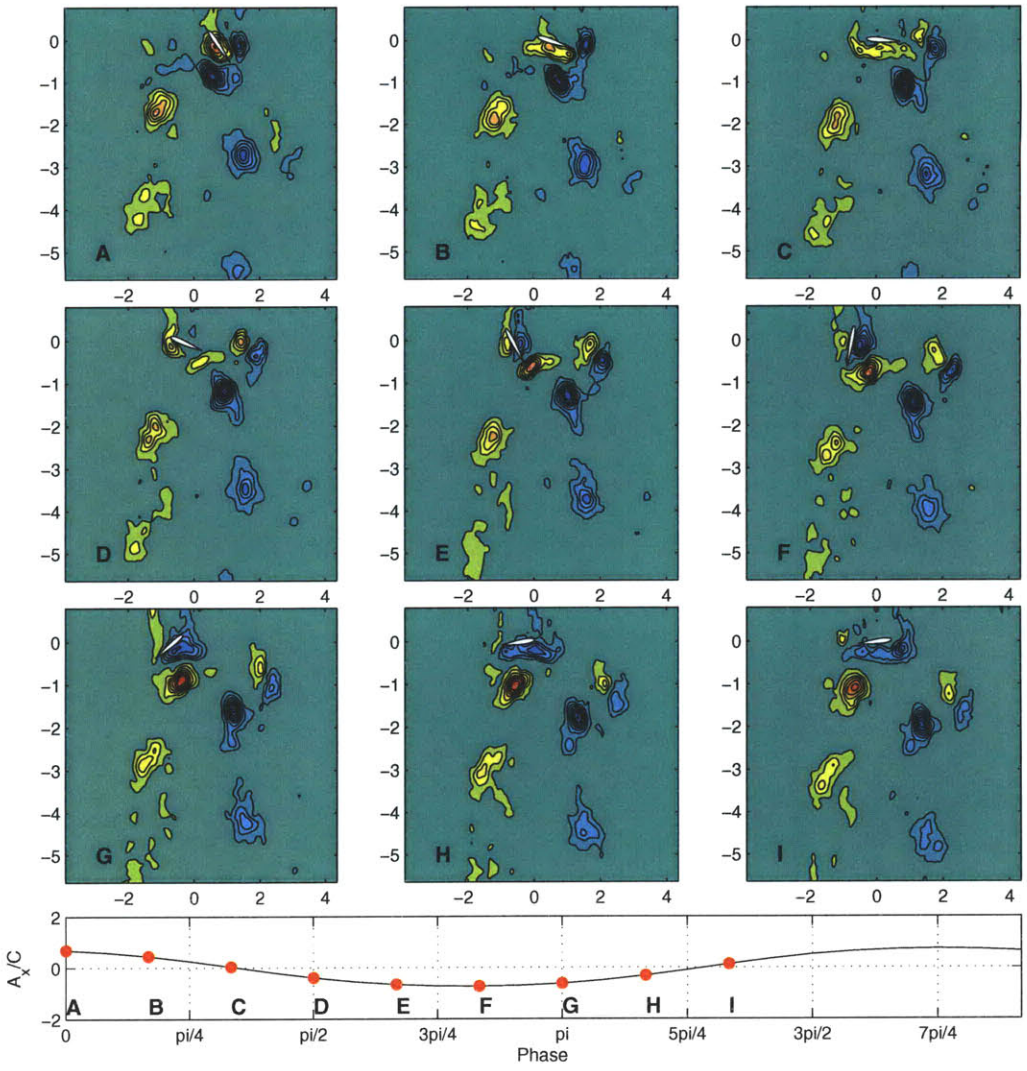

Figure F-14: Selected DPIV Images for $h_0/c = 0.75$, $St = 0.5$ and $\alpha_{max} = 25°$

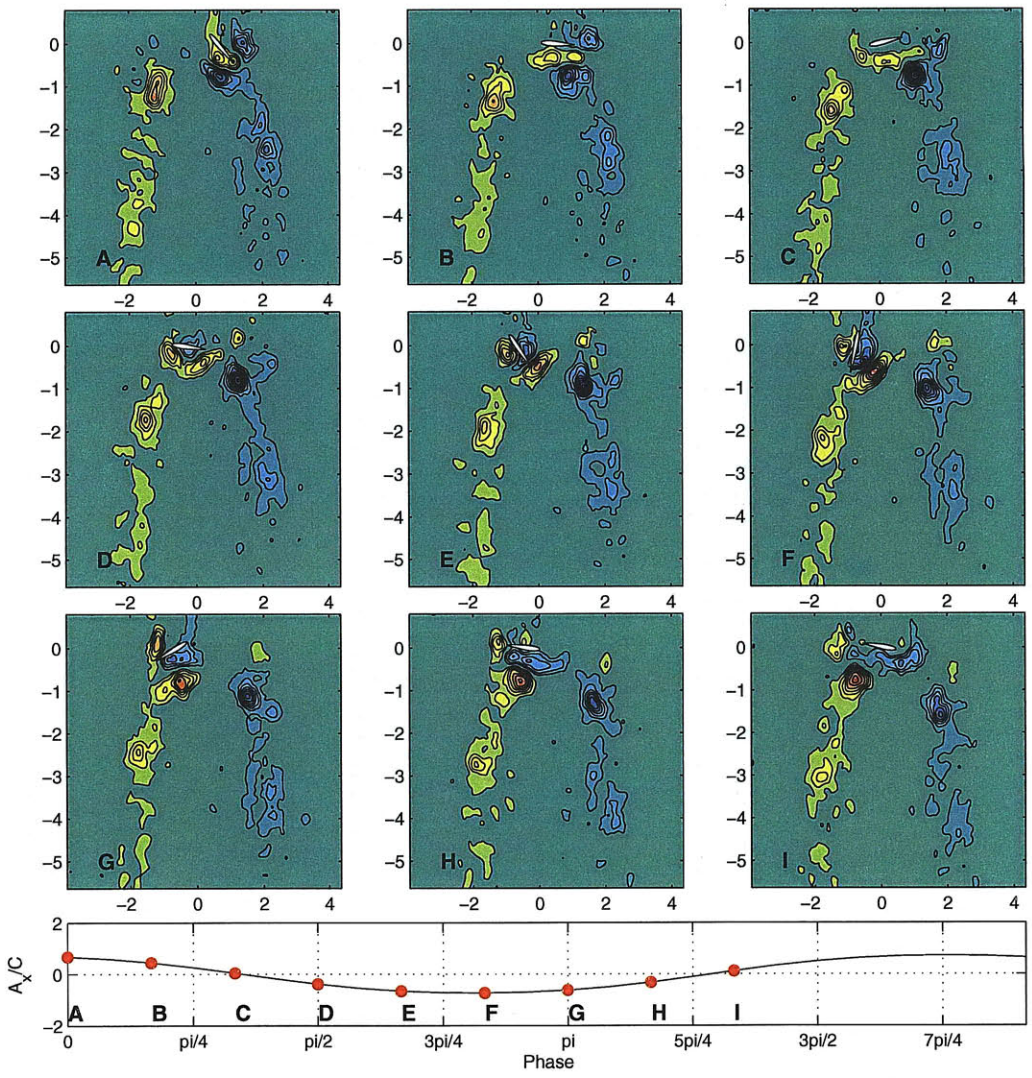

Figure F-15: Selected DPIV Images for $h_0/c = 0.75$, $St = 0.5$ and $\alpha_{max} = 39°$

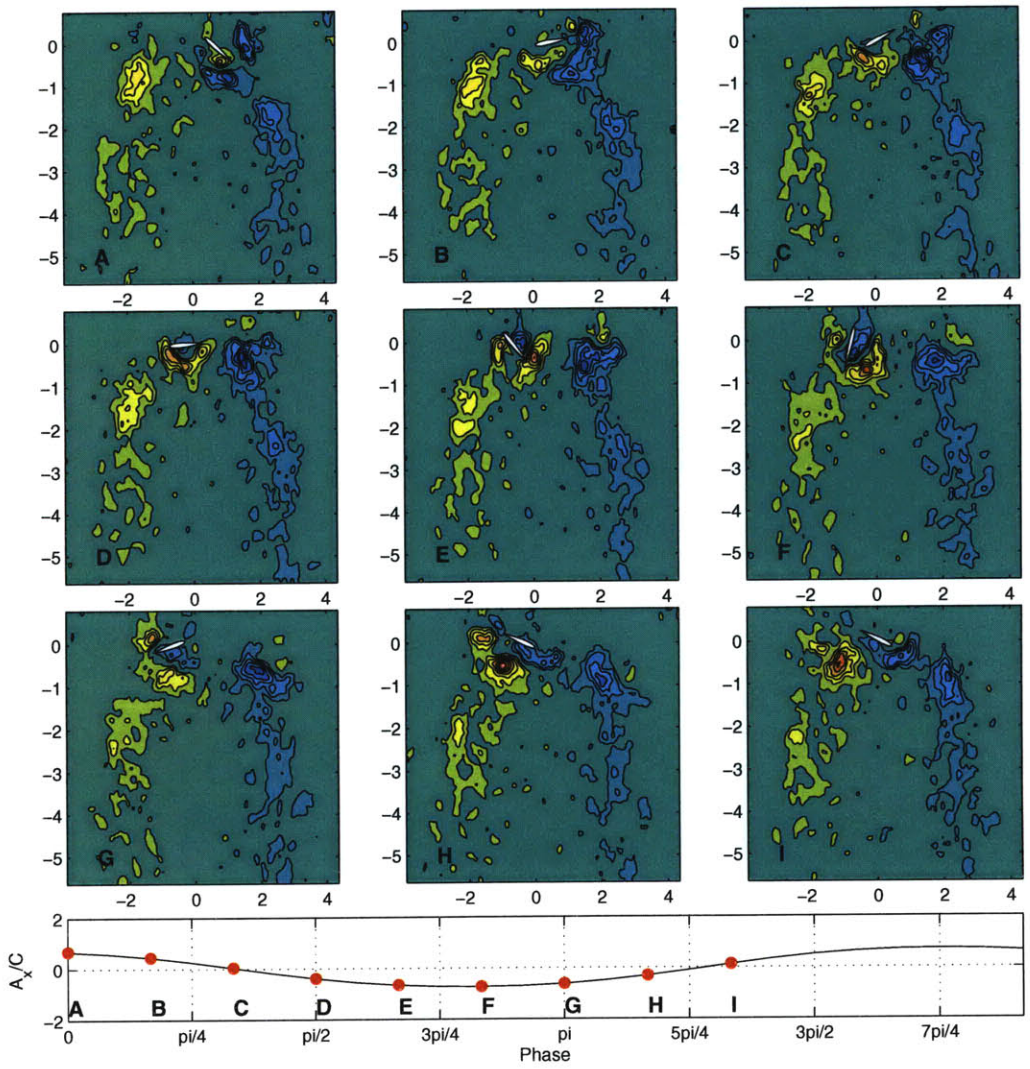

Figure F-16: Selected DPIV Images for $h_0/c = 0.75$, $St = 0.5$ and $\alpha_{max} = 53°$

Appendix G

DPIV Data: $h_0/c = 1.0$

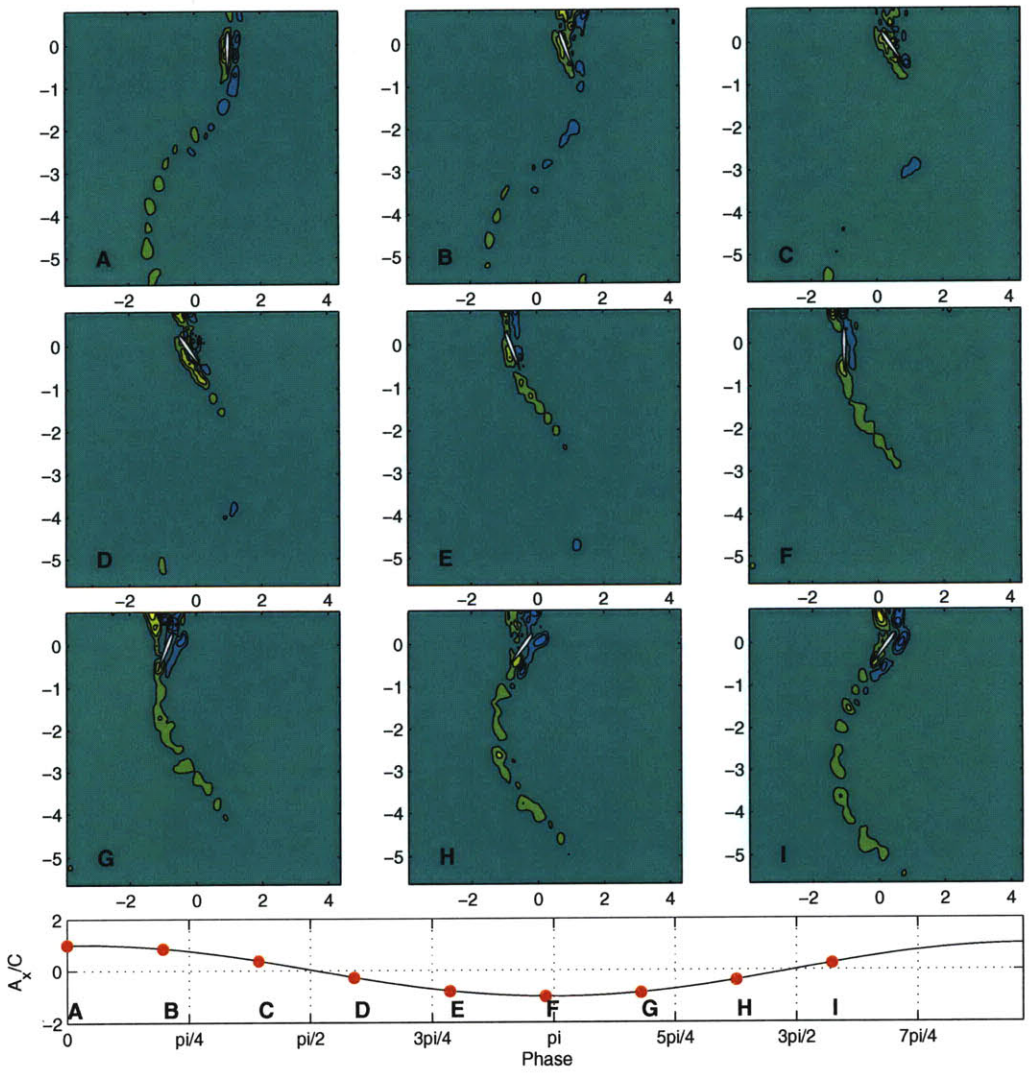

Figure G-1: Selected DPIV Images for $h_0/c = 1.0$, $St = 0.2$ and $\alpha_{max} = 11°$

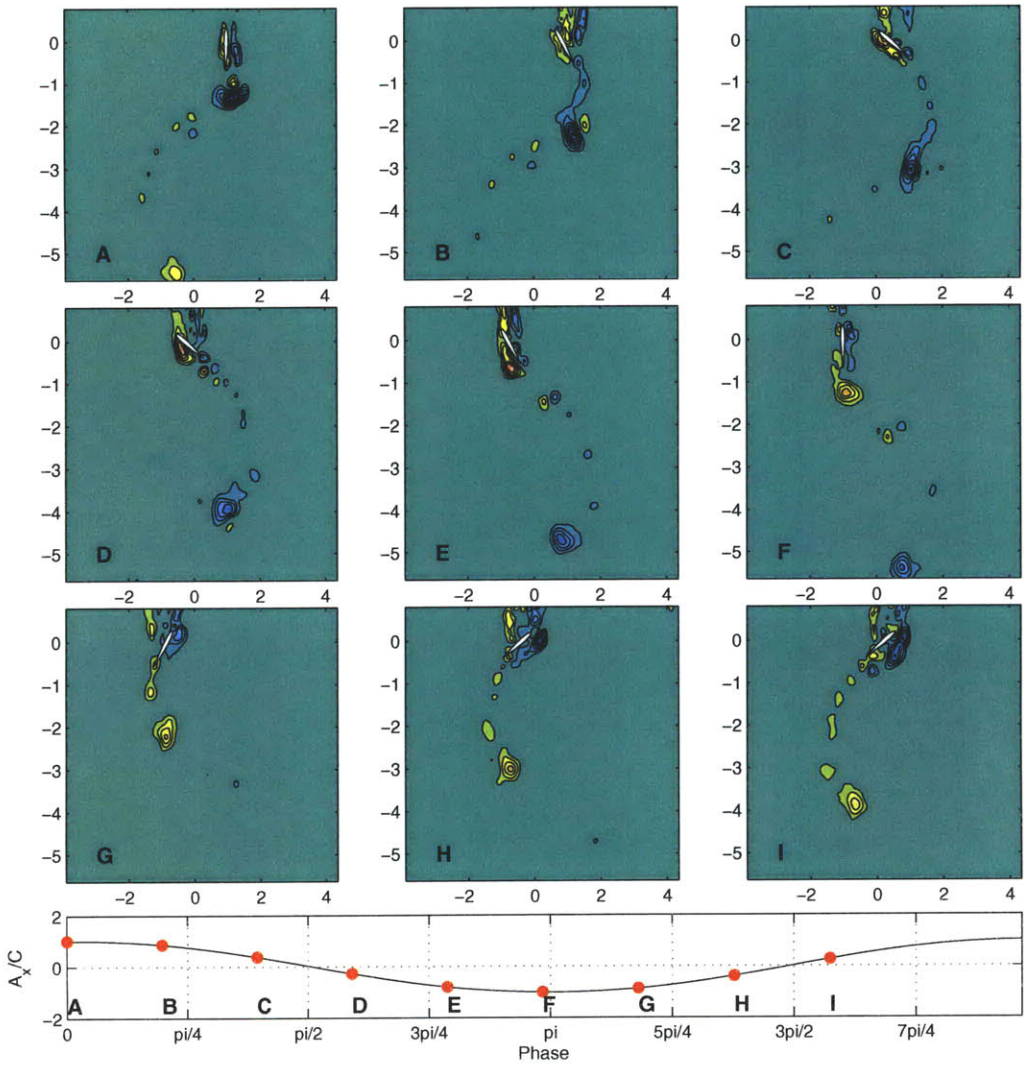

Figure G-2: Selected DPIV Images for $h_0/c = 1.0$, $St = 0.2$ and $\alpha_{max} = 25°$

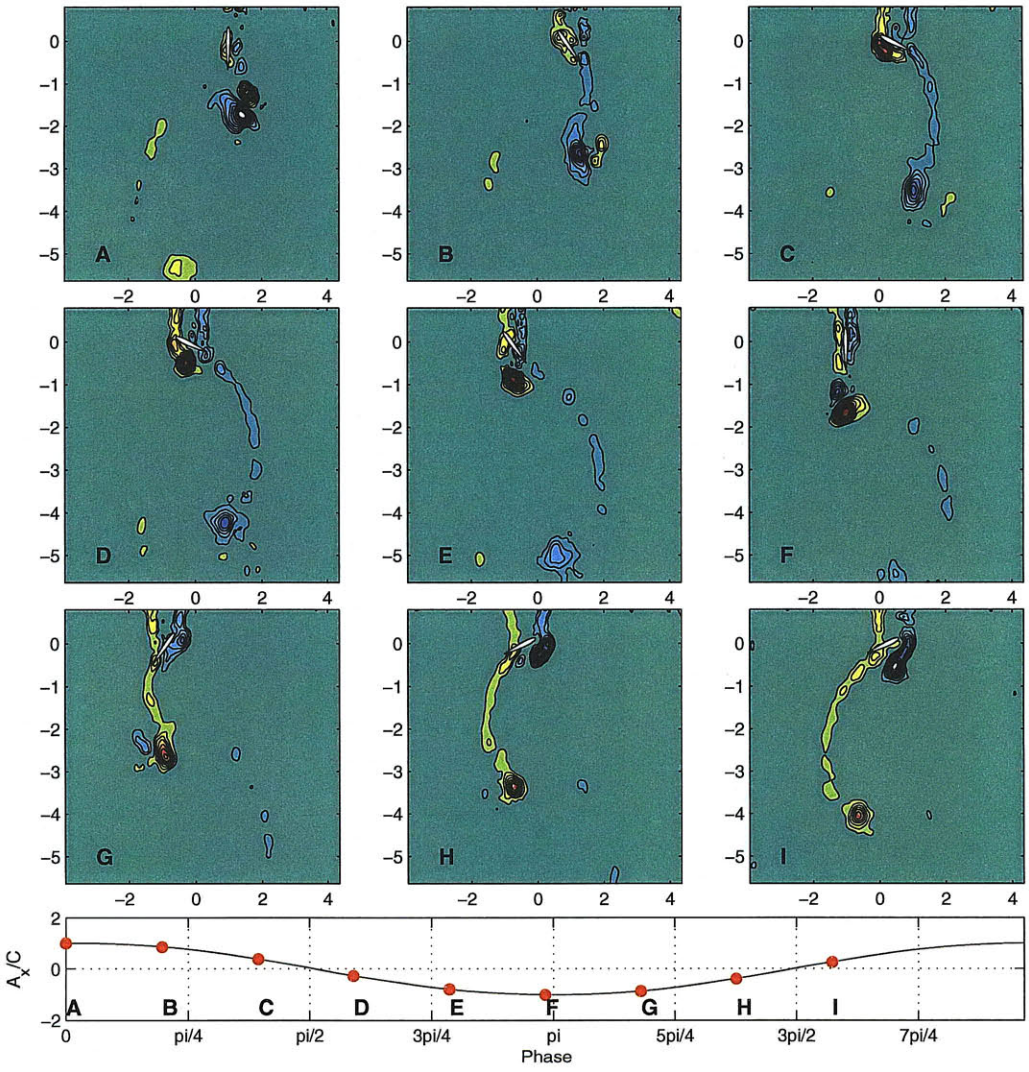

Figure G-3: Selected DPIV Images for $h_0/c = 1.0$, $St = 0.2$ and $\alpha_{max} = 39°$

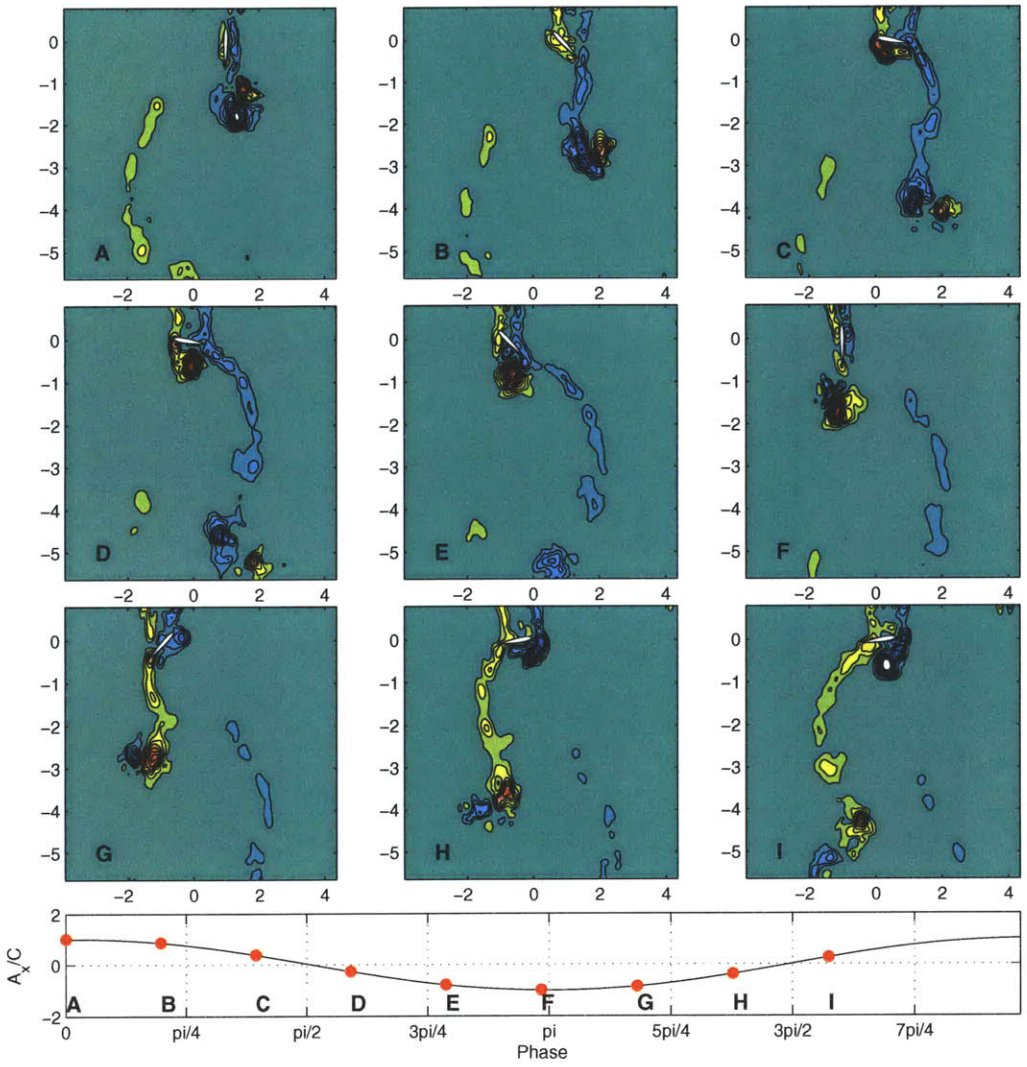

Figure G-4: Selected DPIV Images for $h_0/c = 1.0$, $St = 0.2$ and $\alpha_{max} = 53°$

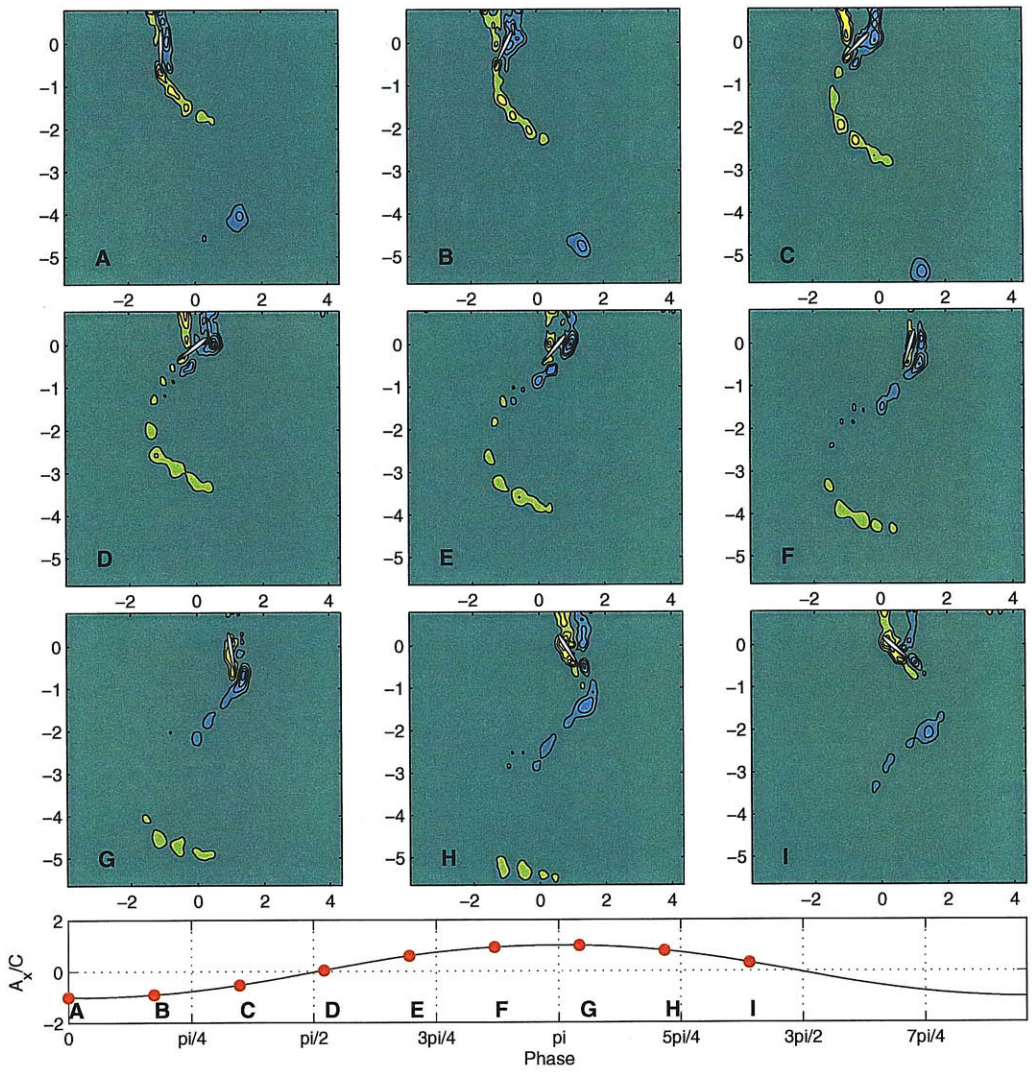

Figure G-5: Selected DPIV Images for $h_0/c = 1.0$, $St = 0.3$ and $\alpha_{max} = 11°$

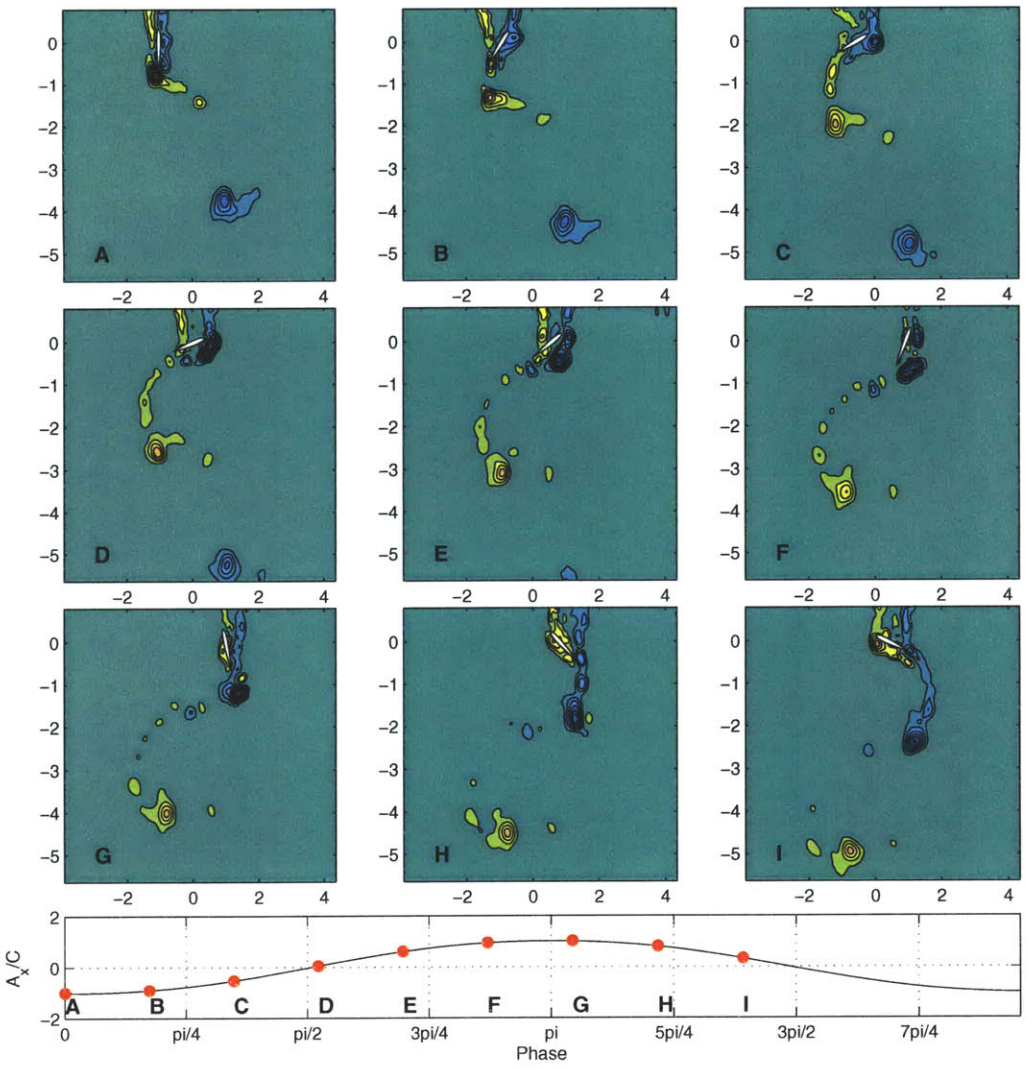

Figure G-6: Selected DPIV Images for $h_0/c = 1.0$, $St = 0.3$ and $\alpha_{max} = 25°$

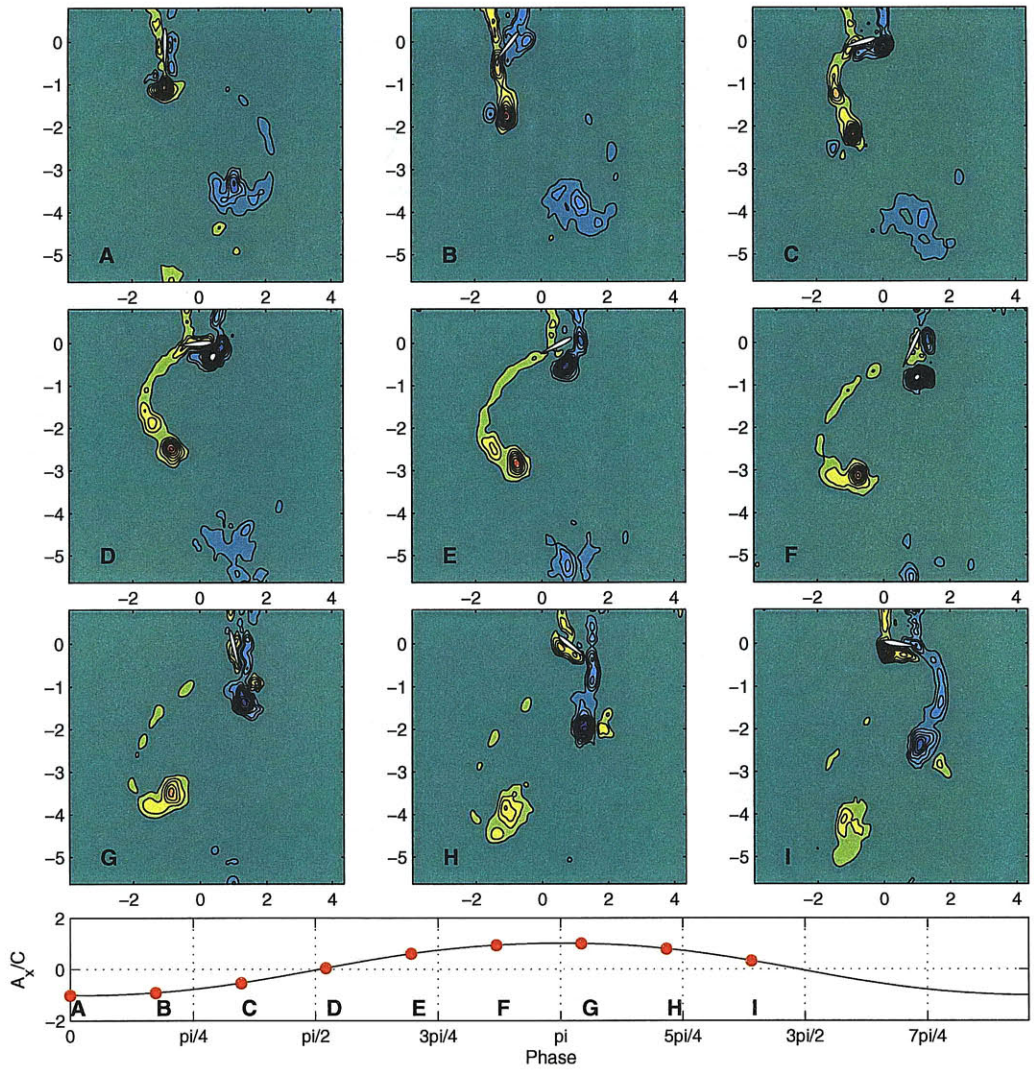

Figure G-7: Selected DPIV Images for $h_0/c = 1.0$, $St = 0.3$ and $\alpha_{max} = 39°$

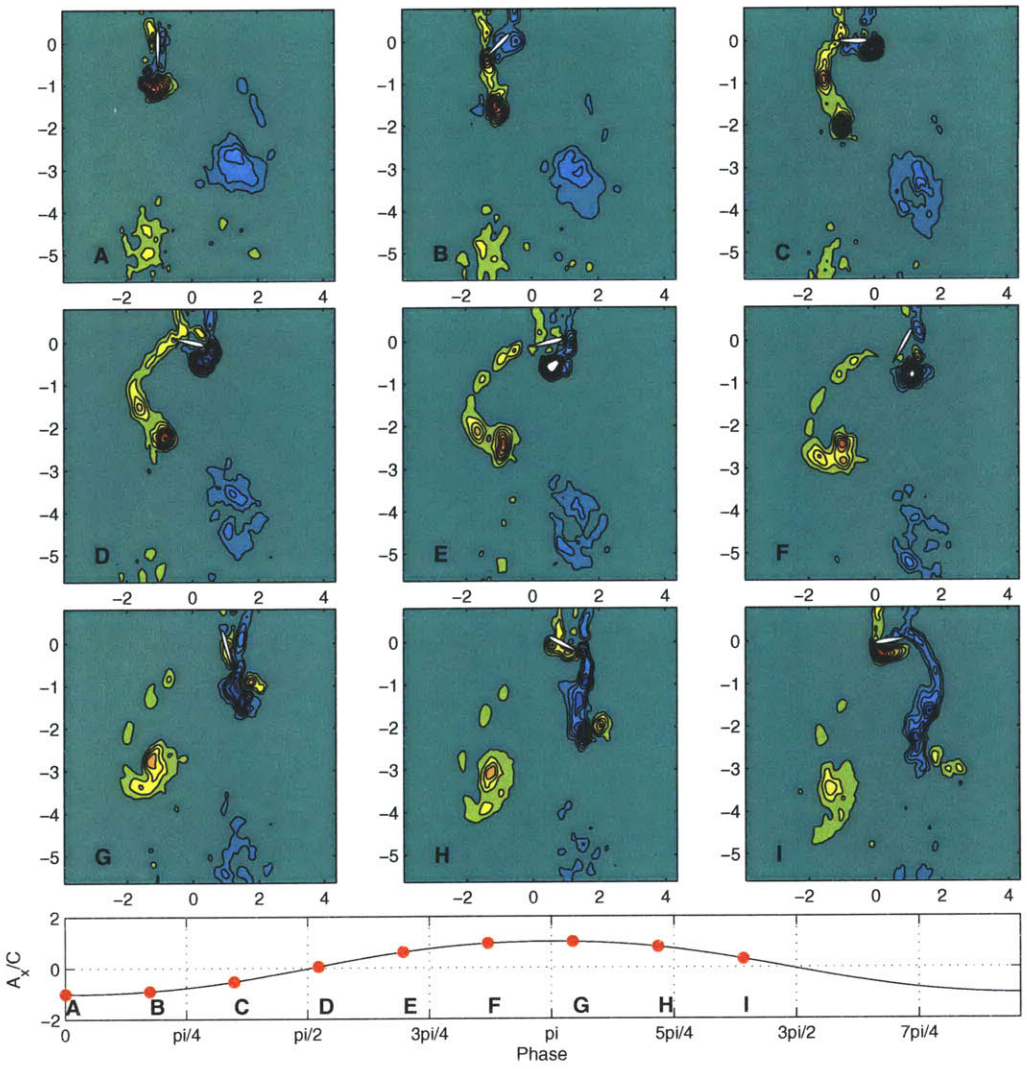

Figure G-8: Selected DPIV Images for $h_0/c = 1.0$, $St = 0.3$ and $\alpha_{max} = 53°$

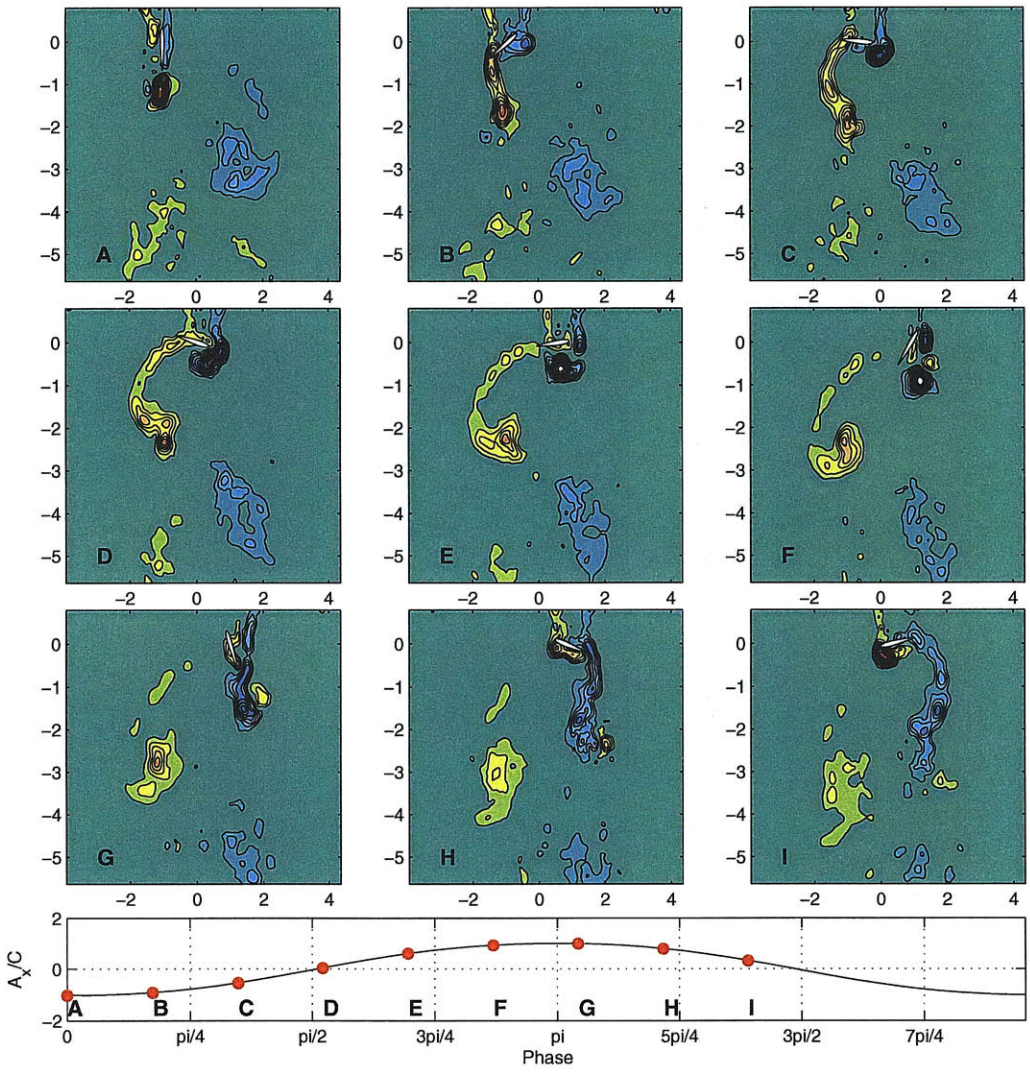

Figure G-9: Selected DPIV Images for $h_0/c = 1.0$, $St = 0.3$ and $\alpha_{max} = 57°$

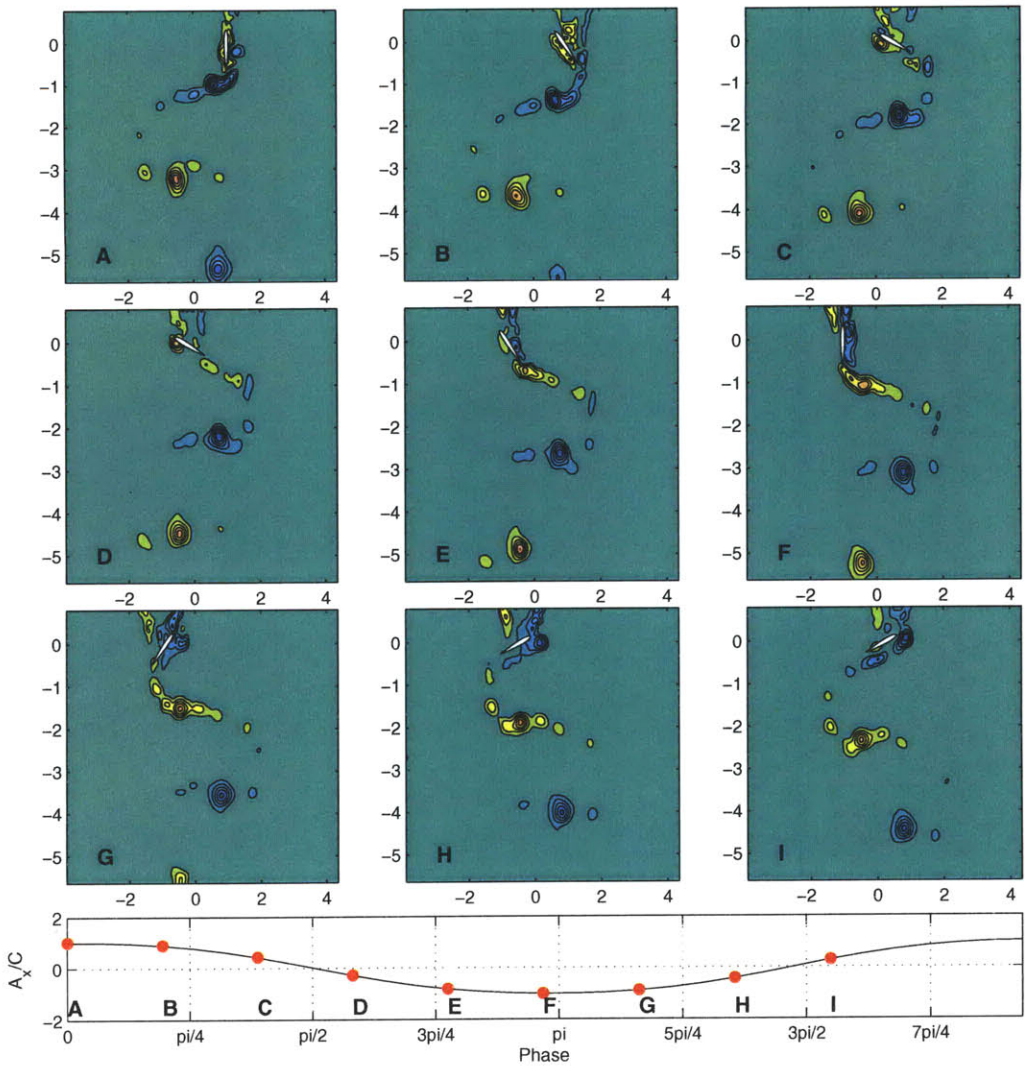

Figure G-10: Selected DPIV Images for $h_0/c = 1.0$, $St = 0.4$ and $\alpha_{max} = 11°$

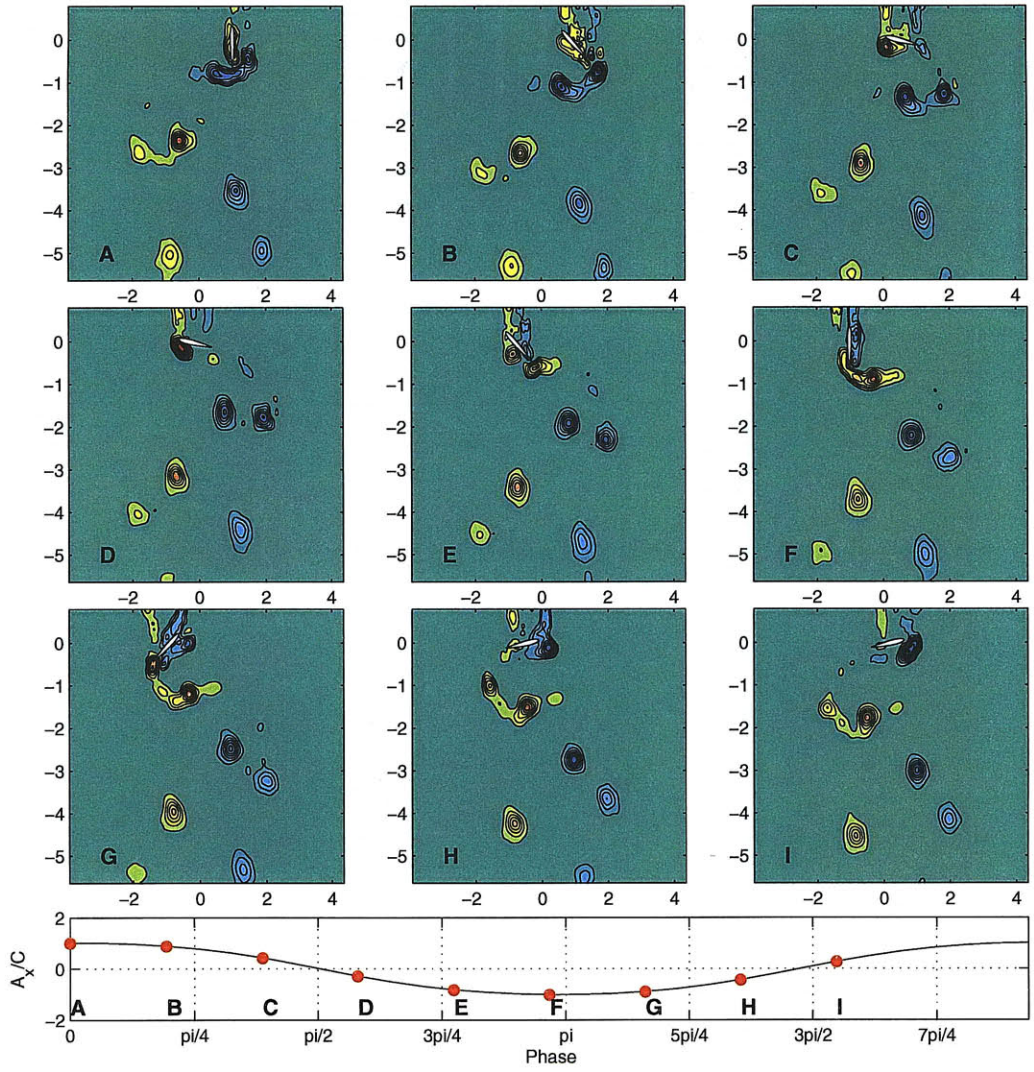

Figure G-11: Selected DPIV Images for $h_0/c = 1.0$, $St = 0.4$ and $\alpha_{max} = 25°$

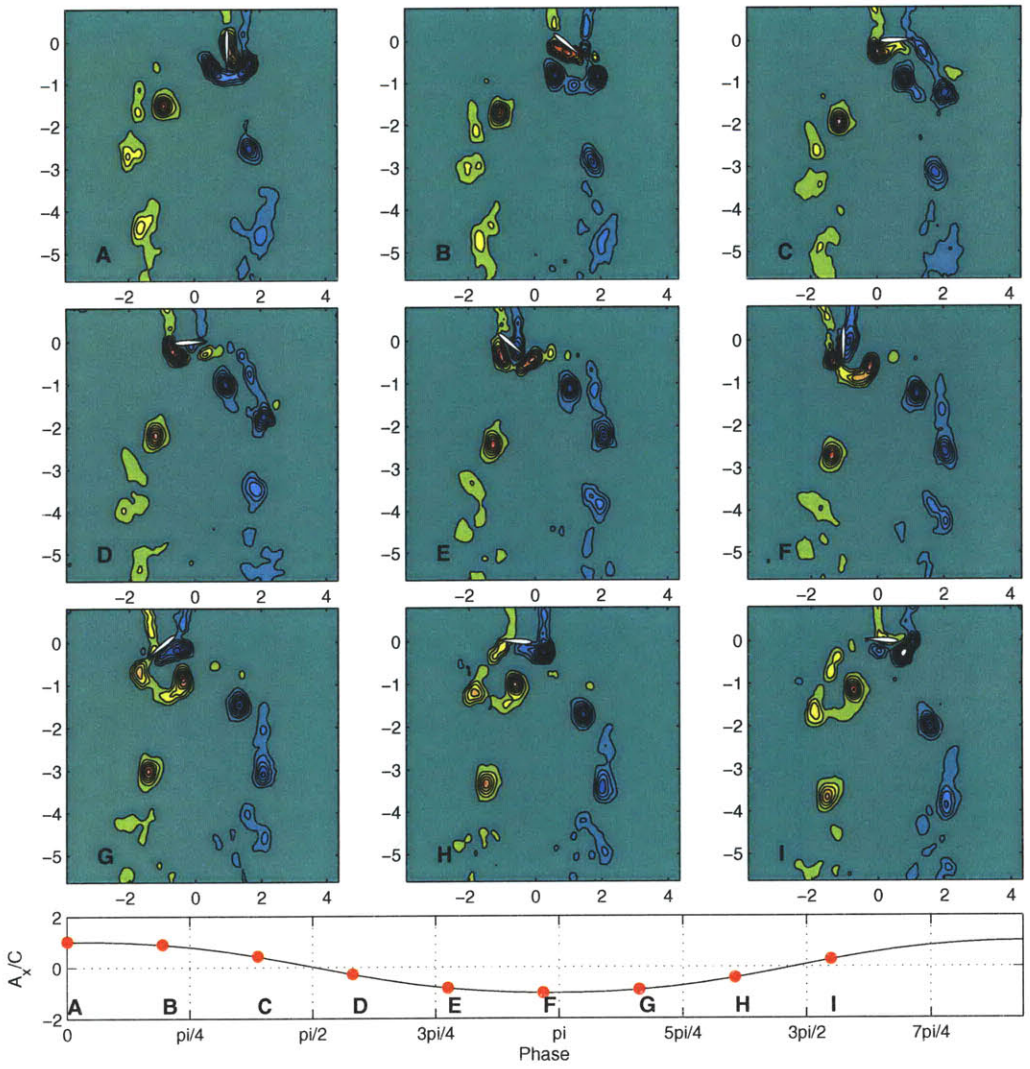

Figure G-12: Selected DPIV Images for $h_0/c = 1.0$, $St = 0.4$ and $\alpha_{max} = 39°$

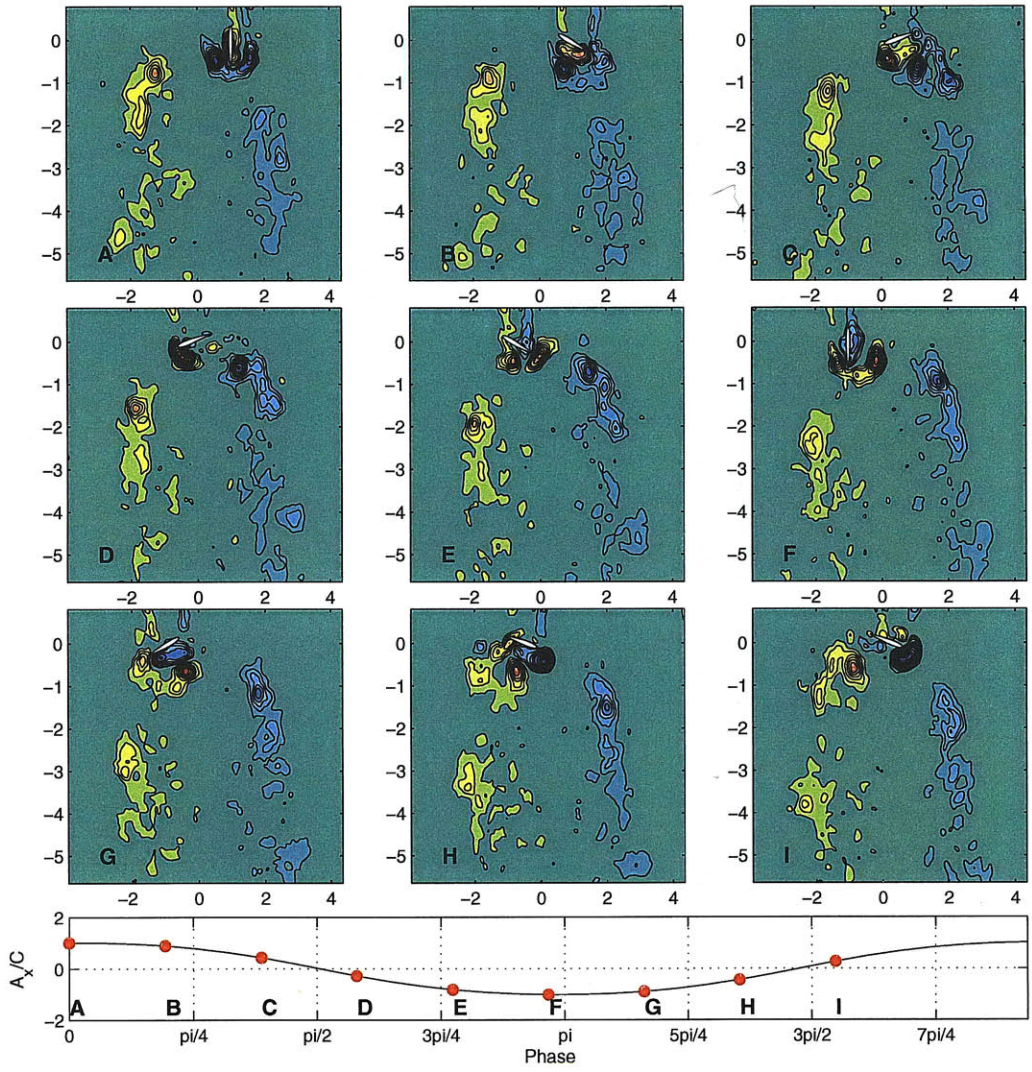

Figure G-13: Selected DPIV Images for $h_0/c = 1.0$, $St = 0.4$ and $\alpha_{max} = 53°$

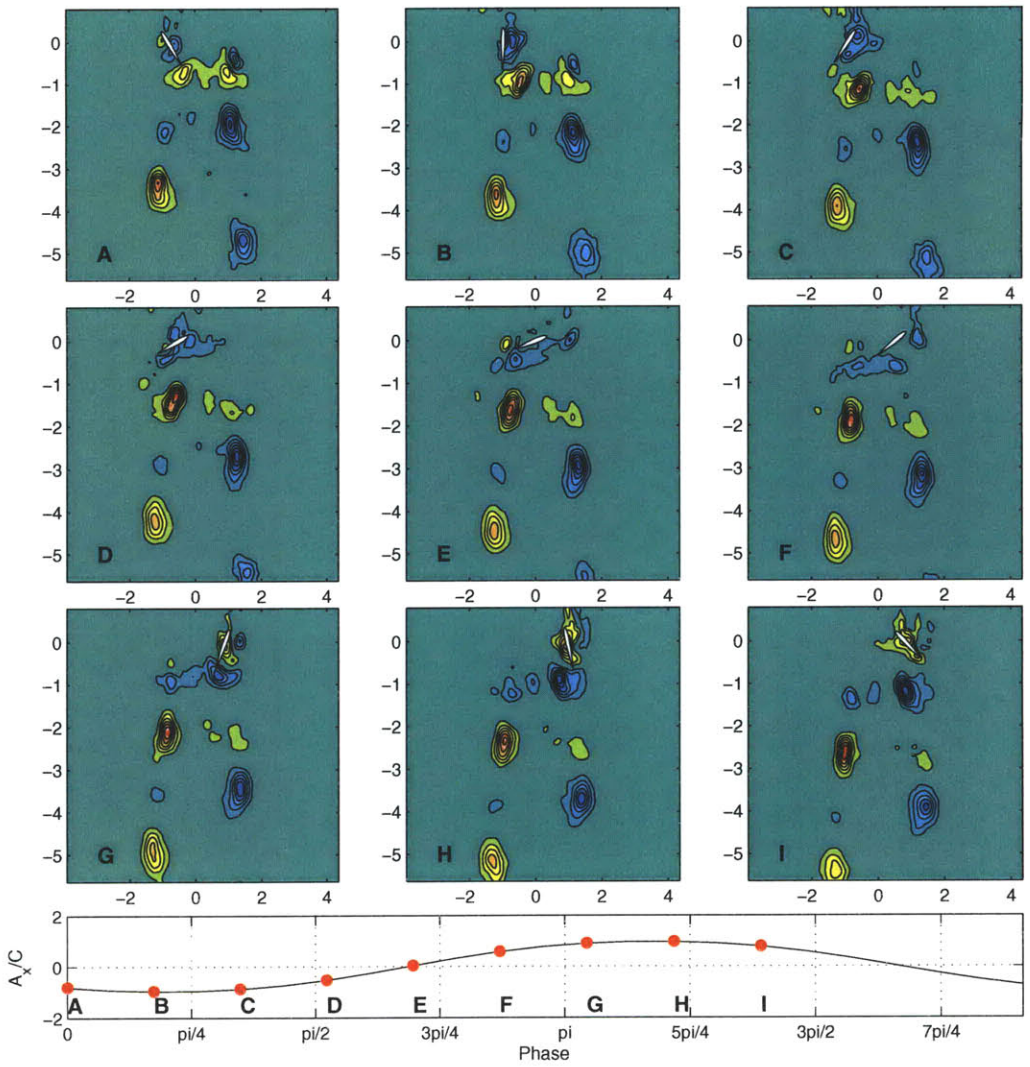

Figure G-14: Selected DPIV Images for $h_0/c = 1.0$, $St = 0.5$ and $\alpha_{max} = 11°$

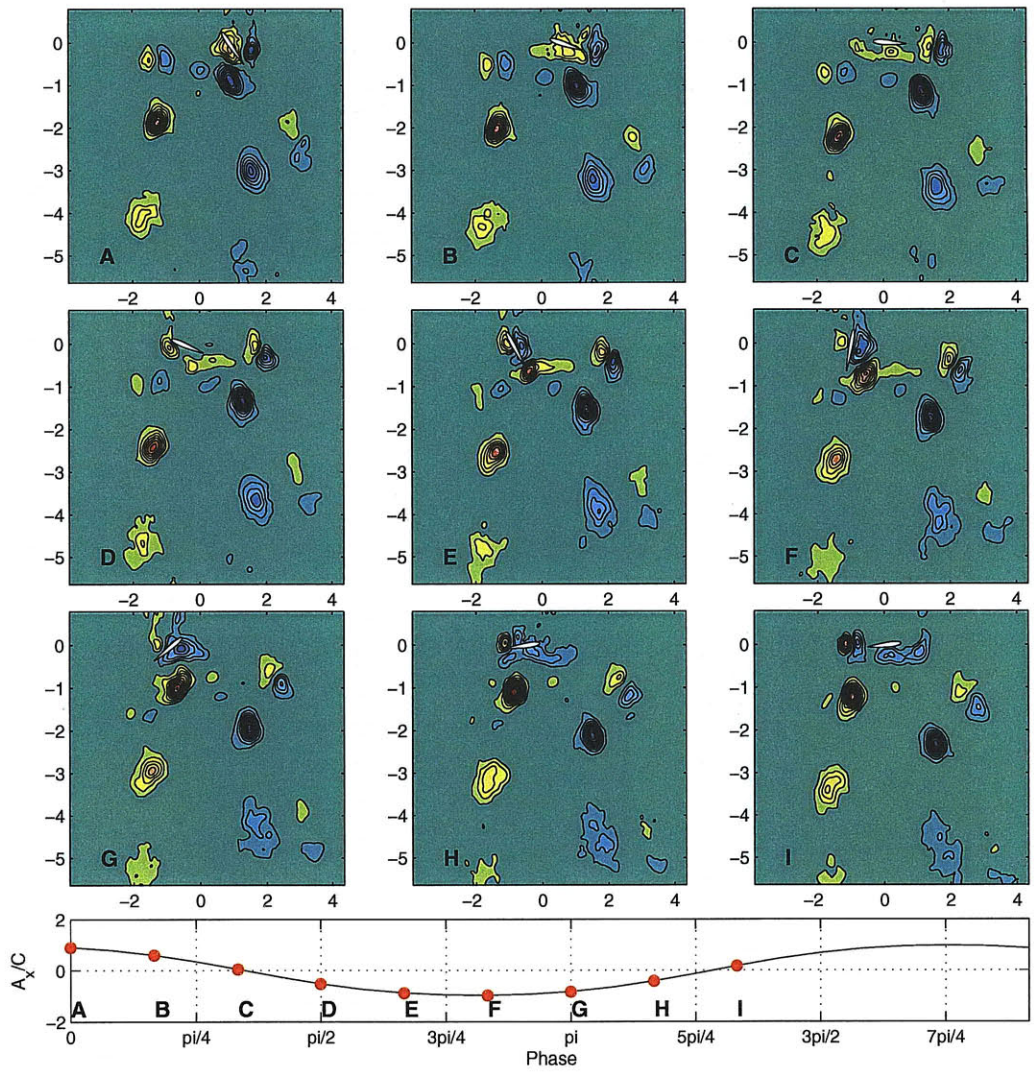

Figure G-15: Selected DPIV Images for $h_0/c = 1.0$, $St = 0.5$ and $\alpha_{max} = 25°$

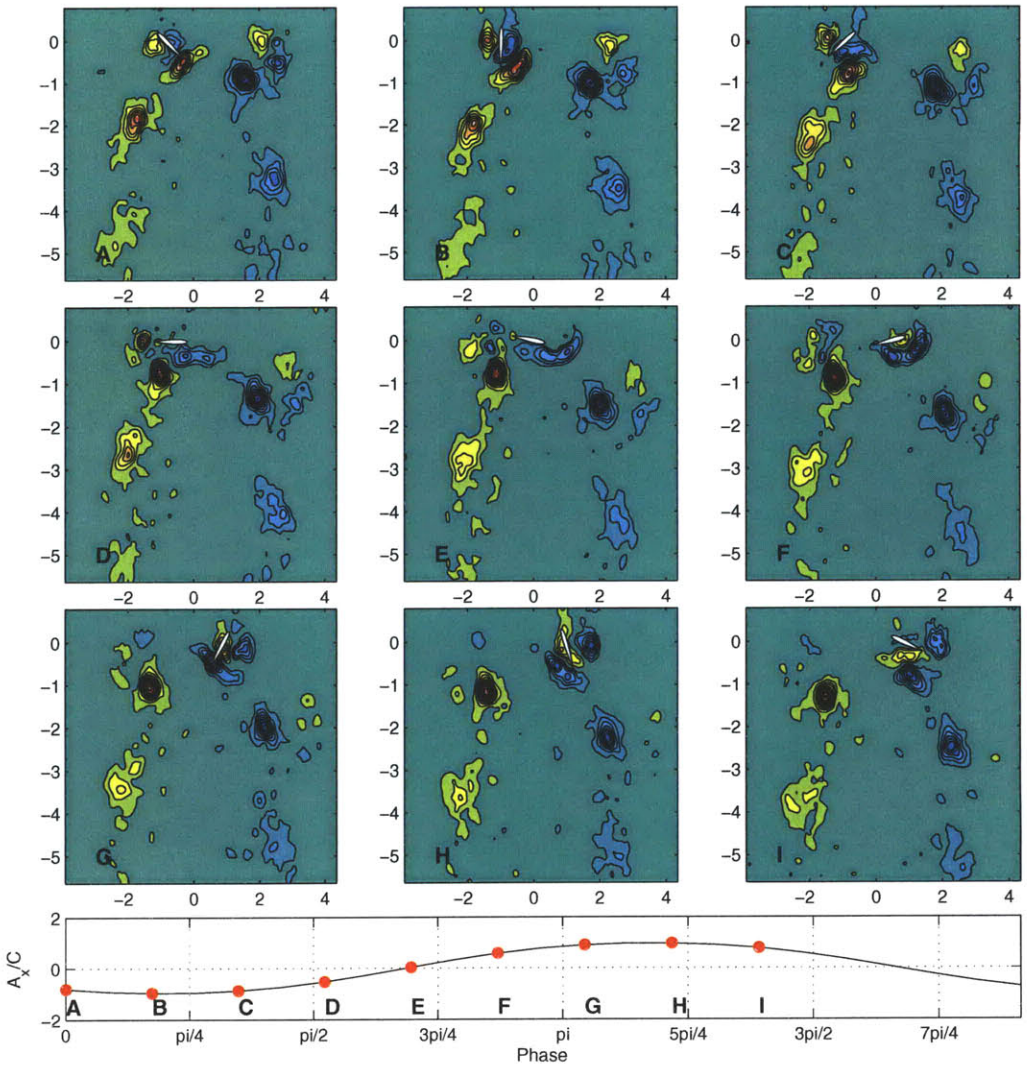

Figure G-16: Selected DPIV Images for $h_0/c = 1.0$, $St = 0.5$ and $\alpha_{max} = 39°$

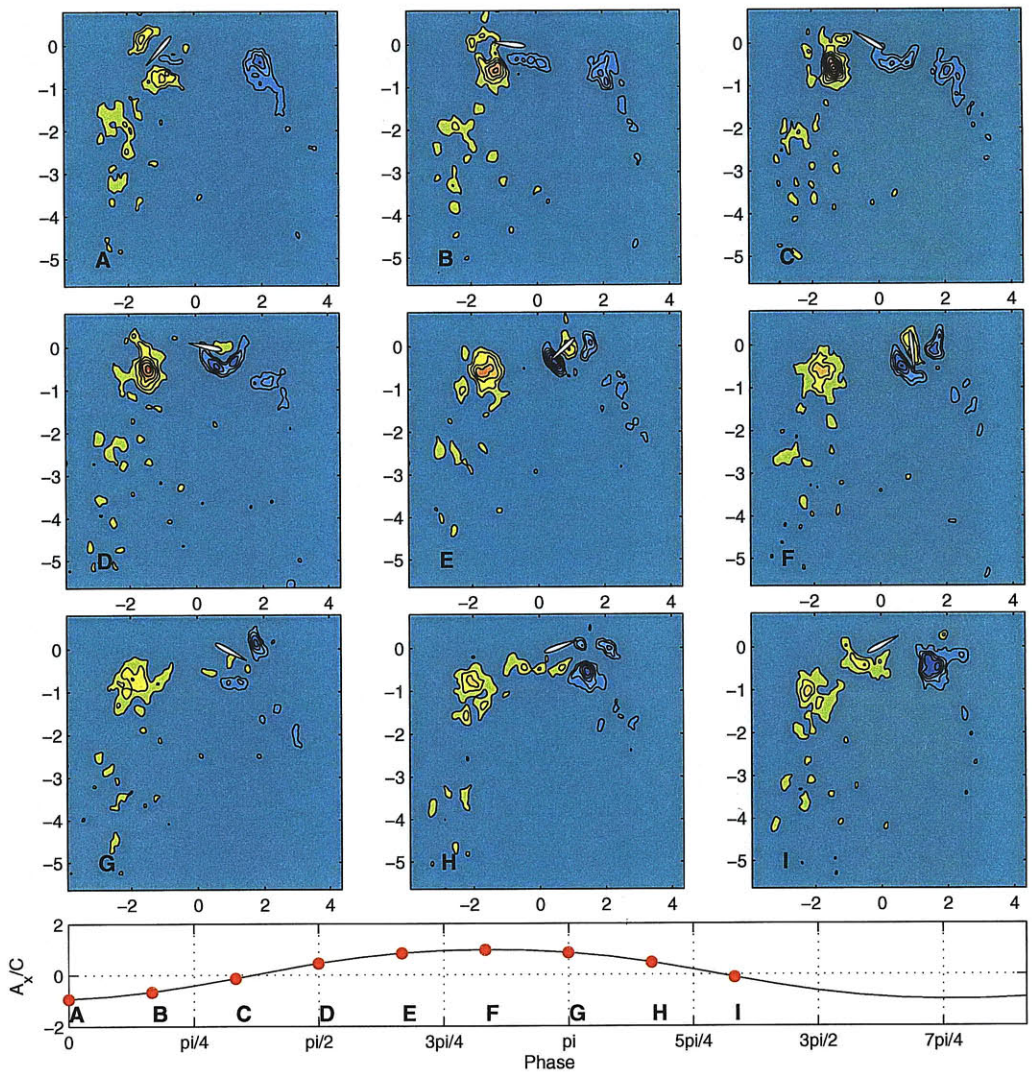

Figure G-17: Selected DPIV Images for $h_0/c = 1.0$, $St = 0.5$ and $\alpha_{max} = 53°$

Appendix H

DPIV Data: $h_0/c = 1.23$

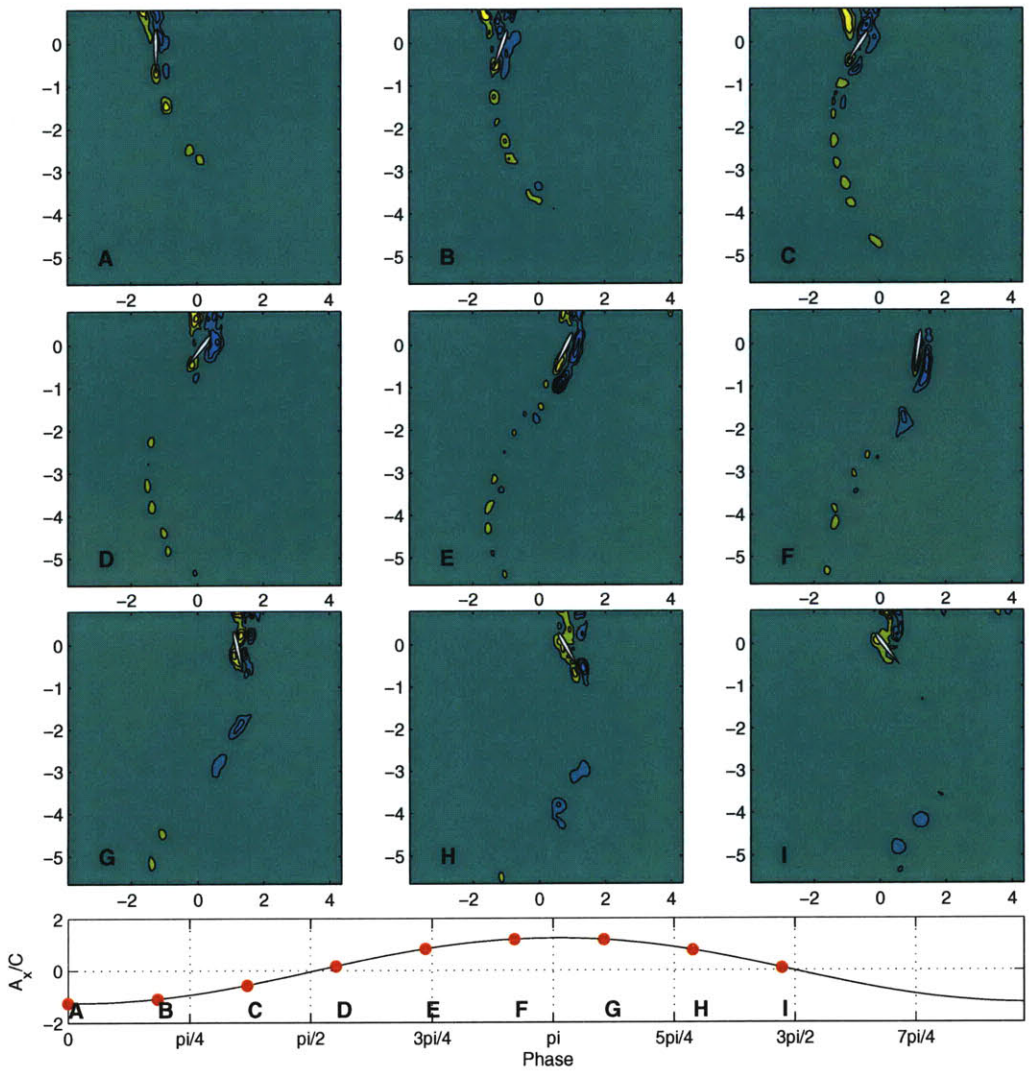

Figure H-1: Selected DPIV Images for $h_0/c = 1.23$, $St = 0.2$ and $\alpha_{max} = 11°$

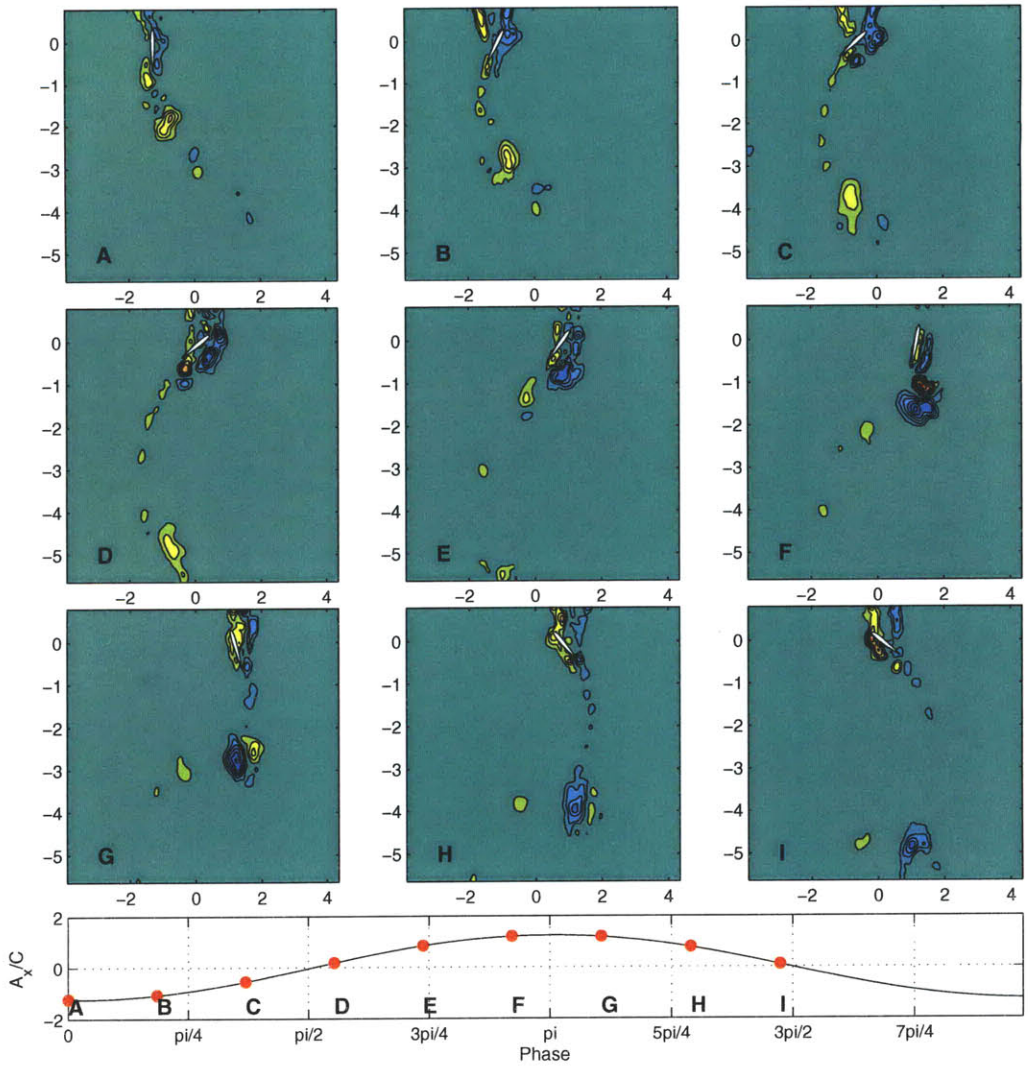

Figure H-2: Selected DPIV Images for $h_0/c = 1.23$, $St = 0.2$ and $\alpha_{max} = 25°$

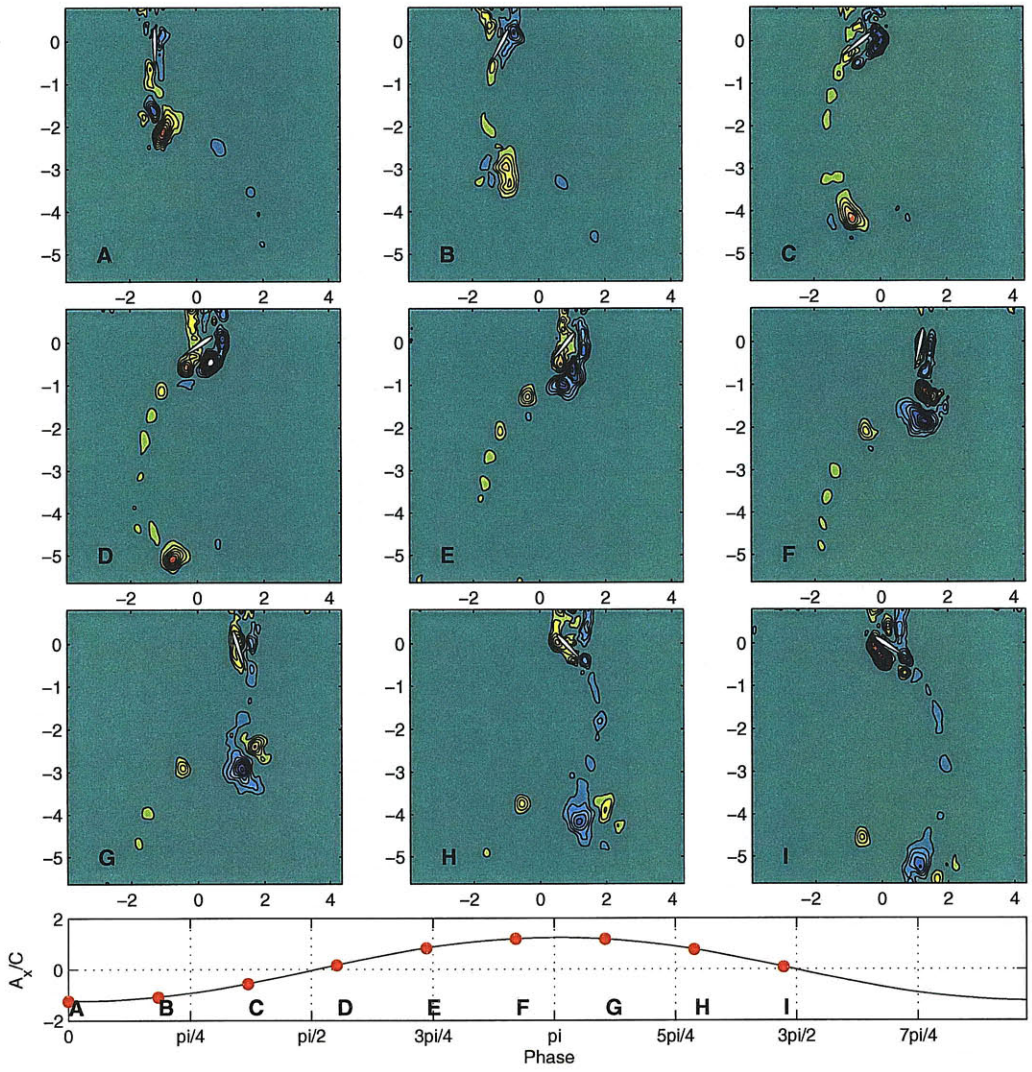

Figure H-3: Selected DPIV Images for $h_0/c = 1.23$, $St = 0.2$ and $\alpha_{max} = 30°$

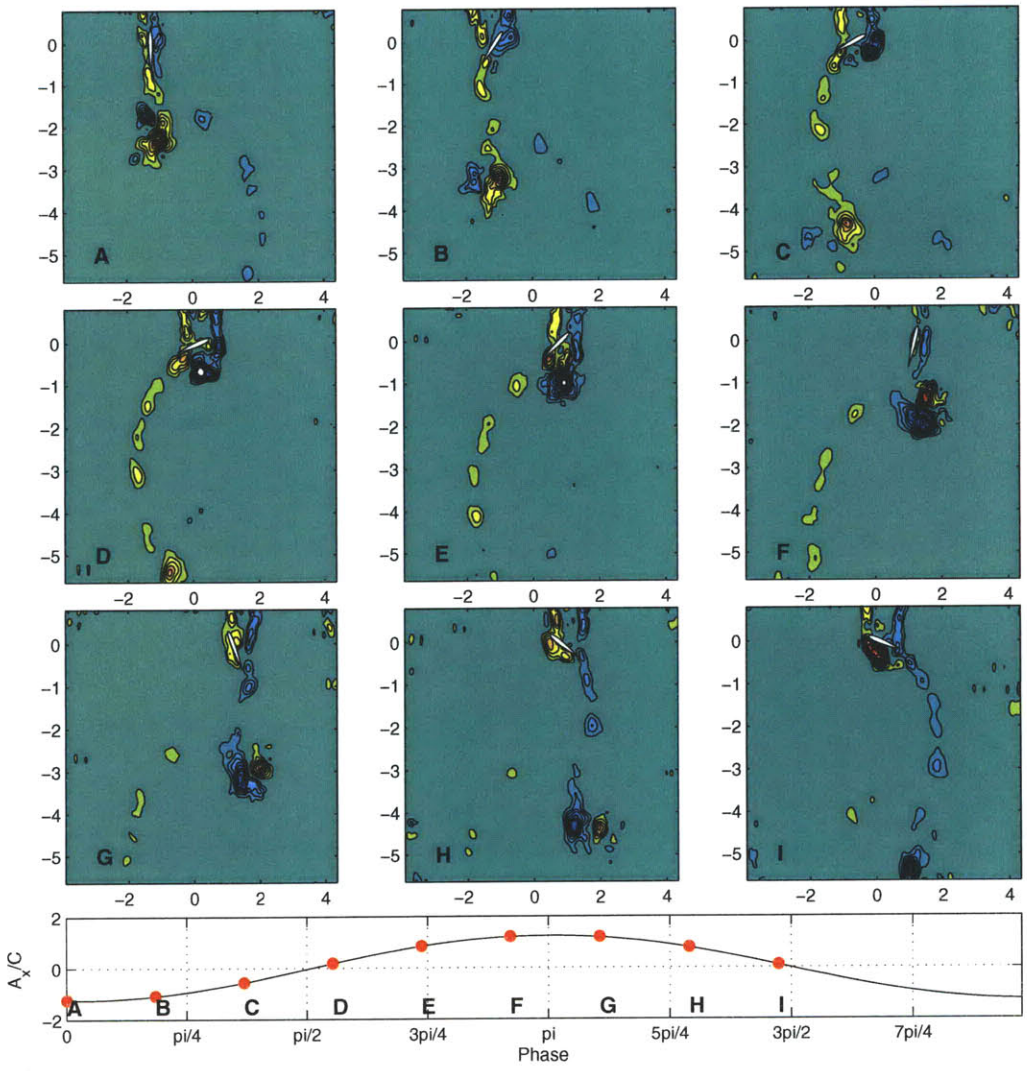

Figure H-4: Selected DPIV Images for $h_0/c = 1.23$, $St = 0.2$ and $\alpha_{max} = 39°$

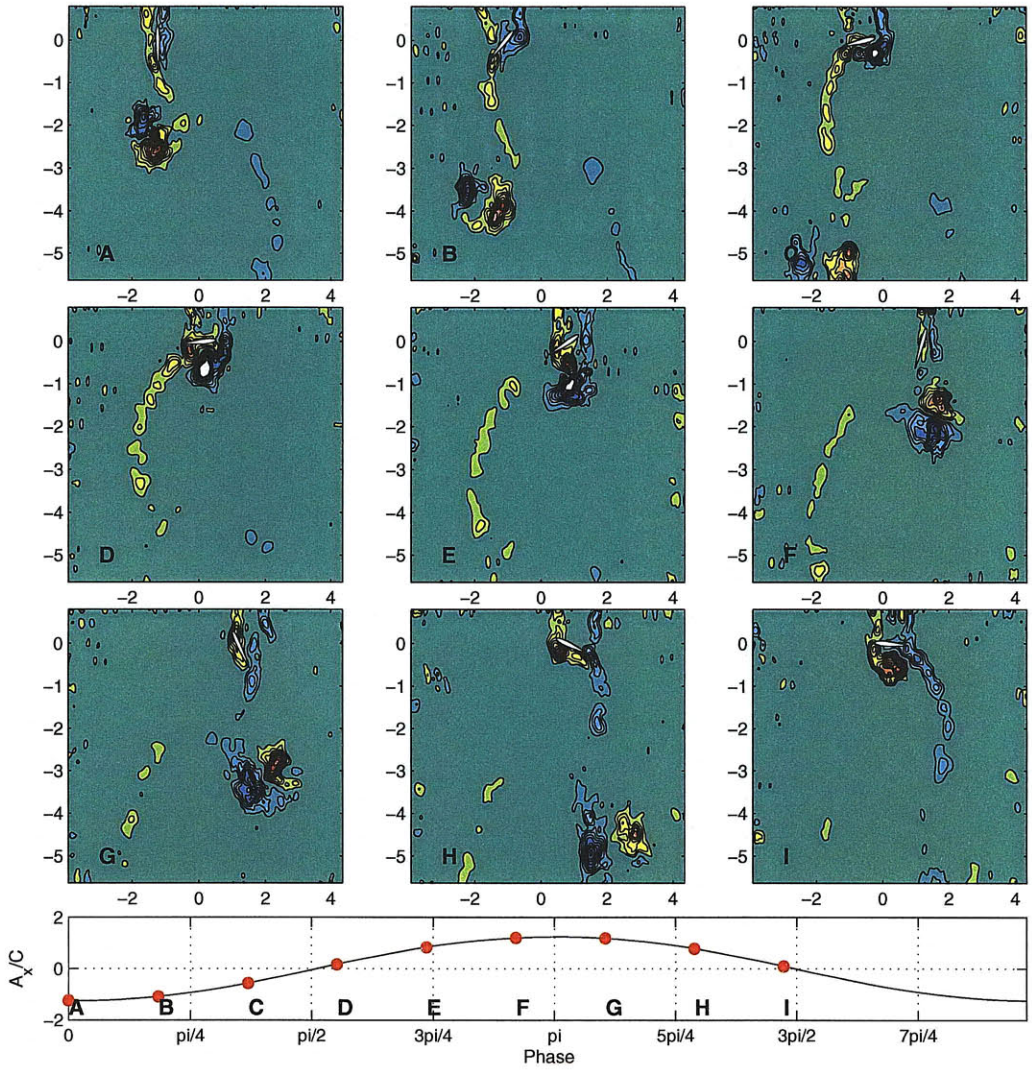

Figure H-5: Selected DPIV Images for $h_0/c = 1.23$, $St = 0.2$ and $\alpha_{max} = 53°$

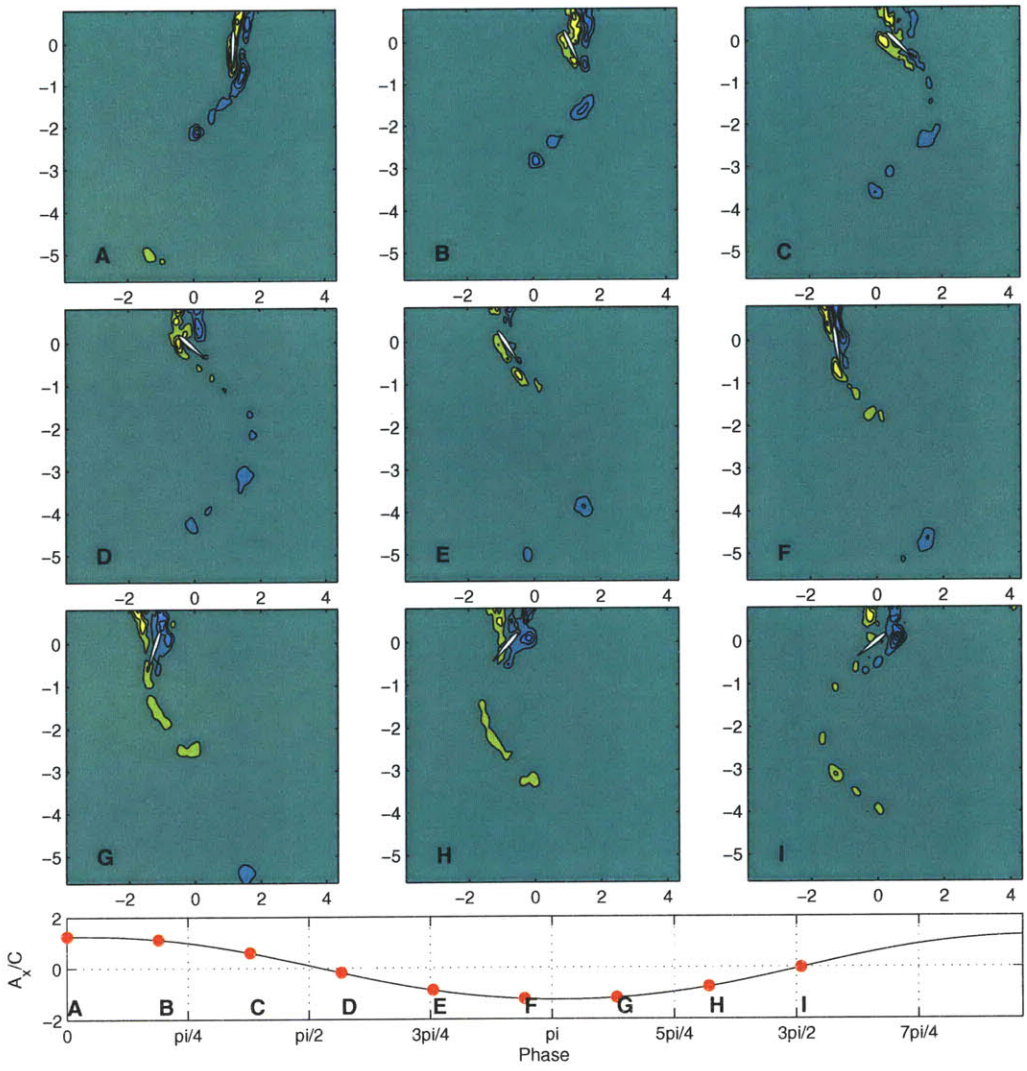

Figure H-6: Selected DPIV Images for $h_0/c = 1.23$, $St = 0.3$ and $\alpha_{max} = 11°$

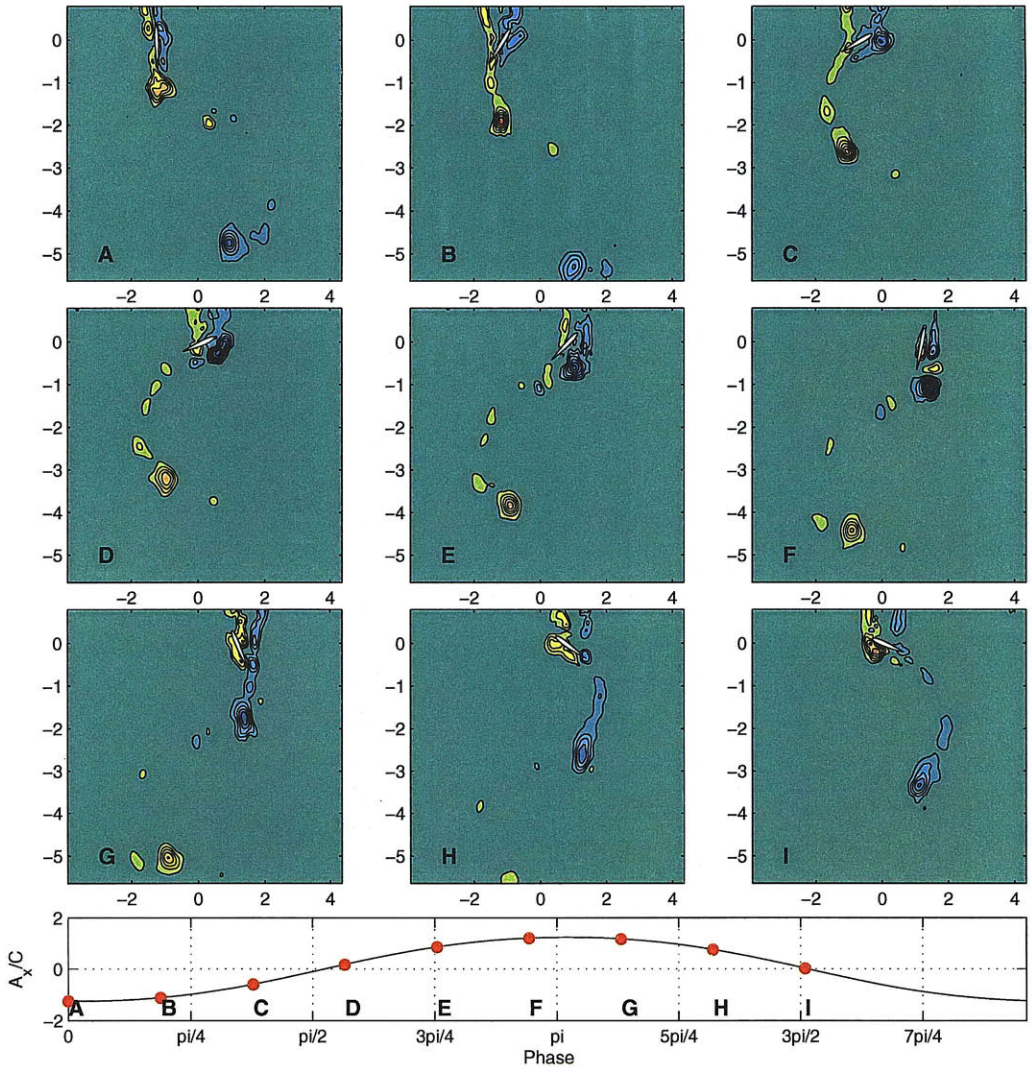

Figure H-7: Selected DPIV Images for $h_0/c = 1.23$, $St = 0.3$ and $\alpha_{max} = 25°$

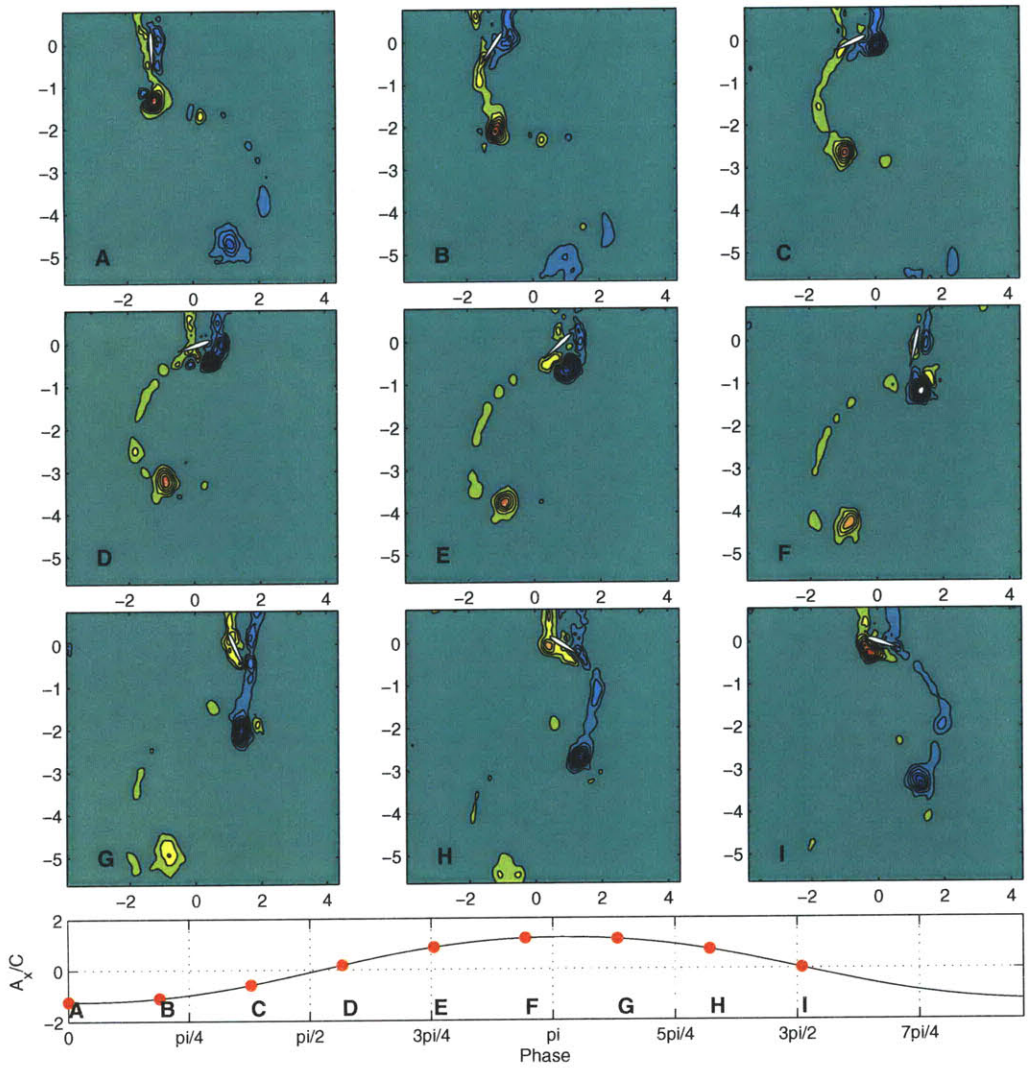

Figure H-8: Selected DPIV Images for $h_0/c = 1.23$, $St = 0.3$ and $\alpha_{max} = 30°$

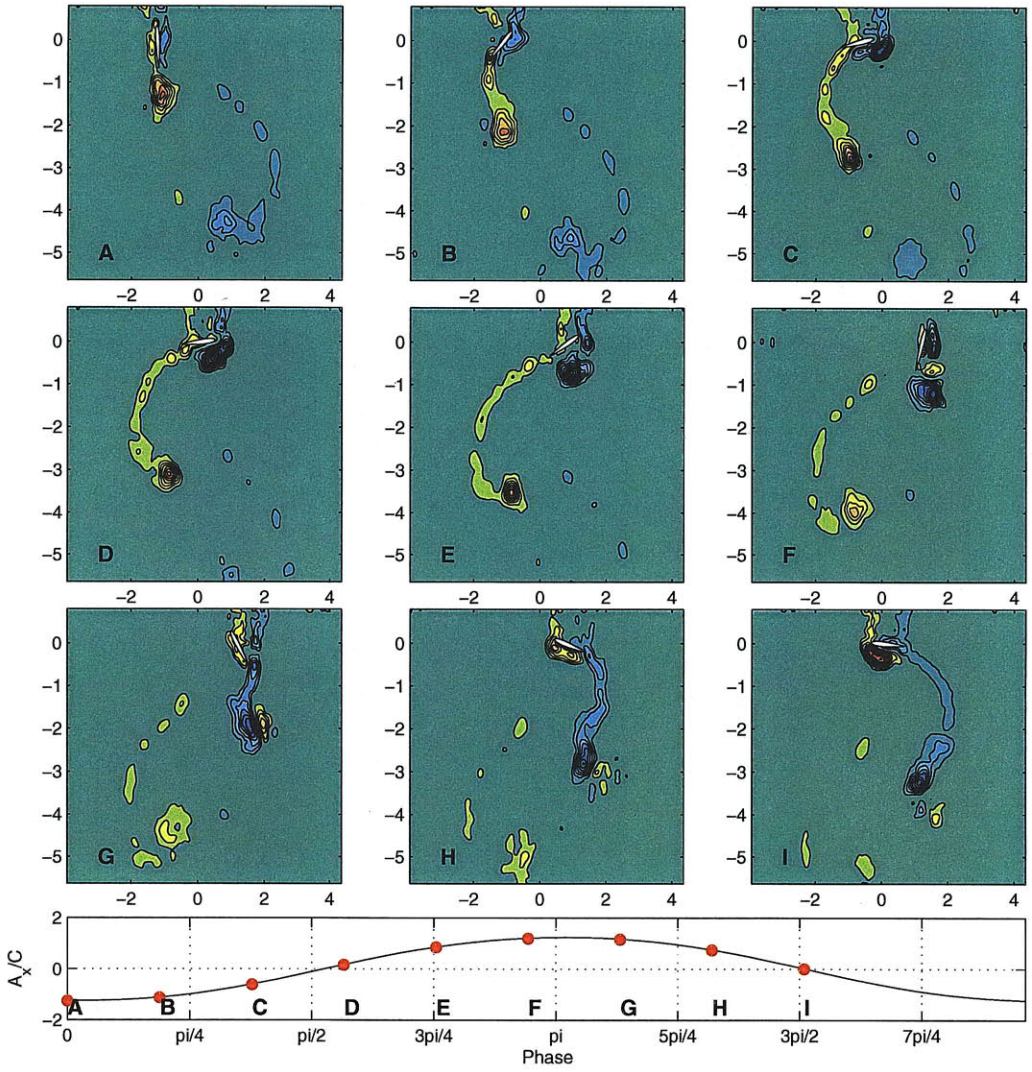

Figure H-9: Selected DPIV Images for $h_0/c = 1.23$, $St = 0.3$ and $\alpha_{max} = 39°$

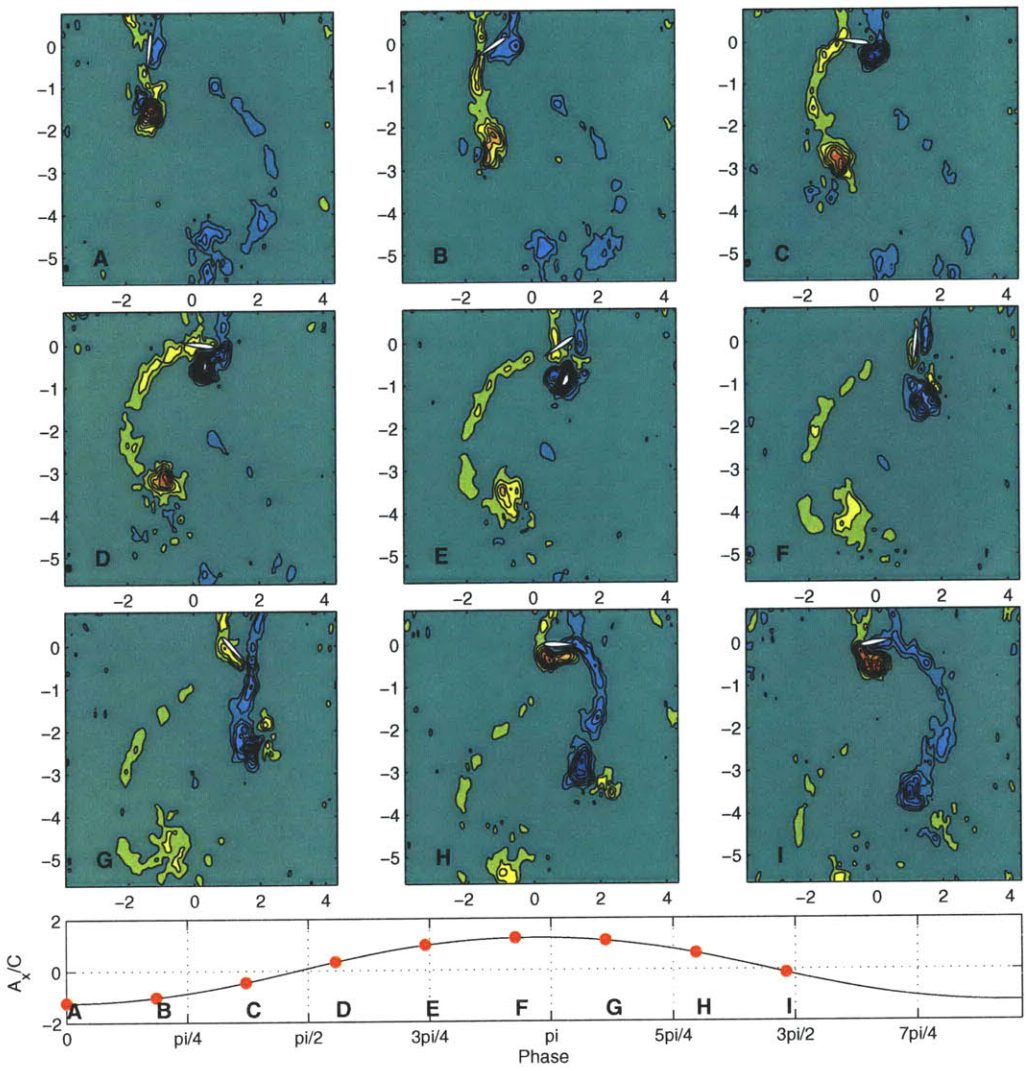

Figure H-10: Selected DPIV Images for $h_0/c = 1.23$, $St = 0.3$ and $\alpha_{max} = 53°$

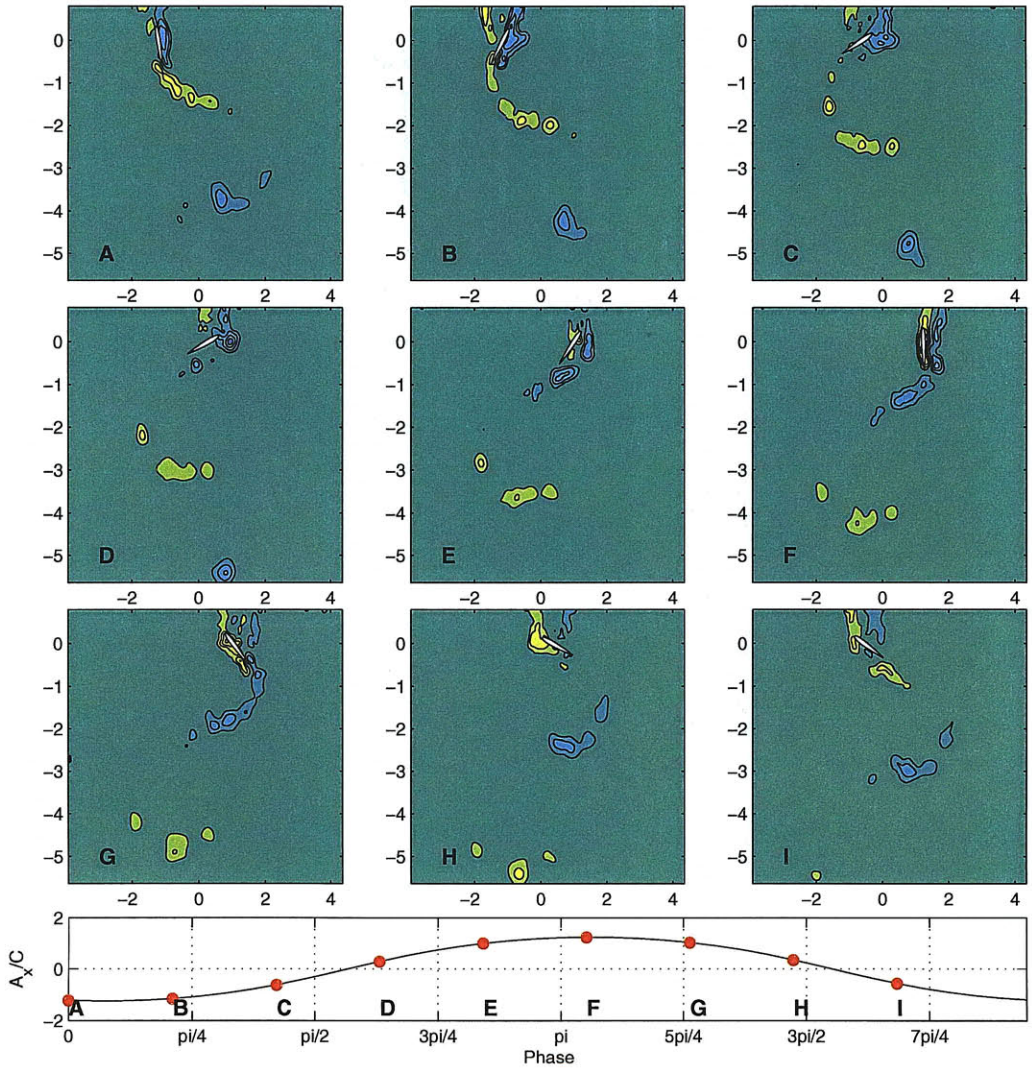

Figure H-11: Selected DPIV Images for $h_0/c = 1.23$, $St = 0.4$ and $\alpha_{max} = 11°$

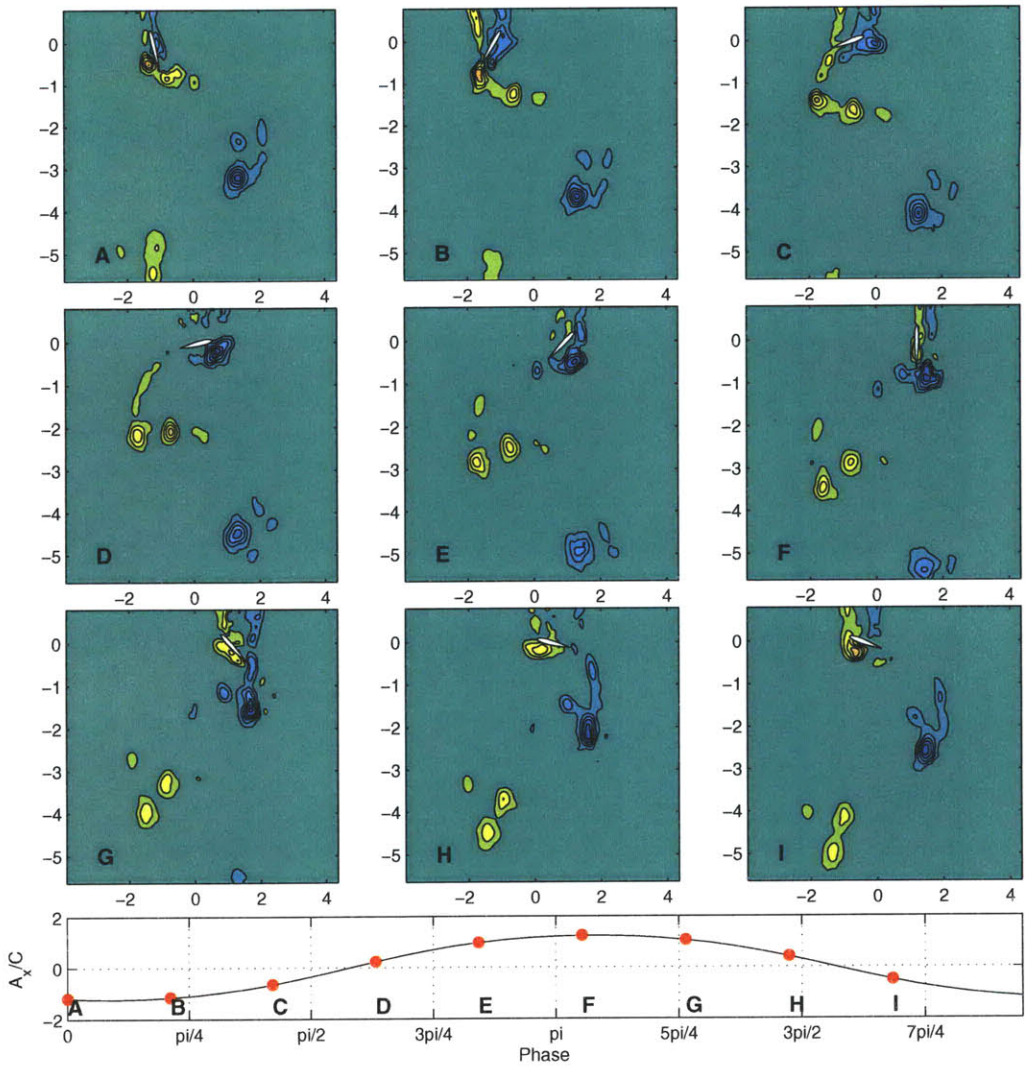

Figure H-12: Selected DPIV Images for $h_0/c = 1.23$, $St = 0.4$ and $\alpha_{max} = 25°$

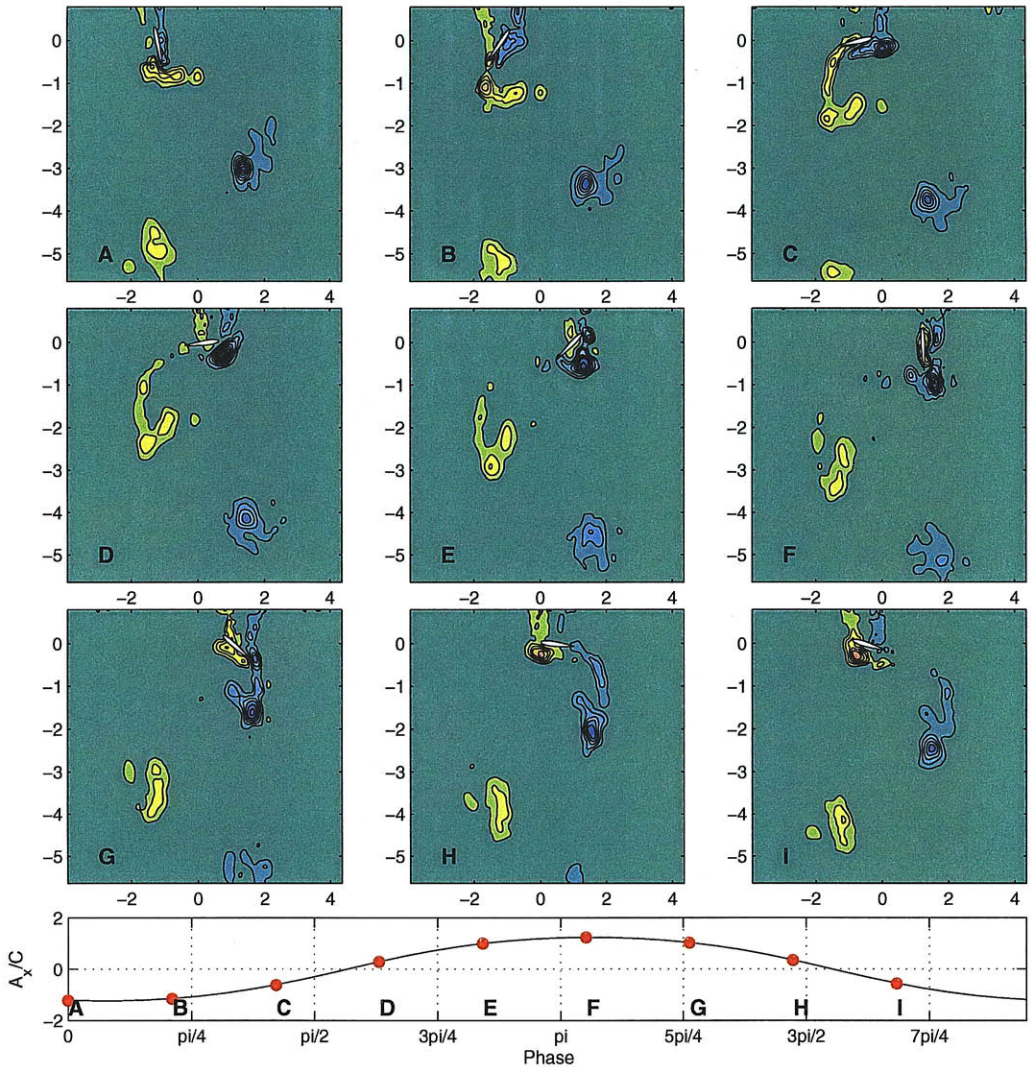

Figure H-13: Selected DPIV Images for $h_0/c = 1.23$, $St = 0.4$ and $\alpha_{max} = 30°$

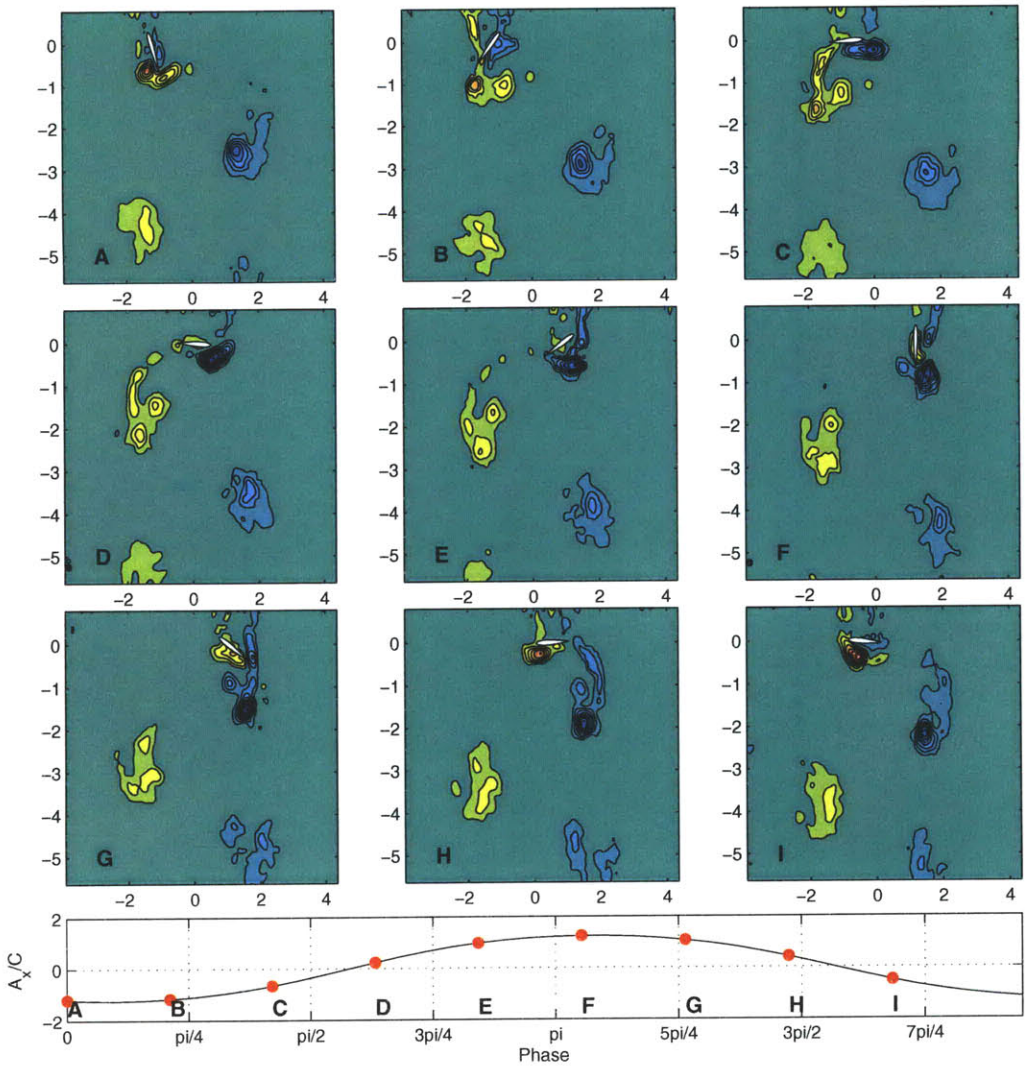

Figure H-14: Selected DPIV Images for $h_0/c = 1.23$, $St = 0.4$ and $\alpha_{max} = 39°$

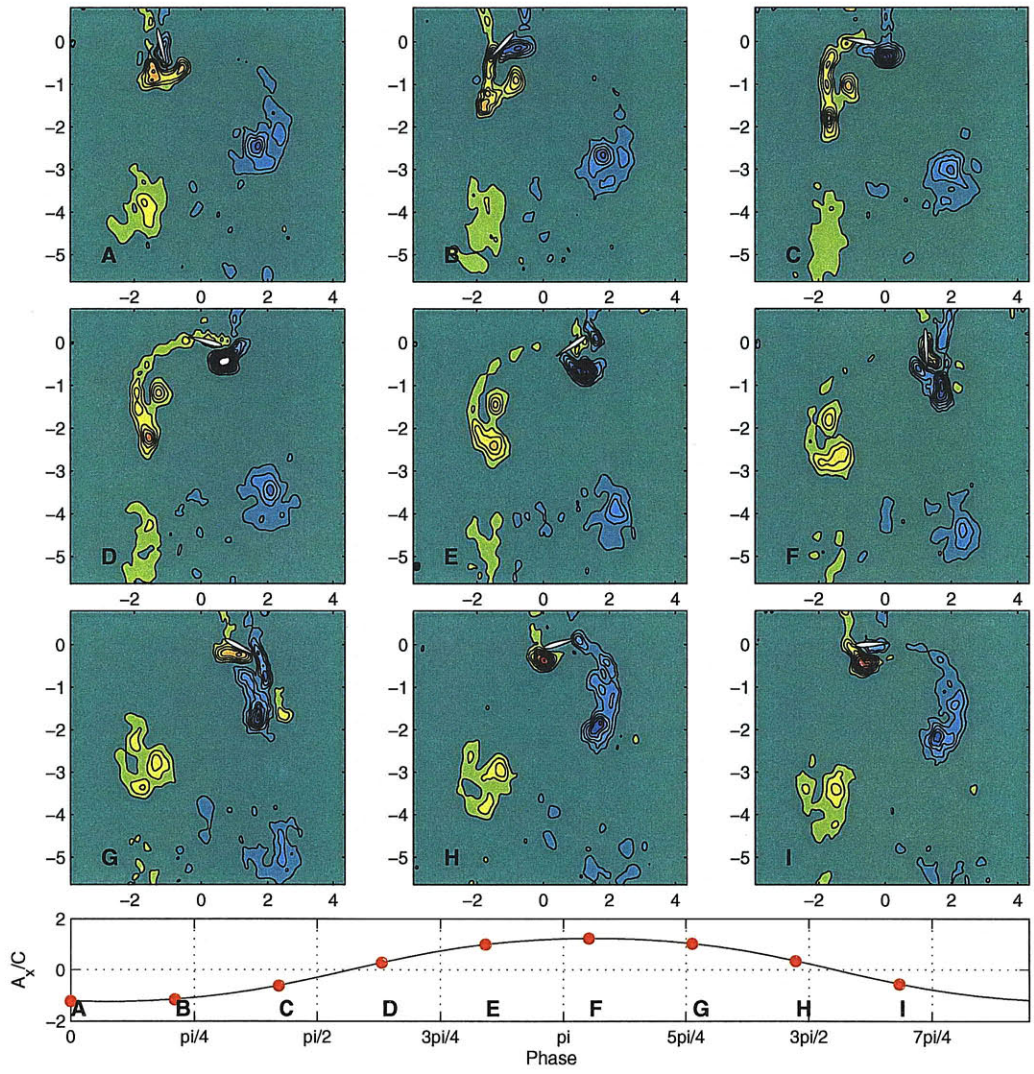

Figure H-15: Selected DPIV Images for $h_0/c = 1.23$, $St = 0.4$ and $\alpha_{max} = 48°$

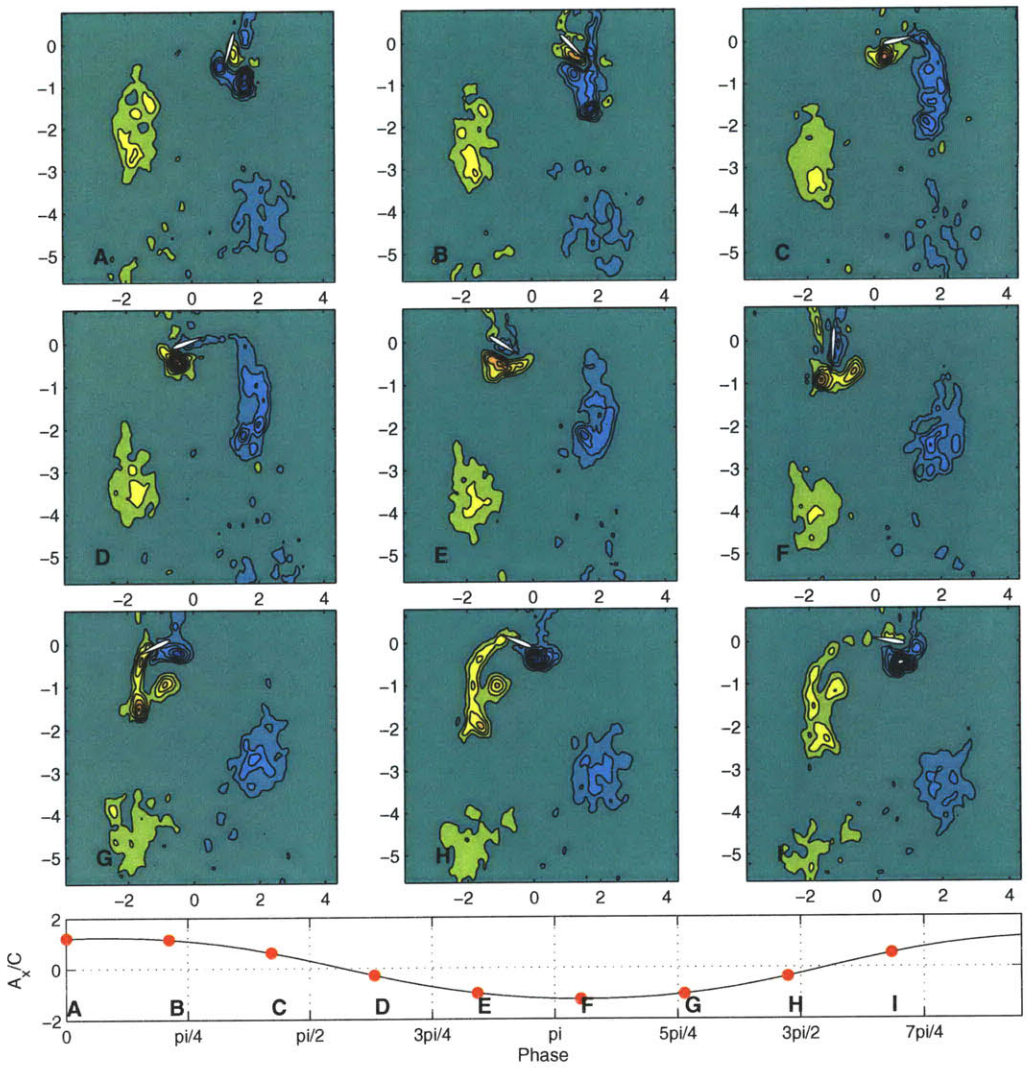

Figure H-16: Selected DPIV Images for $h_0/c = 1.23$, $St = 0.4$ and $\alpha_{max} = 53°$

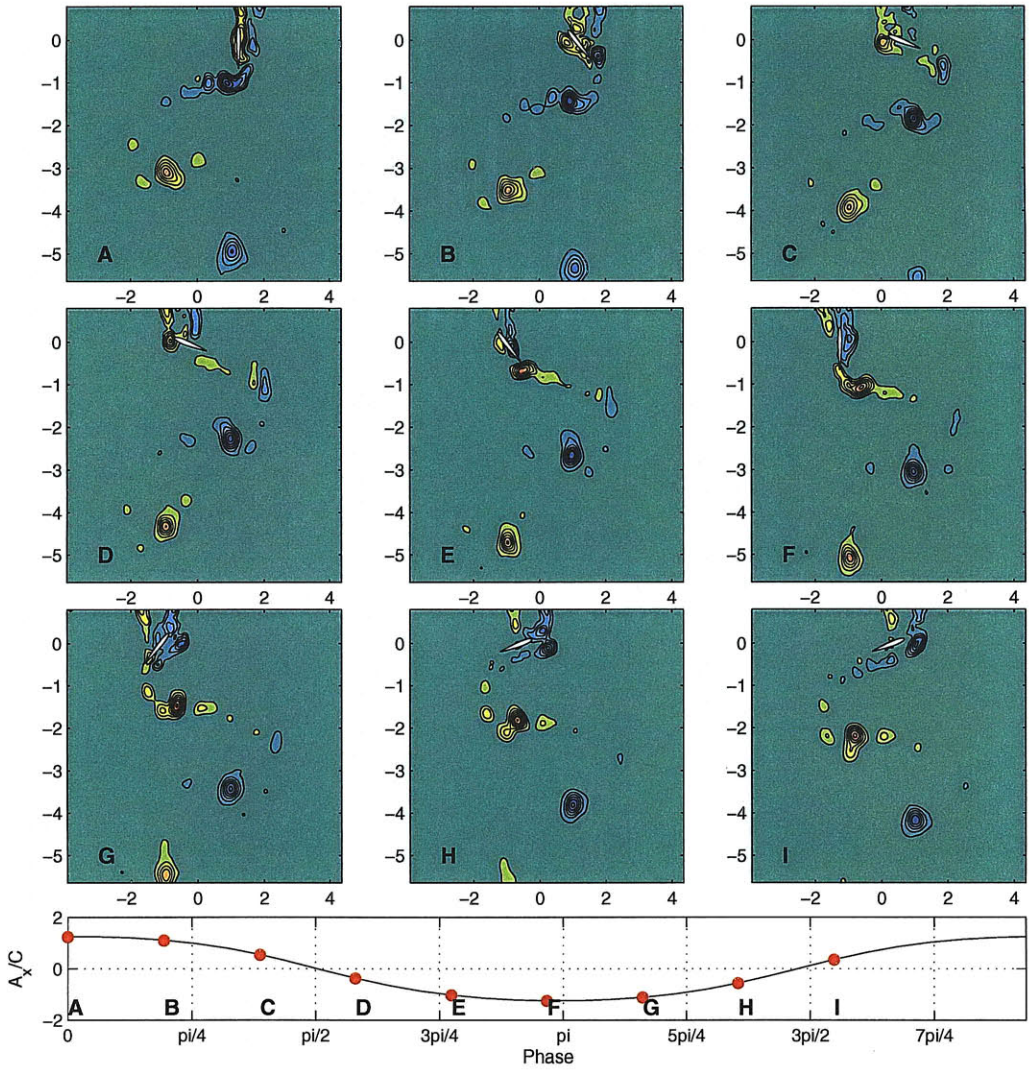

Figure H-17: Selected DPIV Images for $h_0/c = 1.23$, $St = 0.5$ and $\alpha_{max} = 11°$

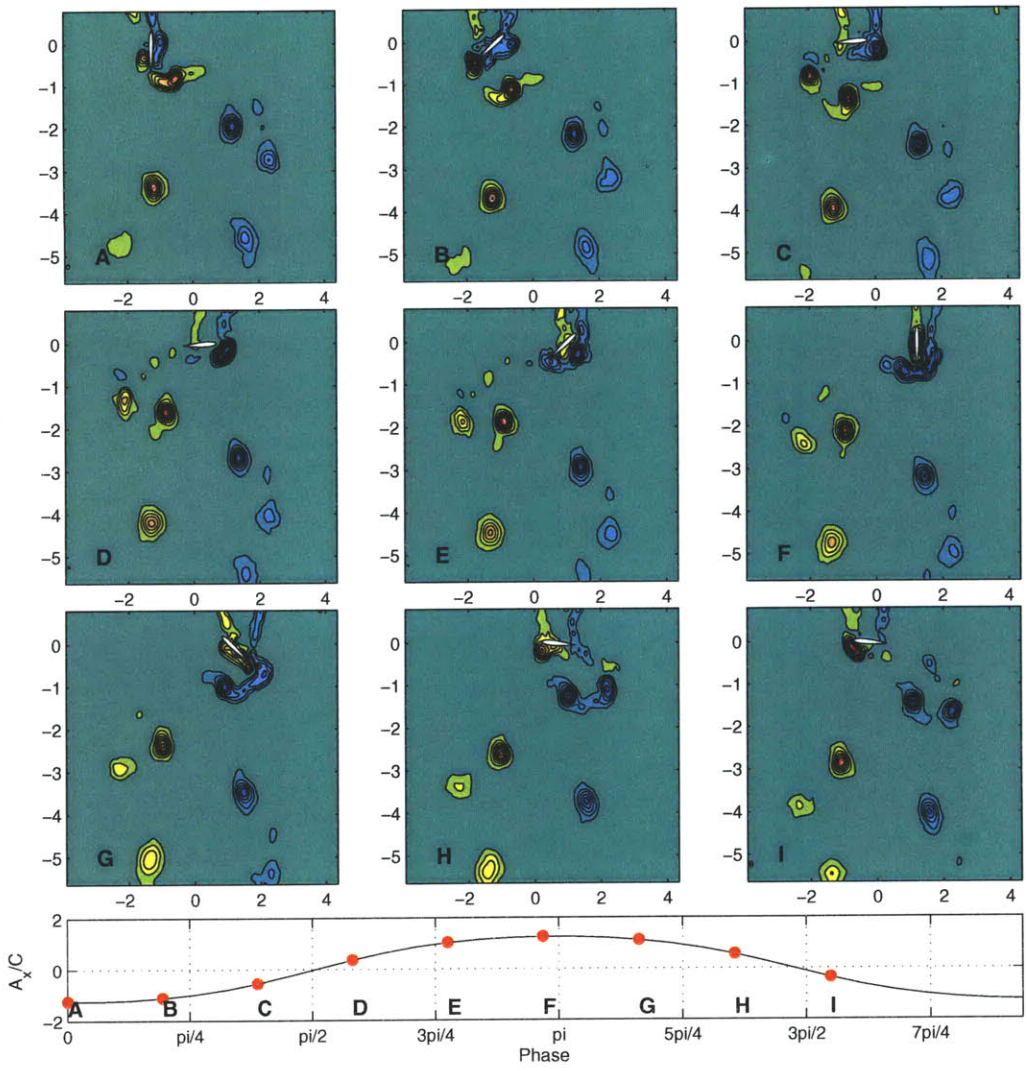

Figure H-18: Selected DPIV Images for $h_0/c = 1.23$, $St = 0.5$ and $\alpha_{max} = 25°$

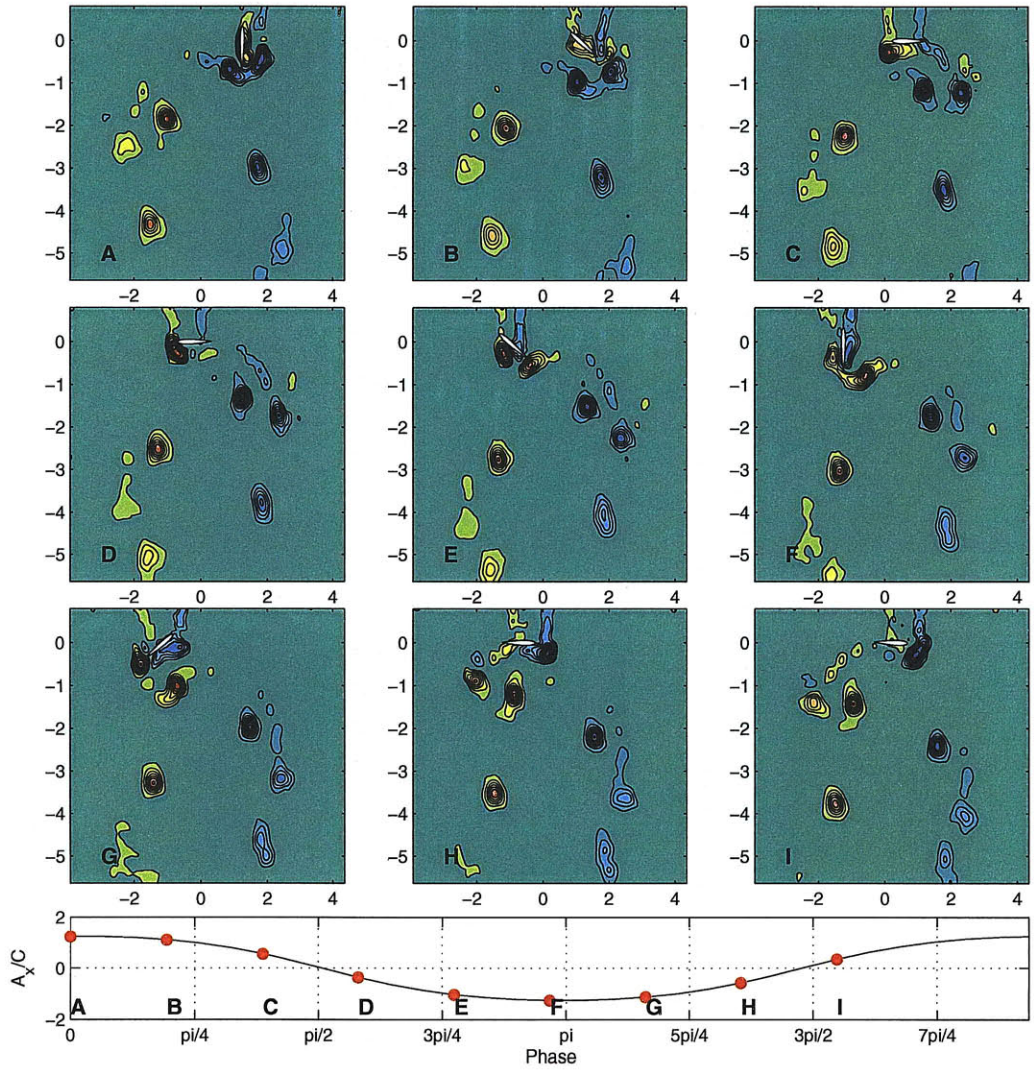

Figure H-19: Selected DPIV Images for $h_0/c = 1.23$, $St = 0.5$ and $\alpha_{max} = 30°$

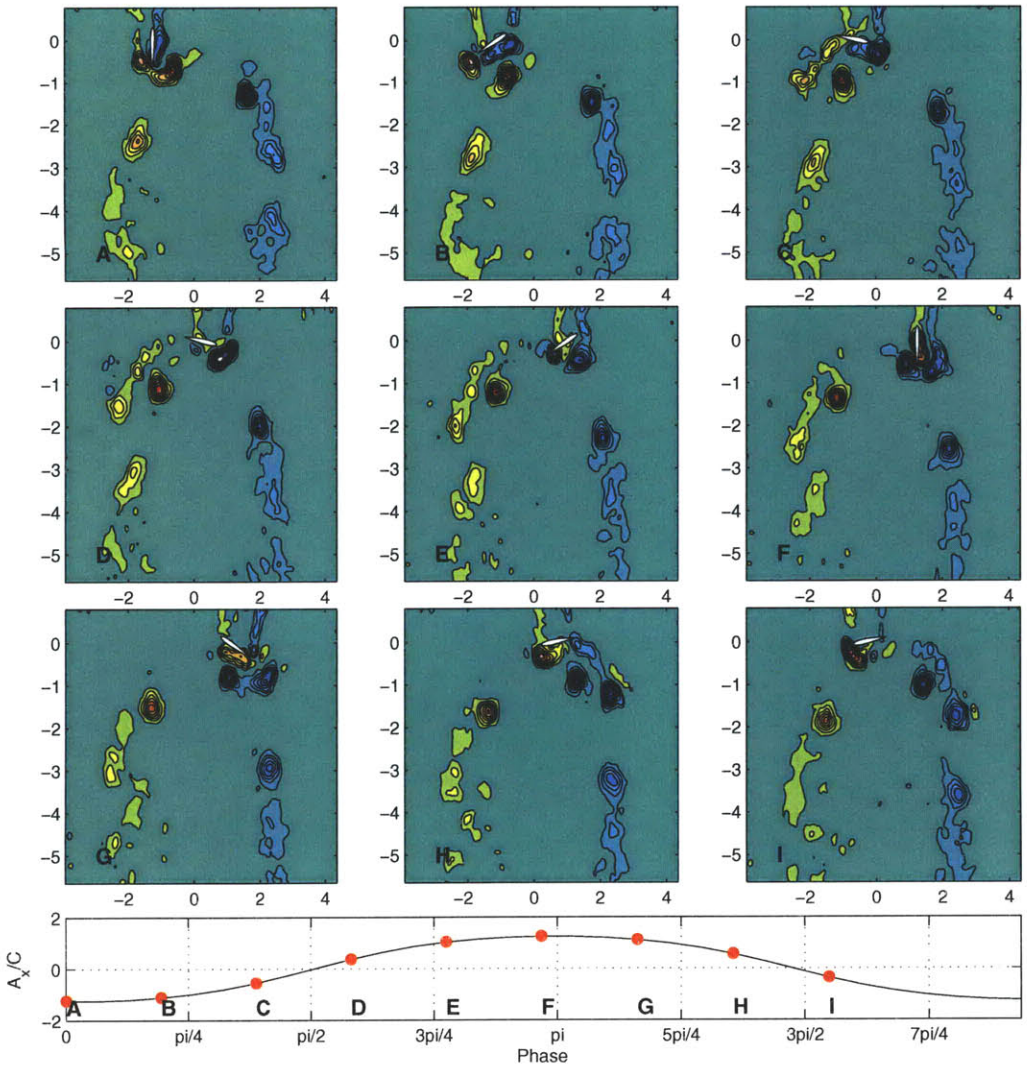

Figure H-20: Selected DPIV Images for $h_0/c = 1.23$, $St = 0.5$ and $\alpha_{max} = 39°$

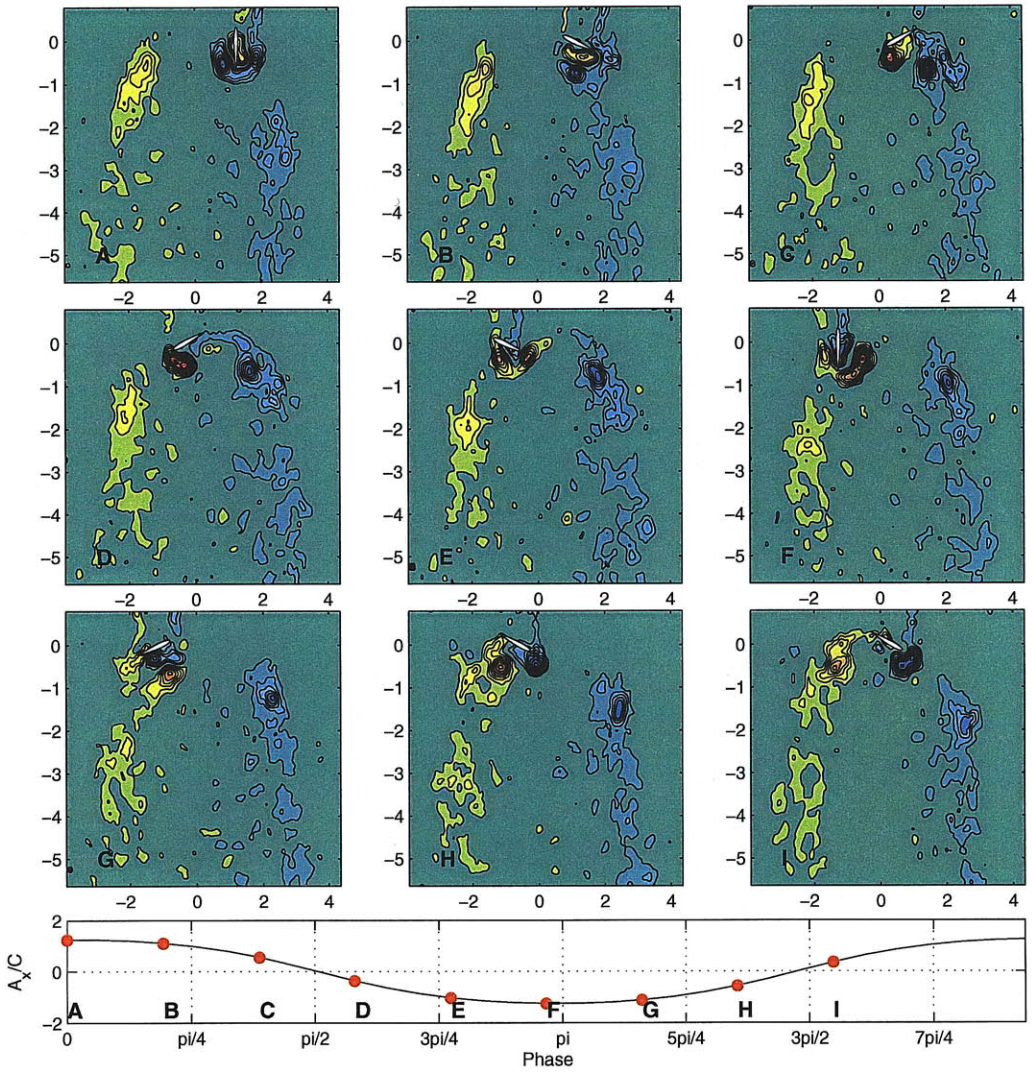

Figure H-21: Selected DPIV Images for $h_0/c = 1.23$, $St = 0.5$ and $\alpha_{max} = 53°$

Bibliography

[1] J. M. Anderson, K. Streitlien, D. S. Barrett, and M. S. Triantafyllou. Oscillating foils of high propulsive efficiency. *Journal of Fluid Mechanics*, 360:41–72, 1998.

[2] D. N. Beal, F. S. Hover, M. S. Triantafyllou, J. C. Liao, and G. V. Lauder. Passive propulsion in vortex wakes. *Journal of Fluid Mechanics*, 549:385–402, 2006.

[3] Paolo Blondeaux, Francesco Fornarelli, Laura Guglielmini, Michael S. Triantafyllou, and Roberto Verzicco. Numerical experiments on flapping foils mimicking fish-like locomotion. *Physics of Fluids*, 17(11):113601, 2005.

[4] N. Bose and J. Lien. Energy absorption from ocean waves: a free ride for cetaceans. *Proceedings of the Royal Society of London. Series B, Biological Sciences*, pages 591–605, 1990.

[5] I. G. Bryden, T. Grinsted, and G. T. Melville. Assessing the potential of a simple tidal channel to deliver useful energy. *Applied Ocean Research*, 26(5):198–204, 2004.

[6] J. D. DeLaurier and J. M. Harris. Experimental study of oscillating-wing propulsion. *Journal of Aircraft*, 19(5):368–373, 1982.

[7] J. Falnes. A review of wave-energy extraction. *Marine Structures*, 20(4):185–201, 2007.

[8] A. A. Fejer and R. H. Backus. Porpoises and the bow-riding of ships under way. *Nature*, 188(4752):700–703, 1960.

[9] J. Grue, A. Mo, and E. Palm. Propulsion of a foil moving in water waves. *Journal of Fluid Mechanics Digital Archive*, 186:393–417, 2006.

[10] L. Guglielmini and P. Blondeaux. Propulsive efficiency of oscillating foils. *European Journal of Mechanics/B Fluids*, 23(2):255–278, 2004.

[11] H. Isshiki and M. Murakami. A theory of wave devouring propulsion. IV: a comparison between theory and experiment in case of a passive-type hydrofoil propulsor. *Journal of the Society of Naval Architects of Japan*, 156:102–114, 1984.

[12] K. D. Jones, S. Davids, and M. F. Platzer. Oscillating-wing power generation. In *ASME/JSME Joint Fluids Engineering Conference, San Francisco, CA*, 1999.

[13] K. D. Jones, K. Lindsey, and M. F. Platzer. An investigation of the fluid-structure interaction in an oscillating-wing micro-hydropower generator. *ADVANCES IN FLUID MECHANICS*, 36:73–84, 2003.

[14] K. D. Jones and M. F. Platzer. Numerical computation of flapping-wing propulsion and power extraction. *AIAA paper*, 5:97–0826, 1997.

[15] T. Kinsey and G. Dumas. Parametric study of an oscillating airfoil in a Power-Extraction regime. *AIAA JOURNAL*, 46(6):1318, 2008.

[16] G. V. Lauder and P. G. A. Madden. Fish locomotion: kinematics and hydrodynamics of flexible foil-like fins. *Experiments in Fluids*, 43(5):641–653, 2007.

[17] James C Liao, David N Beal, George V Lauder, and Michael S Triantafyllou. Fish exploiting vortices decrease muscle activity. *Science*, 302(5650):1566–1569, 2003.

[18] M. E. McCormick and D. R. B. Kraemer. Ocean wave energy utilization. *Marine Technology Society Journal*, 36(4):52–58, 2002.

[19] W. McKinney and J. DeLaurier. The wingmill: An oscillating-wing windmill. *Journal of Energy*, 5(2):109–115, 1981.

[20] A. Muetze and J. G. Vining. Ocean wave energy conversion: A survey. In *Industry Applications Conference, 2006. 41st IAS Annual Meeting. Conference Record of the 2006 IEEE*, volume 3, 2006.

[21] R. Pelc and R. M. Fujita. Renewable energy from the ocean. *Marine Policy*, 26(6):471–479, 2002.

[22] M. F. Platzer, K. S. Neace, and C. K. Pang. Aerodynamic analysis of flapping wing propulsion. *AIAA paper*, pages 93–0484, 1993.

[23] K. Streitlien, G. S. Triantafyllou, and M. S. Triantafyllou. Efficient foil propulsion through vortex control. *AIAA journal*, 34(11), 1996.

[24] Graham K. Taylor, Robert L. Nudds, and Adrian L. R. Thomas. Flying and swimming animals cruise at a strouhal number tuned for high power efficiency. *Nature*, 425(6959):707–711, October 2003.

[25] M. S. Triantafyllou, A. H. Techet, and F. S. Hover. Review of experimental work in biomimetic foils. *IEEE Journal of Oceanic Engineering*, 29(3):585–594, 2004.

[26] M. S. Triantafyllou, G. S. Triantafyllou, and R. Gopalkrishnan. Wake mechanics for thrust generation in oscillating foils. *Physics of Fluids A: Fluid Dynamics*, 3:2835, 1991.

[27] M. S Triantafyllou, G. S Triantafyllou, and D. K. P Yue. Hydrodynamics of fishlike swimming. *Annual Review of Fluid Mechanics*, 32(1):33–53, 2000.

[28] P. W. Ullman. Offshore tidal power generation: A new approach to power conversion of the oceans' tides. *Marine Technology Society Journal*, 36(4):16–24, 2002.

[29] L.A. Vega. Ocean thermal energy conversion primer. *Marine Technology Society Journal*, 36:25–35, 2002.

[30] K. D. von Ellenrieder, K. Parker, and J. Soria. Fluid mechanics of flapping wings. *Experimental Thermal and Fluid Science*, 32(8):1578–1589, 2008.

[31] Q. Zhu and Z. Peng. Mode coupling and flow energy harvesting by a flapping foil. *Physics of Fluids*, 21:033601, 2009.